

12-2014

Thermo-Mechanical Characterization of Glass and its effect on Predictions of Stress State, Birefringence and Fracture in Precision Glass Molded Lenses

Dhananjay Joshi

Clemson University, dhananj@g.clemson.edu

Follow this and additional works at: https://tigerprints.clemson.edu/all_dissertations

 Part of the [Mechanical Engineering Commons](#)

Recommended Citation

Joshi, Dhananjay, "Thermo-Mechanical Characterization of Glass and its effect on Predictions of Stress State, Birefringence and Fracture in Precision Glass Molded Lenses" (2014). *All Dissertations*. 1463.

https://tigerprints.clemson.edu/all_dissertations/1463

This Dissertation is brought to you for free and open access by the Dissertations at TigerPrints. It has been accepted for inclusion in All Dissertations by an authorized administrator of TigerPrints. For more information, please contact kokeefe@clemson.edu.

THERMO-MECHANICAL CHARACTERIZATION OF GLASS AND ITS EFFECT
ON PREDICTIONS OF STRESS STATE, BIREFRINGENCE AND FRACTURE IN
PRECISION GLASS MOLDED LENSES

A Dissertation
Presented to
the Graduate School of
Clemson University

In Partial Fulfillment
of the Requirements for the Degree
Doctor of Philosophy
Mechanical Engineering

by
Dhananjay Joshi
December 2014

Accepted by:
Dr. Paul F. Joseph, Committee Chair
Dr. Sherril Biggers Jr.
Dr. Lonny Thompson
Dr. Vincent Blouin

ABSTRACT

The Precision Glass Molding (PGM) process was established as an economical and sustainable option for the production of aspherical glass optics to satisfy the increased industrial demand. Applications of precision molded aspherical lenses range from consumer electronics products such as cell phone cameras to defense and medical systems. An aspherical lens can eliminate the spherical and optical aberrations as compared to a spherical lens thus making the lens system more compact and lighter. In spite of being a clean and environmentally friendly process, the lens molding operation suffers from a few drawbacks such as lens profile deviation, stress birefringence/refractive index drop and lens cracking. Prior research has identified a lack in accurate and reliable thermo-mechanical characterization of optical glasses as an obstacle to the application of computational mechanics to resolve these issues.

The work presented in this dissertation addresses the importance of a precise determination of the thermo-mechanical material property inputs of optical glass for an accurate prediction of the state of stress during the complex thermo-mechanical loading of a glass preform during the Precision Glass Molding (PGM) process. In addition to an accurate prediction of the residual stress state in a lens, birefringence and fracture were also considered as these are direct consequences of stress. Due to the complexity of glass behavior in the relatively large temperature range where the material behavior transitions from that of an elastic solid to a viscous fluid, it is essential to characterize accurately the time and temperature dependence of the stress relaxation behavior. After understanding the weaknesses in existing stress relaxation characterizations, a set of careful experiments was designed that utilized Parallel Plate Viscometer (PPV) to perform the cylinder compression test on a glass sample. It was determined that the uniaxial compression of a cylindrical sample at an uniform temperature, with a known

friction condition at the interface, yields a high quality creep data that was used to determine accurate viscosity and viscoelastic constants of two moldable glasses – L-BAL35 and NBK-7 glass at the given temperature. Comparison of the computational solutions with closed form approximations used in an ASTM standard, revealed deficiencies at viscosity near and above 10^8 Pa·s due to specimen bulging and interface slip, and led to the development of an approximate expression for a reasonable estimate of viscosity above 10^8 Pa·s for the full range of interface friction behavior.

This study highlighted the importance of an accurate characterization of the stress relaxation function of a moldable glass which enabled the numerical examination of the effect of different levels of modeling detail of the relaxation function on the lens molding simulations. The choice of the material model and the level of detail required in performing the creep and relaxation experiments, is dependent on the problem being solved. The use of simplest viscoelastic stress relaxation function with a single exponential relaxation time that lacks much of the transient effects present in a full viscoelastic relaxation, showed minimal effect on the profile deviation of a lens but leads to an over-estimate of residual stress for the two lens shapes studied. A similar effect was observed on the stress birefringence of a lens after molding. Using numerical experiments, residual stresses were shown to be sensitive to the lower temperature limit of the viscoelastic assumption (T_L). The fracture assessment inside a molded lens was made for both radial and circumferential crack configurations. The stress state for the two configurations revealed that the radial crack orientation was more prone to failure among the two. The full viscoelastic relaxation assumption also led to higher crack tip opening displacement (CTOD) values than the simplified relaxation assumption.

ACKNOWLEDGMENTS

I would like to thank my advisor, Dr. Paul Joseph for his valuable guidance and unwavering support during the research work.

My sincere thanks to Dr. Balajee Ananthasayanam for the critical discussions related to the glass mechanics. I also would like to thank, Dr. Kathleen Richardson, Dr. David Musgraves, and Dr. Peiman Mosaddegh from Clemson's Department of Material Science and Engineering, for their support with the PPV experiments. I would like to extend my thanks to Dr. Kunming Mao, from Dassault Systèmes Corp., for the help on fracture modeling issues in Abaqus.

I would like to thank my committee members for giving good suggestions about improving the research. I also thank my teachers in the ME department who helped me gain better understanding of finite element method and solid mechanics. Finally, I would like to thank my family and friends for their endless love and care during my research.

TABLE OF CONTENTS

	Page
TITLE PAGE	i
ABSTRACT	ii
ACKNOWLEDGMENTS	iv
LIST OF TABLES	ix
LIST OF FIGURES	xi
CHAPTER	
1. INTRODUCTION	1
1.1. Lens Molding: Process and related Issues	2
1.2. Motivation.....	5
1.3. Outline of the Dissertation	11
References.....	13
2. THERMO-MECHANICAL CHARACTERIZATION OF GLASS AT HIGH TEMPERATURE USING THE CYLINDER COMPRESSION TEST: VISCOELASTICITY, FRICTION AND PPV	15
2.1. Introduction.....	15
2.2. Theory	19
2.3. Modeling Details.....	21
2.3.1. Finite Element Model of Axial Compression of Cylinder	21
2.3.2. Material Property Definitions	23
2.4. Experimental Procedure.....	26
2.5. Results.....	27
2.5.1. Convergence Study	27
2.5.2. Response of SLS Glass in the Cylinder Compression Test	30
2.5.3. Effect of Heating and Soaking	35
2.5.4. Effect of Friction on Displacement in a Creep Test	36
2.5.5. Long Time Behavior of the Creep Curve for the Cylinder Compression Test.....	39
2.5.6. Simultaneous Determination of Viscosity and Friction Coefficient	42

Table of Contents (Continued)

	Page
2.5.7. Relation of Computational Results to PPV	45
2.6. Discussion	52
2.7. Conclusion	54
References	55
3. PARALLEL PLATE VISCOMETRY FOR GLASS AT HIGH VISCOSITY	57
3.1. Introduction	57
3.2. Approximate Viscosity Formula	58
3.3. Results	62
3.4. Discussion	66
3.5. Conclusion	68
References	68
4. THERMO-MECHANICAL CHARACTERIZATION OF GLASS AT HIGH TEMPERATURE USING THE CYLINDER COMPRESSION TEST – NO-SLIP EXPERIMENTS, VISCOELASTIC CONSTANTS AND SENSITIVITY	70
4.1. Introduction	70
4.2. Theory, Modeling Details and Material Property Definitions	71
4.3. Experimental Procedure – No-Slip Boundary Condition	72
4.4. Results	73
4.4.1. The Effects of Heating, Soaking, Cooling and Residual Stresses	74
4.4.2. Validation Study of Viscosity Determination Using the No- Slip Specimen	75
4.4.3. Viscosity of L-BAL35 Using the Single Term Prony Series Approach	80
4.4.4. Determination of the Viscoelastic constants	84
4.4.5. Effects of Heating and Cooling on Viscosity Prediction	90
4.4.6. Bulk Relaxation Response of a Thin Cylindrical Sample during Compression Test	93
4.4.7. Sensitivity of Sample Imperfections on Creep Curve	97
4.4.8. Effect of Non-Uniform Temperature Distribution within Sample	99
4.5. Discussion	101
4.6. Conclusion	103
References	104

Table of Contents (Continued)

	Page
5. SENSITIVITY OF LENS SHAPE DEVIATION AND RESIDUAL STRESSES ON STRESS RELAXATION CHARACTERIZATION IN A PRECISION MOLDED LENS.....	106
5.1. Introduction.....	106
5.2. Stress Relaxation Assumptions.....	109
5.3. Validation Examples.....	110
5.3.1. Validation Example 1: Cooling of a Glass Cylinder	112
5.3.2. Validation Example 2: Quenching of infinite Plate of Soda-Lime-Silicate Glass	124
5.3.3. Validation Example 3: Sandwich Seal Test.....	128
5.4. Results.....	132
5.4.1. Convergence Study	132
5.4.2. Molding of a Simple Cylinder	134
5.4.3. High temperature elastic modulus (E)	137
5.4.4. Reference temperature (T_R)	139
5.4.5. Convective heat transfer coefficient ($h_{\text{convection}}$).....	141
5.4.6. Choice of stress relaxation function.....	144
5.4.7. Stress Birefringence Calculations	147
5.5. Discussion.....	156
5.6. Conclusions.....	157
References.....	158
6. STUDY OF LENS CRACKING USING COMPUTATIONAL FRACTURE MECHANICS	161
6.1. Introduction.....	161
6.2. Stress Analysis of Cracks and Stress Intensity Factor Calculations ..	164
6.2.1. Capturing the crack tip singularity using FEM.....	167
6.3. Stress Intensity Factor Validation Studies	170
6.3.1. A through thickness crack in 2-D Infinite plane subjected to remote tension	170
6.3.2. Penny shaped crack in 3D infinite domain subjected to remote tension	175
6.4. Computational Assessment of Stresses Near the Crack in a Viscoelastic Material	178
6.4.1. 2D plate subjected to steady state thermal and tensile loading.....	178
6.4.2. 3D block subjected to tensile and transient thermal loading ..	181
6.5. Important Steps in Modeling Crack inside the Glass Preform Lens ..	183

Table of Contents (Continued)

	Page
6.6. Fracture analysis methodology for lens molding in Abaqus	191
6.7. Computational Results of Crack Modeling Inside the Lens	195
6.8. Discussion	200
6.9. Conclusions.....	201
Reference	202
7. CONCLUSIONS AND FUTURE WORK	204
7.1. Discussion	204
7.2. Conclusions.....	205
7.3. Future work.....	207
Reference	208

LIST OF TABLES

Table		Page
1.1	The three stress relaxation definitions of the molding glasses used in the validation study [2]. Material Set 3 approximates the behavior of the molding glass, L-BAL35, while Material Sets 1 and 2 should be considered as hypothetical glasses. At the reference temperature, T_R , the log of the equilibrium viscosity is 10.0 for all cases.....	9
2.1	Thermal and mechanical properties of Soda-Lime-Silica glass (SLS) from Duffrene et al. [5]. The viscoelastic behaviors of the glass are presented in Table 2.2	24
2.2	The stress relaxation definitions of the Soda-Lime-Silica glass (based on Table I and II from Duffrene et al. [5]) used in the current study. Refer to Equations 2.3 and 2.4 for the functional forms. The values of bulk relaxation parameters (v_i) were modified to the format acceptable to ABAQUS.	25
2.3	Thermo-mechanical properties of L-BAL35 glass (Ananthasayanam et al. [1], OHARA [24]), N-BK7 Glass [25] and Inconel (Precision Cast parts Corp. [26]).....	25
2.4	Convergence study for creep displacement, bulge radius and folded distance (refer to Figure 2.2) for different levels of mesh refinement. The times $t = 1475$ s and 22,209 s in the table correspond to 10% and 50% deformation levels achieved for the Baseline mesh (2000 elements)	30
2.5	Mesh convergence study for time and creep displacement when a node originally 0.1 mm away from the corner first comes into contact with the mold	30
3.1	Log of normalized viscosity predicted by the no-slip formula when $\eta = 10^8$ Pa·s and the special value μ^*	60
3.2	Prediction of $\text{Log}(\bar{\eta})$ using Eqns. (3.2-3.4) and viscoelastic creep data.....	64
4.1	Sample parameters and viscosity values used to match the experimental creep data in Figure 4.5. The non-isothermal results correspond to the numerical experiment presented in Section 4.4.5	81

List of Tables (Continued)

Table	Page
4.2 Stress relaxation prony series coefficients obtained using the experimental data for L-BAL35 in Figure 4.5 for the case of $H/D = 0.68$, $T = 575^{\circ}\text{C}$ and $\log(\eta_{\text{eq}}) = 8.958$ Pa·s. The dilatational (bulk) response was assumed to be similar to that of SLS glass	85
4.3 Stress relaxation prony series coefficients obtained using the experimental data for N-BK7 in Figure 4.1 for the case of $H/D = 0.7$, $T = 644.1^{\circ}\text{C}$ and $\log(\eta_{\text{eq}}) = 8.98$ Pa·s. The dilatational (bulk) response was assumed to be similar to that of SLS glass	89
4.4 Thermo-mechanical properties of fused silica glass from [18]	91
5.1 Residual stresses at the center of the cylinder at room temperature for cooling from 430°C to 20°C for three different material behavior assumptions.....	114
5.2 Convergence study of steep meniscus lens during various stages of lens molding. Reported values indicate percentage change of values obtained for a refined mesh (20,499 elements) relative to values for a baseline mesh (13,641 elements)	133

LIST OF FIGURES

Figure	Page
1.1	Comparison of temperature dependent viscosity for L-BAL35 6
1.2	The Deviation on upper and lower surface of steep meniscus lens from experimental and computational results. Material set 3 and modified set have the same initial elastic modulus (E) but the different terms in the shear and bulk relaxation function [2]. Refer to Table 1.18
1.3	Deviation of the steep meniscus and bi-convex lenses for the three different stress relaxation behaviors listed in Table 1.1. For Material Sets 1 and 2 the press time, $t_p = 127$ s, which agrees with the press time in the actual process. Press time was lowered for the Material Set 3 results as indicated, in order to maintain a constant value of center thickness. (Taken from [2])10
2.1	Finite element mesh used in the simulations of the cylinder compression test, including details of the interaction property definitions and coupling constraints. 22
2.2	Schematic of a deformed and undeformed cylindrical specimen for a creep test with no-slip boundary conditions to define parameters used in Tables 2.4 and 2.5..... 28
2.3	Creep-relaxation response to (a) shear loading ($\tau = 25$ MPa) and (b) hydrostatic compression ($\Delta P = 25$ MPa) for an SLS glass for the four different material behaviors outlined in Section 2.5.2 32
2.4	Initial elastic and short time viscoelastic responses of an SLS glass for four different material behaviors in a numerical experiment of the cylinder compression test where $P = 10$ N, $D = 10$ mm, $H = 10$ mm and (a) $\mu = 0$, (b) $\mu = \infty$. The displacement component δ_{VE} that is defined in (a) denotes the additional displacement caused by viscoelastic mechanisms, while δ_b is the displacement caused purely by the dilatational (bulk) viscoelastic response 34
2.5	Deformed shape and axial stress distribution ($S_{22} = \sigma_y$ in Pa) for a cylindrical SLS glass sample ($H/D = 0.2$) during the cylinder compression creep test for conditions of no-slip after 1 hour has elapsed..... 37

List of Figures (Continued)

Figure	Page
2.6 Effect of interface friction on the creep curve for (a) $H/D = 1$ and (b) $H/D = 0.2$ using SLS glass.....	39
2.7 Viscoelastic displacements, δ_{VE} and δ_b , as a function of time for (a) $H/D = 0.1$ and (b) $H/D = 1$ for no slip ($\mu = \infty$) and no friction ($\mu = 0$) using SLS glass.....	41
2.8 Experimental (dots) and computational (solid lines) creep curves for N-BK7 glass samples ($H/D = 0.22$) pressed with Pt and Ni foil at 651.5°C and 631°C , respectively. The eight cases (#1 - #8) of viscosity and friction combinations, presented as “ $\log(\eta)/\mu$,” are for Pt foil: 1) $8.74/0$, 2) $8.653/0.11$, 3) $8.554/0.22$, 4) $8.174/\infty$; and for Ni foil: 5) $9.33/0$, 6) $9.259/0.1$, 7) $9.176/0.2$, 8) $8.777/\infty$	44
2.9 Viscosity estimate based on no-slip and no-friction formulae of creep experimental data from Figure 2.7. Pt foil results (top) and Ni foil (bottom).....	47
2.10 The effect of friction and slip on the viscosity predictions made using the no-friction and no-slip analytical formulas for a sample having $H/D = 0.5$. The creep data was generated computationally with SLS glass and the indicated coefficient of friction	49
2.11 Same as Figure 10 for very small deformation plotted with respect to time. The transient effect of active viscoelastic mechanisms at short time scales is visible.....	50
2.12 Maximum value of Log viscosity predicted using the no-slip and no-friction formulas as a function of the height to diameter ratio of the glass cylinder. The creep data was computationally generated using the indicated coefficient of friction and SLS glass properties in Table 2.2 with relaxation times adjusted to have $\text{Log}(8.0)$	51
3.1 Schematic of a parallel plate viscometer	57
3.2 Viscosity predictions using Eqns. (1-3) applied to computational viscoelastic creep data. Equation (4) is based on the linear approximations presented as dashed lines for $H/D = 1$ and solid lines for $H/D = 0.5$. The vertical lines identify μ^* for each cases.....	61

List of Figures (Continued)

Figure	Page
3.3 Viscosity predictions using computational, viscoelastic creep data for the three combinations of μ & $\text{Log}(\bar{\eta}) = 0.55 \text{ \& } 8, 0.353 \text{ \& } 9$ and $0.15 \text{ \& } 10$ using Eqn. (3.2) (dashed line), Eqn. (3.3) (light solid line) and Eqn. (3.4) (dark solid line). The exact viscosity values are indicated with dotted lines	63
3.4 Bulged shapes for an L-BAL35 glass cylinder with $H/D = 0.5$ after 50% of axial compression.....	65
3.5 Normalized position of the original radius (R_c) after sliding along the mold surface as a function of friction coefficient. A change in the scale occurs at $\mu = 0.1$	66
4.1 Validation of the sticking boundary condition approach using N-BK7 and two different cylinder geometries (see also Figure 4.4). Viscosity at the reported temperature according to the glass manufacture is in the range of 8.80 - 8.94 Pa·s [10].....	76
4.2 The displacement, δ_{VE} , obtained from the difference of the curves in Figure 4.1 for selected values of viscosity to show how precisely the viscosity can be determined using this approach.....	77
4.3 The displacement, δ_{VE} , obtained from the difference of the curves for the case of $H/D = 0.7$ in Figure 4.1 for selected values of viscosity to show how precisely the viscosity can be determined using this approach.....	78
4.4 Viscosity prediction of N-BK7 experimental data from Figure 4.1 using ASTM formula [14] (solid line). Viscosity values obtained from the simulations associated with Figure 4.1 are plotted as dashed lines.....	80
4.5 Comparison of experimental and computational creep curves for L-BAL35 at three different temperatures. The viscosity results are summarized in Table 4.1.....	81

List of Figures (Continued)

Figure	Page
4.6	Viscosity prediction of L-BAL35 experimental data from Figure 4.5 using the ASTM standard formula [14] (solid line). Viscosity values obtained from the simulations associated with Figure 4.5 are plotted as dashed lines 82
4.7	Viscosity-Temperature (η -T) plot for L-BAL35: Comparison of calculated isothermal viscosity (symbols) with the viscosity data obtained from OHARA [15] (dotted) and Gaylord [17] (solid) (see Table 4.1 for values) 83
4.8	Viscoelastic displacement (δ_{VE}) for L-BAL35 for two no-slip experiments presented in Figure 4.5 compared to computational results. The data used for the prony series fit (Table 4.2) is presented in Figure 4.8 (a) ($H/D = 0.68$ at 575°C) and the prediction is presented in Figure 4.8(b) ($H/D = 0.73$ at 567.8°C) 86
4.9	Viscoelastic displacement (δ_{VE}) for N-BK7 from three experiments compared to computational results: (a) prony series fit (Table 4.3) using no-slip data from Figure 4.1 ($H/D = 0.7$ at 644.1°C), (b) prediction for Pt foil slip data from Figure 2.7 in the Chapter 2 and (c) prediction for Ni foil slip data from Figure 2.7 in Chapter 2 88
4.10	Comparison of creep curves plotted using isothermal and non-isothermal computational approaches for the L-BAL35 sample with $H/D = 0.73$ at 575°C and material property data presented in Table 4.2 using $\log(\eta_{eq}) = 8.954$ Pa·s. The isothermal results assume the creep test is conducted at a constant temperature, while the non-isothermal approach simulates the full thermo-mechanical loading cycle, which includes raising the temperature to 625°C before lowering to 575°C 93
4.11	The bulk viscoelastic response of SLS glass [3] as a percentage of the total viscoelastic response ($100\% \times \delta_b / \delta_{VE}$) as a function of time for a numerical creep experiment. The circles at $t = 250$ s indicate the values reached by the respective curves at $t = 100,000$ s 94
4.12	The effect of the equilibrium bulk modulus, K_∞ , on the percentage of the bulk viscoelastic response relative to the total viscoelastic response ($100\% \times \delta_b / \delta_{VE}$) 96

List of Figures (Continued)

Figure	Page
4.13 The effect of geometric imperfections of the test sample on the creep curve for an SLS glass. The result for a geometrically perfect sample (1) is compared to results for a sample with conical top with a 0.5° taper (2) and a sample having non-parallel top and bottom faces that are off by 0.5° (3)	98
4.14 The effect of a linear temperature variation in the axial direction of the cylinder on the creep curve ($H/D = 1, \mu = 0$). The top and bottom faces of the cylinder are kept at different temperatures during the entire test. TRS behavior is assumed using the parameters: $T_R = 550^\circ\text{C}$, $C_1 = 25$ and $C_2 = 129^\circ\text{C}$	99
4.15 Comparison of the creep curve for a non-uniform temperature distribution ($\Delta T = 10$ degree case from Figure 4.14) with uniform temperature creep curves using different viscosity ($H/D = 1, \mu = 0$). TRS behavior is assumed using the parameters: $T_R = 550^\circ\text{C}$, $C_1 = 25$ and $C_2 = 129^\circ\text{C}$	100
5.1 Viscosity for L-BAL35 glass (solid line) near the T_{SL} (440°C)	116
5.2 Variation in the value of the steady state, maximum principal stress in $r-\theta$ plane at the center of the cylinder for three different material behavior assumptions after uniform surface cooling from an initial temperature of T_0 . In Figure 5.2a a log scale with units of Pa is used, in Figure 5.2b, a scale of MPa is used, while in Figure 5.2c and 5.2d, a scale of Pa is used.....	118
5.3 Cooling of cylinder from $T_0 = 590^\circ\text{C}$ at rate of $q_0 = 0.25^\circ\text{C/s}$ (a) Cooling rate for surface and center of cylindrical sample, (b) and (c) details of (a) at the given times, (d) temperature difference (ΔT) between the center and surface of the cylinder, (e) Maximum principal stress in the $r-\theta$ plane at the center of the sample	120
5.4 Stress distribution inside a cylindrical sample subjected to cooling from 590°C to 20°C at the rate of 0.25°C/s	121

List of Figures (Continued)

Figure	Page
5.5 Comparison of the maximum principal stress in the r- θ plane for cooling from 590°C to 20°C using structural relaxation and the two different stress relaxation behaviors: a) elastic, b) viscoelastic	122
5.6 Effect of choice of T_{SL} on the maximum (residual) principal stress in the r- θ plane at the four given locations within the lens. The vertical and horizontal scales are normalized with respect to the baseline values of $\sigma_0 = 4.24e06$ and $T_{SL0} = 440^\circ\text{C}$	123
5.7 Comparison of different thermal expansion behavior of glass based simple assumptions (α_L and α_G) and structural relaxation properties from literature [18 and 20]	125
5.8 Stresses inside a quenched Soda-Lime-Silicate plate from literature [34] and using simulations with a different expansion behaviors given in Figure 5.7	126
5.9 Viscosity of G-11 glass predicted based on Equation (5.7) and experimental data [19] (solid line), FEA simulation output from UTRS (circles) and WLF fit (dashed line) of the entire data.....	130
5.10 Stresses in the sandwich seal with UTRS subroutine implementation (solid line), with WLF parameter input (dashed line), and effect of no structural relaxation (letting $x=1$ in Equation 5.7) (dash and dotted line) compared with the experimental predictions (circles).....	131
5.11 Convergence of In-Plane principal stresses at a vertical section 5 mm away from central axis of the steep meniscus lens for different meshes and different molding stages considered. (a) End of Pressing, (b) End of Slow Cooling, (c) End of Gap creation, (d) End of Process.....	134
5.12 (a) Temperature-viscosity relationship calculated by best fit of WLF equation and corresponding data (b) Evolution of stress with respect to cooling time for various TRS fits. Vertical lines indicate the value of T_L for respective curve obtained by using the best fit	136
5.13 Sensitivity of high temperature Elastic modulus on shape deviation for (a) Bi-Convex (b) steep meniscus Lens	138

List of Figures (Continued)

Figure	Page
5.14 Sensitivity of Reference Temperature (T_R) on shape deviation for (a) Bi-Convex (b) Steep meniscus lens	140
5.15 Sensitivity of convective coefficient ($h_{convection}$) on shape deviation for (a) Bi-Convex (b) Steep meniscus lens.....	143
5.16 Bi-Convex: Effect of Stress relaxation modeling detail on stress state at a vertical section 5 mm away from central axis. (a) End of Pressing, (b) End of Slow Cooling, (c) End of Gap creation, (d) End of Process.....	145
5.17 Steep Meniscus: Effect of Stress relaxation modeling detail on stress state at a vertical section 5 mm away from central axis. (a) End of Pressing, (b) End of Slow Cooling, (c) End of Gap creation, (d) End of Process.....	146
5.18 Stress birefringence (nm/cm) inside the Bi-convex lens shape after molding for different material behavior assumptions (a) Full Viscoelastic (Eq. 5.4) (b) Shear Viscoelastic (Eq. 5.3) and (c) Single term Shear model (Eq. 5.2).....	148
5.19 Figure 5.19. Stress birefringence (nm/cm) inside the steep meniscus lens shape after molding for different material behavior assumptions (a) Full Viscoelastic (Eq. 5.4) (b) Shear Viscoelastic (Eq. 5.3) and (c) Single term Shear model (Eq. 5.2)	150
5.20 Stress birefringence distribution (nm/cm) inside the bi-convex lens shape after molding for different material behavior assumptions along the thickness of the lens at different section of lens. (a) At the central axis of the lens (b) at 5 mm away from the axis of lens.....	151
5.21 Stress birefringence distribution (nm/cm) inside the steep meniscus lens shape after molding for different material behavior assumptions along the thickness of the lens at different section of lens. (a) At the central axis of the lens (b) at 5 mm away from the axis of lens	152

List of Figures (Continued)

Figure	Page
5.22 Stress birefringence (nm/cm) inside the steep meniscus lens shape after molding for different TRS assumptions (a) based on WLF fit of data from [2] (b) based on UTRS subroutine (the same relaxation times for viscosity and volume, Refer to Equation 5.7)	153
5.23 Stress birefringence (nm/cm) inside the steep meniscus lens shape after molding for different slow cooling rates during molding cycle (a) baseline case with $q_0 = 0.288^\circ\text{C/s}$ (b) with $q = 0.33 \times q_0 = 0.096^\circ\text{C/s}$ (c) with $q = 3 \times q_0 = 0.864^\circ\text{C/s}$	154
5.24 Stress birefringence (nm/cm) inside the steep meniscus lens shape after molding for TRS and slow cooling rate sensitivity study (a) At the central axis of the lens (b) at 5 mm away from the axis of lens	155
6.1 Representation of stress field around the crack tip. Crack tip also acts as an origin of cylindrical coordinate system used to define the stresses and displacements	165
6.2 Regular Second order quadrilateral element (left), singular element with mid-side nodes 5 and 7 moved to a quarter length away from collapsed nodes 1, 4, 8 which share the same geometric coordinates (right)	168
6.3 Comparison of the nodal stresses along the radial direction with the analytical solution for two different meshes. K estimates based on the nodal stresses for the data selected in the given range, are shown in the right. The error value in the legend indicates the percentage error in value of estimate of K with respect to the normalized value (unity). (a) 1x4x4 elements (b) 1x4x16 elements	173
6.4 The relative error in calculation of stress intensity factor from Abaqus (K_A) and analytical solution (K_0). (Left) first order elements and (right) second order elements. Horizontal lines correspond to the mean value of the respective data points	175
6.5 (a) Schematic of penny shaped crack subjected to remote tensile stresses. (b) Quarter-section of an actual finite element mesh near crack tip	176

List of Figures (Continued)

Figure	Page
6.6	The relative error in calculation of stress intensity factor from Abaqus (K_A) and analytical solution (K_0). (Left) coarse mesh and (right) fine mesh. Horizontal lines indicate the mean value of the respective data points 177
6.7	(a) Normalized stresses ahead of the crack tip at given temperature for three different cases and (b) 590°C case at different time/deformation levels (close-up view on the right). Deformation level can be inferred from the horizontal scale. For example, top curve has deformed to 25% of its original width 180
6.8	(a) Normalized stress distribution ahead of the crack tip during slow cooling (Cooling1) stage at given times (close-up view on the right) (b) normalized stresses at end slow cooling and end of process stages for different material behaviors (VE - Viscoelastic, ST -Single Term in shear) 182
6.9	Crack tip opening displacement for different material models 183
6.10	(a) The location of maximum radial stresses (S_{11}) inside the lens at end of slow cooling (one half of lens shown) (b) Comparison of S_{11} at two locations: at the center of lens (solid) and near outer radius of lens (dashed) 185
6.11	Bubble fogs generated during reheat-Pressing of the N-BK7 [®] preform that was damaged as result of crack. The length of pattern in above picture is smaller than 2 mm. This picture is obtained from [15] 187
6.12	Representation of circumferential crack in a sector model 189
6.13	Global Mesh Model of 2.5° with detail of the mesh near the crack-line for the circumferential crack 190
6.14	The partial geometric model (Left) for the steep meniscus lens preform having a circumferential crack and (right) meshing detail across the section A-A 191

List of Figures (Continued)

Figure	Page
6.15 Crack tips used in reporting stress intensity factor results, radial crack (left) and circumferential crack (right)	194
6.16 Normal stress distribution near the crack tip for (a) Circumferential crack, (b) Radial crack	196
6.17 Comparison of CTOD for Full VE material (solid) and Single term shear relaxation (dashed) for (a) Radial, (b) Circumferential cracks. Circles indicate respective asymptotic values at end of final cooling stage	197
6.18 Comparison of CTOD for two cooling rates: $q_0 = 0.288^\circ\text{C/s}$ (solid) and $q = 3 \times q_0 = 0.864^\circ\text{C/s}$ (dashed) for two crack configurations (a) Radial, (b) Circumferential. The Viscoelastic material behavior (VE) was assumed. Circles indicate respective asymptotic values at end of final cooling stage	199

INTRODUCTION

Precision Glass Molded optics is widely used in an array of commercial as well as special application areas such as biotechnology, defense and health care. Aspherical lenses, which help to eliminate aberrations associated with spherical lenses, are gaining popularity due to their compact design as compared to their spherical counterparts. Conventional manufacturing of an aspherical lens involves several concerns such as, the higher cost and longer duration of the production process, as well as environmental issues due to the generation of micro-particles from grinding. The process of lens molding, on the other hand, is cost-effective and is one of the cleanest and environmentally friendly procedures of producing the lenses. In spite of these advantages, the lens molding operation suffers from a few drawbacks such as lens profile deviation, stress birefringence/refractive index drop and lens cracking.

Computational mechanics has been used to account for the complex thermo-mechanical behavior of glass during forming processes such as lens molding, hot embossing, injection molding, thermoforming and extrusion. Compared to more costly empirical approaches that are commonly used, computational mechanics has the potential to efficiently address issues in precision lens molding such as lens profile deviation [1-3], stress birefringence [4, 5], and lens cracking, as well as similar issues in extrusion processes such as preform die swell in glass [6] and polymers [7], and cavity shape distortion for polymers [8] and recently for glass [9].

As shown by Ananthasayanam et al. [1,2] an obstacle to reliable computational solutions of these problems is the lack of an accurate set of thermo-mechanical glass property inputs, which include viscosity (η), the initial elastic response (E , G), viscoelastic parameters in both

shear ($G_1(t)$) and dilatation ($G_2(t)$), structural relaxation parameters and the temperature dependence of these quantities. While there have been recent studies that address the structural relaxation behavior of so-called moldable glasses [10-12], there has been very limited data on the viscoelastic characterization of these types of glasses. There have been studies [13] to characterize viscoelastic properties of soda-lime-silica glass using an independent experiment for the deviatoric (shear) and dilatational (bulk) part of the deformation. This work involved a novel approach to measure the shear relaxation using a spring sample while, a cylindrical sample for bulk relaxation. Unfortunately, the same approach cannot be easily applied to optical glasses that have low glass transition temperature and different thermal expansion characteristics.

The goal of the current study is to extend the work of Ananthasayanam [1] from an examination of the final size and shape of a molded lens, which is a global characteristic, to an investigation of the consequences of the thermo-mechanical history on the quality of the lens, which, from a continuum point of view, is a local characteristic. While the study by Ananthasayanam [1] demonstrated the ability to predict such phenomena as residual stresses, birefringence and fracture, there were some material property weaknesses that needed to be addressed.

1.1 Lens Molding: Process and related Issues

Lens molding is a type of hot forming process in which a lens is manufactured by pressing a glass gob of suitable optical glass at high temperature against a pair of polished mold surfaces that assume the designed profile of the lens. If an aspherical lens shape is desired to be molded, the mold cavity would have an aspherical profile, and the resulting molded lens would be very close to that profile. The substrate or molds are typically made of

metals such as tungsten carbide, which are machined to a very precise cavity shape and are coated with suitable coating material to improve life and prevent the mold surfaces from sticking to the glass. The ideal materials for the mold would have low thermal expansion behavior, high thermal conductivity along with minimal chemical interaction with glass. The molds are enclosed inside the chamber having a controlled environment. The molds along with the glass preform /gob are heated to a high enough temperature and allowed to soak for a suitable amount of time usually in a nitrogen environment. Once the preform reaches a uniform pressing temperature, the molds move closer and a suitable pressing force is applied beginning the molding operation. The glass preform starts to take shape of the mold cavity as the molds continue to move closer to one another. Once the designed center thickness (CT) of the lens is achieved, the applied force is reduced and the lens-mold assembly is cooled slowly under a nitrogen environment. The terms such as molding temperature, pressing force, cooling rate are commonly referred to as “process parameters” in the technical jargon. Once the glass lens cools below its glass transition temperature (T_g), the molds are opened by a small amount creating a gap, thus reducing the pressing force to zero. Subsequently, the lens is subjected to a faster cooling rate until eventually the lens is cooled to room temperature.

One of the important issues in this process is the degree of “closeness” of the actual lens profile to the designed lens profile. This degree of closeness is referred to as the lens profile deviation or simply “deviation” – which is a geometric difference between the desired and the obtained profile of the manufactured lens. The deviation is mainly due to the mismatch between the thermal expansion behavior of the mold material and the glass. It is noted that the volume change of glass is highly non-linear around the glass transition, i.e., T_g , temperature range, which is also very sensitive to changes in temperature and rate of cooling.

This rate dependent expansion behavior of glass is commonly referred to as “volume or structural relaxation.”

As mentioned before, other issues in lens molding involve stress birefringence (described in Chapter 5) and fracture (Chapter 6) that are closely affected by the thermo-mechanical properties and process parameters. Stress birefringence is an artifact of the effect of the thermal and mechanical loading history on the lens during the molding cycle. The loading history induces an optical anisotropy within the lens which creates the double refraction phenomenon, which is the splitting of an incident ray into two rays that take different paths. Birefringence inside the molded lens induced by thermo-mechanical stresses during molding is undesirable and can make the lens unusable. Similar to this birefringence phenomenon, residual stresses can also cause a serious failure of a lens in form of cracking during molding. A small inclusion or bubble trapped inside the lens preform can grow/propagate if high enough stresses are experienced within its vicinity.

The complex interplay between the glass’s material behavior and external loadings can lead to the desired shape of a lens that is free of birefringence and cracks. This goal makes the glass molding process a challenging mechanics problem. The manufacturing related issues can potentially be resolved by making an efficient use of an accurate knowledge of thermo-viscoelastic behavior of the optical glass coupled with computational mechanics. The computational mechanics approach to lens molding to resolve the above issues will be explored in the rest of this dissertation.

1.2 Motivation

As stated earlier the motivation for this study mainly came from the previous study by Ananthasayanam [1] that lacked the reliable thermo-mechanical property input to simulate the lens molding process beyond seeking the lens shape deviation. In that study, the computational approach was successfully applied to validate the experimental lens shape deviation, which is measured in microns, of a Bi-convex lens. This approach was later applied to a Steep Meniscus type of lens. After performing simulations, it was realized that the final profile and press time of the molded meniscus lens were not matching with the experimentally determined values under the same process conditions. The deviation of the lens profile was over-predicted by a factor of about two and the press time was under-predicted by more than a factor of three. These incorrect predictions from the model were due primarily to the temperature dependent viscoelastic material characterization of L-BAL35 glass. This characterization was based on force-displacement data from ring compression tests that was assumed to be at uniform temperature, but was later determined to be off by about 9-18°C [1]. The data that shows this error in viscosity and/or temperature is presented in Figure 1.1.

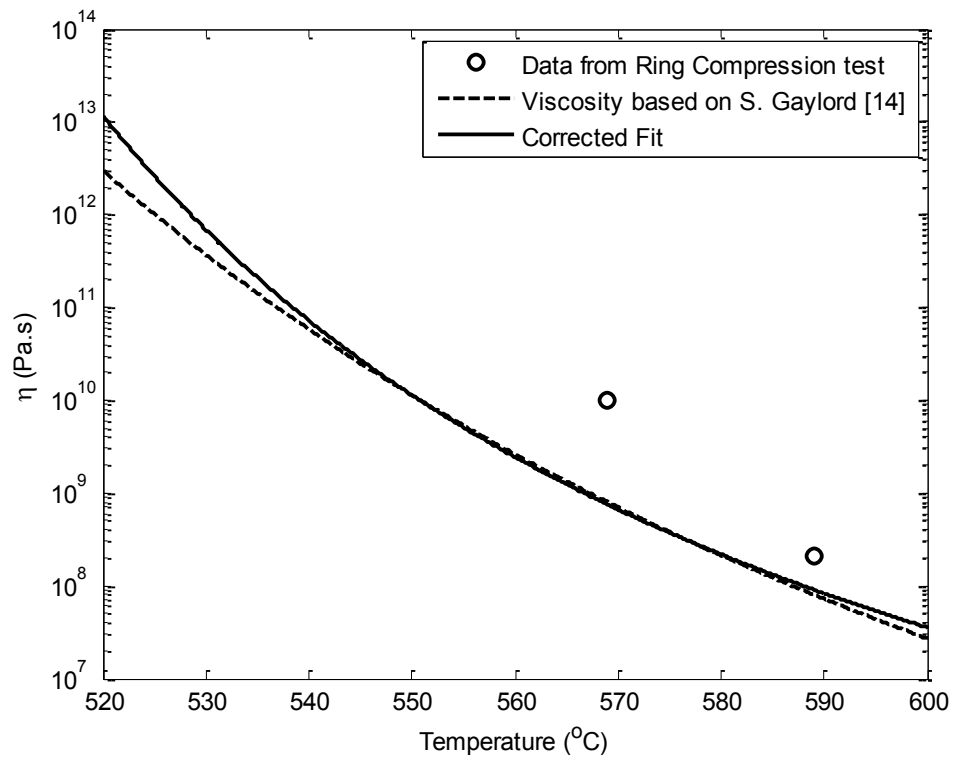


Figure 1.1. Comparison of temperature dependent viscosity for L-BAL35.

The first aspect that had to be corrected was the temperature dependence of the viscosity and the viscoelastic material properties. The conclusion from the data in Figure 1.1 was that the glass samples from the ring compression test were at a lower temperature, the magnitude of which was determined by a horizontal shift to the data from [14] in the figure. A revised fit of the viscosity data based on data from the glass manufacturer was generated as shown in Figure 1.1. However, from the point of view of the validation of the steep meniscus lens, this correction alone was not enough to explain the mismatch. As a result of the improved TRS behavior, the deviation dropped by about 5 microns, which was still off by about 7 microns from the target value.

While the explanation of the additional 7 microns is explained below, the primary motivation in this Chapter concerns this TRS behavior. As will be described in Chapters 2-4, the issues encountered in characterization of glass based on the ring compression test were understood and a combined experimental-computational approach was adopted in obtaining more precise viscosity and viscoelastic material characterization of an optical glass.

In addition to the difficulty with temperature dependence, the incorrect creep data obtained from the ring compression test led to too low of an estimate of the initial elastic modulus of the glass at high temperature. While the actual data of the elastic modulus of L-BAL35 at high temperatures was not available, the literature [15] suggested the drop of about 1/10 of its room temperature value of glass at higher temperatures. This idea was tested in the lens molding simulations and it was found that the high temperature elastic modulus of glass had an effect on the deviation and the simulation predicted the experimental results with a close match.

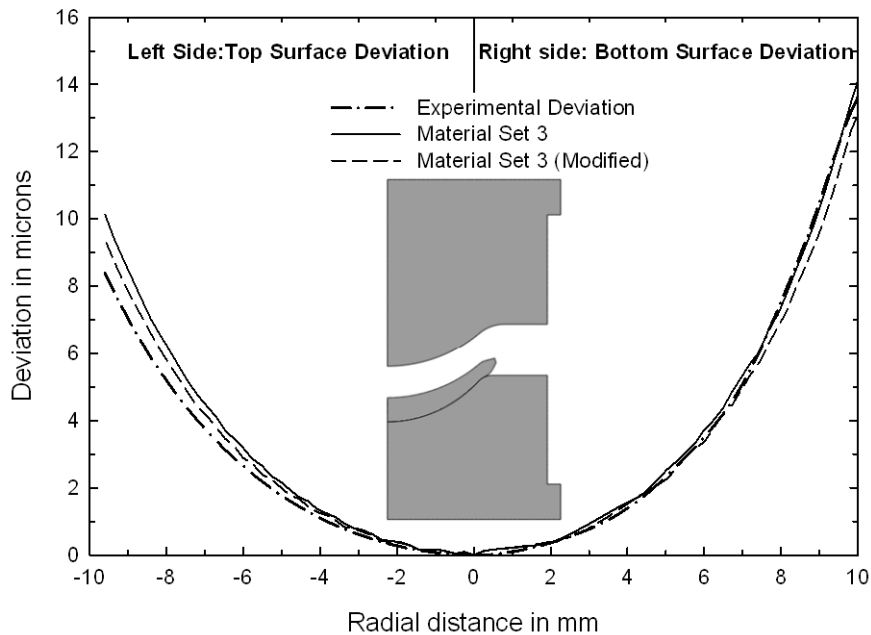


Figure 1.2. The Deviation on upper and lower surface of steep meniscus lens from experimental and computational results. Material set 3 and modified set have the same initial elastic modulus (E) but the different terms in the shear and bulk relaxation function [2]. Refer to Table 1.1.

Figure 1.2 reveals the effect of increasing the elastic modulus to 10 GPa on the deviation of the steep meniscus lens. The computational results match closely with the experimental results and that the difference between the two different material sets used is small. The simulation performed with elastic modulus close to its room temperature value ($E=100$ GPa) reveal very small difference in deviation [2] than that plotted in Figure 1.1. It was found that the sensitivity of high temperature elastic modulus on the profile deviation for the steep meniscus was negligible for the case of the Bi-convex lens shape as explained later.

In the light of these results, the effect of stress relaxation function and elastic modulus was examined for two lens shapes. The three choices of materials sets that were selected for the study differed mainly in the following aspects: level of detail in modeling stress relaxation

function (multiple prony term vs. single term representation of the relaxation function), initial elastic modulus at high temperature and temperature-viscosity relationship of glass. The choices are given in the Table 1.1 below are taken from [2].

Stress Relaxation Definitions							
Shear Relaxation Function, $\psi_1(t) = \frac{G_1(t)}{2G_0}$		Hydrostatic Relaxation Function, $\psi_2(t) = \frac{G_2(t)}{3K_0}$		TRS Behavior			Temperature Dependent Elastic Modulus
Material Set 1							
w_i	τ_i (s)	$v_i = 1 - \frac{K_z}{K_0}$	λ_i (s)	T_R (°C)	C_1	C_2 (°C)	E(T) (GPa)
0.5794458	4.75	0.85	10	569	12.41	129	100.8,
0.3624554	6						$T \leq 510^\circ\text{C}$
0.03	11						0.8, $T \geq 560^\circ\text{C}$
0.028	930						
Material Set 2							
0.5794458	0.38	0.85	10	569	12.41	129	100.8,
0.3624554	0.48						$T \leq 510^\circ\text{C}$
0.03	0.88						10, $T \geq 560^\circ\text{C}$
0.028	74.4						
Material Set 3							
1.0	2.504	0.85	10	550.8	7.96	110.8	100.8, $T \leq 510^\circ\text{C}$ 10, $T \geq 560^\circ\text{C}$

Table 1.1. The three stress relaxation definitions of the molding glasses used in the validation study [2]. Material Set 3 approximates the behavior of the molding glass, L-BAL35, while Material Sets 1 and 2 should be considered as hypothetical glasses. At the reference temperature, T_R , the log of the equilibrium viscosity is 10.0 for all cases.

The above material definitions include temperature dependent stress relaxation behavior of the glass, which mainly includes the shear and bulk relaxation parameters and temperature

dependence of these properties was modeled as per WLF equation [1]. These quantities will be re-introduced in detail in Chapter 2 of this dissertation. Viscoelastic material properties along with the structural relaxation definition for glass from [1] was used to predict the effect on deviation of the Bi-convex and a theoretical steep meniscus lens shape selected based on [1]. The results are plotted in the Figure 1.3.

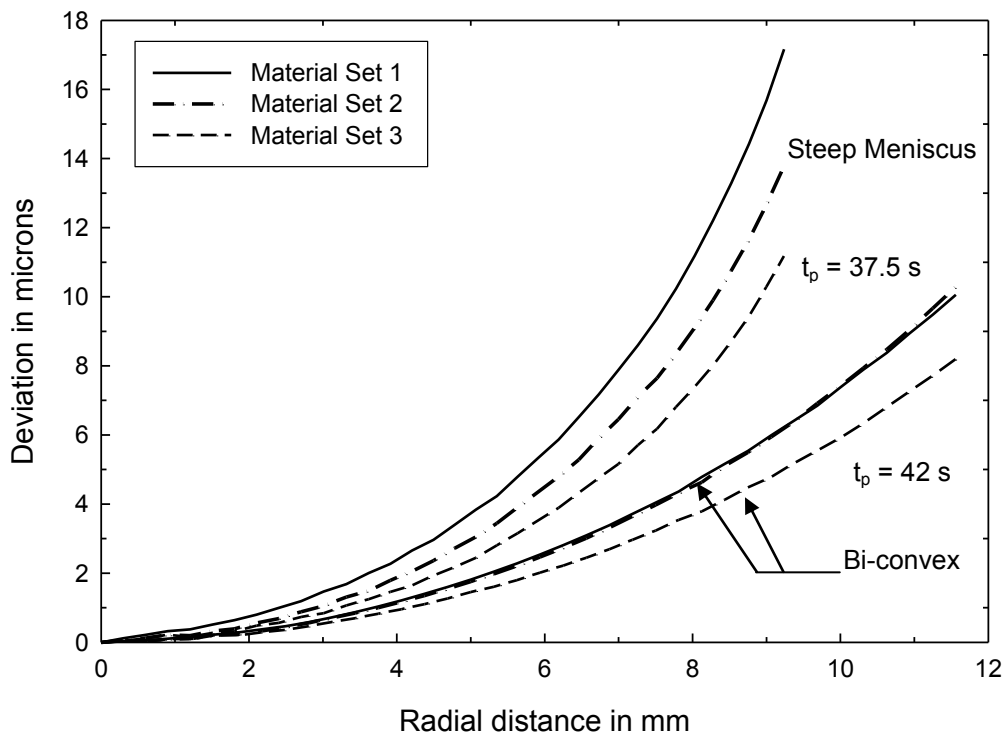


Figure 1.3. Deviation of the steep meniscus and bi-convex lenses for the three different stress relaxation behaviors listed in Table 1.1. For Material Sets 1 and 2 the press time, $t_p = 127$ s, which agrees with the press time in the actual process. Press time was lowered for the Material Set 3 results as indicated, in order to maintain a constant value of center thickness. (Taken from [2])

The process parameters other than the press time (t_p) were kept the same in respective simulations of the lens shape. The results in Figure 1.3 reveal that the steep meniscus lens shape

is sensitive to both elastic modulus and TRS behavior of glass. The general effect of the change in elastic modulus at high temperature is a reduction of the deviation only for the steep meniscus lens due to the geometry of how this shape is supported by the molds after the gap is opened.

These examples highlight the importance of an accurate thermo-mechanical material property characterization of optical glass for lens molding application from the shape change point of view. This conclusion is even more significant for an accurate prediction of the residual stresses within the molded lens [18], which therefore also has an effect on birefringence and fracture. A brief outline of the work done in this study will be presented next.

The research work presented here was performed mainly into two parallel directions: finding reliable and accurate material property data for optical glass (L-BAL35) through a combined experimental-computational approach and implementation of this data into the numerical simulations of lens molding to predict displacements, stresses and cracking inside lens. In the first part of each effort, the relevant experimental work was conducted by COMSET group at School of Material Science Engineering, Clemson University. Computational modeling efforts were accomplished by using the commercial finite element code ABAQUS and analysis runs were made using Dell Precision WorkStation (Intel Xeon[®] CPU, 2.66 GHz, 16GB RAM) and Clemson University's High Performance Computing (HPC) resource – Palmetto Cluster. A brief outline of the work done in this study will be presented next.

1.3 Outline of the Dissertation

The work presented in this dissertation is divided mainly into five Chapters. Each chapter discusses the literature related to its topic separately. The content of these five primary chapters is summarized below:

- Chapter 2 focuses on the methodology adopted to predict the viscosity of glass using a simple cylinder compression test that requires a very minimal slip at the interface of sample and substrate material. It also describes the approach developed to measure interfacial friction coefficient for a glass having viscosity precisely known at the given temperature.
- Chapter 3 extends the idea of viscosity extraction presented in Chapter 2 and explores the role of friction, viscoelastic displacements and sample geometry in determining the viscosity based on a simple expression. This chapter also provides the necessary correction in the ASTM standard formula for viscosity prediction for viscosity corresponding to $\log(\eta/(\text{Pa}\cdot\text{s})) = 8.0$ and higher.
- Chapter 4 focuses on the viscoelastic characterization of optical glass L-BAL35 using the data obtained in a creep test of the cylindrical specimen. The viscoelastic prony coefficients for L-BAL35 and NBK-7 are evaluated using the given approach.
- Chapter 5 focuses on the prediction of residual stress during annealing of glass utilizing the characterization of L-BAL35 obtained in Chapter 4. This chapter also provides the residual stress and birefringence results inside two lens shapes for different choices of stress relaxation function.
- In Chapter 6, the issue of cracking of lens is briefly discussed. The methodology for incorporating a crack inside a lens within the 3D Abaqus simulations is developed and results for two possible modes of lens failure are briefly discussed.

References:

1. B. Ananthasayanam, "Computational modeling of precision molding of aspheric glass optics," Ph.D Dissertation, Clemson University, December 2008
2. B. Ananthasayanam, P.F. Joseph, D. Joshi, S. Gaylord, L. Petit, V.Y. Blouin, K.C. Richardson, D.L. Cler, M. Stairiker, M. Tardiff, "Final shape of precision molded optics: Part I – Computational approach, material definitions and the effect of lens shape," *Journal of Thermal Stresses*, **35** (2012a) pp. 550-578.
3. M. Sellier, C. Breitbach, H. Loch, N. Siedow, "An iterative algorithm for optimal mould design in high-precision compression molding," *Proceedings of the I MECH E Part B Journal of Engineering Manufacture*, **221** (9) (2007), pp. 25-33.
4. Y. Chen, A. Yi, L. Su, F. Klocke, G. Pongs, "Numerical simulation and experimental study of residual stresses in compression molding of precision glass optical components," *Journal of Manufacturing Science and Engineering*, **130** (2008), pp. 051012-1 to 051012-9.
5. J.W. Na, S.H. Rhim, S.I. Oh, "Prediction of birefringence for optical glass lens," *Journal of Materials Processing Technology*, **187-188** (2007), pp. 407-411.
6. H.J. Mayer, C. Stiehl, E. Roeder, "Applying the finite element method to determine the die swell phenomenon during the extrusion of glass rods with non-circular cross-sections," *Journal of Materials Processing Technology*, **70** (1997), pp.145-150.
7. V. Ganvir, A. Lele, R. Thaokar, B.P. Gautham, "Prediction of extrudate swell in polymer melt extrusion using an Arbitrary Eulerian Lagrangian (AEL) based finite element method," *Journal of Non-Newtonian Fluid Mechanics*, **156**, Issue 1-2 (2009), pp. 21-28.
8. S. Xue, G. Barton, M. Large, "Inverse prediction of die shape in the direct extrusion of preforms for microstructured optical fibers," *Proceedings of 16th International Conference on Plastic Optical fibers*, (2007), pp. 120-123.
9. Trabelssi, Mohamed. "Numerical analysis of the extrusion of fiber optic and photonic crystal fiber preforms near the glass transition temperature," PhD Dissertation, Clemson University, May 2014.
10. S. Gaylord, B. Ananthasayanam, L. Petit, C. Cox, U. Fotheringham, P. F. Joseph, K. Richardson, "Thermal & structural property characterization of commercially moldable glasses," *J. Am. Ceram. Soc.*, **93** (2010), pp. 2207-2214.
11. E. Koontz, V. Blouin, P. Wachtel, J. D. Musgraves, and K. Richardson, "Prony series spectra of structural relaxation in N-BK7 for finite element modeling," *The Journal of Physical Chemistry A*, **116** (50), (2012), pp. 12198-12205.

12. W. Liu, H. Ruan, and L. Zhang, "Revealing Structural Relaxation of Optical Glass through the Temperature Dependence of Young's Modulus," *Journal of the American Ceramic Society*, Available online as an early view. DOI: 10.1111/jace.13179
13. L. Duffrene, R. Gy, H. Burlet, and R. Piques, "Multiaxial linear viscoelastic behavior of soda-lime-silica glass based on a generalized Maxwell model," *Soc. Rheol.*, **41** (1997), pp. 1021-1038.
14. Gaylord, "Thermal and Structural Properties of Candidate Moldable Glass Types," M.S Thesis, Clemson University, (2008).
15. H. Loch, D. Krause, *Mathematical Simulation in Glass Technology*, Springer, 2002.
16. Scherer, G. *Relaxation in glass and composites*. John Wiley and Sons, New York, 1986.
17. A. Markovsky, T.F Soules, V. Chen, and M.R. Vukceovich, "Mathematical and computational aspects of a general viscoelastic theory," *Journal of Rheology* **31**(8), (1987), pp. 785-813.
18. M. Brown, "A review of research in numerical simulation for the glass pressing process," *Proceedings of IMechE Part B, Journal of Engineering Manufacture*, **221**, 2007, pp. 1377-1386.

THERMO-MECHANICAL CHARACTERIZATION OF GLASS AT HIGH TEMPERATURE USING THE CYLINDER COMPRESSION TEST: VISCOELASTICITY, FRICTION AND PPV

2.1. Introduction

Glass forming processes finds wide applications in products from automotive wind shields, glass panels for TV and consumer electronics to optical lenses used in cameras, bar-code readers, microscopes, and other medical devices. The computational mechanics has been widely applied to many glass forming processes such as blowing, molding and extrusion to understand and resolve the outstanding issues. Related to precision lens molding application, some of issues identified in Chapter 1 include, deviation in lens profile, residual stresses and birefringence and cracking. It was also identified in [1, 2] that the influencing material parameters that can lead to errors in lens molding simulations. This lack of accurate material property has led to explore reliable techniques to characterize the accurate material properties required for lens molding application.

In the following paragraphs, a brief literature survey is presented related to characterization of temperature dependent viscoelastic material property of glass. Next, a short background theory containing viscoelastic equations is presented followed by experimental procedure adopted and computational results for the cylinder compression test.

Important contributions on viscoelastic data for Soda-Lime-Silica (SLS) glass do exist. While SLS glass is not suitable for applications such as precision lens molding, the experimental approaches in these studies can be applied to other glass types. Kurkjian et al. [3] studied the

stress relaxation response of an SLS glass sample subjected to torsion below the glass transition temperature. This test has the advantage of a pure shear loading and because only relaxation is involved, eliminates the effect of viscosity from the material's response. As such, the data is "pure" and can be used to determine the shear relaxation function without knowledge of other time-dependent properties. Rekhson et al. [4] performed relaxation experiments on a spring sample to measure the relaxation and retardation functions within and below the transition temperature region. They showed that both functions have the same shape within experimental error. The complete viscoelastic behavior of an SLS glass at one temperature near the glass transition temperature was obtained by Duffrene et al. [5]. The shear relaxation response was extracted by applying tension to a sample in the shape of a helical spring. In a second test tension was applied to a sample with a rectangular cross-section that results in a combination of shear and hydrostatic loading of the material. Knowing the pure shear relaxation data from the prior test made it possible to isolate the hydrostatic response in the uniaxial test. The procedure to make the spring sample is usually non-trivial which makes this experimental technique difficult to extend to certain types of optical glasses. Also non-trivial is the achievement of a uniform, known temperature in the sample since glass behavior is very sensitive to temperature. Reliable data is therefore more difficult to obtain for larger and/or more complex shaped specimens. The study by Sellier et al. [6] presents an approach to determine shear and structural relaxation parameters by measuring the thickness variation of a glass plate as it is cooled from the T_g to room temperature. A stretched exponential function was used to represent the shear and structural relaxation functions, while the bulk response was assumed to behave elastically.

Following naturally from parallel plate viscometer (PPV) studies (Dienes and Klemm [7], Gent [8], Fontana [9]) the cylinder compression test has been an attractive choice for material characterization of optical glasses by several researchers with an interest in lens molding [10-14].

Advantages of this test are the simplicity of specimen preparation and the availability of high temperature testing machines, such as lens molding machines and parallel plate viscometers, which can achieve accurate and uniform temperatures. Jain et al. [10] determined the viscosity and elastic parameters of BK7 and SK5 optical glasses using the cylinder compression test and analytical expressions for viscosity and stress. These parameters were then used in finite element simulations to compare stress-time predictions with measured curves. In these simulations the authors selected a coefficient of friction of 0.5 and assumed that glass was incompressible with shear deformation accounted for by a single Maxwell element. A generalized Maxwell model for a viscoelastic solid was used by Arai et al. [11] to characterize the relaxation function for the optical glasses, TaF3 and BK7. Zhou et al. [12] modeled the response of L-BAL42 optical glass using a Burger's model consisting of a single Maxwell element and a single Kelvin-Voigt element in series. The glass behavior of K-PBK40 above the glass transition temperature was studied by Chang et al. [13] by modeling glass for isothermal conditions using flow stress proportional to strain rate to a power less than one. Yan et al. [14] also modeled the behavior of L-BAL42 glass assuming the stress proportional to a power of the strain rate. All of the above mentioned studies neglect the volumetric relaxation during the compression test, i.e., the bulk modulus behavior of the material is assumed as rigid or elastic. From a theoretical point of view, the creep and relaxation responses in the cylinder compression test are a combination of the shear and bulk responses, which is a disadvantage of this test.

Another issue encountered in the cylinder compression test is the possibility of interfacial slip between the glass specimen and the mold. In the above mentioned cylinder compression studies, assumptions range from no friction [11, 12] to no slip [13, 14] and include an arbitrarily selected coefficient of friction due to the lack of data by Jain et al. [10]. It is well-known from the parallel plate viscometer literature ([7], [8] and [15]) that friction plays a role in the correct

interpretation of the data. In these studies analytical expressions for the viscosity based on no-slip and no-friction boundary conditions are developed by Dienes and Klemm [10], Gent [8] and used by Varshneya et al. [15], Joshi et al. [16] to determine viscosity as a function of the creep data from the cylinder compression test. Varshneya et al. [15] showed the importance of using the correct formula and recommend using materials between the glass and mold surfaces that have high friction. They showed that a high friction response was obtained when platinum foil was used between the glass cylinder and the mold surfaces. The ASTM standard [17] for the PPV test specifies the use of platinum foil and provides a formula for extracting the viscosity based on no slip, which corresponds to infinite friction. However, in another PPV study, Neuville and Richet [18] observe very low friction using a platinum foil, raising the question about the degree of slip that might occur depending on conditions such as mold material, glass type, temperature and viscosity.

The actual determination of a friction coefficient between a glass and mold surface has been considered in the literature. The ring compression test was used by Ananthasayanam [19] to determine a coefficient of friction of about 0.05 between L-BAL35 glass and a tungsten carbide mold with a Diamond-Like Carbon (DLC) coating. Chang et al. [13] used the “barrel shape” from the cylinder compression test to evaluate the coefficient of friction of a newly developed molding glass K-PBK40. They compared barrel shapes obtained from the finite element simulations for different values of friction coefficient with the deformed geometry of the test sample to estimate the coefficient of friction between glass and mold. Based on this comparison, a coefficient of friction of 1 was chosen which represents the condition of essentially no-slip. The literature therefore shows behaviors that range from no-slip to no-friction; such breadth of conditions must be taken into consideration when modeling the cylinder compression test.

In next couple of chapters, the detailed viscoelastic characterization of Duffrene et al. [5], along with the thermo-mechanical properties of L-BAL35 and N-BK7 glass presented in Table 3, will be used to perform numerical creep experiments using the cylinder compression test. Factors such as friction, viscoelasticity, compressibility, temperature non-uniformity and cylinder geometry will be studied in detail in order to assess the feasibility of using the cylinder compression test to accurately determine the viscosity, the shear relaxation function and the bulk relaxation function. The focus of this chapter is on the accurate determination of the viscosity using PPV, taking into account viscoelastic effects, frictional slip and cylinder geometry.

2.2. Theory

The material property inputs required in computational simulations include a complete viscoelastic characterization to model strain as a function of stress history, structural relaxation parameters to model volume change as a function of thermal history and the temperature dependence of the material properties. All of this theory is presented, for example, in the study by Ananthasayanam et al. [1]. Since most of the results in the current study are for isothermal conditions, only the theory of viscoelasticity will be reviewed herein. For details on structural relaxation and material dependence on temperature, the reader is referred to pages 556 – 560 of Ananthasayanam et al. [1].

The constitutive equations for the linear viscoelasticity of glass Scherer [20] are given by

$$s_{ij}(t) = \int_0^t G_1(t-t') \frac{\partial e_{ij}(t')}{\partial t'} dt' \quad (2.1)$$

$$\sigma(t) = \int_0^t G_2(t-t') \frac{\partial \varepsilon(t')}{\partial t'} dt' \quad (2.2)$$

where, s_{ij} and σ are respectively the deviatoric and dilatational stresses, e_{ij} and ε are the corresponding deviatoric and dilatational strains, and $G_1(t)$ and $G_2(t)$ are the deviatoric and dilatational (volumetric) relaxation moduli. Using a generalized Maxwell model, the relaxation moduli can be expressed in the n-term prony series form,

$$\psi_1(t) = \frac{G_1(t)}{2G_0} = \sum_{i=1}^{n_1} w_i e^{-t/\tau_i} \quad (2.3)$$

$$\psi_2(t) = \frac{G_2(t)}{3K_0} = \frac{K_\infty}{K_0} - \frac{K_\infty - K_0}{K_0} \sum_{j=1}^{n_2} v_j e^{-t/\lambda_j} \quad (2.4)$$

where G_0 is the instantaneous elastic shear modulus, K_0 is the instantaneous bulk modulus, K_∞ is the equilibrium bulk modulus, w_i and v_j are the weighting factors for the deviatoric and volumetric relaxation functions, respectively, and τ_i and λ_j are the corresponding relaxation times for the deviatoric and volumetric relaxation functions. The weights of the two relaxation moduli are normalized such that their sums are unity. Furthermore, the shear relaxation function, $\Psi_1(t)$, is related to the equilibrium viscosity (or simply viscosity) of the glass, η , as given by Scherer [20]

$$\frac{\eta}{G_0} = \sum_{i=1}^{n_1} w_i \tau_i. \quad (2.5)$$

In this study, the units of viscosity are always in Pa·s, i.e., units of Poise are not used.

From an experimental point of view, ideally, independent experiments should be designed to determine: 1) the instantaneous elastic constants, G_0 and K_0 , Duffrene [21], 2) the viscosity, η , Dehoff and Anusavice [22], 3) the deviatoric relaxation moduli, $G_1(t)$ Kurkjian [3], Duffrene et al. [5] and 4) the dilatational relaxation function, $G_2(t)$, Corsaro [23]. Of these tests the hydrostatic test to determine the dilatational relaxation function is the most complex, which has led most researchers to either make assumptions concerning compressibility of the material or

to determine this behavior in a mixed loading test after the deviatoric behavior has been quantified, such as in the study by Duffrene et al. [5].

2.3. Modeling Details

2.3.1 Finite Element Model of Axial Compression of Cylinder

The simulations in this study were performed using the commercial finite element software, ABAQUS. In most cases a 2D axisymmetric analysis was used since the molds and glass specimen are cylindrical in shape and both the thermal and mechanical loadings can be approximated as axisymmetric. The ABAQUS analysis definition, *COUPLED-TEMPERATURE DISPLACEMENT, was used. The finite element model illustrated in Figure 2.1 below consisted of a deformable mold and glass cylinder meshed with 4 node axisymmetric quadrilateral elements (CAX4T) with full integration formulation. This element type has bilinear shape functions for both displacement and temperature degrees of freedom. The entire upper surface of the upper mold (S_{TOP}) and the entire lower surface of the lower mold (S_{BOT}) move in the vertical direction as defined by the respective reference points (RP_{TOP} and RP_{BOT}) shown in the figure. Points along these surfaces are allowed to move freely in the radial direction. Full integration was required due to convergence in the region of the edge of contact when analyzing cases with a high coefficient of friction. In all cases considered in this study the interface behavior between the glass and the upper and lower mold surfaces is the same for entire surface of the glass, which includes the top and bottom flat surfaces, as well as the curved cylindrical surface. Contact of the cylindrical glass surface with the molds occurs as deformation progresses for all but low friction cases.

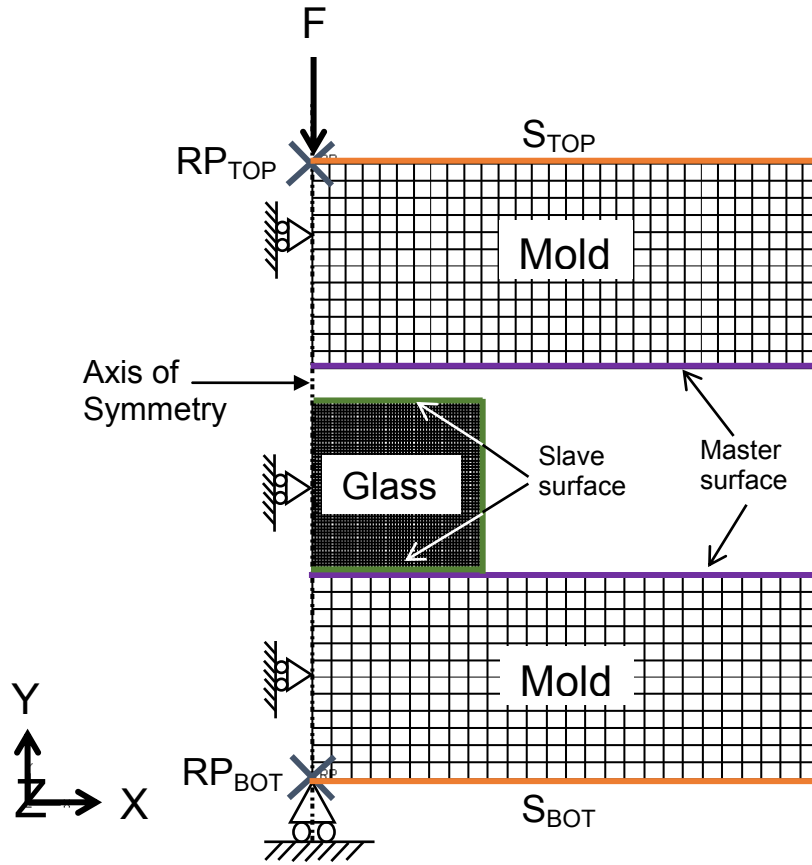


Figure 2.1. Finite element mesh used in the simulations of the cylinder compression test, including details of the interaction property definitions and coupling constraints.

The two master-slave types of contact interaction pairs were created as indicated in Figure 2.1. The Surface to Surface contact discretization method was used to define contact between the mold (Master surface) and the cylindrical sample surface (Slave surface). Finite sliding formulation was used between contacting pairs. Contact in the normal direction was modeled using a “hard” contact formulation, while the behavior in the tangential contact direction was modeled using the Coulomb friction model. The Coulomb friction model simply states that

the bodies in contact will slip if the magnitude of frictional shear stress (τ) developed at the interface reaches a critical value, otherwise, they will stick. Mathematically, this is given by

$$\tau < \mu\sigma, \text{ for sticking} \quad (2.6)$$

$$\tau = \mu\sigma, \text{ for slipping,}$$

where ' μ ' is the Coulomb friction coefficient and ' σ ' is the normal stress. As the cylinder compression test is typically a force controlled process and the glass flows more easily at molding temperatures when compared to metals, the shear stresses at the interface are not high. Hence, a limiting value of the shear stress, which is often used in bulk metal forming simulations, is not used in this analysis. In all the creep tests conducted in this study, a constant force was applied to the top mold and appropriate boundary conditions were applied to the finite element model as shown in Figure 2.1. The default implicit time-integration scheme in Abaqus was used with automatic time stepping procedure. Time increments were controlled by setting the tolerance value for a controlling parameter – maximum allowable strain rate error tolerance (CETOL) to 0.005 to ensure the accuracy of creep integration. Vertical displacement of the upper mold, which is equal to the creep displacement of the sample, was recorded as a function of time. A detailed convergence study, which is presented in Section 2.5.1, was performed to ensure convergence of the creep displacement.

2.3.2 Material Property Definitions

The numerical experiments described in Section 2.5 make use of the material properties that are summarized in Tables 2.1 and 2.2. Table 2.1 provides thermal and mechanical properties of SLS glass, while Table 2.2 summarizes the shear and bulk stress relaxation parameters used in most of the numerical experiments in this study. To our knowledge, the investigation by Duffrene

et al. [5] is the only viscoelastic characterization of both the shear and bulk stress relaxation parameters for a glass that is available in the open literature.

The material property data used to analyze the optical glasses L-BAL35 and N-BK7 is given in Table 2.3. While the actual creep experiments involve the four stages of heating, soaking, pressing and cooling, since the data is obtained at the constant pressing temperature, the cooling stage does not affect the results. Furthermore, it was shown using L-BAL 35 glass that the thermal expansion effects on the

Thermo-mechanical properties of Soda-Lime-Silica Glass	
Property	Glass
Density, ρ (kg/m ³)	2500
Young's Modulus, E (GPa)	See Table 2
Poisson's Ratio	0.22
Specific Heat, c_p (J/kg/K)	880
Thermal Conductivity, κ (W/m/K)	0.937
Glass Transition Temperature, T_g (°C)	550

Table 2.1. Thermal and mechanical properties of Soda-Lime-Silica glass (SLS) from Duffrene et al. [5]. The viscoelastic behaviors of the glass are presented in Table 2.2.

Shear Relaxation Function, $\psi_1(t) = \frac{G_1(t)}{2G_0}$		Hydrostatic Relaxation Function, $\psi_2(t) = \frac{G_2(t)}{3K_0}$		Temperature Dependent Elastic Modulus
w_i	τ_i (s)	v_j	λ_j (s)	E(T) (GPa)
5.52214e-02	8.0790e-05	1.81630e-02	1.3110e-05	72, $T \leq 510^\circ\text{C}$
8.20598e-02	1.4580e-03	1.83030e-02	2.6020e-04	
1.21502e-01	1.8460e-02	2.34580e-02	5.2900e-04	
2.28594e-01	2.0380e-01	1.74563e-01	5.0320e-03	62, $T \geq 550^\circ\text{C}$
2.86077e-01	9.1391e-01	3.21949e-01	3.1380e-02	
2.26545e-01	4.0130e+00	2.60561e-01	5.3210e+00	

Table 2.2. The stress relaxation definitions of the Soda-Lime-Silica glass (based on Table I and II from Duffrene et al. [5]) used in the current study. Refer to Equations 2.3 and 2.4 for the functional forms. The values of bulk relaxation parameters (v_i) were modified to the format acceptable to ABAQUS.

Thermo-mechanical properties of Glass and Mold Material			
Property	L-BAL35	N-BK7	Inconel
Density, ρ (kg/m ³)	2550	2510	8430
Young's Modulus, E (GPa)	100.8, $T \leq 510^\circ\text{C}$ 10, $T \geq 560^\circ\text{C}$	83	214
Poisson's Ratio	0.252	0.206	0.324
Specific Heat, c_p (J/kg/K)	1100, $T \leq 470^\circ\text{C}$	858	444
Thermal Conductivity, κ (W/m/K)	1.126	1.114	14.9
Glass Transition Temperature, T_g	527	557	-

Table 2.3. Thermo-mechanical properties of L-BAL35 glass (Ananthasayanam et al. [1], OHARA [24]), N-BK7 Glass [25] and Inconel (Precision Cast parts Corp. [26]).

displacement that occur during the heating and soaking stages are negligible as long as the heating and soaking periods are sufficiently long to allow the specimen to reach a constant

temperature. As such, in this chapter, isothermal pressing is used, thus, the structural relaxation and Thermo-rheologically Simple (TRS) behaviors of glass are not needed in the material property definition in ABAQUS. In next chapter, however, a more complex thermal history is required before conducting the creep test, which is demonstrated to have a slight effect on the creep curve. In this case the full use of the structural relaxation and TRS behaviors from Ananthasayanam et al. [1] are used.

2.4. Experimental Procedure

Two creep experiments were performed using the Parallel Plate Viscometer, Orton PPV-1000 and the molding glass, N-BK7. A Linear Variable Displacement Transducer (LVDT) sensor, attached to the probe rod made of silica glass, measures the axial displacement of the top mold with respect to time. A reference thermocouple that records the temperature near the glass sample was located inside the chamber close to the lower mold. The load on the sample can be adjusted by placing static weights on the either side of counter-weighted pulley system. The top and bottom molds were made from Inconel and were ground parallel and polished. Following ASTM standard [17], platinum foil was used between the glass specimen and the molds for one of the tests, while nickel foil was used in a second test.

Calibration and repeatability experiments were performed on the PPV machine that aimed at determining the error associated with the temperature measurements of the sample during creep testing. These experiments give an indication of the expected error in the single measurement as well as the nature of repeatability from experiment-to-experiment or day-to-day. The sample temperature was determined using a polynomial interpolation of the temperature values recorded by the reference thermocouple inside the instrument. Also, the repeatability error on the sample temperature measurements was determined to be $\pm 1.5^{\circ}\text{C}$ at a temperature around

600 °C. Finally, the deformed shapes of all specimens were axisymmetric and symmetric about the mid-plane, indicating that the loading was applied correctly and that the temperature was uniform.

2.5. Results

All of the results presented in Figures 2.2 and 2.4-2.12 are for the cylinder compression test. In these results “creep displacement” refers to the downward displacement of the center of the top surface of the cylinder relative to the center of the bottom surface, which is fixed. An axisymmetric two-dimensional model is used for all of these results. Unless stated otherwise, the diameter of the cylinder is 10 mm. Furthermore, all computational results in this Chapter are for isothermal pressing except for a validation study discussed in Section 2.5.3. SLS glass properties from Duffrene et al. [5] and Tables 2.1 and 2.2 are used in Figures 2.3-2.7 and 2.10-2.12 while N-BK7 properties from the SCHOTT glass catalogue and Table 2.3 are used in Figure 2.8, which compares simulations with experimental data. In Figure 2.8, a single term prony series for shear is used with viscosity treated as an input parameter.

2.5.1 Convergence Study

The results in this study rely on the accurate prediction of the creep displacement for a cylinder subjected to compression. As a cylinder is compressed between mold surfaces, and interface slip with friction occurs as deformation progresses, the cylindrical surface of the cylinder bulges outward. Depending on the level of friction, eventually the cylinder will contact the mold surfaces, which adds a complication to the analysis and potentially to the experimental data. The purpose of this section is to study convergence of the creep displacement both before and after such contact takes place. The three quantities to be studied, which are defined in Figure 2.2, are the creep displacement, d_{creep} , the bulged radius, R_{bulge} and the folded length, d_{fold} .

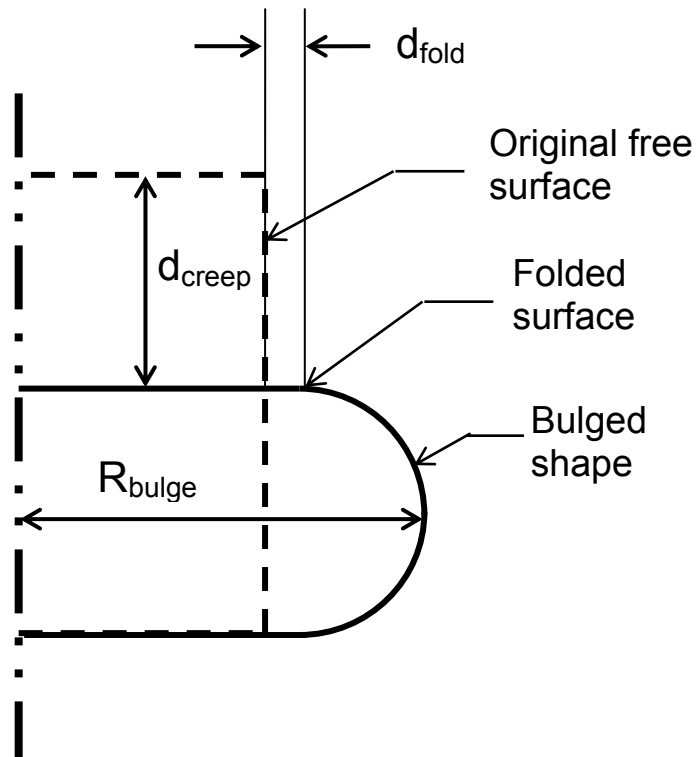


Figure 2.2. Schematic of a deformed and undeformed cylindrical specimen for a creep test with no-slip boundary conditions to define parameters used in Tables 2.4 and 2.5.

This convergence study is based on 2-D axisymmetric simulations for no-slip boundary conditions using a glass cylinder with $H = 4$ mm, $D = 10$ mm, $F = 1000$ N and SLS viscoelastic glass properties. The results for four different uniform meshes for the creep displacement at 10% ($d_{\text{creep}} = 0.4$ mm) and 50% ($d_{\text{creep}} = 2$ mm) levels of creep deformation are presented in Table 2.4. The baseline mesh, which has 2000 elements, was used to determine the times required to achieve 10% and 50% levels of deformation. These times were respectively, $t = 1475$ s and 22,209 s. At these same times the quantities in the table were determined for the other three meshes and compared to the corresponding results from the baseline mesh. It is seen that within 1% error, the baseline mesh provides converged values of the creep displacement and the bulged radius. The folded length at 50% deformation, which is on the order of 1.4 mm, is more difficult to converge,

but has converged for the case of 8000 elements. In order to study folding behavior more closely, the results in Table 2.5 provide predictions for four different meshes when a node that is originally 0.1 mm ($d_{\text{fold}}/D = 0.01$) away from the corner first comes into contact with the mold, which occurs at a deformation level of about 17%. These results show that the baseline mesh provides a very reasonable estimate of when folding can be expected to start to play a role in the deformation of the cylinder. The actual initiation of folding, which can be quantified as when the slope of the edge of the glass rotates through 90 degrees and becomes parallel to the molds, was determined to occur after about 40 seconds. In addition to convergence with respect to the mesh, it was determined that the solution is not sensitive to parameters such as element order, time step size or the strain rate error tolerance parameter (CETOL).

Mesh	No. of Elements	% change in d_{creep} (m) relative to baseline mesh at		% change in R_{bulge} (m) relative to baseline mesh at		% change in d_{fold} (m) relative to baseline mesh at
		t = 1475 s	t = 22,209 s	t = 1475 s	t = 22,209 s	t = 22,209 s
Coarse	480	-0.60	0.006	-0.008	0.126	1.6
Baseline	2000	0.0 (4e-04)	0.0 (2e-03)	0.0 (5.3527e-03)	0.0 (7.2483e-03)	0.0 (1.41083e-03)
Fine	8000	0.31	0.003	0.005	-0.025	7.5
Refined	32,000	0.45	0.000	0.008	-0.027	7.4

Table 2.4. Convergence study for creep displacement, bulge radius and folded distance (refer to Figure 2.2) for different levels of mesh refinement. The times $t = 1475$ s and $22,209$ s in the table correspond to 10% and 50% deformation levels achieved for the Baseline mesh (2000 elements).

Parameters	No. of Elements	Values when a node 0.1mm from corner contacts the mold		
		time (s)	creep displacement (m)	% change
Baseline	2000	2790	6.81742E-04	0.00
Fine	8000	2923	7.11322E-04	4.34
Refined - 1	32,000	2749	6.78417E-04	-0.49
Refined - 2	128,000	2769	6.82505E-04	0.11

Table 2.5. Mesh convergence study for time and creep displacement when a node originally 0.1 mm away from the corner first comes into contact with the mold.

2.5.2 Response of SLS Glass in the Cylinder Compression Test

In order to accurately obtain the viscosity, it is necessary to understand all the deformation mechanisms. Therefore, in this section computational simulations are used to visualize the effects of the shear and bulk deformation mechanisms on creep-recovery tests of pure shear, hydrostatic compressive loading and the cylindrical compression test. The full

viscoelastic characterization of an SLS glass from Duffrene et al. [5] and Tables 2.1 and 2.2 is used for the material behavior. In order to understand the effects of individual deformation mechanisms, the following four sets of material properties, which include different subsets of the full viscoelastic behavior, are used:

1. Purely elastic shear and bulk:

$$G_1(t) = 2G_0 \qquad G_2(t) = 3K_0 \qquad (2.7)$$

2. Viscous shear (Single term prony series) and elastic bulk:

$$G_1(t) = 2G_0 e^{-t/\tau} \qquad G_2(t) = 3K_0 \qquad (2.8)$$

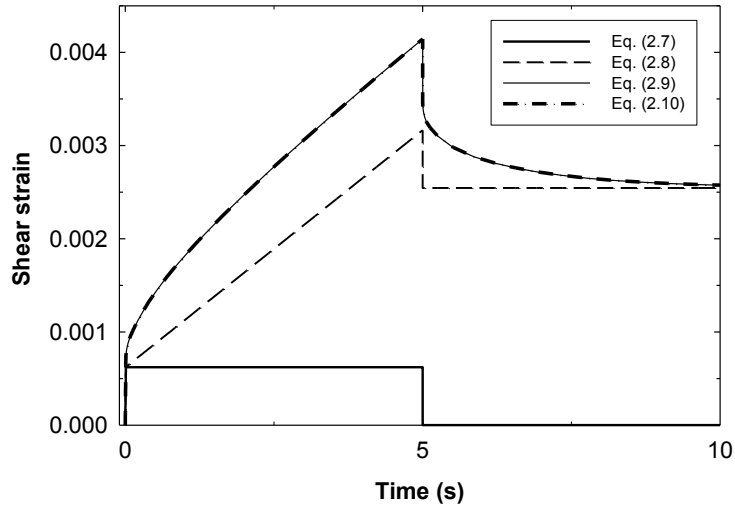
3. Viscoelastic shear and elastic bulk response:

$$G_1(t) = 2G_0 \sum_{i=1}^{n_1} w_i e^{-t/\tau_i} \qquad G_2(t) = 3K_0 \qquad (2.9)$$

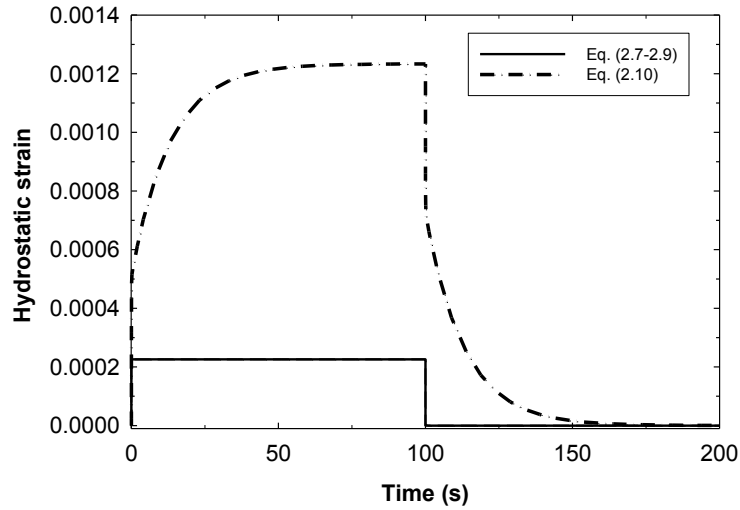
4. Viscoelastic shear and viscoelastic bulk:

$$G_1(t) = 2G_0 \sum_{i=1}^{n_1} w_i e^{-t/\tau_i} \qquad G_2(t) = 3K_0 + (3K_\infty - 3K_0) \left(1 - \sum_{j=1}^{n_2} v_j e^{-t/\lambda_j} \right) \qquad (2.10)$$

The cases 2, 3 and 4 are subject to the constraint that the equilibrium viscosity, as defined in (2.5), must be kept constant. The first numerical experiment is for pure shear loading where at $t = 0$ s, a shear stress is applied to a material element. The load is removed at $t = 5$ s. The results in Figure 2.3a give the shear strain as a function of time for all four material behaviors listed in Equations 2.7-2.10.



(a)



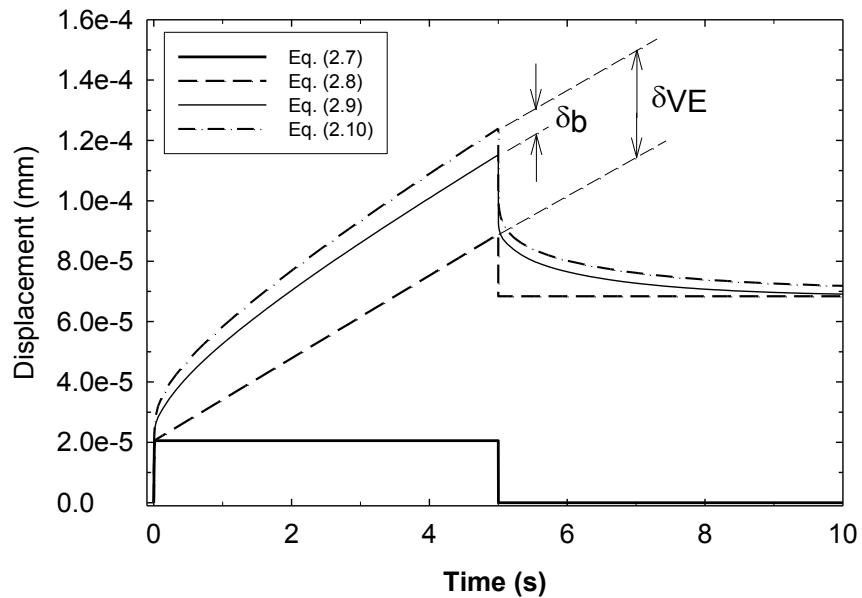
(b)

Figure 2.3. Creep-relaxation response to (a) shear loading ($\tau = 25$ MPa) and (b) hydrostatic compression ($\Delta P = 25$ MPa) for an SLS glass for the four different material behaviors outlined in Section 2.5.2.

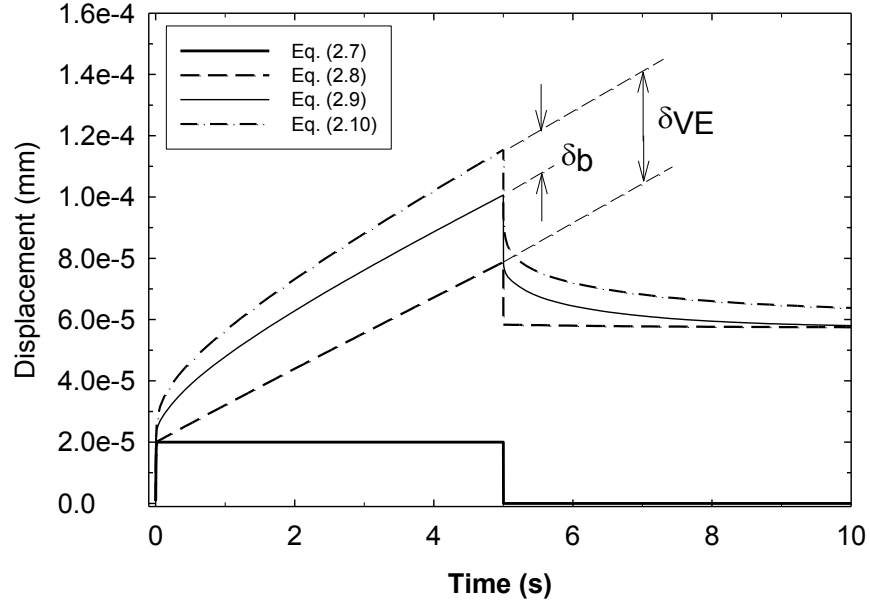
In Figure 2.3b the analogous experiment for hydrostatic compression is given, where now the load is removed at $t = 100$ s, to more clearly show the slower material response to this mode of loading. It is observed that in these pure loading cases the bulk behavior change from Equation

2.9 to 2.10 does not affect the shear response in Figure 2.3a, and similarly the shear behavior differences in Equations 2.7-2.9 do not affect the bulk response in Figure 2.3b. Furthermore, the shear deformation resulting from the viscous term is permanent, while all other mechanisms produce displacements that are recoverable.

For the case of the cylinder compression test, a cylindrical specimen with diameter (D) = 10 mm and height (H) = 10 mm was subject to a creep-recovery test using a compressive loading of 10 N for the first five seconds. The downward vertical displacements of the center of the top surface (at $r = 0$) as a function of time for the four material behavior cases are presented in Figure 2.4.



(a)



(b)

Figure 2.4. Initial elastic and short time viscoelastic responses of an SLS glass for four different material behaviors in a numerical experiment of the cylinder compression test where $P = 10\text{ N}$, $D = 10\text{ mm}$, $H = 10\text{ mm}$ and (a) $\mu = 0$, (b) $\mu = \infty$. The displacement component δ_{VE} that is defined in (a) denotes the additional displacement caused by visco-elastic mechanisms, while δ_b is the displacement caused purely by the dilatational (bulk) viscoelastic response.

The conditions of no-friction and no-slip at the glass and mold interface were considered for the four material behaviors. As shown in this figure, contrary to the results of Figure 2.3, the simulated creep-recovery curves are different for each type of relaxation moduli studied. For case 1 in both Figure 2.4a and 2.4b the material behaves as an elastic solid and responds instantaneously to the applied load, which remains unchanged with time. For case 2 the material is a viscous solid that has a time-dependent viscous deformation after an instantaneous elastic response. For case 3 a recoverable viscoelastic response due to shear is added, while for case 4, a recoverable viscoelastic response is added due to compressibility. As defined in Figure 2.4, the total viscoelastic response is denoted as δ_{VE} , while the portion due to compressibility alone is δ_b .

An important observation for both the creep and recovery stages of the cylinder compression test is that for the SLS glass modeled, the effect on the displacement due to compressibility (δ_b) for any level of friction is a significant part of the total viscoelastic response. Compressibility affects both the magnitude of the displacement and time period over which relaxation occurs. Clearly if this glass is assumed to be incompressible, the shear relaxation function will not be determined correctly. Within this context, based on the characterization from Duffrene et al. [5], this type of SLS glass has a high degree of compressibility relative to other glasses as shown in the Chapter 4. As a second observation, considering the short time response, the displacement at $t \sim 1/4$ seconds for case 4 is approximately twice that of the initial elastic response. This makes accurate short time viscoelastic material characterization very difficult unless the actual value of the elastic moduli as a function of temperature is known from a separate test.

In creep-recovery experiments using the cylinder compression test, precise measurement of the displacement during the recovery phase is more difficult to achieve than during the creep phase. Furthermore, the displacement during the recovery stage is dependent on the viscosity of the glass, contrary to the pure shear loading represented in Figure 2.3a. Since the usual advantages of applying creep-recovery do not apply to the cylinder compression test, the computational and experimental results in the remainder of this study are for creep loading.

2.5.3 Effect of Heating and Soaking

The creep tests of glass that are of interest in the current study are done near the glass transition temperature. Since the thermo-mechanical properties of glass are highly temperature dependent, it is necessary to perform the tests after the glass has reached a uniform, known temperature. In order to understand what is required to achieve a uniform temperature and to study the thermo-mechanical effects due to varying temperature, the complete cycle of heating,

soaking and then pressing was modeled using different heating scenarios. Due to changing temperature this modeling required the use of the structural relaxation and TRS behaviors for L-BAL35 glass presented by Ananthasayanam et al. [1]. The results of this study supported the choice of a two hour heating time followed by a three hour soaking time that were used in the experimental work, since this schedule produced a uniform temperature and creep displacements indistinguishable from the isothermal results, and hence, were not presented in a figure. In the heat transfer analysis, a conservative value of the gap conductance parameter, $h = 250 \text{ W/m}^2/\text{K}$, was used so as not to underestimate the time required to achieve uniform temperature [1, 6]. In all the remaining computational results presented in this Chapter, it was assumed that adequate time was used to reach the target temperature. The transient effects are revisited in the chapter 4 due to the more complex heating schedule that can be required for the no-slip tests conducted.

2.5.4 Effect of Friction on Displacement in a Creep Test

Friction at the mold/glass interface is usually unknown. The coefficient of friction can depend on, for example, surface finish, normal pressure, relative sliding velocity, temperature, glass type and mold material. In a creep test of a cylindrical specimen under a compressive load, the deformed shape of the sample at the end of the pressing stage can reveal information about the presence of friction at the interface. Following, for example, Varshneya et al. [15] and Neuville and Richet [18], if the diameter of the cylindrical sample increases without much barreling, the friction coefficient is negligible. On the other hand, the presence of high friction causes the cylindrical surface to experience significant barreling [13]. Furthermore, this behavior is dependent on specimen geometry, which is quantified by the height to diameter ratio, H/D . To illustrate the effect of friction, in this section numerical creep experiments were done with $H/D = 1$ and 0.2 . Each sample was subjected to a constant load of 1000 N for a period of 3600 seconds

for a range of friction coefficients varying from no friction ($\mu = 0$) to no slip ($\mu = \infty$). As an example of barreling, the deformed cylinder shape for case of no slip is illustrated in Figure 2.5 using the sample with $H/D = 0.2$. This result is particularly interesting since, contrary to the no-friction case which has uniform stress, the normal stress in the loading direction is a strong function of the radial coordinate and that tensile stresses occur in the barreled portion of the deformed material. Furthermore, in the no-slip case material in the barreled section flows toward the nearest mold surface. This point is revisited in Section 2.5.7.

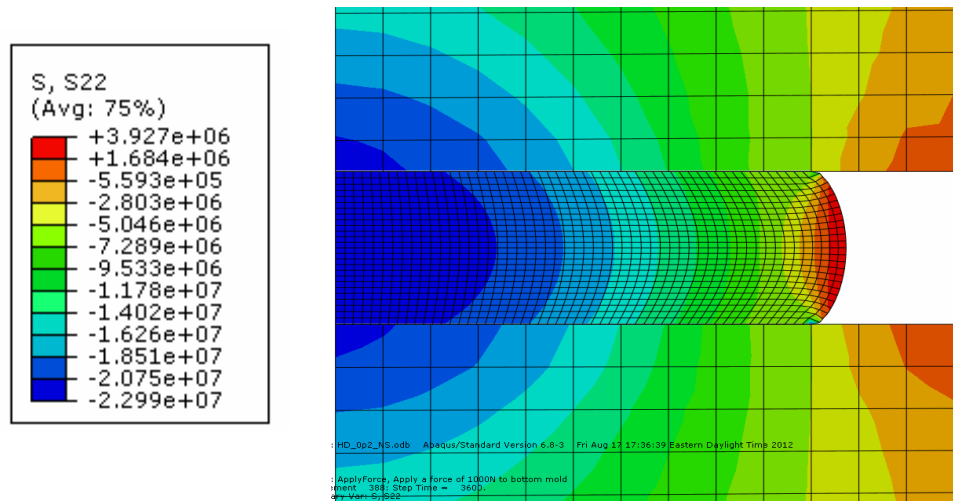
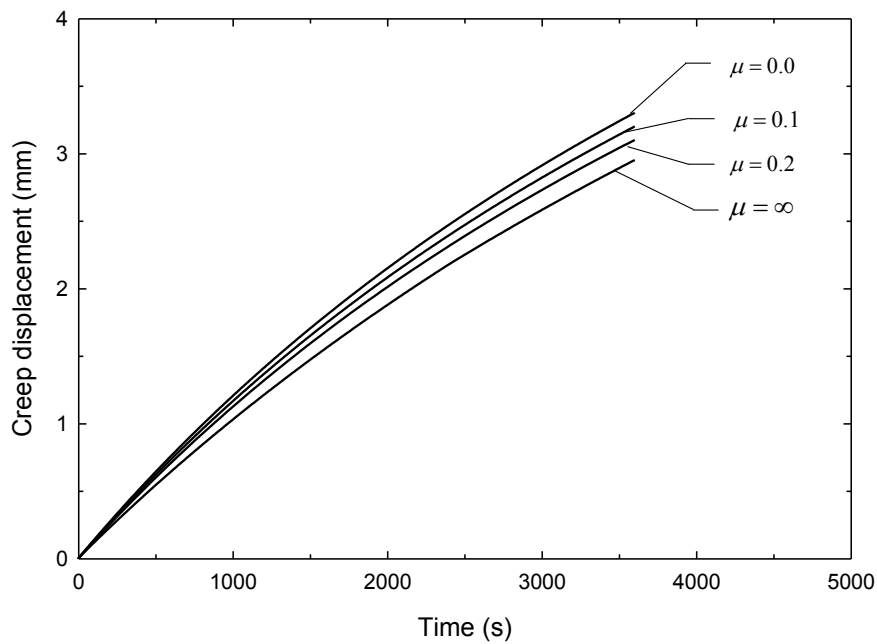


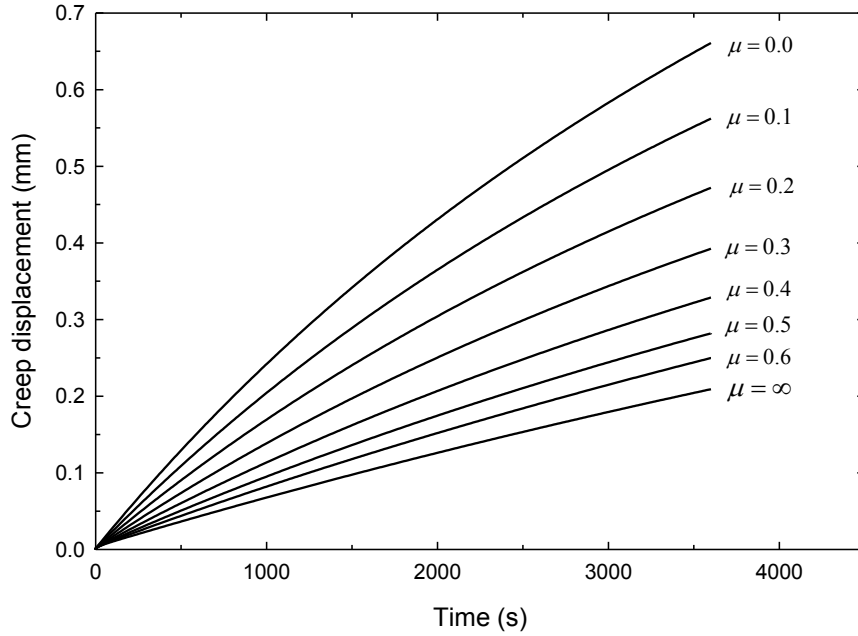
Figure 2.5. Deformed shape and axial stress distribution ($S22 = \sigma_y$ in Pa) for a cylindrical SLS glass sample ($H/D = 0.2$) during the cylinder compression creep test for conditions of no-slip after 1 hour has elapsed.

Another qualitative measure of friction at the interface is the magnitude of the creep displacement reached during the creep test. For the same amount of loading and duration of testing, the total displacement of a glass specimen with high interface friction is always less than that for a specimen with less friction if the initial specimen geometry is the same. As shown in Figure 2.6a, the displacement curves ranging from $\mu = 0$ to $\mu = \infty$ are relatively close to each other

for $H/D = 1$, while for $H/D = 0.2$, the curves presented in Figure 2.6b are farther apart, indicating higher sensitivity to changes in friction for a thinner specimen. The result in Figure 2.6 quantifies how the effect of the no-slip boundary condition diminishes as the specimen becomes taller, but is significant for a thin specimen. As seen from the results in Figure 2.6a, for $H/D = 1$, at the end of the test the displacement for the case of $\mu = \infty$ is about 90% of the displacement for $\mu = 0$, while for the thinner specimen this percentage drops to 31%. These results show clearly that friction must be taken into account to predict the viscosity, especially for thin specimens. As a point of interest, the deformation result in Figure 2.5 is from the end of the 3600 s test for the no-slip case in Figure 2.6b.



(a)



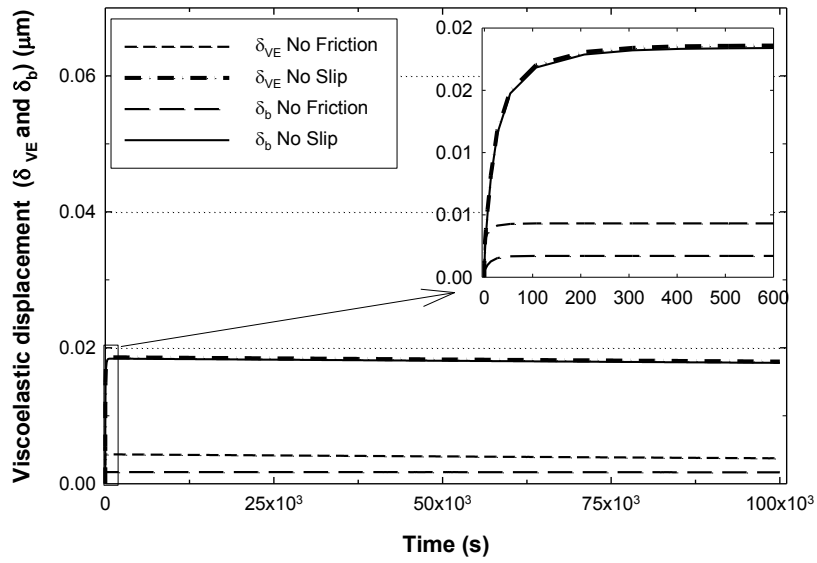
(b)

Figure 2.6. Effect of interface friction on the creep curve for (a) $H/D = 1$ and (b) $H/D = 0.2$ using SLS glass.

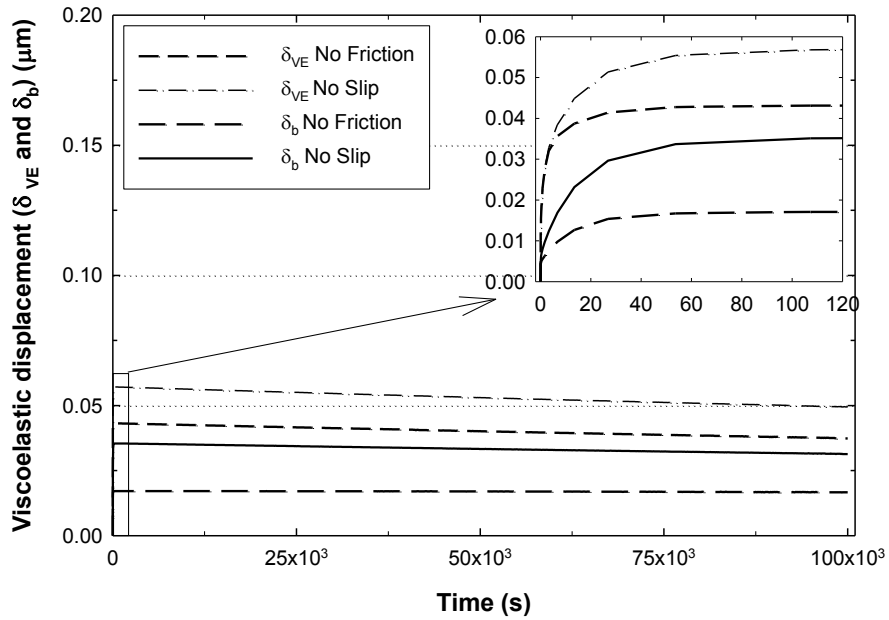
2.5.5 Long Time Behavior of the Creep Curve for the Cylinder Compression Test

In this section the viscoelastic properties of SLS glass from Duffrene et al. [5] are used to determine the long time behavior of the viscoelastic displacement quantities, δ_{VE} and δ_b as defined in Figure 2.4. The results of this long time study are important in this study and as such must be done with high precision. In order to perform these calculations and avoid round-off error associated with the large time shear response, the shear function weights reported by Duffrene et al. [5] had to be adjusted slightly to be three orders of magnitude closer to unity, i.e., to be off by 10^{-9} instead of 10^{-6} . This was achieved by multiplying each prony weight by the same constant. While this leads to converged results at large time, the modification to the material behavior is nearly imperceptible. Two sample geometries having H/D ratios of 1.0 and 0.1 are used, where D

= 10 mm. The sample with $H/D = 1$ is a relatively tall sample which is at the upper limit of the ASTM recommendation for cylinder height. The other sample having $H/D = 0.1$ is much thinner than what is typically used in the literature. For this study the two extreme cases of friction boundary conditions are used, namely frictionless ($\mu = 0$) and no slip ($\mu = \infty$). In the simulations, the constant force of 10 N was applied for 100,000 seconds (~28 hours).



(a)



(b)

Figure 2.7. Viscoelastic displacements, δ_{VE} and δ_b , as a function of time for (a) $H/D = 0.1$ and (b) $H/D = 1$ for no slip ($\mu = \infty$) and no friction ($\mu = 0$) using SLS glass.

The results of these creep tests are presented in Figure 2.7, with the $H/D = 0.1$ case presented in Figure 2.7a and the $H/D = 1$ case in Figure 2.7(b). The inset figures highlight the transient behavior of the viscoelastic displacement quantities, δ_{VE} and δ_b , during the initial period. The results from this study showed that these quantities decrease very slowly in time, which is due to an increasing area over which a constant load is applied, i.e., the true stress decreases. With decreasing stress, the viscoelastic components of the displacement decrease. If this rate of decrease is ignored, both the cases studied in Figure 2.7 suggest that after a sufficiently long time, except for a constant shift, the creep response of a material having both shear and bulk relaxation mechanisms is the same as for a material with a single prony series term in shear and an elastic bulk modulus, i.e., the material behavior in Equation 2.8. Thus, this analysis quantifies for a real material with realistic time dependent behaviors that two materials having different relaxation

mechanisms but the same equilibrium viscosity values have similar long time behavior in terms of the rate of the creep displacement. This also suggests that by comparing the experimental creep curve with the numerical curve assuming Equation 2.8 material behavior, the viscosity of the glass at high temperature can be estimated. In order to distinguish this from a full viscoelastic treatment, this is referred to as a single term prony series approach. Possible error introduced by ignoring the very small non-zero rate of decrease of δ_{VE} in Figure 2.7 is shown to be insignificant in the next chapter.

2.5.6 Simultaneous Determination of Viscosity and Friction Coefficient

In this section the feasibility of using creep curves to determine both viscosity and friction coefficient is considered. The first step in comparing the data to the results of a single term prony series is to subtract the initial elastic response from the creep curve. As shown in Figures 2.3 and 2.4, it is very difficult to determine the initial elastic constants from cylinder creep data and this was not attempted. After subtracting the estimated initial elastic response, using the finite element model described in Section 2.3, the following iterative procedure is used:

1. Perform numerical simulation on the given geometry with an initial guess of viscosity, η^0 , which corresponds to a single relaxation time τ_1
2. Calculate the difference between displacements of the experimental and numerical creep curves

$$(\delta_{VE})^i = d_{exp} - (d_{num})^i \quad \forall (0 \leq t \leq t_{test}) \quad (2.11)$$

3. If $(\delta_{VE})^i$ approaches a constant for long time, the viscosity of the glass is η^0

4. Otherwise increase or decrease the viscosity, η^i (single relaxation time τ_i) until the $(\delta_{VE})^i$ value asymptotically approaches a constant (to within experimental error) with respect to time.

Using this approach the simulation and experimental creep results are presented in Figure 2.8 for N-BK7 glass cylinders with $H/D = 0.22$ ($D = 9$ mm), which, as shown in Figure 2.6(b), will be sensitive to the friction coefficient. The experimental data in this figure includes a specimen with a nickel foil pressed at $631 \pm 1.5^\circ\text{C}$, which corresponds to a range of the log of viscosity of 9.27 - 9.38 (Pa·s), and a specimen with a platinum foil pressed at $651.5 \pm 1.5^\circ\text{C}$, which corresponds to $\log(\eta) = 8.554 - 8.653$ (Pa·s).

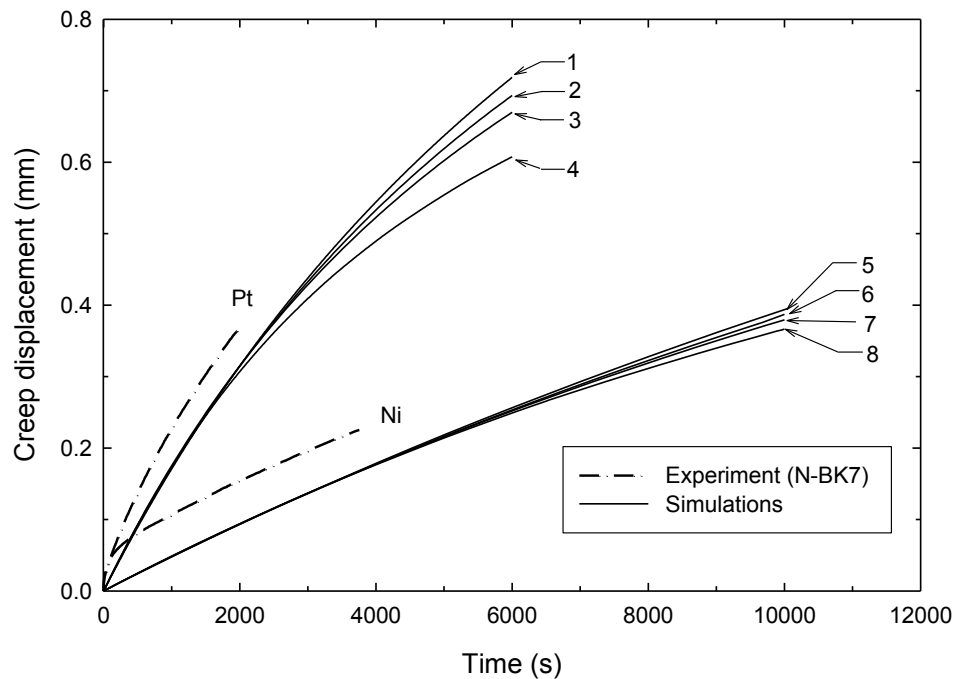


Figure 2.8. Experimental (dots) and computational (solid lines) creep curves for N-BK7 glass samples ($H/D=0.22$) pressed with Pt and Ni foil at 651.5°C and 631°C , respectively. The eight cases (#1 - #8) of viscosity and friction combinations, presented as “ $\log(\eta)/\mu$,” are for Pt foil: 1) $8.74/0$, 2) $8.653/0.11$, 3) $8.554/0.22$, 4) $8.174/\infty$; and for Ni foil: 5) $9.33/0$, 6) $9.259/0.1$, 7) $9.176/0.2$, 8) $8.777/\infty$.

From the point of view of the simulations, the results in this figure show that for data in the given time ranges, multiple combinations of viscosity and friction coefficient lead to approximately the same creep displacement. In Figure 2.8, four combinations are presented for each foil type: cases #1 - #4 for platinum foil and #5 - #8 for nickel foil. This is especially true for the Ni foil case, where the creep curves for no friction and no slip are almost identical within the range of the data. This behavior shows how changes in friction can be incorrectly attributed to changes in viscosity, and vice versa. Since the creep curves for the different pairs of viscosity and friction coefficient diverge beyond the range of the data, if the data were available to higher levels of deformation the range of the coefficient of friction could be more precisely determined. This also suggests that if

sufficient data is available, both the viscosity and the friction coefficient can be determined. However, if the data is limited and both viscosity and friction coefficient are unknown, this combined approach for the determination of both parameters is not possible. While this is a disadvantage for the determination of viscosity, it is an advantage for the identification of the displacement, δ_{VE} from experimental data. This data can be used for characterization, however, only if the true viscosity is known. In the case presented in Figure 2.8, the viscosity of N-BK7 glass is known to within the experimental error associated with the temperature. Given that the temperature of the 631 °C nickel foil case corresponds to $\log(\eta) = 9.27 - 9.38$ (Pa·s), the coefficient of friction appears to be between 0 and 0.08, while for the 651.5 °C platinum foil specimen with $\log(\eta) = 8.554 - 8.653$ (Pa·s), the coefficient of friction appears to be between 0.11 and 0.22. These values of friction are consistent with the observed level of barreling of the cylinders. The experimental data in Figure 2.8 will be revisited in the next section.

2.5.7 Relation of Computational Results to PPV

The ASTM standard [17] for the conversion of creep data to viscosity makes use of the analytical expression [7, 8] for the case of no slip,

$$\eta = \frac{2\pi F h^5}{30V(2\pi h^3 + V)} \left(\frac{dh}{dt} \right)^{-1}, \quad (2.12)$$

where F is the force applied to the cylinder, h is the change in height and V is the initial volume. A kinematic assumption in the development of Equation 2.12 is that horizontal planes remain plane, which is clearly violated in the barreled section shown in Figure 2.5. Therefore Equation 2.12 is approximate and the degree of approximation can be quantified by numerical experiments. The companion expression for the no-friction case, which is more accurate than Equation 2.12 since the no-friction condition is easier to model, is given by

$$\eta = \frac{Fh^2}{30V} \left(\frac{dh}{dt} \right)^{-1} \quad (2.13)$$

The analytical expressions for viscosity given by Equations 2.12 and 2.13 are understood to be approximations of the viscosity that is more precisely predicted by the current computational procedure. Given the creep data from Figure 2.8, it is a simple matter to predict the viscosity as a function of time for the nickel and platinum foil cases using the Equations 2.12 and 2.13. With the help of a smoothing technique making use of local polynomial regression, these predictions as a function of percent reduction in height are presented in Figure 2.9. For the nickel case it took about 500 seconds to reach 4% deformation, while for the hotter platinum foil case, it took about 250 seconds to reach 3% deformation.

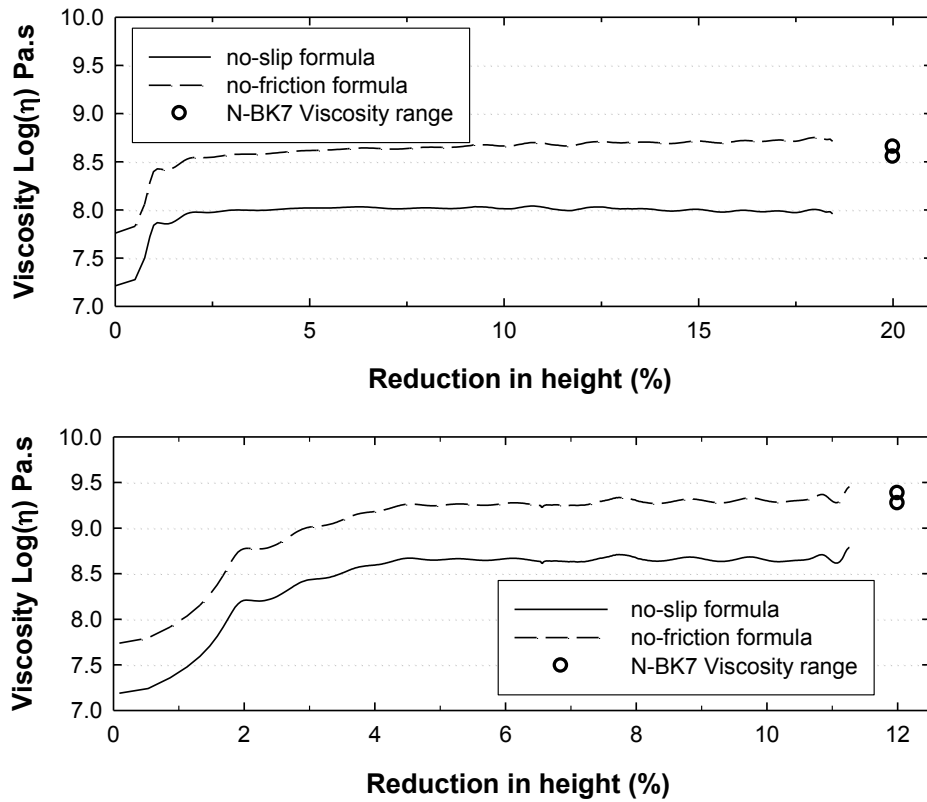


Figure 2.9. Viscosity estimate based on no-slip and no-friction formulae of creep experimental data from Figure 2.7. Pt foil results (top) and Ni foil (bottom).

These levels of deformation coincide approximately with the end of the transient phase. The results in this figure show two important behaviors. First, due to the viscoelastic effects of N-BK7 at these temperatures, it is necessary to run the experiment for a significant amount of time to reach a constant value of viscosity. Second, the no-friction formula is a better approximation for the known answer, which is consistent with the relatively low predictions for friction coefficients obtained in the previous section. The nickel case had a lower coefficient of friction (0 – 0.08) and the viscosity is very close to the no-friction prediction, while the platinum foil case, which has a higher coefficient of friction (0.11 – 0.22), is slightly overestimated by the no-friction case. If the molding glass (N-BK7) in Figure 2.9 is replaced by SLS glass in a numerical simulation, the

maximum waiting time until the viscosity curve reaches a steady state value is in the range of 50-100 seconds. This suggests that the molding glass N-BK7 has more significant viscoelastic mechanisms within the molding temperature range than SLS glass, making time dependence even more important to account for in PPV when predicting viscosity.

In general when viscosity is predicted by PPV, the coefficient of friction is unknown. This friction coefficient is a function of the glass type, the foil type, the molds and also the temperature. While the no-slip and the no-friction extremes are ideal, neither is easy to achieve. This provided a motivation to perform a computational experiment using known coefficients of friction to assess the error involved in using the Equations 2.12 and 2.13 and also to quantify the effect of viscoelasticity. This was done using SLS glass for $H/D = 0.5$ as follows: 1) the equilibrium viscosity was artificially adjusted by changing the relaxation times to have a log of viscosity of 8.00 (Pa·s), which is a typical value for precision lens molding, 2) creep curves were generated for a given coefficient of friction value, and 3) the creep displacement was used in the Equations 2.12 and 2.13 to calculate a viscosity value. The results of this computational experiment are presented in Figure 10. This figure shows that the no-friction Equation 2.13 is exact for significant deformation when there is no friction ($\mu = 0$) and that the Equation 2.12 is approximate when there is no slip, although reasonably accurate when the deformation is less than about 10%. The approximate nature of the no-slip result is traced to the displacement behavior in the barreled region shown in Figure 2.5.

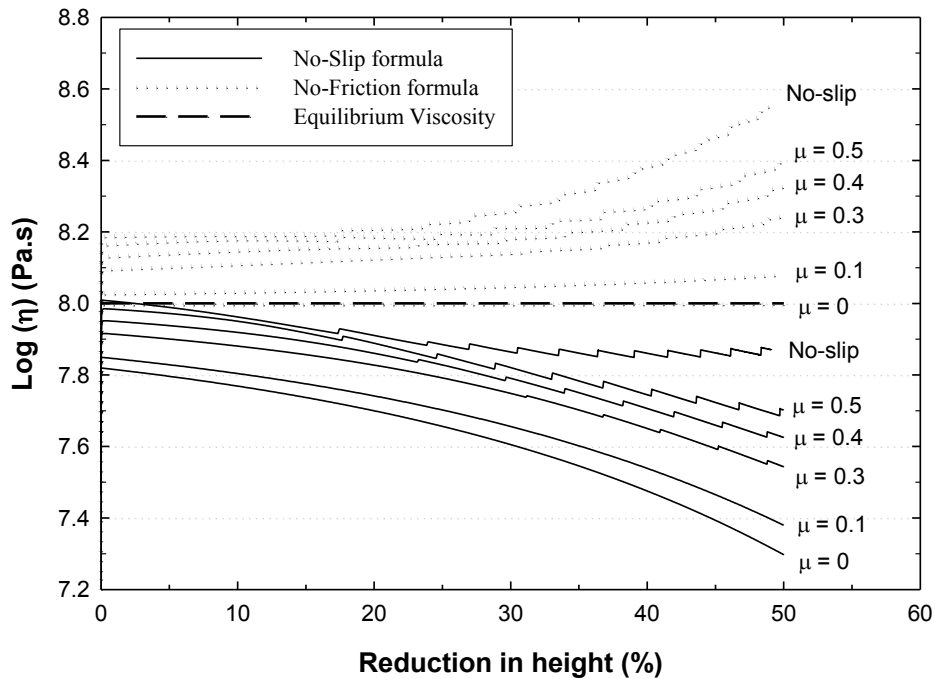


Figure 2.10. The effect of friction and slip on the viscosity predictions made using the no-friction and no-slip analytical formulas for a sample having $H/D = 0.5$. The creep data was generated computationally with SLS glass and the indicated coefficient of friction.

In the development of the analytical Equation 2.12 for no slip, it is assumed that horizontal planes remain plane, which is clearly violated in the barreled region of the specimen for large levels of deformation.

In addition to the two extreme friction cases discussed above, which correspond to the correct friction levels for the respective formulas, the errors introduced in each case *when slip with friction is assumed to occur* are shown for a full range of friction coefficients. The general observation is that if slip occurs when using the no-slip formula, the viscosity will be underestimated. Similarly, if friction exists when using the no-friction formula, viscosity will be overestimated. Furthermore, the result is more accurate at low levels of deformation, providing

enough time has elapsed for viscoelastic effects to dissipate. This transient effect is demonstrated in Figure 2.11, which shows the small time portion of Figure 2.10. The equal spacing of the friction curves in Figure 2.10 indicates an interesting relationship that exists between the viscosity and friction coefficient while using Equation 2.12-2.13, which will be explored in the Chapter 3.

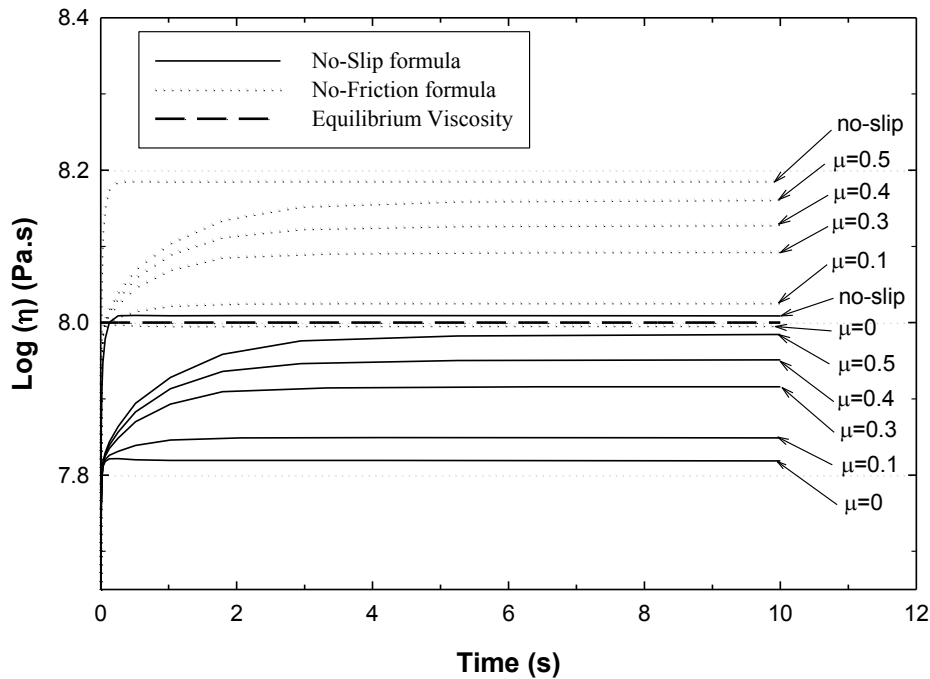


Figure 2.11. Same as Figure 10 for very small deformation plotted with respect to time. The transient effect of active viscoelastic mechanisms at short time scales is visible.

In this case, for the material behavior given by SLS glass by Duffrene et al. [5], it is necessary to wait for about ten seconds. Recall from the results of Figure 2.9 that this waiting period for N-BK7 glass was about 1000 seconds at 631 degrees C, and 250 seconds 20 degrees higher. Since glass types have different and often unknown viscoelastic behaviors, the waiting period has to be determined with each experiment.

The results in Figures 2.10 and 2.11 were for the cylinder geometry of $H/D = 0.5$. The effect of cylinder geometry is summarized in Figure 2.12 for the two formulas. In this figure a single maximum value of viscosity is taken from each creep curve for different levels of friction and different cylinder geometry ranging from 0.2 to 1.0.

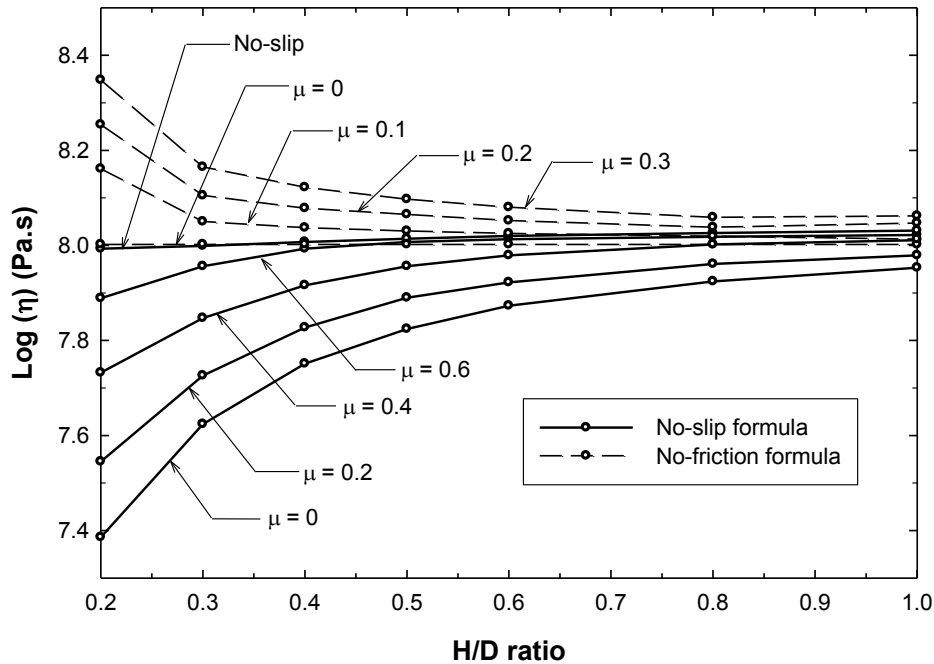


Figure 2.12. Maximum value of Log viscosity predicted using the no-slip and no-friction formulas as a function of the height to diameter ratio of the glass cylinder. The creep data was computationally generated using the indicated coefficient of friction and SLS glass properties in Table 2.2 with relaxation times adjusted to have $\text{Log}(8.0)$.

The results in this figure can be used to approximate the viscosity if the friction coefficient can be determined using, for example, the barrel profile [13]. This figure quantifies how taller specimens are more reliable from the point of view of potential slip when following the ASTM standard [17]. Furthermore, for this viscosity the two formulae give about the same error for a coefficient

of friction near 0.3, indicating that the no-friction formula is better for $\mu < 0.3$, the no-slip estimate is better for $\mu > 0.3$ and an average can be used close to $\mu = 0.3$.

2.6. Discussion

In this chapter computational mechanics was used to understand how friction, cylinder geometry and viscoelastic behavior affect the determination of the viscosity of glass at high temperature using a PPV or the cylinder compression test. This is especially important within the transition temperature range where glass can slip, viscoelastic effects occur and processes such as precision lens molding are performed. The study relies on two key factors: 1) the use of a complete (realistic) viscoelastic characterization of one glass type and 2) very precise, carefully controlled experiments to provide creep data. The importance of the former is that since material properties are being sought, it is necessary to understand the consequence of all the assumptions concerning material behavior. For example, it is often assumed that glass is incompressible, which may or may not be an appropriate assumption for the intended application. The importance of the latter is that it creates the necessary synergy that guides both the computational and experimental investigations. For example, the experimental results for the moldable glass, N-BK7 revealed much more significant time-dependent effects than for the SLS glass.

The most important results, which are presented in Figures 2.9-2.12, extend standard PPV measurements to log of viscosity values above 8, using units of Pa·s. As explained below, this is accomplished by applying the most appropriate formula, either no slip or no friction, to displacement data within the most appropriate time interval, after viscoelastic transients have dissipated, but before the level of deformation is significant. Following the ASTM standard [17], which is recommended for $4 \leq \log(\eta) \leq 8$, a viscous flow formula for no slip should be used, which may or may not be an appropriate choice at the upper limit of the range. If the glass type

being studied experiences slip relative to the mold surface, the no-slip formula will underestimate the viscosity. In addition, the approximate nature of the no-slip formula causes an underestimation of viscosity that increases as the level of deformation increases. In higher viscosity cases when slip occurs with relatively low levels of friction, the no-friction formula gives excellent results that continue to be accurate as deformation progresses. For both the no-slip and no-friction cases, if the displacement data is used before the viscoelastic mechanisms have been allowed to dissipate, viscosity will be underestimated even when the interface boundary conditions are satisfied. Therefore, in all cases the data should be used after this transient phase, which for N-BK7 can take several minutes. An example of possibly underestimating viscosity using PPV for L-BAL35 glass above approximately $\log(\eta/(\text{Pa}\cdot\text{s})) = 7.7$ is presented as manufacturer data in Figure 4.7 of Chapter 4 of this study. This value appears to be the upper limit of viscosity for the routine application of the PPV measurement approach for this glass type.

The most common foil used with PPV is platinum, which according to the literature can have different coefficients of friction. Varshneya et al. [15] report a very high coefficient of friction which approximates no slip, whereas Neuville and Richet [18] report a very low coefficient of friction based on limited barreling of the specimen; see Chang et al. [13] for an approach to quantify the barreled profile with the friction coefficient. The results obtained in the current study favor a lower coefficient of friction for platinum foil. These results do not contradict each other since the current results and those of Neuville and Richet [18] are for log of viscosity above 8 where glass can behave more like a solid than a fluid, whereas Varshneya et al. [15] perform their tests at lower viscosity where the no-slip fluid mechanics condition is applicable.

2.7. Conclusions

Concerning creep data of the cylinder compression test within the transition temperature range, the following conclusions can be made:

- Material compressibility can add significantly to the viscoelastic material response, especially when there is a large friction coefficient (Figure 2.4).
- Interface slip can contribute significantly to the displacement in the cylinder compression test and can be comparable to the effect of a large change in viscosity (Figures 2.6 and 2.8).
- If either friction or viscosity is known, the so-called single term prony series approach can be used to determine the other. Results suggest that if there is sufficient data, both the friction coefficient and the viscosity can be determined (Figure 2.8).
- Standard PPV approaches can be extended to estimate viscosity for the log of viscosity in the range of about 8 and higher by taking into account: 1) viscoelastic material behavior by using a viscosity estimate after transient behavior has died out (Figures 2.9 and 2.11), 2) the coefficient of friction if slip occurs (Figures 2.10-2.12), 3) the geometric ratio, H/D (Figure 2.12) and 4) the total deformation of the specimen since the error of the estimate increases as deformation increases (Figure 2.10).
- The no-slip formula underestimates the viscosity when slip occurs; while the no-friction formula overestimates viscosity when friction is present (Figures 2.10 and 2.12). The no-slip formula further underestimates viscosity when the data is taken during the transient, viscoelastic period of deformation. The no-friction formula

initially underestimates viscosity during this period and then overestimates it (Figure 2.11).

References

1. B. Ananthasayanam, P.F. Joseph, D. Joshi, S. Gaylord, L. Petit, V.Y. Blouin, K.C. Richardson, D.L. Cler, M. Stairiker, M. Tardiff, “Final shape of precision molded optics: Part I – Computational approach, material definitions and the effect of lens shape,” *Journal of Thermal Stresses*, **35** (2012a) pp. 550-578.
2. B. Ananthasayanam, P.F. Joseph, D. Joshi, S. Gaylord, L. Petit, V.Y. Blouin, K.C. Richardson, D.L. Cler, M. Stairiker, M. Tardiff, “Final shape of precision molded optics: Part II – Validation and sensitivity to material properties and process parameters,” *Journal of Thermal Stresses*, **35** (2012b), pp. 614-636.
3. C.R. Kurkjian, Relaxation of torsional stress in the transformation range of a soda-lime-silica glass, *Phys. and Chem. of Glasses*, **4** (1963), pp. 128-136.
4. S.M. Rekhson, N. Gonchukova, and M.A. Chernousov, “Creep and stress relaxation in and below transition region,” *Proceedings of the 11th International Congress on Glass, Prague*, **1** (1977), pp. 329-338.
5. L. Duffrene, R. Gy, H. Burlet, and R. Piques, “Multiaxial linear viscoelastic behavior of soda-lime-silica glass based on a generalized Maxwell model,” *Soc. Rheol.*, **41** (1997), pp. 1021-1038.
6. M. Sellier and C.E. Hann, “Identification of Relaxation Functions in Glass by Mean of a Simple Experiment,” *Journal of the American Ceramic Society*, **90** (2007b), pp. 2980–2983.
7. G. J. Dienes and H. F. Klemm, “Theory and Application of the Parallel Plate Plastometer,” *J. Appl. Phys.*, **17** (1946), pp. 458-471.
8. A.N. Gent, “Theory of the parallel plate viscometer,” *British Journal of Applied Physics*, **11** (1960), pp. 85-87.
9. E.H. Fontana, “A versatile parallel-plate viscometer for glass viscosity measurements to 1000°C,” *American Ceramic Society Bulletin*, **49** (1970), pp. 594-597.
10. A. Jain, G.C. Firestone, A.Y. Yi, “Viscosity Measurement by Cylindrical Compression for Numerical Modeling of Precision Lens Molding Process,” *J. Am. Ceram. Soc.*, **88** (2005), pp. 2409-2414.
11. M. Arai, Y. Kato, and T. Kodera, “Characterization of the thermo-viscoelastic property of glass and numerical simulation of the press molding of glass lens,” *J of Therm. Stresses*, **32** (2009), pp. 1235-1255.

12. T. Zhou, J. Yan, J. Masuda, and T. Kuriyagawa, "Investigation on the viscoelasticity of optical glass in ultra precision lens molding process," *J of Mat. Process Tech.*, **209** (2009), pp. 4484-4489.
13. S.H. Chang, Y.M. Lee, T.S. Jung, J.J. Kang, S.K. Hong, G.H. Shin, Y.M. Heo, "Simulation of an aspheric glass lens forming behavior in progressive GMP process," *NUMIFORM '07, Materials processing and design*, (2007), pp. 1055-1060.
14. J. Yan, T. Zhou, J. Masuda, T. Kuriyagawa, "Modeling high-temperature glass molding process by coupling heat transfer and viscous deformation analysis," *Precision Engineering*, **33** (2009), pp. 150-159.
15. A.K. Varshneya, N.H. Burlingame, W.H. Schultze, "Parallel plate viscometry to study deformation-induced viscosity changes in glass," *Glastech. Ber.* **63K**, (1990) pp. 447-459.
16. D. Joshi, P. Mosaddegh, J.D. Musgraves, K.C. Richardson, P.F. Joseph, "Thermo-Mechanical Characterization of Glass at High Temperature Using the Cylinder Compression Test: Part II – No-slip Experiments, Viscoelastic Constants and Sensitivity Analysis," *Journal of Rheology*, **57**(5), (2013), pp. 1391-1410.
17. ASTM standard C1351M - 96 (2012).
18. D. Neuville and P. Richet, Viscosity and Mixing in molten (Ca, Mg) pyroxenes and garnets, *Geochimica et Cosmochimica Acta*, **55** (1991), pp. 1011-1019.
19. B. Anathasayanam, "Computational modeling of precision molding of aspheric glass optics," Ph.D Dissertation, Clemson University, (2008).
20. G. Scherer, *Relaxation in glass and composites*, John Wiley and Sons, New York, 1986.
21. L. Duffrene, "Comportement viscoélastique d'un verresilico-sodo-calcique dans le domaine des températures intermédiaires: approche phénoménologique et modélisation en triaxialité," Ph.D Thesis, Ecole Nationale Supérieure des Mines de Paris, Paris, France (1994).
22. P.H. Dehoff and K.J Anusavice, "Creep functions of dental ceramics measured in a beam-bending viscometer," *Dental Materials*, **20** (2004), pp.297-304.
23. R.D. Corsaro, "Volume relaxation of dry and wet boron trioxide in glass transformation range following a sudden change of pressure," *Phys. Chem. Glasses*, **17** (1976), pp.13-22.
24. OHARA specification sheet for L-BAL35 glass, Japan. (www.ohara-inc.co.jp)
25. SCHOTT glass catalogue (<http://www.us.schott.com>)
26. Precision Cast Parts Corp. specification sheet for Inconel-600 from (<http://www.specialmetals.com>)

PARALLEL PLATE VISCOMETRY FOR GLASS AT HIGH VISCOSITY

3.1 Introduction

The computational results described at the end of the Chapter 2 for the Parallel Plate Viscometer (PPV) motivated this detailed study that aims to explore the role of viscoelastic behavior, friction and geometry of sample on viscosity determination. Parallel Plate Viscometry (PPV) is the standard approach for obtaining the viscosity of glass in the range $10^4 \text{ Pa}\cdot\text{s} \leq \eta \leq 10^8 \text{ Pa}\cdot\text{s}$. The theory was established by Dienes and Klemm [1] and Gent [2] and described as an ASTM standard [3]. A schematic of a parallel plate viscometer [1, 3] is presented in Figure 3.1. For higher viscosity Beam Bending Viscometry (BBV) is recommended, which is valid for $10^8 \leq \eta \leq 10^{13} \text{ Pa}\cdot\text{s}$ following the ASTM standard [4].

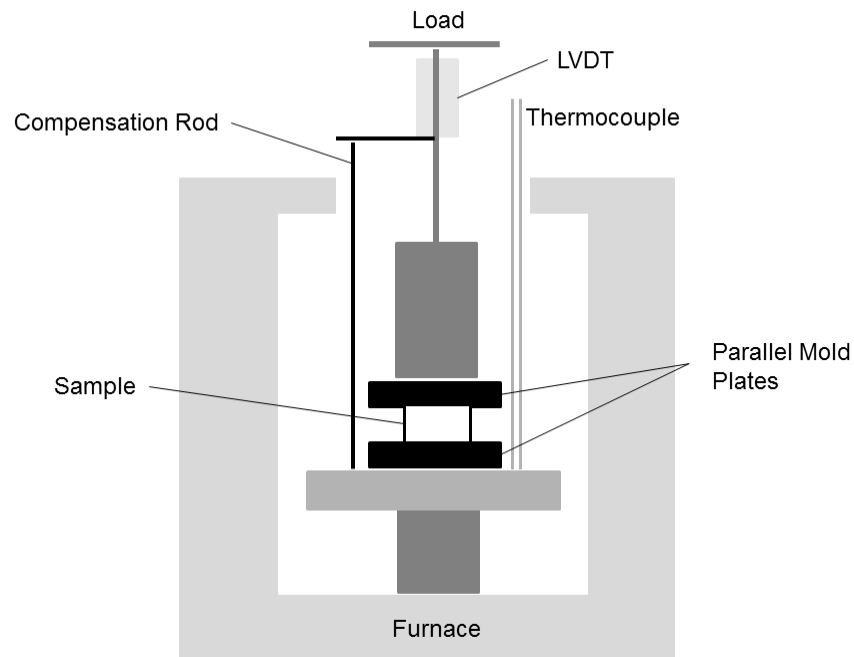


Figure 3.1. Schematic of a parallel plate viscometer.

Glass forming processes such as precision glass molding (PGM) and extrusion of preforms for photonic-crystal fibers typically occur near and slightly above $\eta = 10^8$ Pa·s, which is a difficult range for an accurate characterization, being near the limits of applicability of PPV and BBV. The computational PGM study of Ananthasayanam et al. [5] is an example of the need for accurate viscosity as a function of temperature for $10^8 \text{ Pa}\cdot\text{s} \leq \eta \leq 10^{10} \text{ Pa}\cdot\text{s}$, which includes the pressing and slow cooling stages. Motivated by this problem, Joshi et al. [6, 7] applied computational mechanics to the cylinder compression test to extend the ASTM standard [3] to high viscosity by accounting for viscoelastic effects and slip with friction. Unfortunately, the general use of their procedure is limited due to the computational detail required. To make this work more accessible to those who practice PPV and to promote the gathering of data in this important viscosity range, an approximate expression is developed.

In this chapter, a simple formula is provided to estimate viscosity of glass using parallel plate viscometry (PPV) well above 10^8 Pa·s, which is the upper limit of the recommended range. The following work is mainly based on the computational studies that account for viscoelastic material behavior and frictional slip, which justify the use of linear interpolation to estimate viscosity between well-known upper and lower bounds. The formula takes into account variations in friction coefficient and cylinder height to diameter ratio for a viscosity range of $10^7 - 10^{11}$ Pa·s. A simple procedure to determine the coefficient of friction using PPV is provided in following sections.

3.2 Approximate Viscosity Formula

While Joshi et al. [6] extended PPV above the recommended range of viscosity of $10^4 - 10^8$ Pa·s, their procedure has the following disadvantages: 1) the coefficient of friction between the glass and mold surface must be known and 2) the computational model, including material property

inputs, is required. This latter difficulty can be addressed by using established PPV viscosity formulae to approximate the viscosity when slip with friction occurs. Considering PPV creep displacement data for a solid glass cylinder of height, H , and diameter, D , the no-slip and no friction expressions from Dienes and Klemm [1] and Gent [2] are respectively,

$$\eta_{no-slip} = \frac{2\pi Fh^5}{30V(2\pi h^3 + V)} \left(\frac{dh}{dt} \right)^{-1}, \quad (3.1)$$

$$\eta_{no\ friction} = \frac{Fh^2}{30V} \left(\frac{dh}{dt} \right)^{-1}, \quad (3.2)$$

where F is the force applied to the cylinder, h is the change in height and V is the initial volume. In order to account for viscoelastic glass behavior, it was proposed in Chapter 2 of taking the estimates from Equations 3.1 and 3.2 when the no-slip profile reaches its maximum value, which allows the small time transient effects to dissipate and avoids large deformation effects at long times. Furthermore, it was observed in Chapter 2 that the no-slip formula has a slight error which leads to the correction,

$$\eta_{Corrected\ no-slip} = \frac{2\pi Fh^5}{30V(2\pi h^3 + V)} \left(\frac{dh}{dt} \right)^{-1} \frac{8}{\text{Log}(\bar{\eta}^*)}, \quad (3.3)$$

where $\text{Log}(\bar{\eta}^*) = \text{Log}(\eta^*/(\text{Pa}\cdot\text{s}))$ is the value predicted by Eqn. (1) when the exact answer should be 8. The over-bar on η indicates normalization with respect to $\text{Pa}\cdot\text{s}$. This error is caused by the kinematic assumption that material flows parallel to the mold surfaces. Using Equations 3.2 and 3.3 and taking advantage of behavior identified in Figures 2.10- 2.12 of Chapter 2, an approximation for $0.25 < H/D < 1.0$ and viscosity ranging from $10^7 - 10^{11}$ $\text{Pa}\cdot\text{s}$ was determined to be

$$\text{Log}(\bar{\eta}) = \text{Log}(\bar{\eta}_{no\ friction}) + \frac{\mu}{2\mu^*} [\text{Log}(\bar{\eta}_{Corrected\ no-slip}) - \text{Log}(\bar{\eta}_{no\ friction})], \quad 0 \leq \mu \leq 2\mu^*, \quad (3.4)$$

where $\eta = \eta_{Corrected\ no-slip}$ from Equation 3.3 for $\mu > 2\mu^*$ and values of μ^* and $\text{Log}(\bar{\eta}^*)$ for a range of H/D are given in Table 3.1. After substituting Equations 3.2 and 3.3, Equation 3.4 is an approximation for viscosity taking into account frictional slip. The values in Table 3.1 were obtained using the computational procedure presented by Joshi et al. [6 and 7], which was validated using experimental data. The focus of the current study is on the computational validation of Equation 3.4.

H/D	$\log(\bar{\eta}^*)$: viscous	$\log(\bar{\eta}^*)$: viscoelastic	μ^* : viscous
0.25	7.9957	7.9910	0.353
0.3	7.9994	7.9940	0.339
0.4	8.0081	8.0013	0.316
0.5	8.0155	8.0083	0.299
0.6	8.0206	8.0136	0.287
0.7	8.0245	8.0181	0.279
0.8	8.0269	8.0211	0.273
0.9	8.0285	8.0232	0.268
1	8.0294	8.0247	0.262

Table 3.1. Log of normalized viscosity predicted by the no-slip formula when $\eta = 10^8$ Pa·s and the special value μ^* .

The table shows the slight effect of material behavior on the correction factor, $\text{Log}(\bar{\eta}^*)$, by comparing a purely viscous result to a fully viscoelastic result for L-BAL35 glass [7]. The tabulated value of the special parameter μ^* , which is defined below, is for a viscous material since Equations 3.1 and 3.2 were derived for this behavior.

Justification of Equation 3.4 is presented in Figure 3.2 and is based on linear interpolation and the following behaviors: 1) the no friction formula provides a very accurate result for $\mu = 0$ and the corrected no-slip case provides an accurate result for high friction, 2) at the special value of friction, $\mu = \mu^*$, the true viscosity is the average of the no friction (upper bound) and corrected no-slip (lower bound) predictions, and 3) the errors of the Log of the viscosity predictions as a function of the coefficient of friction are very close to linear and have the same slope for the range $0 \leq \mu \leq 2\mu^*$. Furthermore, the results for $H/D = 1$ in Figure 3.2 show the importance of the correction in Equation 3.3.

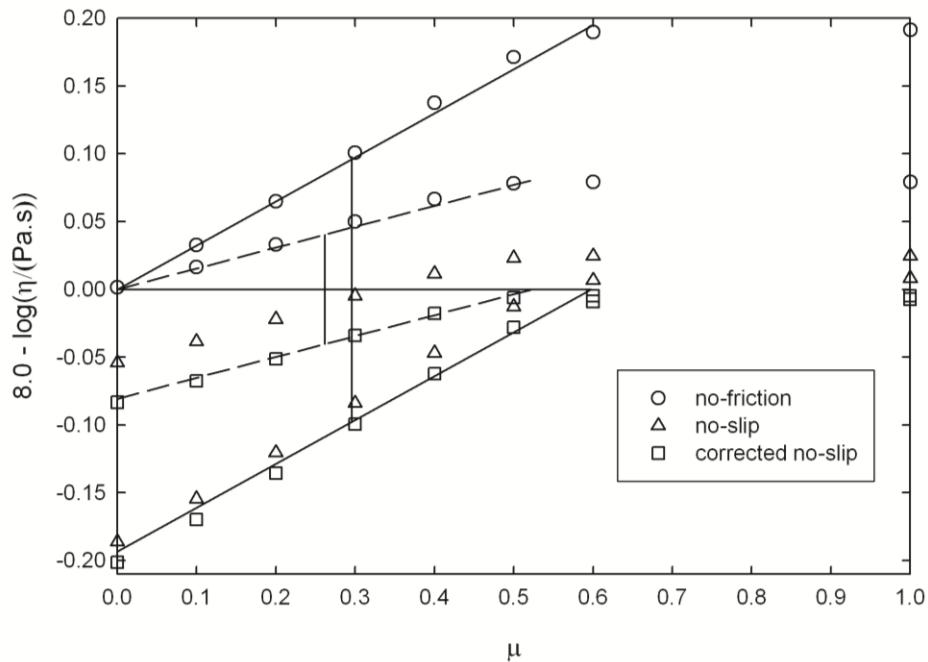


Figure 3.2. Viscosity predictions using Eqns. (1-3) applied to computational viscoelastic creep data. Equation (4) is based on the linear approximations presented as dashed lines for $H/D = 1$ and solid lines for $H/D = 0.5$. The vertical lines identify μ^* for each cases.

As a final comment in this section, for the proposed method to be useful, its application must be independent of material behavior. In Figure 3.2 the purely viscous parameters were used in Equation 3.4, while the computational data was obtained using a fully viscoelastic model of L-BAL35. This material difference introduces only the slight error seen in the limit as the friction coefficient increases and the Log of the equilibrium viscosity is not exactly 8. This error is believed to be negligible and based on additional investigations it was concluded that Equation 3.4 can be applied to a viscoelastic glass using the purely viscous parameters. Furthermore, the correction factor $\text{Log}(\bar{\eta})/\text{Log}(\bar{\eta}^*)$ is nearly independent of the equilibrium viscosity. For example, for a purely viscous material when $\text{Log}(\bar{\eta}) = 8$ and $H/D = 1$, this factor is 0.9963 and for $\text{Log}(\bar{\eta}) = 10$ it is 0.9973.

3.3 Results

Computational simulations of the cylinder compression test using L-BAL35 glass were conducted to demonstrate application of Equations 3.2-3.4. . The temperature dependent viscoelastic material behavior of L-BAL35 required by the computational procedure is presented in the study by Joshi et al. [7]. Three combinations of equilibrium viscosity and friction coefficient were used: 1) $\eta = 10^8$ Pa·s with $\mu = 0.55$, 2) $\eta = 10^9$ Pa·s with $\mu = \mu^* = 0.353$ and 3) $\eta = 10^{10}$ Pa·s with $\mu = 0.15$. In each case molds were assumed rigid, $H = 2.5$ mm, $D = 10$ mm, $F = 4.905$ N (500 gr.) and deformation was to a level of 10%. The viscosity results as a function of deformation are presented in Figure 3.3, which shows the importance of allowing viscoelastic effects to dissipate before determining the viscosity. Equations 3.2-3.4 were applied to each creep curve with Equation 3.3 giving the lower bound, Equation 3.2 giving the upper bound and

Equation 3.4 approximating the actual viscosity. The times and axial deformation levels when the no-slip viscosity estimates reach their maximum values for the three cases are: 1) $\eta = 10^8$ Pa·s: 96 s and 1.1%; 2) $\eta = 10^9$ Pa·s: 1026 s and 1.6%; 3) $\eta = 10^{10}$ Pa·s: 12130 s and 2.2%.

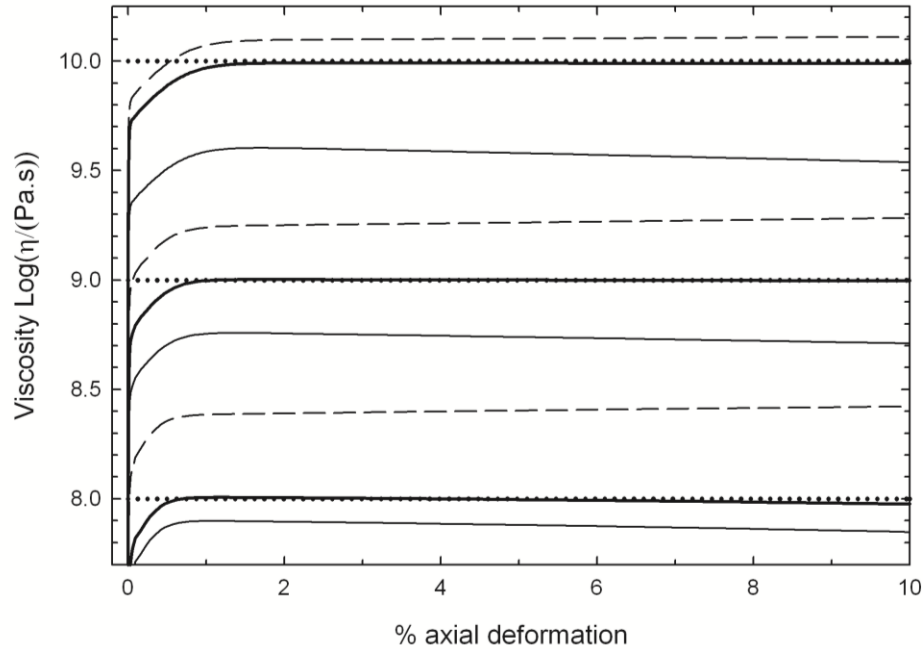


Figure 3.3. Viscosity predictions using computational, viscoelastic creep data for the three combinations of μ & $\text{Log}(\bar{\eta}) = 0.55 \text{ \& } 8, 0.353 \text{ \& } 9$ and $0.15 \text{ \& } 10$ using Eqn. (3.2) (dashed line), Eqn. (3.3) (light solid line) and Eqn. (3.4) (dark solid line). The exact viscosity values are indicated with dotted lines.

Evidence that Eqn. 3.4 and the results in Table 3.1 are accurate for different coefficients of friction and different viscosity is provided in Table 3.2 for $H/D = 0.5$. Two studies were conducted: 1) for a fixed viscosity value of 10^8 Pa·s, the coefficient of friction was varied from 0.1 to 0.5 in increments of 0.1 and 2) for a fixed coefficient of friction of $\mu = \mu^* = 0.299$, viscosity was varied using $\text{Log}(\bar{\eta}) = 7, 8, 9, 10$ and 11.

μ	First study: $H/D = 0.5$, $\eta_{eq} = 10^8$ Pa·s, $\mu^* = 0.299$		
	No-friction Eqn. (3.2)	No-slip Eqn. (3.3)	Equation (3.4)
0.1	8.0312	7.8304	7.99762
0.2	8.065	7.8644	7.99791
0.3	8.1009	7.9007	8.00047
0.4	8.1373	7.9377	8.00379
0.5	8.1711	7.9719	8.00454
$\text{Log}(\bar{\eta}_{eq})$	Second study: $H/D = 0.5$, $\mu = \mu^* = 0.299$		
7	7.1008	6.9024	7.00160
8	8.1004	7.9004	8.00040
9	9.1004	8.8985	8.99945
10	10.1004	9.8965	9.99845
11	11.1003	10.8946	10.99745

Table 3.2. Prediction of $\text{Log}(\bar{\eta})$ using Eqns. (3.2-3.4) and viscoelastic creep data.

The Table 3.2 computational data was obtained using the viscoelastic representation of L-BAL35, while purely viscous parameters from Table 3.1 were used in Equation 3.4. This accounts for the slight inaccuracy of $\text{Log}(\bar{\eta}) = 8.00040$ from Equation 3.4 instead of 8.0 for the $\text{Log}(\bar{\eta}) = 8$ case in the second study. The later study shows how the special μ^* value obtained at 10^8 Pa·s is relatively insensitive to change in viscosity.

For completeness, the simplest procedure [8] for identifying the coefficient of friction using PPV is presented in Figure 3.4 for $H/D = 0.5$. The bulged shapes of a PPV specimen pressed to a deformation level of 50% are presented for a range of friction coefficients. Only the portion of the cylinder not in contact with the molds is included, so the results reveal the special point that defines the edge of contact. The actual scale is on the left, while a radially expanded scale of four is used on the right. These shapes are nearly independent of material behavior and load and can therefore be used to approximate the coefficient of friction for any glass.

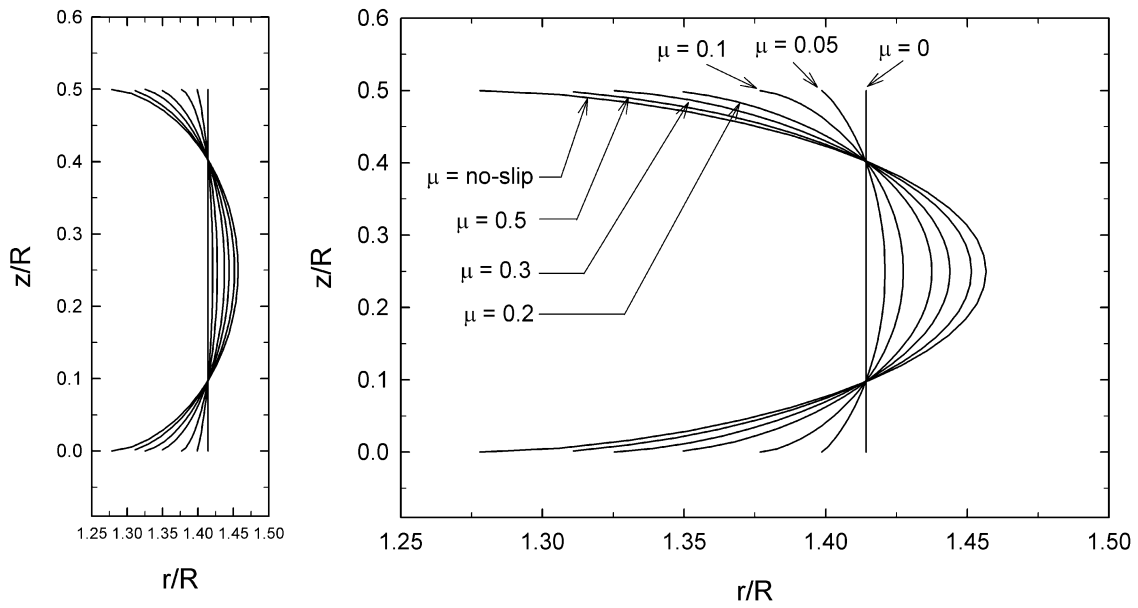


Figure 3.4. Bulged shapes for an L-BAL35 glass cylinder with $H/D = 0.5$ after 50% of axial compression

Another special point along the mold surface is the location of the original radius that can slide radially as the cylinder deforms. This location, referred to as R_c , moves radially outward for all but the no-slip case. In Figure 3.5 this location is presented as a function of coefficient of friction for $H/D = 0.5$ and 1.5 for levels of deformation of 50% and 60%, respectively.

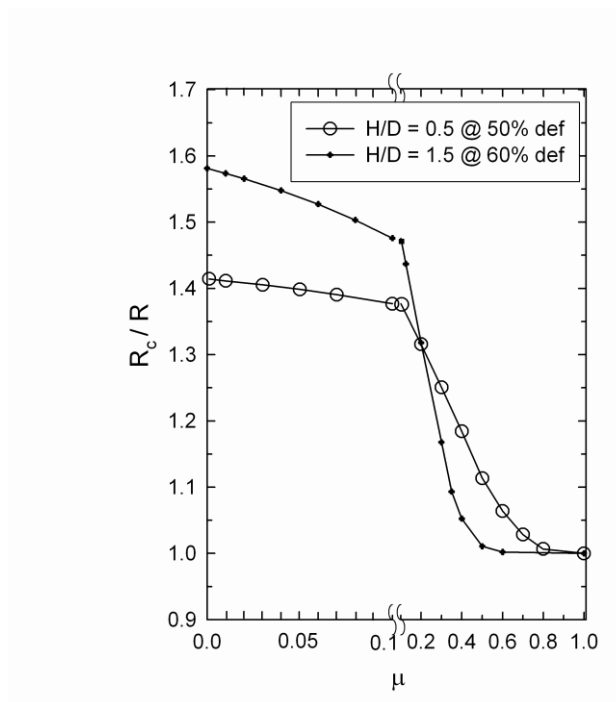


Figure 3.5. Normalized position of the original radius (R_c) after sliding along the mold surface as a function of friction coefficient. A change in the scale occurs at $\mu = 0.1$.

This measure is sensitive to the coefficient of friction and can potentially be used to quantify the level of friction, especially for coefficients of friction above 0.1. Ananthasayanam et al. [9] present a more accurate approach to characterize friction using the ring compression test.

3.4 Discussion

The standard use of PPV applies the no-slip formula, Equation 3.1, to estimate viscosity in the range of $10^4 \text{ Pa}\cdot\text{s} \leq \eta \leq 10^8 \text{ Pa}\cdot\text{s}$. A slight correction to this formula was introduced in Equation 3.3 using the computational procedure described in Chapter 2. At viscosity above about $10^8 \text{ Pa}\cdot\text{s}$, viscoelastic material behavior and possible slip with friction can either complicate or invalidate the standard procedure. As shown in Figure 3.3, the approximate viscosity expressions must be applied after viscoelastic effects have dissipated. The correction for slip with friction is

more involved. In the limiting case of very little or no friction, which can be identified by minimal bulging, Equation 3.2 applies. However, at higher viscosity slip with friction is possible and Equation 3.4 can be applied as long as the friction coefficient is known. If no-slip is incorrectly assumed in this case, as the friction coefficient decreases, the viscosity appears to decrease. Similarly, if no friction is incorrectly assumed, as friction increases the viscosity appears to increase. The approximate expression takes advantage of established upper and lower bounds and the special behaviors identified herein to provide an accurate correction with very little effort. While this expression and the key parameters provided in Table 1 were obtained for specific loading and material behavior, these results are valid for a much wider range of parameters. For example, at higher viscosity a mass of 500 grams will take a considerable time to achieve a reasonable level of deformation. A much larger mass can be used without adjusting the parameters in Table 3.1. For example, increasing the load to 1000 N changes the $\text{Log}(\bar{\eta}^*)$ value in Table 1 for $H/D = 1$ from 8.0294 to 8.0293. The correction parameters show a slight sensitivity to viscoelastic material behavior for an equilibrium viscosity of 10^8 Pa-s, but this sensitivity was shown to be very small in generating the results for Figure 3.2 and Table 3.2. Furthermore, the correction parameters do not change significantly as the viscosity is changed. The alternative to the use of the simple expression Eqn. (3.4) is to perform the full computational simulation as detailed by Joshi et al. (2013a). Regardless of which approach is used, the primary error is in the experimental determination of the coefficient of friction. In this note a simple procedure is presented. For a more accurate determination the procedure of Ananthasayanam et al. [9] that makes use of the ring compression test can be followed.

3.5 Conclusions

The conclusions are:

- PPV can easily be extended to viscosity above 10^8 Pa·s as long as the friction coefficient is known for the glass/mold combination at the temperature of interest.
- An approximate viscosity expression provides a reasonable estimate of the viscosity for the full range of friction behavior ($0 \leq \mu \leq 2\mu^*$), cylinder geometry ($0.25 \leq H/D \leq 1.0$) and viscosity (10^7 Pa·s $\leq \mu \leq 10^{11}$ Pa·s).
- The primary error in the approach is due to the evaluation of the friction coefficient.
- The approximate viscosity expression can be used to estimate the interface friction coefficient if the viscosity at the test temperature is known.

References

1. G. J. Dienes and H. F. Klemm, "Theory and Application of the Parallel Plate Plastometer," J. Appl. Phys., **17**, (1946), pp. 458-471.
2. A. N. Gent, "Theory of the parallel plate viscometer," Br. J. Appl. Phys., **11**, (1960), pp. 85-87.
3. ASTM standard C1351M - 96 (2012)
4. ASTM standard C1350M – 96 (2008)
5. B. Ananthasayanam, *et al.*, "Final shape of precision molded optics: Part I – Computational approach, material definitions and the effect of lens shape," J. Therm. Stresses, **35**, (2012), pp. 550-578.
6. D. Joshi, P. Mosaddegh, J. D. Musgraves, K. C. Richardson, P. F. Joseph, "Thermo-Mechanical Characterization of Glass at High Temperature Using the Cylinder Compression Test: Part I –Viscoelasticity, Friction and PPV," J. Rheol., **57**, (2013), pp. 1367-1389.
7. D. Joshi, P. Mosaddegh, J. D. Musgraves, K. C. Richardson, P. F. Joseph, "Thermo-Mechanical Characterization of Glass at High Temperature Using the Cylinder Compression Test: Part II – No-Slip Experiments, Viscoelastic Constants and Sensitivity," J. Rheol., **57**, (2013), pp. 1391-1410.

8. S. H. Chang, Y. M. Lee, T. S. Jung, J. J. Kang, S. K. Hong, G. H. Shin and Y. M. Heo, "Simulation of an aspheric glass lens forming behavior in progressive GMP process," NUMIFORM '07, Materials processing and design, (2007), pp. 1055-1060.
9. B. Ananthasayanam, D. Joshi, M. Stairiker, M. Tardiff, K. Richardson, P. F. Joseph, "High Temperature Friction Characterization for Viscoelastic Glass Contacting a Mold," J. Non-Cryst. Solids, **385**, (2014), pp. 100-110.

THERMO-MECHANICAL CHARACTERIZATION OF GLASS AT HIGH TEMPERATURE USING THE CYLINDER COMPRESSION TEST – NO-SLIP EXPERIMENTS, VISCOELASTIC CONSTANTS AND SENSITIVITY

4.1. Introduction

As detailed in the Introduction section of Chapter 2 of this thesis, the lack of accurate viscoelastic characterizations of moldable glasses limits the application of computational mechanics to study processes such as precision lens molding with a high degree of confidence. While various successes have been reported, such as predictions of final size and shape by Ananthasayanam, et al. [1, 2], and the lack of data for different glass types suitable for lens molding is perhaps the greatest obstacle to allowing computational mechanics to support manufacturing.

The primary obstacles to accurate characterizations are accurate measurements are required at high and uniform temperatures. Furthermore, the measurements must be made at multiple temperatures to quantify the temperature dependence of the material behavior. Duffrene, et al., [3] provided a complete viscoelastic characterization at one temperature of an Soda-Lime-Silica (SLS) glass, which is not suitable for molding. What is needed is the ability to characterize moldable glasses at multiple temperatures.

Several researchers [4-8] have applied the cylinder compression test to provide creep data for use in thermo-mechanical characterizations. This test has the advantage of simplicity, both in specimen preparation and availability of high temperature testing machines, such as parallel plate viscometers and lens molding machines. While this test is simple to perform, as discussed in Chapter 2, in the transition temperature range where glass is viscoelastic it is difficult to

determine the viscosity accurately. Accurate determination of viscosity and friction coefficient are required to identify the displacement component from the cylinder compression test that is attributed to the viscoelastic shear and bulk responses.

In this chapter, experimental creep data from the cylinder compression test using a unique no-slip test specimen will be used to determine viscosity and the shear relaxation function for the two moldable glasses N-BK7 and L-BAL35. As shown in the Chapter 2, the uncertainty in friction translates directly to uncertainty in viscosity. The no-slip specimen eliminates friction as a variable and provides data that can be used to determine the viscosity with a high degree of accuracy.

4.2. Theory, Modeling Details and Material Property Definitions

All of the theory used in the current study is presented by Ananthasayanam, et al., [1] and reviewed in the Chapter 2. In particular this includes the linear theory of viscoelasticity, thermorheologically simple (TRS) behavior to account for temperature dependence of material properties and structural relaxation to account for thermal history dependent thermal expansion and contraction. TRS behavior and structural relaxation are necessary to include in the analysis when temperature change occurs, especially within the transition temperature range where glass thermo-mechanical behavior is very sensitive to temperature change. In this study an “isothermal” analysis corresponds to a computation done at the pressing temperature without accounting for the effects of heating and/or cooling to reach the pressing temperature. The more realistic non-isothermal analysis, which gives results that are almost the same as the isothermal analysis, is carried out in Section 4.4.5.

The finite element software, ABAQUS is used to perform the computations. In addition to axisymmetric analysis, which is described in Chapter 2, a three-dimensional analysis is used to help to understand possible anomalous displacement contributions.

The material properties used throughout this study are presented in Tables 2.1-2.3 of Chapter 2 and Tables 2 and 3 of Ananthasayanam, et al. [1]. The combination of computational model and glass properties for L-BAL35 glass were validated in the study of Ananthasayanam, et al. [2] by using measurements of lens profile deviation resulting from precision lens molding. The precision lens molding process is very similar to the cylinder compression test, so the validation is applicable to this study.

4.3. Experimental Procedure – No-Slip Boundary Condition

Creep experiments were performed using the Parallel Plate Viscometer, Orton PPV-1000 as described Chapter 2. The creep data presented in the current study corresponds to the case of infinite friction, which does not allow relative slip between the glass and mold surfaces. In order to achieve this condition of “no-slip,” a fused silica disc (15 mm in diameter and 2 mm thick) was placed between the Inconel molds and the glass sample at both the top and bottom surfaces. During the heating cycle for N-BK7 glass, the temperature of the glass was raised approximately 100 °C above the transition temperature T_g of the test glass. This allowed a chemical diffusion process to take place between the fused silica and the test sample at the interfacial layers of the two materials, which created a bond between the two glasses. Thus, the testing sample essentially stuck to the fused silica disc and a "no-slip" boundary condition was generated. Once a good bond was achieved between the glass sample and fused silica, the temperature of the heating chamber was adjusted to the testing temperature and the glass sample was soaked until the temperature reading on the thermocouple reached a steady state temperature. For L-BAL35 glass,

the test temperature was sufficiently high to create a good bond and an additional temperature increase was not used. For both glass types, it was important to have the samples soaked for sufficient time during the creep testing at high temperatures to ensure the uniform temperature distribution within the sample. At the end of the soaking period, a fixed value of load was applied to the sample and displacement response was recorded as a function of time. The initial elastic response during this test, which is of very small order of magnitude, was subtracted from all the experimentally generated creep curves.

4.4. Results

All of the computational results presented in this study are for the cylinder compression test. An axisymmetric two-dimensional model is used for all results except for the three-dimensional study (case (3)) in Figure 4.13. All results are for isothermal pressing except for the study presented in Figure 4.10 which accounts for structural relaxation and temperature dependence of the material constants during heating, soaking and cooling. N-BK7 glass properties from Table 2.3 of Chapter 2 are used in Figures 4.1 – 4.4 and 4.9, L-BAL35 properties from [1] and Table 2.3 of Chapter 2 are used in Figures 4.5 – 4.8 and 4.10, and SLS glass properties from [3] and Tables 2.1 and 2.2 from Chapter 2 are used in Figures 4.11-4.15. In Figures 4.1 – 4.3 and 4.5, which include experimental data, a single term prony series for shear is used with viscosity treated as an input parameter. Full viscoelastic analysis is compared to experimental data in Figures 4.8 and 4.9. Throughout this Chapter, the units of viscosity are always in Pa·s.

4.4.1. The Effects of Heating, Soaking, Cooling and Residual Stresses

The creep tests of glass in the current study are done near the glass transition temperature. Since the thermo-mechanical properties of glass are highly temperature dependent, it is necessary to perform the tests after the glass has reached a uniform, known temperature. In the experiments discussed in Chapter 2, a two hour heating time followed by a three hour soaking time was used and the computational heat transfer results indicate that these times are sufficient to reach the uniform target temperature. Furthermore, the computational results for creep curves generated using this five hour heating period were indistinguishable from isothermal creep curves that neglected the transient effects. Modeling of a variable temperature case requires the use of the structural relaxation and TRS behaviors of the glass, so is much more involved than an isothermal press.

Within the context of the no-slip experiments, for a bond to occur between the glass sample and the silica plates the sandwiched sample is heated and soaked to an elevated temperature of one hundred degrees above the glass transition temperature, and subsequently cooled to the testing temperature before the start of the pressing stage. Contrary to the slip experiments described in the Chapter 2, the transient effects now have a small effect on the creep curves, which is due to the cooling of the specimen that is now bonded to the relatively rigid silica plates. As will be shown in Section 4.4.5, when the entire process is modeled by taking into account structural relaxation and TRS behavior, slightly less creep displacement is predicted, which for the L-BAL35 cases studied, amounted to a prediction of a viscosity that was 0.07% lower than predicted using an isothermal analysis. Since this “correction” is so small, for the validation case using N-BK7, isothermal analysis is used in Sections 4.4.2 and 4.4.3. The primary

obstacle to performing the full analysis for N-BK7 is that the viscoelastic behavior of N-BK7 is not known, which will be addressed in Section 4.4.4.

4.4.2 Validation Study of Viscosity Determination Using the No-Slip Specimen

In this section the combined experimental and numerical methodology to calculate the viscosity of glass at a temperature within the transition temperature range is used for a glass with known viscosity. This approach, which was presented in Section 2.5.6 of Chapter 2, is based on the long time creep displacement of the cylinder compression test for a glass having both shear and bulk relaxation mechanisms, differing essentially by a constant from a material exhibiting only viscous flow. As discussed in the Chapter 2, friction at the interface between the glass specimen and the molds affects the displacement response of the creep curve. The uncertainty in knowing the coefficient of friction can be eliminated either by producing a perfectly slipping condition ($\mu = 0$) across the interface or by making the sample stick to the mold ($\mu = \infty$). In this study the latter approach is used, with the details described in Section 4.3. In this section the optical glass, N-BK7, was used in the experiments since the viscosity as a function of temperature is known [10]. To further validate the approach, the different values of $H/D = 0.4$ and 0.7 were used. The data was obtained for 60,000 seconds, but only the first 10,000 seconds were used since the cylindrical surface of the glass cylinder “folds” and comes into contact with the molds beyond this time and it is believed that sticking at the pressing temperature does not occur upon contact.

The results from the iterative procedure provide a computational creep curve that is compared to the experimental curve in Figure 4.1 for the two H/D ratios of 0.4 ($D = 8.92$ mm) and 0.7 ($D = 8.95$) at temperatures of 643.3 °C and 644.1 °C, respectively. The creep load was 0.25 Kg. The calculated viscosity values using units of Pa·s at these temperatures are,

respectively, $\log(\eta) = 9.08$ and 8.98 , which compare to values of 8.8 and 8.93 that were obtained from the manufacturer [10]. As shown in Chapter 2 in this temperature range the tendency is to underestimate the viscosity due to both time dependent effects and slip, which provides a possible explanation for the current prediction of viscosity above what is reported. An isothermal assumption was used to obtain these estimates, which will be

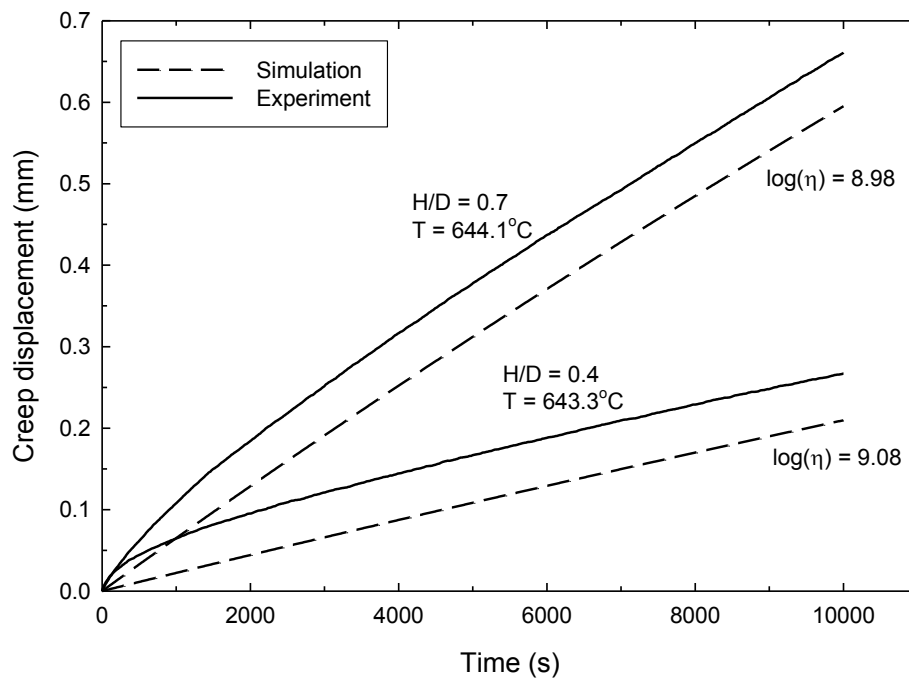


Figure 4.1. Validation of the sticking boundary condition approach using N-BK7 and two different cylinder geometries (see also Figure 4.4). Viscosity at the reported temperature according to the glass manufacture is in the range of $8.80 - 8.94$ Pa·s [10].

shown in Section 4.4.5 to overestimate viscosity very slightly after the viscoelastic and TRS behaviors of N-BK7 glass are obtained. It is seen from the creep curves that the experimental and numerical curves are almost parallel to each other over the period of testing, except at the

beginning where the delayed (viscoelastic) deformation mechanism is most active. This is seen more clearly in Figure 4.2 where the differences between the curves in Figure 4.1 are shown to asymptotically approach a constant. Furthermore, as shown in Figure 4.3 for the $H/D = 0.7$ case, a very small change in viscosity introduces a relatively large slope, making the precise determination of viscosity possible. The upper and lower bound curves in Figure 4.3, for example, correspond to a change of about $\pm 0.1\%$. Concerning the neglect of the non-zero slope of δ_{VE} in Figure 2.7 of the Chapter 2, it was determined using the single term prony series approach for viscosity values in the range of $8.5 < \log(\eta) < 10.5$, that this slope is equivalent to underestimating the viscosity by only 10^{-5} percent, which is negligible considering the accuracy demonstrated by the results of Figure 4.3. As a final comment on the quality of the creep data, it

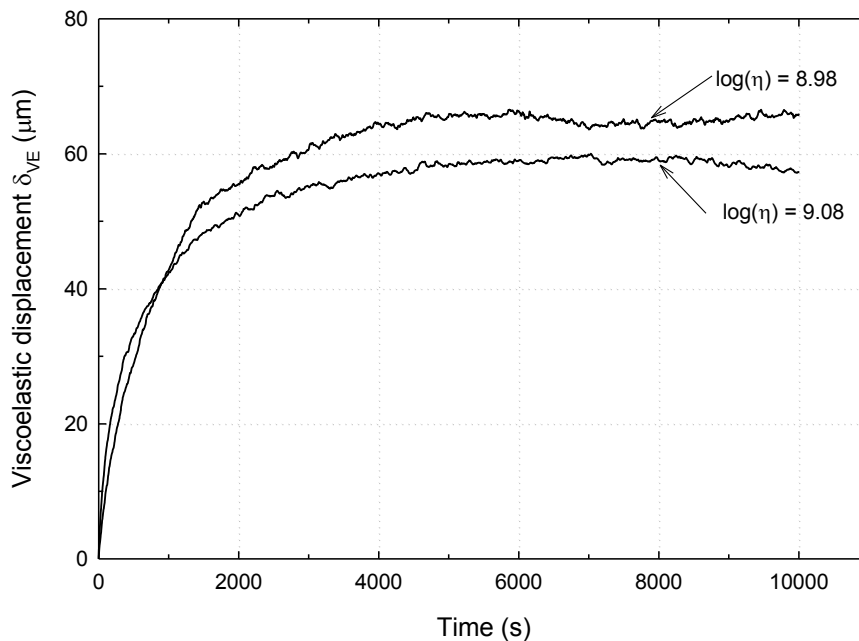


Figure 4.2. The displacement, δ_{VE} , obtained from the difference of the curves in Figure 4.1 for selected values of viscosity to show how precisely the viscosity can be determined using this approach.

is observed from the data in Figure 4.2 that during the transient phase an anomalous viscoelastic displacement must occur for the $H/D = 0.4$ case, since a shorter specimen should always have less displacement, which it does not.

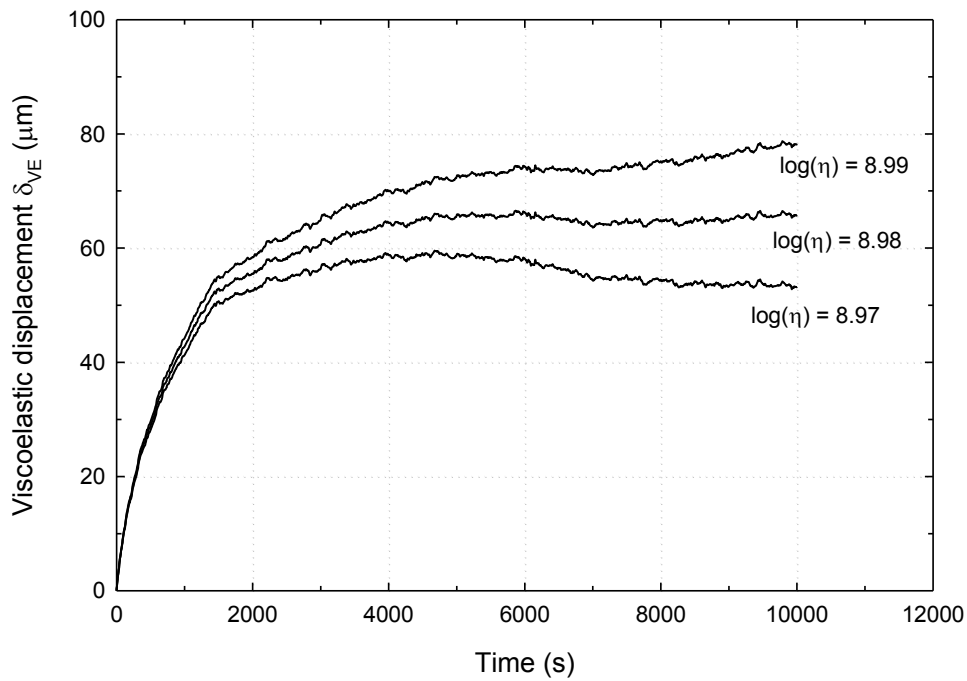


Figure 4.3. The displacement, δ_{VE} , obtained from the difference of the curves for the case of $H/D = 0.7$ in Figure 4.1 for selected values of viscosity to show how precisely the viscosity can be determined using this approach.

The source of this additional displacement is unknown and will be considered in Section 4.4.7.

The entire set of creep data for the $H/D = 0.7$ N-BK7 case is assumed to be valid, and as will be shown below, for the determination of viscosity, both data sets are valid.

The viscosity values obtained for the two cases in Figure 4.1 are evaluated using the no-slip PPV formula [11-14],

$$\eta = \frac{2\pi F h^5}{30V(2\pi h^3 + V)} \left(\frac{dh}{dt} \right)^{-1}, \quad (3.1)$$

in Figure 4.4, where F is the force applied to the cylinder, h is the change in height of the cylinder and V is the initial volume. It is observed that as long as the transient viscoelastic effects are allowed to dissipate, the Equation 3.1 agrees very well with the simulation results from Figure 4.1 for both cases. This agreement helps to confirm that the specimen has a no-slip boundary condition and demonstrates that any anomalous displacement in the difference plotted in Figure 4.2 does not affect the determination of the viscosity.

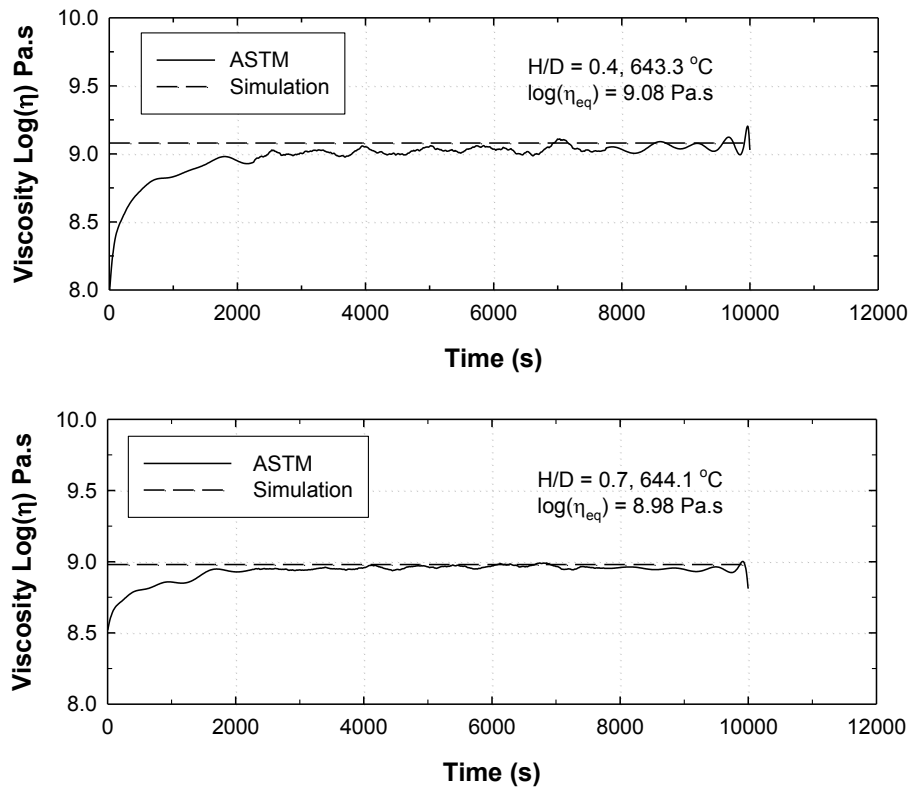


Figure 4.4. Viscosity prediction of N-BK7 experimental data from Figure 4.1 using ASTM formula [14] (solid line). Viscosity values obtained from the simulations associated with Figure 4.1 are plotted as dashed lines.

As a final comment in this section, the finite element model used in the current study was validated in [2] using measurements of lens profile deviation and has now been validated further by the viscosity predictions in Figures 4.1 and 4.4.

4.4.3 Viscosity of L-BAL35 Using the Single Term Prony Series Approach

Experiments similar to those of Figure 4.1 for N-BK7 were conducted using L-BAL35 glass. In this case three cylindrical samples having H/D ratio of 0.73, 0.68 and 0.40 were pressed at 567.8, 575.0 and 588.8 °C, respectively and in this case the mass was 0.5 Kg. The data for

these three samples along with the results of the iterative approach are presented in Figure 4.5.

The viscosity results from these three tests are summarized in the isothermal column of Table 4.1.

Summary of results of viscosity determination of L-BAL35 glass						
Height (H) (mm)	Diameter (D) (mm)	H/D	Sample Temperature ($\pm 1.5^\circ\text{C}$)	Isothermal Log (η) (Pa·s)	Non-isothermal Log (η) (Pa·s)	Non-isothermal VE correction Log (η) (Pa·s)
7.24	9.9	0.73	567.8	9.30	9.294	9.290
6.82	9.9	0.68	575.0	8.958	8.952	8.9485
3.9	9.9	0.40	588.8	8.355	8.348	8.345

Table 4.1. Sample parameters and viscosity values used to match the experimental creep data in Figure 4.5. The non-isothermal results correspond to the numerical experiment presented in Section 4.4.5.

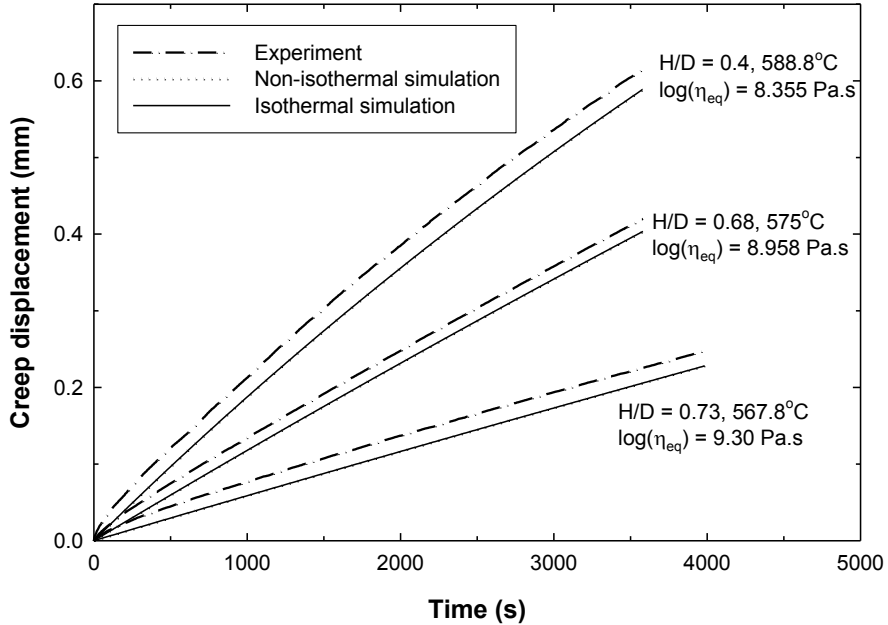


Figure 4.5. Comparison of experimental and computational creep curves for L-BAL35 at three different temperatures. The viscosity results are summarized in Table 4.1.

Similar to the results in Figure 4.4 for N-BK7 glass, these viscosity values for L-BAL35 are shown in Figure 4.6 to agree well with predictions from the no-slip PPV formula presented in Equation 4.1.

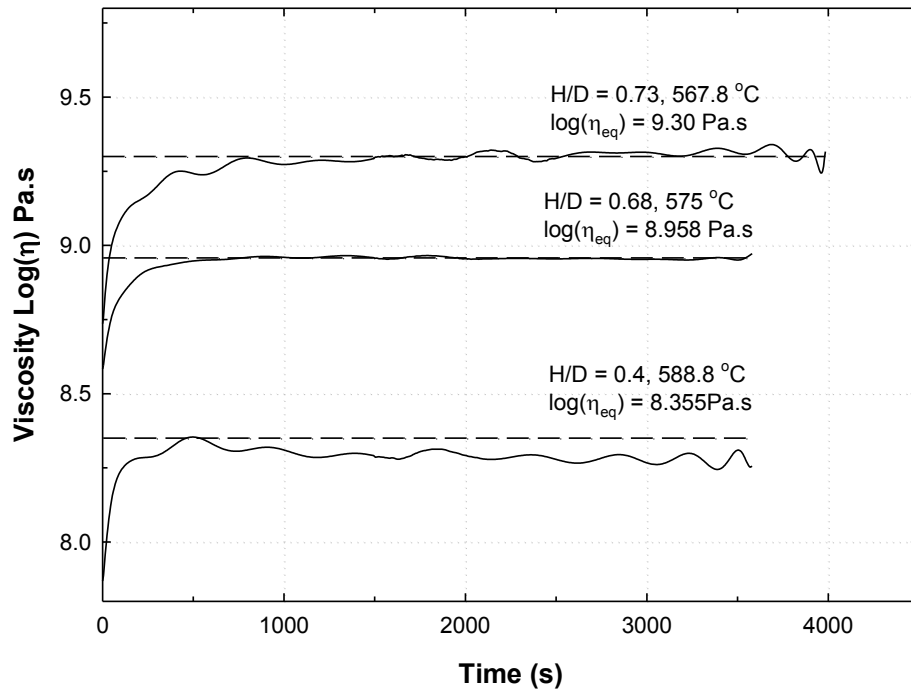


Figure 4.6. Viscosity prediction of L-BAL35 experimental data from Figure 4.5 using the ASTM standard formula [14] (solid line). Viscosity values obtained from the simulations associated with Figure 4.5 are plotted as dashed lines.

The three viscosity values are presented in Figure 4.7 along with the viscosity values obtained from the glass manufacturer [15] and available literature [10]. The horizontal error bars on the computed values

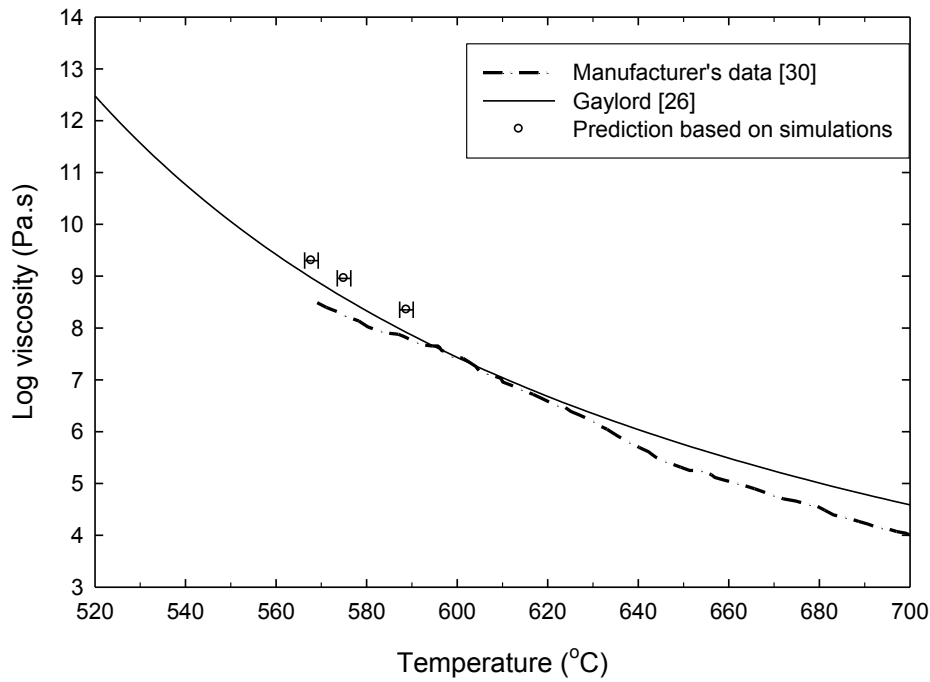


Figure 4.7. Viscosity-Temperature (η -T) plot for L-BAL35: Comparison of calculated isothermal viscosity (symbols) with the viscosity data obtained from OHARA [15] (dotted) and Gaylord [17] (solid) (see Table 4.1 for values).

indicate repeatability error of 1.5°C in temperature measurement as explained in Section 2.4 of Chapter 2. The viscosity values provided by the manufacturer seem to deviate around $\log(\eta) = 7.7$, indicating possible error above this viscosity for this glass that can be attributed to viscoelastic effects and/or slip as described in Chapter 2. The data taken from the literature was based on fitting the Vogel-Fulcher-Tammann (VFT) equation using the viscosity value calculated near T_g and at very high temperatures. Using the current approach, the viscosity is determined by direct calculation at the test temperatures.

4.4.4 Determination of the Viscoelastic constants

The cylinder compression test data can also be used to calculate the viscoelastic response of the material after the viscosity of the glass has been calculated. However, in order to make use of δ_{VE} to characterize the viscoelastic response, it is required that the data be very precise since the displacement due to viscous flow is so dominant. There is also the issue of anomalous displacement as discussed in connection with the $H/D = 0.4$ data from Figures 4.1 and 4.2. Anomalous displacement must also be present in the $H/D = 0.4$ data set of Figure 4.5. Given that the glass transition temperature of L-BAL35 is $527\text{ }^{\circ}\text{C}$, the temperatures and heights for the three cases in Figure 4.5 (see Table 4.1) indicate that the $H/D = 0.4$ case should have the smallest δ_{VE} , since it has the smallest height. The other two data sets ($H/D = 0.68$ and 0.73) have behavior more consistent with their temperature and size. It was therefore decided that the $575.0\text{ }^{\circ}\text{C}$ case would be used to determine the viscoelastic constants by curve fitting and that the $567.8\text{ }^{\circ}\text{C}$ case would be used to validate the fit. The viscoelastic parameter fitting was accomplished using a manual procedure and did not involve the use of an optimization algorithm.

Before proceeding with the curve fit, there is another observation that must be taken into account. The experimental values of δ_{VE} in Figures 4.1 and 4.5, as well as Figure 2.8 of Chapter 2, are about three orders of magnitude larger than for SLS glass. One consequence is that the portion of δ_{VE} attributed to compressibility, i.e., δ_b , is a much smaller fraction for the molding glasses. Therefore, it is not possible to use the creep data and current approach to assess the G_2 function for L-BAL35 or N-BK7. As such, the bulk relaxation function was approximated by making two adjustments to the SLS function in Table 2.2 of Chapter 2. First, a ratio of infinite to instantaneous bulk modulus of 0.35 was used, which is in the middle of the range of possible

values [16]. Second, relaxation times were modified to have a similar response as the δ_{VE} data, which was achieved by multiplying the SLS relaxations times by 50.

Based on the reasoning above, the experimental creep curve data for L-BAL35 in Figure 4.5 at $T = 575.0^\circ\text{C}$ was selected to fit with a prony series representation of the shear relaxation function. The prony series parameters resulting from this analysis are presented in Table 4.2.

Shear Relaxation Function, $\psi_1(t) = \frac{G_1(t)}{2G_0}$		Hydrostatic Relaxation Function, $\psi_2(t) = \frac{G_2(t)}{3K_0}$		Temperature Dependent Elastic Modulus
w_i	τ_i (s)	v_i	λ_i (s)	E(T) (GPa)
6.814500e-01	9.850e-03	1.445015e-02	6.5550e-04	100.8, $T \leq 510^\circ\text{C}$
2.310000e-01	6.500e-02	1.456195e-02	1.3010e-02	
5.000000e-02	2.810e-01	1.866345e-02	2.6460e-02	
3.558410e-02	1.960e+00	1.3888095e-01	2.5160e-01	10, $T \geq 560^\circ\text{C}$
1.588045e-03	7.700e+00	2.5614095e-01	1.5690e+00	
3.778540e-04	2.850e+02	2.073006e-01	2.6605e+02	

Table 4.2. Stress relaxation prony series coefficients obtained using the experimental data for L-BAL35 in Figure 4.5 for the case of $H/D = 0.68$, $T = 575^\circ\text{C}$ and $\log(\eta_{eq}) = 8.958$ Pa·s. The dilatational (bulk) response was assumed to be similar to that of SLS glass.

Given these parameters for $T = 575.0^\circ\text{C}$, the relaxation times in Table 4.2 for $T = 567.8^\circ\text{C}$ were obtained by multiplication of a factor proportional to the ratio of the corresponding viscosity values, i.e., by using the TRS assumption, [16]. Using this approach a predicted creep curve was obtained for the $T = 567.8^\circ\text{C}$ case. The results of the fit and the prediction are presented in

Figures 4.8a and 4.8b, respectively. In these plots the computationally determined viscous flow portion of the creep curve was

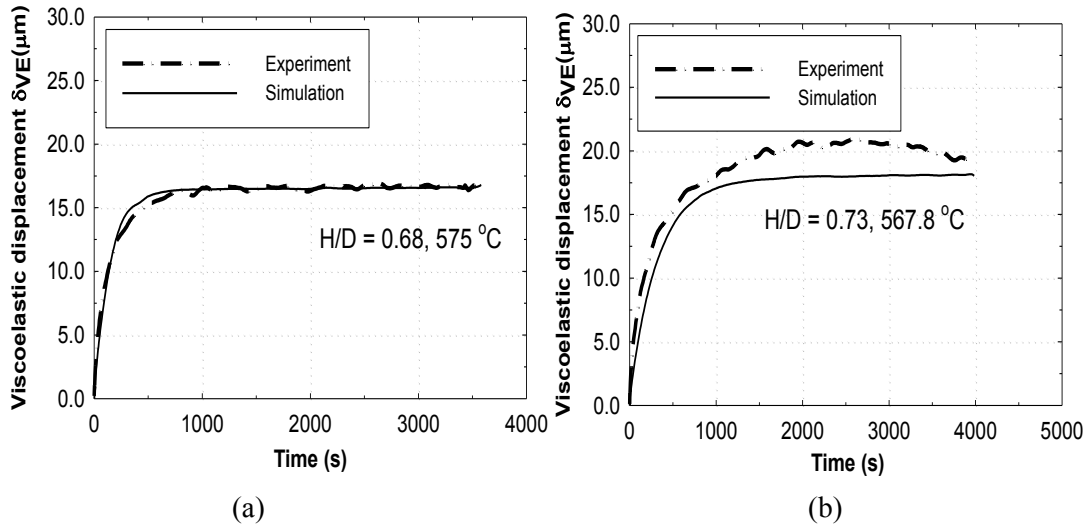


Figure 4.8. Viscoelastic displacement (δ_{VE}) for L-BAL35 for two no-slip experiments presented in Figure 4.5 compared to computational results. The data used for the prony series fit (Table 4.2) is presented in Figure 4.8 (a) ($H/D = 0.68$ at $575\text{ }^\circ\text{C}$) and the prediction is presented in Figure 4.8(b) ($H/D = 0.73$ at $567.8\text{ }^\circ\text{C}$).

subtracted from both the simulation and the data, leaving only the viscoelastic displacement, δ_{VE} . For the $H/D = 0.4$ case, which has an anomalous displacement component, the simulation underpredicts δ_{VE} by a factor of four. The lens profile deviation study by Ananthasayanam, et al. [2] can be used to further test the current viscoelastic fit for L-BAL35. In that study, due to the lack of accurate creep data, it was necessary to approximate the viscoelastic material behavior of L-BAL35. Compared to Material Set #2 from Ananthasayanam, et al. [2], the current shear relaxation function predicts a δ_{VE} that is approximately 10-15 times higher for the same creep loading. However, when the relaxation function from Table 4.2 was used in lens molding

simulations to predict the deviation of the bi-convex and steep meniscus lenses from Ananthasayanam, et al. [2], there were no significant changes in the deviation results.

In similar fashion to the L-BAL35 results in Table 4.2 and Figure 4.8, viscoelastic results for N-BK7 are presented in Table 4.3 and Figures 4.9a-c. The no-slip data for $H/D = 0.7$ from Figure 4.1 was used for the fit that is presented in Figure 4.9a. The $H/D = 0.4$ case in Figure 4.1 is the only other available no-slip data set for N-BK7, but this case has an obvious anomalous contribution to the viscoelastic displacement that makes it twice what is expected based on the characterization in Table 4.3. Therefore, the predictions in Figure 4.9 were made using the slip data from Figure 2.8 of Chapter 2. In Figure 4.9b the platinum foil data was used, while in Figure 4.9c the nickel foil data was used. Both slip cases had $H/D = 0.22$, showing that reasonable results can be obtained with a short specimen.

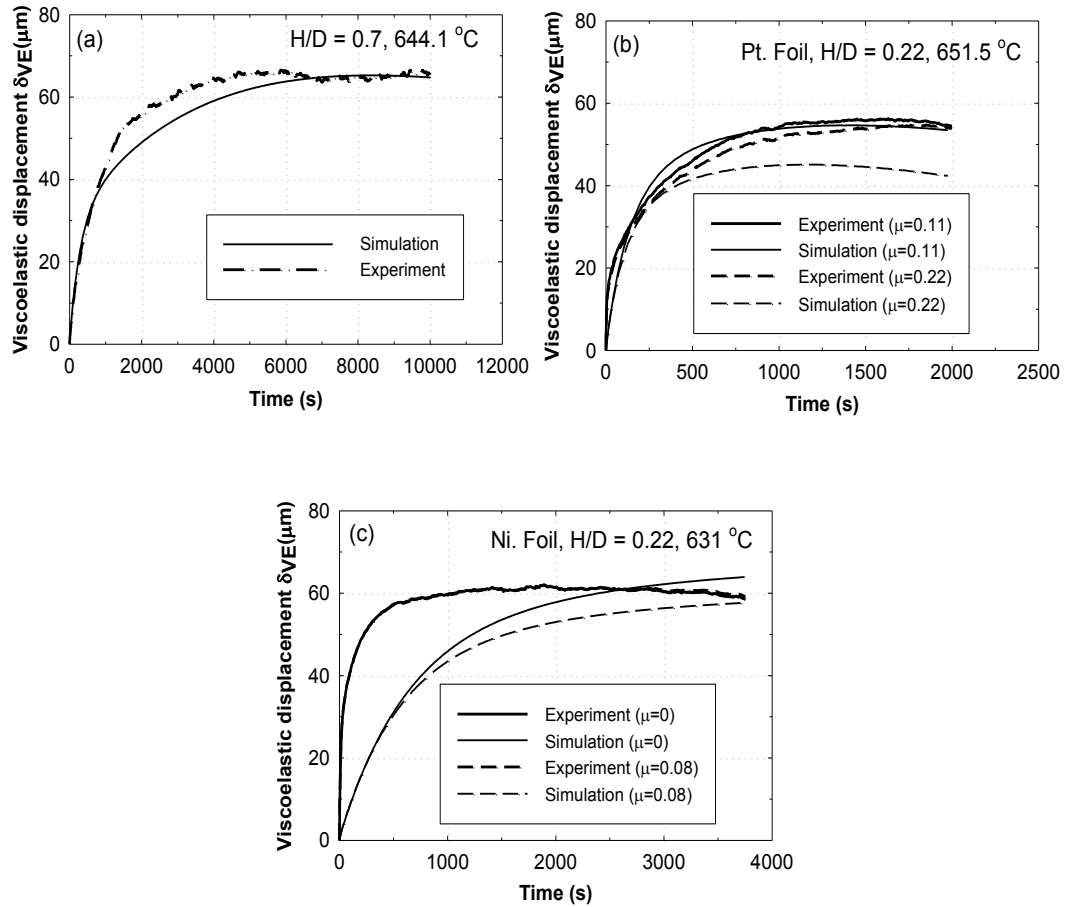


Figure 4.9. Viscoelastic displacement (δ_{VE}) for N-BK7 from three experiments compared to computational results: (a) prony series fit (Table 4.3) using no-slip data from Figure 4.1 ($H/D = 0.7$ at $644.1\text{ }^\circ\text{C}$), (b) prediction for Pt foil slip data from Figure 2.7 in the Chapter 2 and (c) prediction for Ni foil slip data from Figure 2.7 in Chapter 2.

A complication with the use of the slip data from Chapter 2 in Figure 4.9 is that the coefficients of friction for the two data sets could only be defined as ranges based on uncertainty in temperature. As discussed in the Chapter 2, for the Ni foil specimen the range was defined by $0 < \mu < 0.08$, while for the Pt foil specimen the range is $0.11 < \mu < 0.22$. Results for both the upper and lower values from the range are included in Figures 4.9b and 4.9c. These viscoelastic results

are clearly sensitive to slight changes in the coefficient of friction, which, besides showing the advantage of using a no-slip specimen, suggests that if the data/characterization were of higher quality, the coefficient of friction could be determined with high accuracy. It could be argued that for the Pt foil case, a coefficient of friction closer to 0.11 is a better choice than 0.22.

Shear Relaxation Function, $\psi_1(t) = \frac{G_1(t)}{2G_0}$		Hydrostatic Relaxation Function, $\psi_2(t) = \frac{G_2(t)}{3K_0}$		Elastic Modulus
w_i	τ_i (s)	ν_i	λ_i (s)	E (GPa)
7.200e-01	1.200e-03	1.445015e-02	6.5550e-04	83, T \geq 560°C
2.400e-01	8.000e-03	1.456195e-02	1.3010e-02	
3.800e-02	9.000e-02	1.866345e-02	2.6460e-02	
1.800e-03	9.000e-01	1.3888095e-01	2.5160e-01	
1.800e-04	1.000e+02	2.5614095e-01	1.5690e+00	
1.900e-06	6.600e+02	2.073006e-01	2.6605e+02	
9.990e-07	5.600e+03			

Table 4.3. Stress relaxation prony series coefficients obtained using the experimental data for N-BK7 in Figure 4.1 for the case of H/D = 0.7, T = 644.1°C and $\log(\eta_{eq}) = 8.98$ Pa·s. The dilatational (bulk) response was assumed to be similar to that of SLS glass.

The transient portions of the simulation results in Figure 4.9c are not in very good agreement with the data. The rate of change of displacement with respect to time in Figures 4.8 and 4.9 is affected primarily by temperature and friction. This rate increases as temperature increases and as friction decreases. Clearly the rate is not predicted as well as the steady state magnitude of the viscoelastic response, especially in Figure 4.9c. Of the three predictions, the

temperature in Figure 4.9c is the farthest from the reference temperature. The predictions made in Figures 4.9b, 4.9c and 4.8b are based purely on the viscosity/temperature relationships of the two glasses and the TRS assumption.

As a final statement on these viscoelastic comparisons, while the presence of anomalous displacement for the two no-slip $H/D = 0.4$ creep curves in Figures 4.1 and 4.5 is somewhat disturbing, it is non-trivial that the predictions in Figures 4.8 and 4.9 give the correct order of magnitude for different interface conditions and H/D ratios. It is therefore believed that these fits are reliable for many applications and that the method to characterize these behaviors is valid.

Now that the thermo-mechanical behaviors of these glasses are known, it is possible to reexamine the prediction of the viscosity and the determination of the δ_{VE} data using the actual heating and cooling cycle, which is considered in the next section.

4.4.5 Effects of Heating and Cooling on Viscosity Prediction

Now that the full thermo-mechanical characterization of L-BAL35 is known, the error associated with the isothermal assumption for the process used in Sections 4.4.2 and 4.4.3 can be quantified by performing numerical experiments. This is especially important if the current no-slip test specimen approach is applied to a glass type that requires a bonding temperature higher than the test temperature. In the current study the L-BAL35 specimens were bonded at the test temperature, while a temperature higher than the test temperature was used for the N-BK7 specimens. In order to understand the effect of temperature change on the predictions of viscosity and viscoelastic constants, two isothermal and two non-isothermal approaches were considered in numerical experiments for the case of L-BAL35 glass. L-BAL35 glass was selected for this numerical experiment since the full set of material parameters required for the analysis was

known. The two isothermal approaches either assume full viscoelastic behavior as presented in Table 4.2 or use a single term prony series. The two non-isothermal approaches are similarly distinguished by these two viscoelastic assumptions, but both account for structural relaxation and TRS behavior to account for temperature dependence of the material constants. For the non-isothermal case, the idea was to simulate the actual condition experienced by the glass sample during the process of heating, soaking and pressing, including a 50 °C increase above the test temperature to create bonding. The glass sample was sandwiched between the two silica plates with properties presented in Table 4.4.

Thermo-mechanical properties of Glass and Mold Material	
Property	Fused Silica
Density, ρ (kg/m ³)	2210
Young's Modulus, E (GPa)	72.5
Poisson's Ratio	0.17
Specific Heat, c_p (J/kg/K)	772, $T \leq 100^\circ\text{C}$ 964, $T \geq 500^\circ\text{C}$
Thermal Conductivity, κ (W/m/K)	1.38
Glass Transition Temperature, T_g (°C)	1100

Table 4.4. Thermo-mechanical properties of fused silica glass from [18].

Temperature boundary conditions were applied to the bottom and side faces of the lower mold. A value of the gap conductance heat transfer parameter, $h = 5000 \text{ W/m}^2$ was used between the glass and silica interfaces as well as the silica and mold interfaces [1]. The temperature of the outer surface of the lower mold was increased at 20 degrees per minute from room temperature to $T_g + 100^\circ\text{C}$ (625 °C) and then held at a constant temperature of 625 °C for an hour. After this one hour

soak period, a no-slip boundary condition was enforced in the numerical model simulating the bond between the glass sample and the silica plates. The lower mold was then cooled at a rate of 1 degree per minute to the testing temperature of 575 °C, where it soaked once again for an hour before the prescribed load was applied.

Creep curves using the two isothermal approaches along with the non-isothermal approach with full viscoelastic material behavior are presented in Figure 4.10. The key result in this figure is that there is a noticeable, but small gap between the isothermal and non-isothermal curves for full viscoelastic material behavior. This gap represents the error in the isothermal assumption. Using the procedure presented in Section 2.5.6 of Chapter 2, this gap can be represented by a viscosity change on the order of 0.07% without appreciably affecting the δ_{VE} curve. This small difference is associated almost entirely with the increase of temperature above the test temperature, and not with the heating and soaking periods associated with the test temperature. The results of this more computationally intensive analysis are presented in the last two columns of Table 4.1. It is clear that for this glass and conditions, the

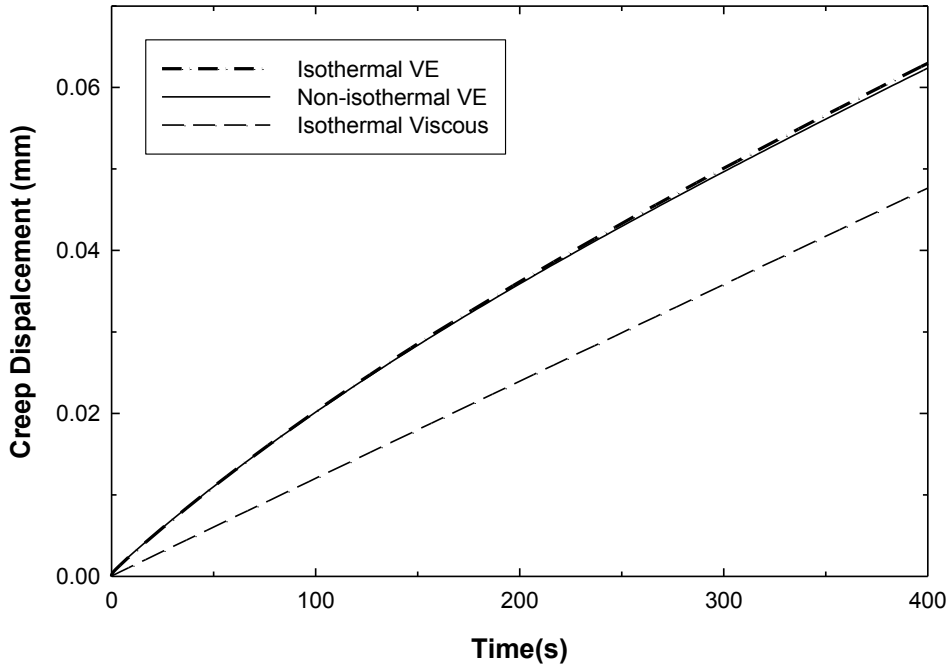


Figure 4.10. Comparison of creep curves plotted using isothermal and non-isothermal computational approaches for the L-BAL35 sample with $H/D = 0.73$ at 575°C and material property data presented in Table 4.2 using $\log(\eta_{eq}) = 8.954 \text{ Pa}\cdot\text{s}$. The isothermal results assume the creep test is conducted at a constant temperature, while the non-isothermal approach simulates the full thermo-mechanical loading cycle, which includes raising the temperature to 625°C before lowering to 575°C .

isothermal approach is adequate. Furthermore, the above non-isothermal procedure was repeated with a gap conductance parameter of $h = 250 \text{ W/m}^2$ without significant change.

4.4.6 Bulk Relaxation Response of a Thin Cylindrical Sample during Compression Test

In this section it is shown that the cylinder compression test can potentially be used to determine the viscoelastic bulk response using a creep test with the no-slip boundary condition. The results of this section were performed using an SLS glass sample having different H/D ratios and the viscoelastic material behavior listed in Tables 2.1 and 2.2 of Chapter 2. The no-slip boundary condition was used for all the simulations and a constant creep load was applied to the

sample. The results in Figure 4.11 quantify the percent contribution of the bulk mechanism to the total viscoelastic displacement as a function of cylinder geometry. As shown in this figure, for a sample with $H/D = 0.1$, the percentage of

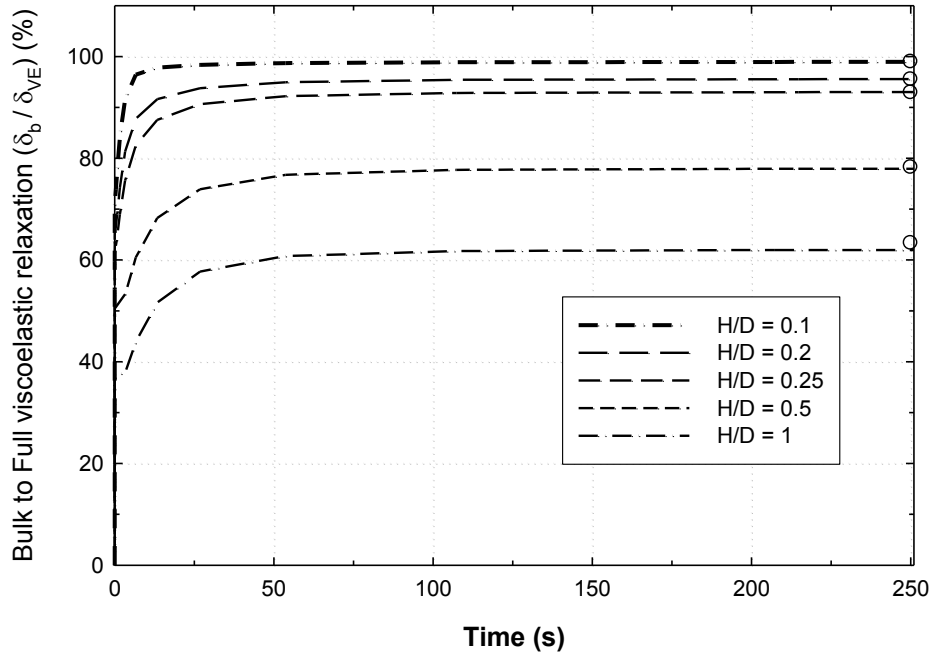


Figure 4.11. The bulk viscoelastic response of SLS glass [3] as a percentage of the total viscoelastic response ($100\% \times \delta_b / \delta_{VE}$) as a function of time for a numerical creep experiment. The circles at $t = 250$ s indicate the values reached by the respective curves at $t = 100,000$ s.

the bulk viscoelastic displacement (δ_b) in the total viscoelastic displacement (δ_{VE}) is approximately 98%. The interpretation is that when a compressive load is applied to such a thin cylindrical sample having the no-slip boundary condition on its top and bottom faces, the displacement due to shear deformation is greatly restricted, which helps to isolate the bulk

relaxation response. However, when this calculation is applied to L-BAL35 using the shear and relaxation functions listed in Table 4.2, the ratio of the bulk contribution decreases from 98% to about 8%. This significant reduction occurs since the total viscoelastic response increases significantly for L-BAL35, not because L-BAL35 is much less compressible than SLS. A practical application of the results in Figure 4.11 is presented in the next paragraph.

The results of the numerical experiment in Figure 4.11 can be used to quantify the effect of compressibility of a glass with known shear relaxation function and unknown bulk relaxation function. If the glass is assumed to be incompressible and a computational prediction of the creep curve significantly underestimates the experimental data, then the bulk relaxation function is significant and this creep data can be used to generate the bulk relaxation function. Conversely, if an incompressible assumption is very close to predicting the creep data for a thin specimen, then relative to the shear relaxation function, it is reasonable to neglect the effects of the bulk relaxation function.

Returning to SLS glass, this numerical experiment can also be used to provide information about the effect of the value of equilibrium bulk modulus (K_∞) of the material. While there is limited volume relaxation data in the literature, according to Scherer [16] the ratio of K_∞/K_0 is in the range of 0.25 - 0.5 for oxide glasses. The ratio for the SLS glass from [3], which is also an oxide glass, was determined to be 0.183, which indicates a relatively high degree of compressibility. Therefore it is necessary to study the effect of increasing the ratio, K_∞/K_0 .

The numerical experiment in Figure 4.11 was repeated for the $H/D = 0.1$ case, by artificially modifying the equilibrium bulk modulus. As seen from the results in Figure 4.12 below, the ratio of the bulk viscoelastic displacement to the total viscoelastic displacement (δ_b/δ_{VE}) is about 95% for K_∞/K_0 as high as 0.5. Furthermore, even for large values of $K_\infty/K_0 \sim$

0.9, the percentage contribution of bulk viscoelastic displacement (δ_b/δ_{VE}) is about 70%.

Therefore, for oxide glasses that behave like the SLS glass characterized by Duffrene, et al., [3] with $K_\infty/K_0 \sim 0.18 - 0.5$, this type of test can isolate about 95% - 98% of the bulk relaxation displacement, which can be utilized for extracting the viscoelastic relaxation parameters after the viscosity of the glass has been determined. As with the results from Figure 4.1 for the $H/D = 0.4$ case, such a process assumes that there are no other contributions to the displacement, which is especially difficult for such a thin sample. In the next section one example of an anomalous viscoelastic displacement contribution will be considered.

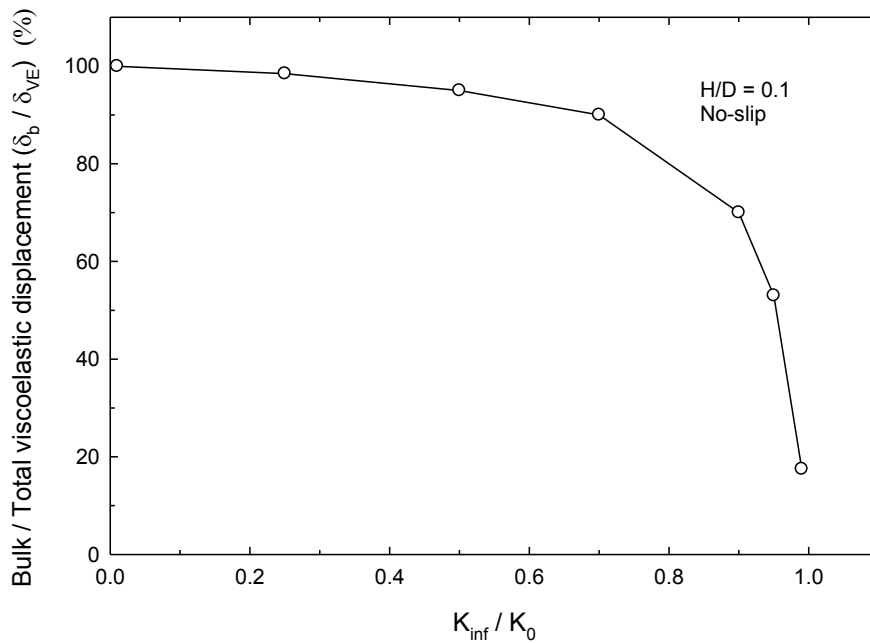


Figure 4.12. The effect of the equilibrium bulk modulus, K_∞ , on the percentage of the bulk viscoelastic response relative to the total viscoelastic response ($100\% \times \delta_b / \delta_{VE}$).

4.4.7 Sensitivity of Sample Imperfections on Creep Curve

The sensitivity of certain geometrical imperfections of the testing specimen on the creep curve during the cylinder compression test is considered in this section. The optical glass is often available commercially in the form of cylindrical rods. These rods can be cut to a required height to make disc-shaped specimens. The top and bottom surfaces of a good sample must be flat and parallel to each other. In the current study specimens were prepared with an accuracy of 1 arc minute of parallelism (0.0167 degrees). Depending on the application, it might also be required to have the entire surface of the cylinder polished since the cylindrical surface can come into contact with the molds. Even for cases involving slip, for coefficients of friction ranging from about 0.1 to 0.4, the cylindrical surface comes in contact with the molds as the axial deformation reaches about 55% to 20% of the original axial dimension, respectively. The high level of accuracy in attaining flatness, parallelism and uniform roughness demands highly precise and costly processes. In this section, the consequences on the creep curve from these types of imperfections are demonstrated by performing numerical experiments, once again using the SLS data for a material with the no-slip boundary condition. Two cases of imperfection are assumed: the first has a conical shape having a 0.5 degree cone angle and the second case has one entire surface that is tilted by 0.5 degrees. This later case requires a full three-dimensional analysis. In this analysis the molds are assumed to be parallel, which involves a complex contact problem in the early stages of the creep curve. The glass is assumed to bond to the molds immediately upon contact.

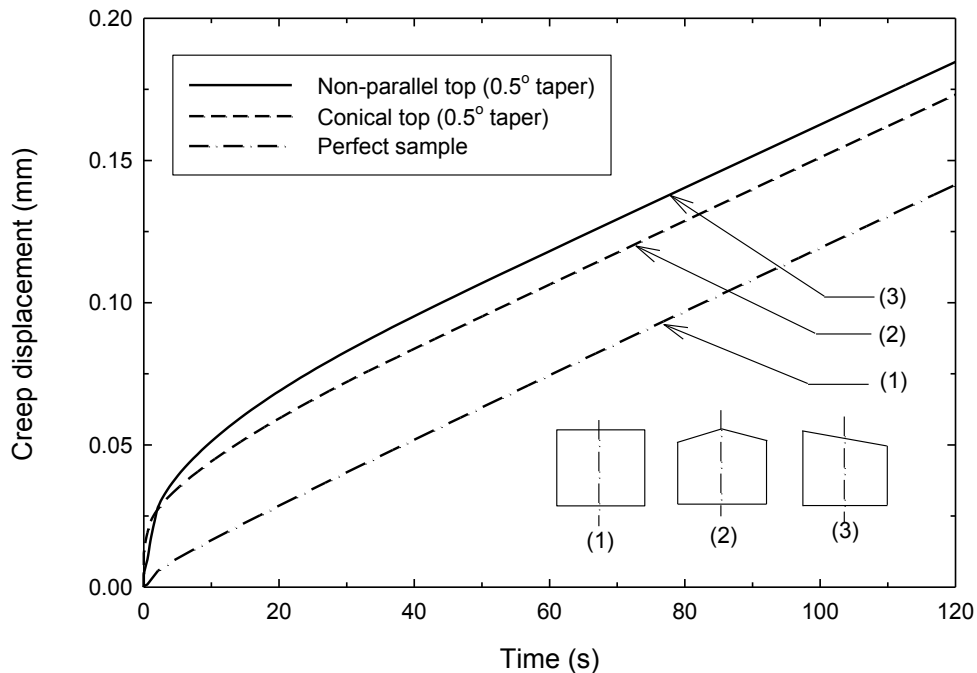


Figure 4.13. The effect of geometric imperfections of the test sample on the creep curve for an SLS glass. The result for a geometrically perfect sample (1) is compared to results for a sample with conical top with a 0.5° taper (2) and a sample having non-parallel top and bottom faces that are off by 0.5° (3).

The results are summarized in Figure 4.13 where the creep curves for these two hypothetical specimens are compared to that for a perfect cylinder. The results reveal a fictitious time dependent displacement in the beginning of the testing period, which is attributed to the geometrical imperfection and the rapidly growing contact area between the upper glass surface and the mold. A key observation from this section is that while the prediction of the viscosity is not affected, the viscoelastic displacement contributions would be greatly exaggerated. Furthermore, the results in Figure 4.13 are also representative of using a perfect glass cylinder with molds and/or silica discs that are the cause of non-parallel surfaces, or even perfect geometry with off-center loading.

4.4.8 Effect of Non-Uniform Temperature Distribution within Sample

The effects of non-uniform temperature distributions within the glass sample on the creep displacement data are significant because viscosity is a strong function of temperature. In this section it was assumed that the steady state temperature distribution within the specimen was non-uniform, i.e., independent of the heating and soaking periods, due to thermal losses and the size of the specimen, the chamber does not allow the specimen to reach a uniform temperature. In this numerical experiment using a condition of no friction, a linear distribution of temperature exists across a sample height of $H/D = 1$. The simulated creep curve is plotted in Figure 4.14 for different cases when the value of ΔT

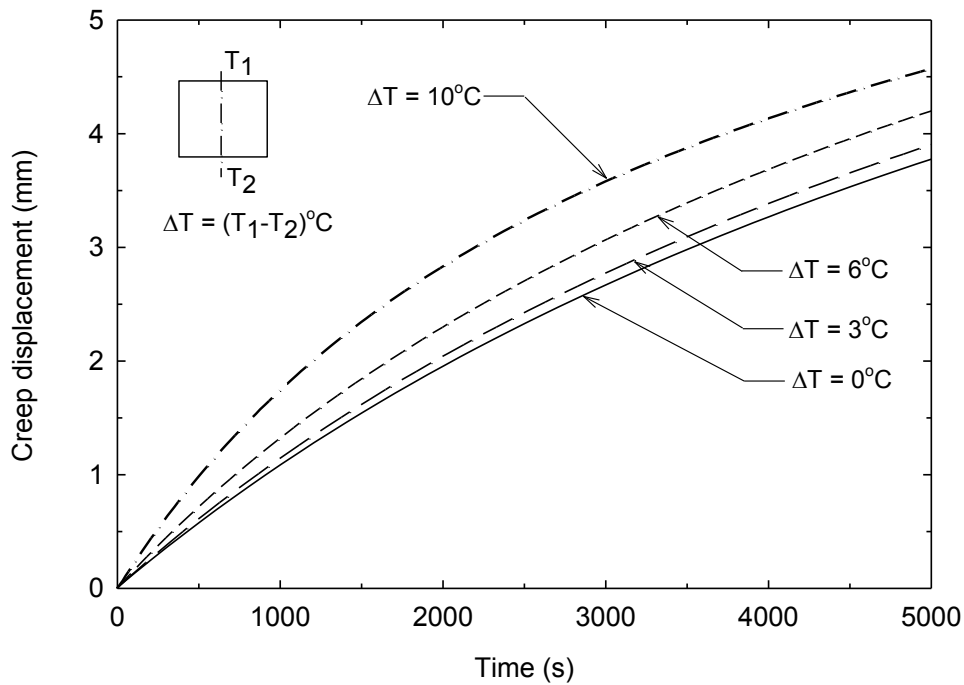


Figure 4.14. The effect of a linear temperature variation in the axial direction of the cylinder on the creep curve ($H/D = 1$, $\mu = 0$). The top and bottom faces of the cylinder are kept at different temperatures during the entire test. TRS behavior is assumed using the parameters: $T_R = 550^\circ\text{C}$, $C_1 = 25$ and $C_2 = 129^\circ\text{C}$.

(difference between max and min temperature) was varied from 0 to 10 °C, with $\Delta T = 0$ °C being the isothermal case that is ideally achieved prior to starting the creep testing. As seen from the results in Figure 4.14, the shape of the creep curve changes significantly for $\Delta T = 6$ and 10 °C. For $\Delta T = 3$ °C and less, the deviation in the creep curve from the isothermal counterpart is relatively small.

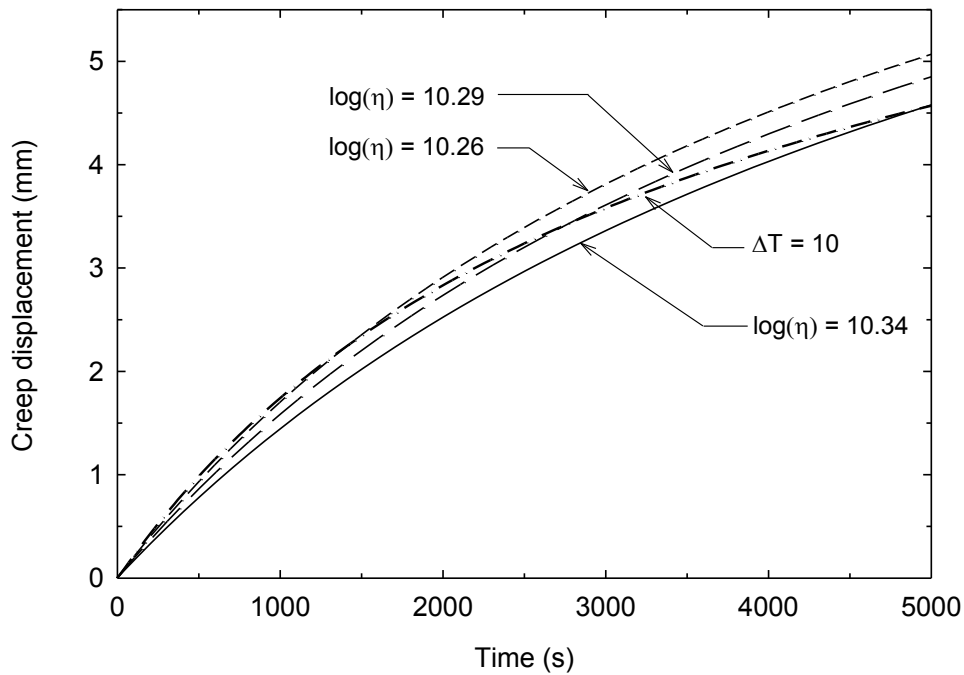


Figure 4.15. Comparison of the creep curve for a non-uniform temperature distribution ($\Delta T = 10$ degree case from Figure 4.14) with uniform temperature creep curves using different viscosity ($H/D = 1$, $\mu = 0$). TRS behavior is assumed using the parameters: $T_R = 550^\circ\text{C}$, $C_1 = 25$ and $C_2 = 129^\circ\text{C}$.

The results in Figure 4.15 show how the non-uniformity in temperature of the same sample from Figure 4.14 can be identified using the single term prony series technique. In this figure the non-isothermal creep curve with $\Delta T = 10$ °C is compared with three isothermal creep

curves generated using single term prony series with different viscosity values as given in Figure 4.15. These results show that none of the isothermal creep curves match closely with the non-isothermal creep curve, suggesting that the specimen was not at uniform temperature.

4.5. Discussion

In this chapter computational mechanics has been used to understand how the cylinder compression test can be used to determine the thermo-mechanical properties of glass at high temperature. The study relies on two key factors: 1) the complete (realistic) viscoelastic characterization of one glass type and 2) very precise, carefully controlled experiments to provide creep data. The importance of the former is that since material properties are being sought, it is necessary to understand the consequence of assumptions concerning material behavior. For example, it is often assumed that glass is incompressible, which may or may not be an appropriate assumption for the intended application. The importance of the later is that it creates the necessary synergy that guides both the computational and experimental investigations. Based on experience, it is very difficult to obtain reliable data for glass at high temperature. One obstacle is achieving a known, uniform temperature in the glass specimen.

Due to experimental considerations, only creep loading was considered in this study. Guided by computational results it was determined that a no-slip specimen was required, since interface slip and viscosity affect the creep displacement by similar orders of magnitude for specimens that are thin enough to achieve and maintain a uniform, known temperature. Such a specimen was achieved, without which little progress could be made, although the results of Figure 2.8 of Chapter 2 show it might be possible to predict both friction and viscosity using the same creep curve. The no-slip specimen, however, reduces error by eliminating the uncertainty associated with the complex process of interface slip. Creep data from the two molding glasses,

N-BK7 and L-BAL35 were used to determine viscosity, the principal error believed to be associated with temperature. An analysis of the PPV system indicated a $\pm 1.5^\circ\text{C}$ uncertainty, along with fluctuations of about $\pm 0.2^\circ\text{C}$ during testing.

It was also demonstrated for L-BAL35 and N-BK7 that the shear component of the viscoelastic portion of the material response can be obtained if the experimental data is very precise. The viscoelastic characterizations provided in Tables 4.2 and 4.3 are believed to be reliable and the non-trivial predictions in Figures 4.8b, 4.9b and 4.9c help to support this claim. Furthermore, the prediction in Figure 4.8b was for a no-slip specimen, while those in Figures 4.9b and 4.9c were for low friction cases, which helps to eliminate the possibility of a consistent error associated with the no-slip specimen. Although the creep data was limited, these predictions show that the data used for viscosity and viscoelastic constants was very accurate. Of the seven creep curves presented in this two-part study, all of which are very accurate for viscosity prediction, only five could be used for viscoelastic characterization. The other two data sets, both no-slip $H/D = 0.4$ specimens, have an obvious anomalous contribution to the viscoelastic displacement component, δ_{VE} . For the N-BK7 specimen from Figure 4.1, the displacement was twice what was predicted, and for the L-BAL35 specimen from Figure 4.5, the displacement was a factor of four too large. The computational study in Figure 4.13 gives an example of an explanation for such an error. In this case a surface that is tilted by 0.5 degrees overpredicts the viscoelastic displacement, δ_{VE} , by a factor of about six. Another explanation for anomalous displacement in a no-slip experiment is that the bond partially failed during the creep test. In the $H/D = 0.4$ cases the interface shear stress was about 15% higher than for the taller specimens ($H/D \sim 0.7$), and the compressive normal stress near the outer radius of the cylinder was about 30% lower. Since it is known that the entire bond was intact when the specimens cooled to room temperature, if the bond failed it must have reformed during the test, which allowed the viscosity to be determined

correctly at large time. Due to such a slipping mechanism, however, the displacement δ_{VE} cannot be attributed entirely to viscoelastic behavior. The current computational approach for the determination of the viscoelastic constants requires both a uniform, known temperature and a constant, known coefficient of friction throughout the test. If interface fracture occurs, even if the bond reforms after partial slip, the “apparent” coefficient of friction is not constant. As a final thought, the possibility of an anomalous displacement due to misalignment or some other reason can occur in any creep experiment, and is not limited to the cylinder compression test. The experimental component of this study was a major effort and additional creep tests were conducted and discarded due to complications associated with non-uniform temperature, folding or slip, before being satisfied with the seven data sets presented in this study.

4.6. Conclusions

Concerning creep data of the cylinder compression test within the transition temperature range, the following conclusions can be made:

- A no-slip specimen created through a process of inter-diffusion between the test sample and the interaction surface, as opposed to mechanical constraint, provides a robust bond that is not impacted at elevated temperatures. This was an essential element in obtaining accurate results.
- The viscosity of glass can be determined very precisely at the test temperature using a no-slip specimen. In addition, the viscoelastic shear relaxation function of the glass can be determined if the data is sufficiently accurate.
- Obstacles for the accurate determination of viscoelastic properties include the experimental error in viscosity, uncertainty in coefficient of friction at the interface, a coefficient of friction that changes in time, non-uniform sample temperature and

imperfect specimen or mold surfaces. It was shown that any of these uncertainties can lead to anomalous displacement response during a creep test which will result in inaccurate viscoelastic property evaluation of the glass.

- By using a thin sample with a no-slip boundary condition at the interface, the bulk response is dominant based on published viscoelastic responses for SLS glass, which provides a relatively simple test to determine this response. For example, for a specimen with $H/D = 0.1$, about 98% of the total viscoelastic displacement during the creep test is attributed to the bulk relaxation mechanism for a wide variety of glass types. However, based on experimental data obtained herein, this percentage is only 8% for L-BAL35, which is a moldable glass.

References

1. B. Ananthasayanam, P.F. Joseph, D. Joshi, S. Gaylord, L. Petit, V.Y. Blouin, K.C. Richardson, D.L. Cler, M. Stairiker, M. Tardiff, "Final shape of precision molded optics: Part I – Computational approach, material definitions and the effect of lens shape," *Journal of Thermal Stresses*, **35** (2012) pp. 550-578.
2. B. Ananthasayanam, P.F. Joseph, D. Joshi, S. Gaylord, L. Petit, V.Y. Blouin, K.C. Richardson, D.L. Cler, M. Stairiker, M. Tardiff, "Final shape of precision molded optics: Part II – Validation and sensitivity to material properties and process parameters," *Journal of Thermal Stresses*, **35** (2012), pp. 614
3. L. Duffrene, R. Gy, H. Burlet, and R. Piques, "Multiaxial linear viscoelastic behavior of soda-lime-silica glass based on a generalized Maxwell model," *Soc. Rheol.*, **41** (1997), pp. 1021-1038.
4. A. Jain, G.C. Firestone, A.Y. Yi, "Viscosity Measurement by Cylindrical Compression for Numerical Modeling of Precision Lens Molding Process," *J. Am. Ceram. Soc.*, **88** (2005), pp. 2409-2414.
5. M. Arai, Y. Kato, and T. Kodera, "Characterization of the thermo-viscoelastic property of glass and numerical simulation of the press molding of glass lens," *J of Therm. Stresses*, **32** (2009), pp. 1235-1255.

6. T. Zhou, J. Yan, J. Masuda, and T. Kuriyagawa, "Investigation on the viscoelasticity of optical glass in ultra precision lens molding process," *J of Mat. Process Tech.*, **209** (2009), pp. 4484-4489.
7. S.H. Chang, Y.M. Lee, T.S. Jung, J.J. Kang, S.K. Hong, G.H. Shin, Y.M. Heo, "Simulation of an aspheric glass lens forming behavior in progressive GMP process," *NUMIFORM '07, Materials processing and design*, (2007), pp. 1055-1060.
8. J. Yan, T. Zhou, J. Masuda, T. Kuriyagawa, "Modeling high-temperature glass molding process by coupling heat transfer and viscous deformation analysis," *Precision Engineering*, **33** (2009), pp. 150-159.
9. D. Joshi, P. Mosaddegh, J.D. Musgraves, K.C. Richardson, P.F. Joseph, "Thermo-Mechanical Characterization of Glass at High Temperature Using the Cylinder Compression Test: Part I –Viscoelasticity, Friction and PPV," *Journal of Rheology*, **57**(5), (2013), pp.1367-1389.
10. Based on SCHOTT glass catalogue. (<http://www.us.schott.com>)
11. G. J. Dienes and H. F. Klemm, "Theory and Application of the Parallel Plate Plastometer," *J. Appl. Phys.*, **17** (1946), pp. 458-471.
12. A.N. Gent, "Theory of the parallel plate viscometer," *British Journal of Applied Physics*, **11**, (1960), pp. 85-87.
13. A.K. Varshneya, N.H. Burlingame, W.H. Schultze, "Parallel plate viscometry to study deformation-induced viscosity changes in glass," *Glastech. Ber.* **63K**, (1990) pp. 447-459.
14. ASTM standard C1351M - 96 (2012)
15. Specification Sheet for L-BAL35 glass, OHARA, Japan. (www.ohara-inc.co.jp).
16. G. Scherer, *Relaxation in glass and composites*, John Wiley and Sons, New York, 1986.
17. S. Gaylord, B. Ananthasayanam, B. Tincher, L. Petit, C. Cox, U. Fotheringham, P. Joseph, and K. Richardson, "Thermal and Structural Property Characterization of Commercially Moldable Glasses," *Journal of the American Ceramic Society*, **93**, (2010), pp. 2207-2214.
18. Based on Heraeus Glass catalogue. (<http://heraeus-quarzglas.com>)

SENSITIVITY OF LENS SHAPE DEVIATION AND RESIDUAL STRESSES ON STRESS RELAXATION CHARACTERIZATION IN A PRECISION MOLDED LENS

5.1. Introduction

The computational mechanics approach is widely used to model the complex thermo-mechanical behavior of an optical glass during simulation of the lens molding, extrusion and other glass forming processes. This approach proves to be an effective tool in understanding and overcoming the associated shortcomings such as lens profile deviation (final shape), stress birefringence, lens cracking etc. in the molding process, while, the preform die swell, cavity shape distortion etc. in the extrusion process. The accuracy of prediction of above parameters strongly depends upon input of the thermo-mechanical properties of the glass to the numerical model. These properties mainly include the stress and structural relaxation parameters, temperature dependent values of elastic modulus and the temperature dependent viscosity (TRS parameters). The thermo-mechanical characterization of glass focusing mainly on the lens molding process is carried out by several researchers [1-15] experimentally and/or computationally by treating the optical glass as either viscous or viscoelastic solid material.

Lens molding process is a hot forming process in which the optical glass material in the form of a gob, ball or a near net shape (preform), is subjected to a molding temperature above its glass transition temperature and is compressed between a two dies to impart the desired shape to the glass. A preform undergoes changes in its mechanical properties as it is being heated from the room temperature up to the molding temperature. This temperature dependent mechanical response of such glass can be modeled using suitable material models available in literature. For example, a viscoelastic stress relaxation function is commonly used by researchers to model the mechanical response behavior of glass during lens molding process. Joshi et al. [1,2] and

Ananthasayanam et al. [3,4] used viscoelastic material to model glass forming process at high temperature using a cylinder and ring compression test respectively. Yi and Jain [6] modeled the hot glass as rigid visco-plastic material during forming/pressing stage while, as an elastic-viscoplastic material during annealing/cooling stage. The flow of glass during forming temperature was assumed to obey the Newtonian law, while the bulk behavior was modeled as elastic. Other researchers [6-10] used time dependent shear modulus (generalized Maxwell model) and elastic bulk modulus to model the behavior of glass at high temperature. Chang et al [11] and Yan et al [12] used power law model that relates stress to a power of strain rate to describe the flow behavior of glass at high temperature. Zhou et al [13] used a Maxwell and a Kelvin element in series to model the viscoelastic relaxation response. Duffrene et al. [15] performed experiments on soda-lime-silica glass near transition temperature (T_g) of glass to extract a complete description of stress relaxation behavior of the soda-lime-silica glass sample. Their data includes both the shear as well as bulk relaxation parameters.

Many authors considered that elastic modulus remains unchanged from its room temperature value throughout the thermal cycle of lens molding process. Loch and Krause [20] considered temperature dependent elastic modulus of glass at high temperature. They performed numerical simulations of glass shaping process at high temperature and they considered value of elastic modulus drops to about 1/10 of its value at the room temperature based on the experimental evidence. Comprehensive data on temperature dependence of elastic modulus is provided in study by T. Rouxel [17]. It reveals that for a group of Chalcogenide glasses, the elastic modulus drops below 10GPa as temperature is further increased above T_g . In an extensive study of sensitivity parameters affecting the lens shape deviation by Ananthasayanam et al [4, 5], it was shown that the TRS behavior of glass within the molding temperature range greatly affects the lens deviation for both types of lenses. On the other hand, they concluded that the reference temperature (T_R) of

the glass does not affect the deviation as long as the lens is heated to the same molding temperature at the beginning of pressing stage. The sensitivity of the thermal contact conductance coefficient and the decay profile on the lens shape deviation was studied by Ananthasayanam et al [4]. They concluded that both factors only affect the pressing time but not the lens shape deviation. The effect of convective heat transfer between the outer surface of preform/lens and the surrounding nitrogen environment in addition to the contact conductance coefficient was considered by Yi et al [6] in their numerical simulations along with the thermal contact conductance between glass and mold. They considered the convective heat transfer coefficient of 20 and 200 W/m²K during heating/soaking and cooling stages respectively.

The focus of the current study is the appropriate choice of a thermo-mechanical model of glass for computational simulations of precision lens molding, which is dependent on the desired outcome. For example, as will be demonstrated, the estimation of lens profile deviation compared to birefringence requires different levels of precision in the characterization. This study was motivated by the difficulty to obtain reliable data and therefore the difficulty/expense of the experimental work that must support such modeling. The results of this study can guide both experimental and the computational investigations.

This study begins by performing three validations for the prediction of residual stress in glass subjected to thermal loading that would occur in glass forming processes. These validations are followed by a presentation of the details of the material behavior and FEA models to be used. A convergence study for the prediction of residual stresses in a steep meniscus lens is then presented. Finally, in addition to a few related sensitivity studies affecting lens profile deviation, the effect of the model used for stress relaxation on the lens profile deviation, residual stresses and birefringence are studied in detail.

5.2. Stress Relaxation Assumptions

This study makes use of material models and lens geometry presented in earlier studies. The basic theory of viscoelasticity from Chapter 4 and [1] will be used herein. The viscoelastic and temperature dependent TRS constants were obtained from Table 2.3 of Chapter 2 and Table 4.2 of Chapter 4 along with the structural relaxation parameters given in [5]. As stated in Chapter 2, the material property data was implemented in the Abaqus software by making use of an input file and a user defined subroutine for the thermal expansion behavior of glass [5]. The bi-convex and steep meniscus lens geometries were obtained from [3].

One of the aims of this study is to determine the level of detail of the stress relaxation model, i.e, the relaxation functions $G_1(t)$ and $G_2(t)$ from Equations (2.7 to 2.10), required for determining the lens profile deviation within a certain level of accuracy. The lens profile deviation is defined as geometrical difference between the desired profile (mold) and the final shape of the molded lens [3]. To understand the effect of stress relaxation on lens profile deviation and stress birefringence, the following three stress relaxation functions were considered: 1) viscous shear relaxation and elastic bulk, 2) viscoelastic shear relaxation and elastic bulk and 3) the viscoelastic shear and viscoelastic bulk relaxation function. In all cases the relaxation times (τ_i) were adjusted such that the equilibrium viscosity (η) was maintained at a constant at value of $\log (\eta/\text{Pa}\cdot\text{s}) = 10$ as per the following equation [18],

$$\frac{\eta}{G_0} = \sum_{i=1}^{n_i} w_i \tau_i . \quad (5.1)$$

The details for the three material models are given below.

The simplest material model involves use of a single Maxwell element for modeling the response in shear and an elastic element for the bulk response. This model requires knowledge of only the equilibrium viscosity at a reference temperature and assumes the material behavior is viscous with an initial elastic shear and bulk response. This model is defined by

$$G_1(t) = 2G_0 e^{-t/\tau} \quad G_2(t) = 3K_0 \quad (5.2)$$

where ' τ ' is the relaxation time in shear and K_0 is the instantaneous bulk modulus of material.

The second model makes use of multiple Maxwell elements for modeling the response in shear and assumes an elastic element for the bulk response, which is given by

$$G_1(t) = 2G_0 \sum_{i=1}^{n_1} w_i e^{-t/\tau_i} \quad G_2(t) = 3K_0 \quad (5.3)$$

The most complex viscoelastic response considered in this study made use of multiple Maxwell elements for modeling the shear and the bulk responses, which are given by

$$G_1(t) = 2G_0 \sum_{i=1}^{n_1} w_i e^{-t/\tau_i} \quad G_2(t) = 3K_0 + (3K_\infty - 3K_0) \left(1 - \sum_{j=1}^{n_2} v_j e^{-t/\lambda_j} \right) \quad (5.4)$$

where K_∞ is the equilibrium bulk modulus, w_i and v_j are the weighting factors for the deviatoric and volumetric relaxation functions, respectively, and τ_i and λ_j are the corresponding relaxation times for the deviatoric and volumetric relaxation functions.

5.3. Validation Examples

In this section three validation examples for the determination of residual stresses are presented. As with the previous Chapters, the finite element software, ABAQUS was used. Structural relaxation following [3] was included using a user defined subroutine. The first example involved a simple cooling schedule of a cylindrical glass body. The second example, which was taken from

the literature [20], quenches a Soda-Lime Silicate (SLS) glass slab from 738°C to room temperature (20°C). The last example, also taken from the literature [19], is a glass-to-metal sandwich seal test that was revisited for the completeness of the discussion on residual stresses. In all examples the residual stresses are the focus of the computation.

In all calculations of residual stresses in glass subjected to thermal loading, a critical element is the manner in which structural relaxation is accounted for. In this study the time and temperature dependent structural relaxation (thermal expansion) of glass was considered by incorporating the TNM model. The details of this model can be found in [5]. A FORTRAN subroutine (UEXPAN) is required to implement the TNM model in ABAQUS, which captures the complex thermal expansion behavior of glass in the transition region. This program essentially computes the expansion coefficient of glass that is dependent on temperature, cooling rate and time amongst other constants. The expression for the expansion of glass is evaluated in the following manner,

$$\text{expansion} = \alpha_{\text{Glass}} \cdot \Delta T + (\alpha_{\text{Liquid}} - \alpha_{\text{Glass}}) \cdot \Delta T_f \quad (5.5)$$

Above the transformation temperature of glass (T_g), the fictive temperature (T_f) is very close to the actual temperature hence, and therefore ΔT_f would be close to ΔT and the expression (5) shows that the expansion coefficient for liquid glass (α_{Liquid}) applies. Within and below the transition temperature, however, the value of the expansion coefficient of glass is a temperature dependent function of the two extremes and the fictive temperature. In the next section, the results of the three different validation cases will be discussed.

5.3.1 Validation Example 1: Cooling of a Glass Cylinder

In the first example a cylindrical glass specimen was cooled from a selected temperature to room temperature. The motivation behind this study was threefold and included: 1) an assessment of the magnitude of error in stresses when using the structural relaxation model of glass within the context of a simple cooling example, 2) an understanding of the relative effects of stress relaxation and structural relaxation on residual stresses and 3) determination of the values of the upper and lower temperatures, T_U and T_L , respectively, during which the viscoelastic glass transitions from a viscous fluid to an elastic solid. Concerning the former point, this study identified an error in the subroutine which over-estimated the residual stresses. The results presented below are for the corrected subroutine.

In all cases in this section the axisymmetric problem of a glass cylinder with diameter, $D = 10$ mm and height, $H = 5$ mm is used. The baseline set of glass thermo-mechanical properties are those of L-BAL35 [1, 2], and include a series of modifications to isolate the stress and structural relaxation behaviors. The constant rate of cooling of the surface temperature of the cylinder was imposed to be 0.25°C/s for all cases considered. This is a realistic value of cooling rate as during the slow cooling cycle of the lens molding operation, a cooling rate is maintained to be close to 0.28°C/s or less. Stresses and strains inside the glass cylinder were calculated as function of the spatial coordinates and time, although only the maximum principal stress in the r - θ plane at the center of the cylinder for large time was used to quantify the stress state. It is assumed that the cylinder was stress free at high temperature and thus, only the effects of cooling as provided by stress and structural relaxation could contribute to residual stresses. The permanent deformation mechanism for stress relaxation is viscous flow and for structural relaxation is non-uniform volume change due to the history of spatially non-uniform cooling and/or heating.

Before studying the effects of these two mechanisms, it is important to assess the base error in the computational solution by cooling from a temperature which should result in no residual stresses. Cooling from 430°C was selected in this initial study since the model for L-BAL35 glass has an infinite equilibrium viscosity at 440°C and below, and therefore the effects of stress relaxation should not produce residual stresses in this numerical experiment. For cooling from 430°C to 20°C for material properties of steel, which makes use of constant values of elastic modulus and coefficient of thermal expansion, the resulting residual stress was on the order of 5E-04 Pa, which is essentially zero and shows that convergence has been achieved. When the same cooling pattern was applied to L-BAL35 glass with only structural relaxation suppressed by assuming a constant value of the thermal expansion coefficient, the maximum in-plane principal stress was 5E-02 Pa, which again is virtually zero. For glass, the non-uniform temperature gradient that exists between the surface and center of cylinder is much higher than the case of a steel cylinder due to its higher thermal conductivity. This causes both the center and surface of the steel cylinder to cool down at more similar rates compared to the glass cylinder, whose center lags further behind the surface temperature.

In the next numerical experiment of cooling from 430°C to 20°C, both stress and structural relaxation for L-BAL35 were fully engaged. This case led to a residual stress of 235 Pa, which as will be shown, is due to a small structural relaxation effect below 440°C. This simple example helped in understanding and correcting an error within the subroutine code, which initially over-predicted the residual stresses due to the incorrect use of an expression for thermal expansion during a very short period of time. A final numerical experiment for this initial cooling study with both stress and structural relaxation fully engaged was for cooling from 590°C, which is a typical temperature for lens molding with L-BAL35 glass. In this case the residual stresses rise to the significant level of 4 MPa. The residual stress results for this study are summarized in

Table 5.1. These results show how stresses convergence to zero when the permanent deformation mechanisms are suppressed and also motivate a more detailed study of the lower temperature limit of the transition temperature range, which is presented below.

	Cooling from 430°C to 20°C	
Material Behavior	Max. In-Plane Principal Stresses (Pa)	Max. Out-of-Plane Principal stresses (Pa)
Elastic and constant thermal expansion (steel)	5×10^{-4}	-3×10^{-4}
Full stress relaxation and constant thermal expansion ($\alpha=8.1 \times 10^{-6}/\text{K}$)	0.049	-0.031
Full stress and structural relaxation	234.8	234.7
	Cooling from 590°C to 20°C	
Full stress and structural relaxation	4.245×10^6	4.244×10^6

Table 5.1. Residual stresses at the center of the cylinder at room temperature for cooling from 430°C to 20°C for three different material behavior assumptions.

The basis for temperature selection in the above cooling study was the transition in the material property definitions from elastic behavior to viscoelastic behavior, which occurs at the “cut-off” temperature, T_L [5]. The pertinent cut-off temperature at which the equilibrium viscosity of the material reaches infinity, which defines the transition from a viscoelastic solid to a viscoelastic fluid, is referred to in this Chapter as T_{SL} . Similarly, the temperature below which the structural relaxation (thermal expansion) is independent of both the rate of cooling and the temperature-time history is referred to as T_{VL} . As stated in Section 5.2, the TRS assumption was

implemented in Abaqus via the WLF equation, which gives a shift factor that enables viscosity calculations at any given temperature. The shift factor is determined as follows,

$$\log_{10}(A(T)) = -\log\left(\frac{\eta_R}{\eta}\right) = \frac{-C_1(T-T_R)}{C_2+(T-T_R)} \quad (5.6)$$

As seen from Eqn. (5.6), the shift factor becomes infinite as the temperature approaches $(T_R - c_2)$ indicating the material response is solid like with an infinite equilibrium viscosity. For L-BAL35 glass the lower limit of the viscoelastic range for L-BAL35 was estimated in [5] to be $T_{SL} = 440^\circ\text{C}$ based on the structural relaxation work of Gaylord [22]. It was further assumed in [5] that the viscosity should approach infinity at this temperature, which was incorporated into the TRS characterization. The variation in viscosity using Eqn. (5.6) and the TRS fit from Chapter 4 and [2] is presented in Figure 5.1. It is noted that while the viscosity becomes infinite at 440°C , the viscosity is still extremely high at temperatures above this value. Therefore, from a practical point of view T_{SL} is closer to 500°C than to 450°C .

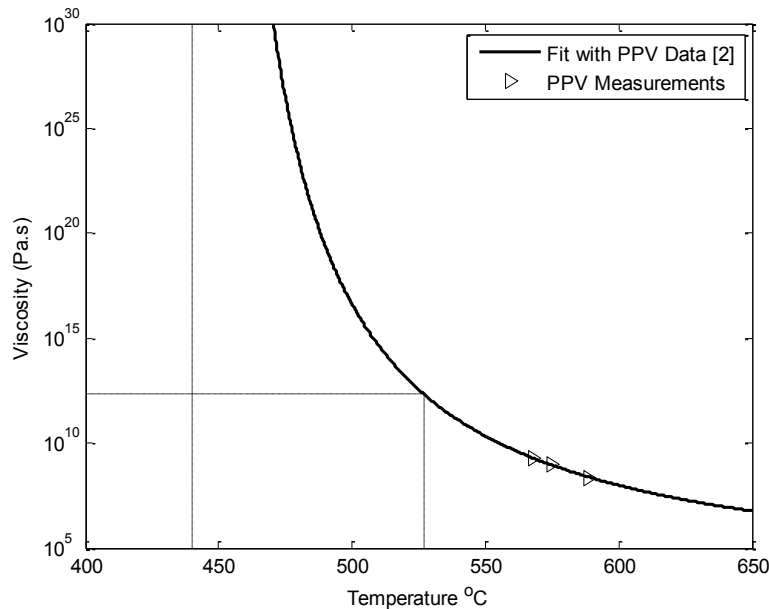
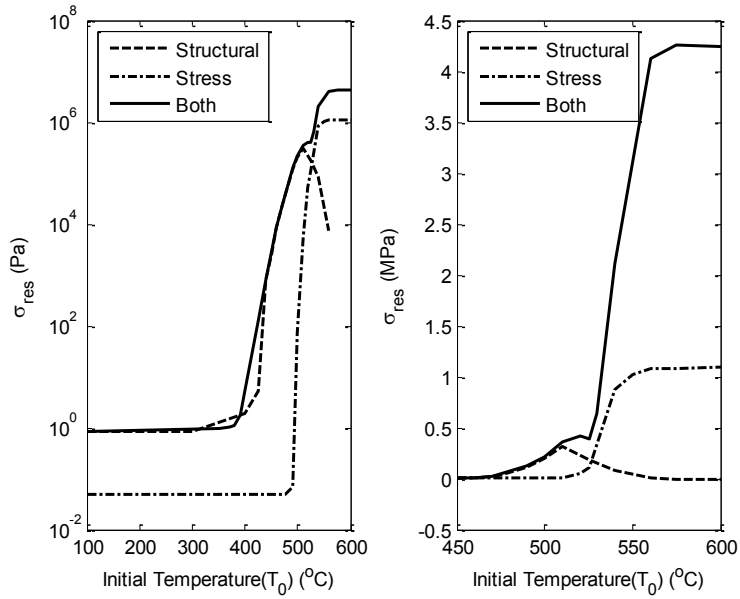


Figure 5.1. Viscosity for L-BAL35 glass (solid line) near the T_{SL} (440°C).

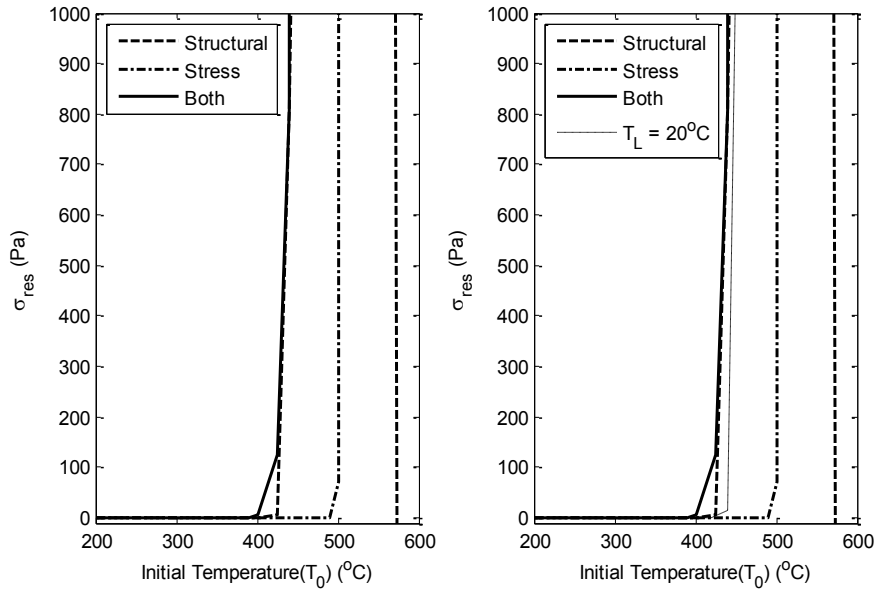
Unlike the defined behavior of viscosity near T_{SL} , the variation of the thermal expansion coefficient with respect to the temperature has a more gradual approach towards its room temperature value (α_g). This weak temperature dependence at relatively low temperatures [22] makes the selection of a structural relaxation cut-off temperature, T_{VL} , somewhat arbitrary. The understanding of such a cut-off temperature (T_{VL}) was made by a numerical study of residual stresses in a glass cylinder that was cooled from a uniform elevated temperature, T_0 , to room temperature. The residual stress was quantified by the maximum principal stress in the r - θ plane at the center of the cylinder and the cylinder was cooled by imposing a uniform surface cooling rate of $q = 0.25^\circ\text{C/s}$. Three different material behavior assumptions were used: 1) both stress and structural relaxation fully active, 2) structural relaxation active and stress relaxation suppressed by assuming elastic behavior, and 3) stress relaxation active and structural relaxation suppressed by assuming a constant coefficient of thermal expansion. The results of this numerical experiment

are presented in Figure 5.2 for three different scales. The results in Figures 5.2a and b show that on a scale of a MPa, when the sample is cooled from an initial temperature of about 440°C the residual stresses are negligible, which justifies assuming $T_{VL} = T_{SL} = 440^\circ\text{C}$. The results in Figure 5.2c, however, quantify how the residual stresses due to structural relaxation do not vanish for cooling from below $T_0 = 440^\circ\text{C}$. In the subsequent residual stress results presented in this chapter, this stress level of about 200 Pa is understood to be present due to this low cooling structural relaxation mechanism. Residual stresses on this order of magnitude are assumed to be negligible since they produce birefringence of order 0.006 nm/cm. To quantify this level of birefringence, the typical photoelastic instrumentation used to measure stress birefringence in glass has a resolution of approximately 6 nm/cm, which corresponds to stress level of approximately 0.1 MPa [30]. The lower cut-off temperature for viscoelastic assumption is hereafter referred to as simply $T_L = 440^\circ\text{C}$. Finally, it should be mentioned that the results in 5.2c also show that from a practical point of view, T_{SL} is closer to 490°C. In order to have the stress relaxation results in Figure 5.2c approach near zero at a temperature of 440°C instead of 490°C, the value of $T_R - C_2$ in Eqn. (5.6) should be about 20°C instead of 440°C. Figure 5.2d shows this numerical simulation result for the residual stresses with $T_L = 20^\circ\text{C}$, which gives a viscosity of about $10^{17.7}$ Pa·s at 440°C.



(a)

(b)

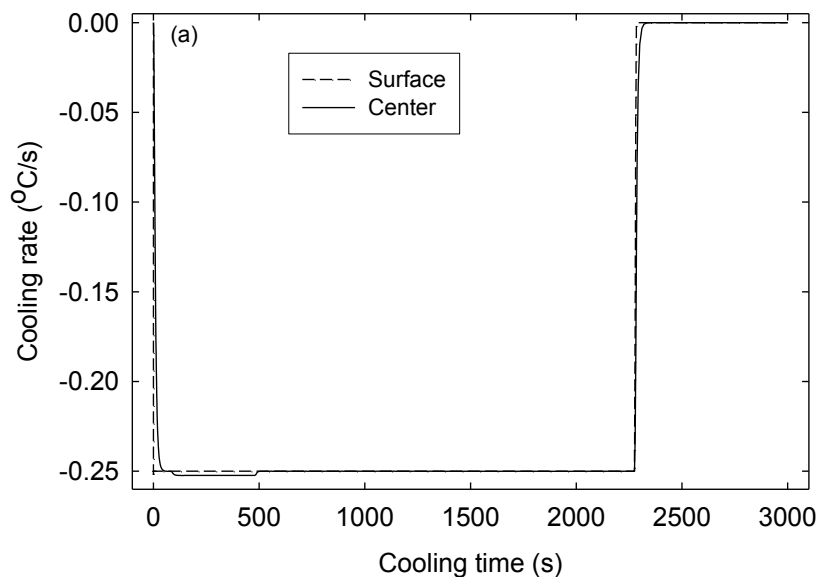


(c)

(d)

Figure 5.2. Variation in the value of the steady state, maximum principal stress in r - θ plane at the center of the cylinder for three different material behavior assumptions after uniform surface cooling from an initial temperature of T_0 . In Figure 5.2a a log scale with units of Pa is used, in Figure 5.2b, a scale of MPa is used, while in Figure 5.2c and 5.2d, a scale of Pa is used.

The sensitivity of residual stresses on T_{SL} using different TRS functions will be discussed from a point of view of lens molding in section 5.4.2. The results in Figure 5.2 for the case where stress relaxation was suppressed reveal an interesting behavior in the residual stresses for large values of the initial temperature. To understand why the stresses are so low for $T_0 = 600^\circ\text{C}$ it is necessary to understand the temperature distribution in the cylinder as a function of time. The cause of residual stress due to the mechanism of structural relaxation is a spatially non-uniform rate of cooling within the cylinder as a function of time within the temperature range, $T_L < T < T_U$. This causes non-uniform, permanent volume change which leads to residual stresses. Therefore, it is necessary to understand the temperature distribution in the cylinder as a function of time. The results in Figure 5.3 quantify this temperature behavior and also show how the residual stresses develop as a function of time for a case where $T_0 = 590^\circ\text{C}$. This thermal behavior of the center and surface of the cylinder with respect to time is representative of most of the cases studied in Validation 1 of this Chapter.



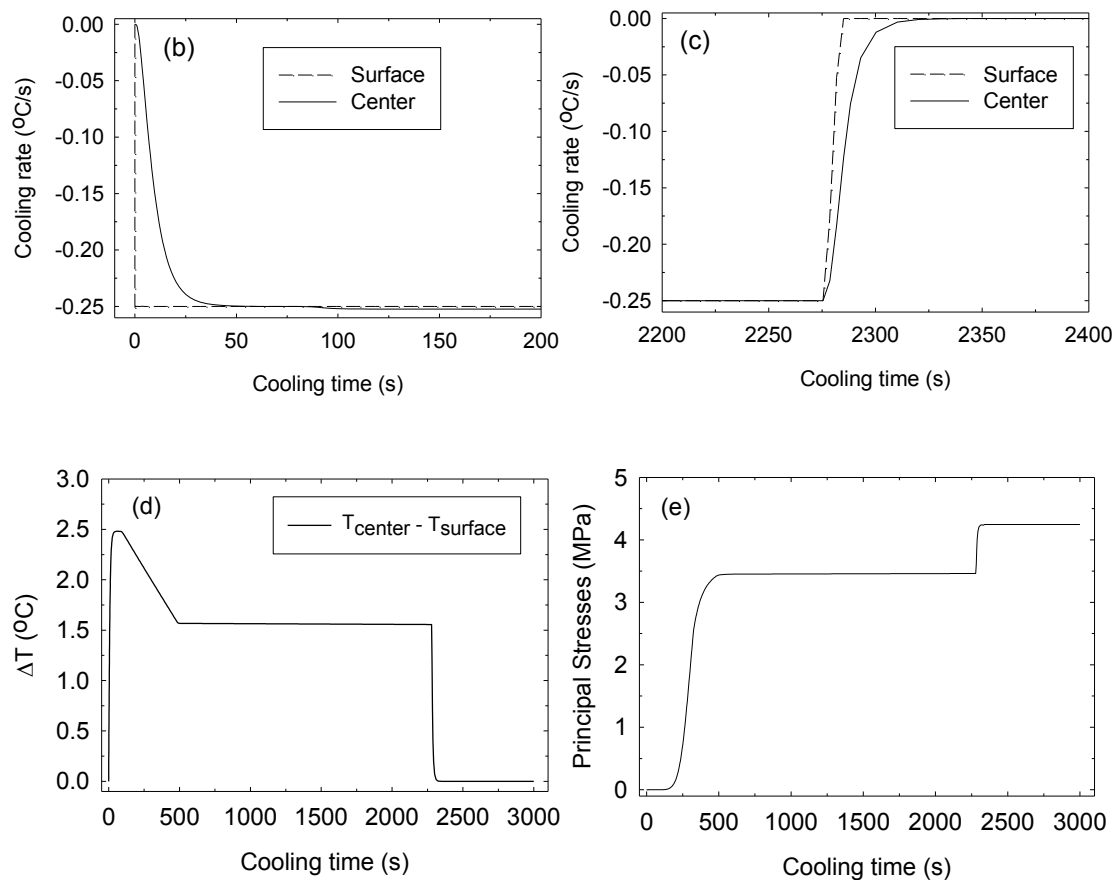


Figure 5.3. Cooling of cylinder from $T_0 = 590^\circ\text{C}$ at rate of $q_0 = 0.25^\circ\text{C/s}$ (a) Cooling rate for surface and center of cylindrical sample, (b) and (c) details of (a) at the given times, (d) temperature difference (ΔT) between the center and surface of the cylinder, (e) Maximum principal stress in the $r-\theta$ plane at the center of the sample.

The results in Figure 5.3 b shows that the rate of cooling is significantly different during approximately the first 50 s, which corresponds to a temperature change of about 12.5 degrees. The results in Figure 5.3d and 5.3e show the temperature difference (ΔT) and a build-up of stress at the center of the cylinder during the cooling time period. The first change in stresses occurs over the first 500 s when there is a difference between the surface and center temperatures as a function of time (Refer to Figure 5.3d). When this difference is a constant, the indication is that

ΔT does not change point to point and therefore no new residual stresses are generated. The transient portion of this plot, however, contributes to residual stresses both because of the initial period affecting volume change and because of non-uniform viscous flow due to the strong dependence of viscosity on temperature. The second significant change in stress occurs after the surface temperature reaches its target of 20°C, which takes 2280 s. In this case permanent elastic thermal stresses are generated during the time it takes for the center of the cylinder to reach 20°C, which takes about 40 s. These stresses are a direct result of permanent deformation that occurred at higher temperature. The stress results in Figure 5.3e are repeated in Figure 5.4 as a function of temperature to more clearly see the response in terms of temperature change.

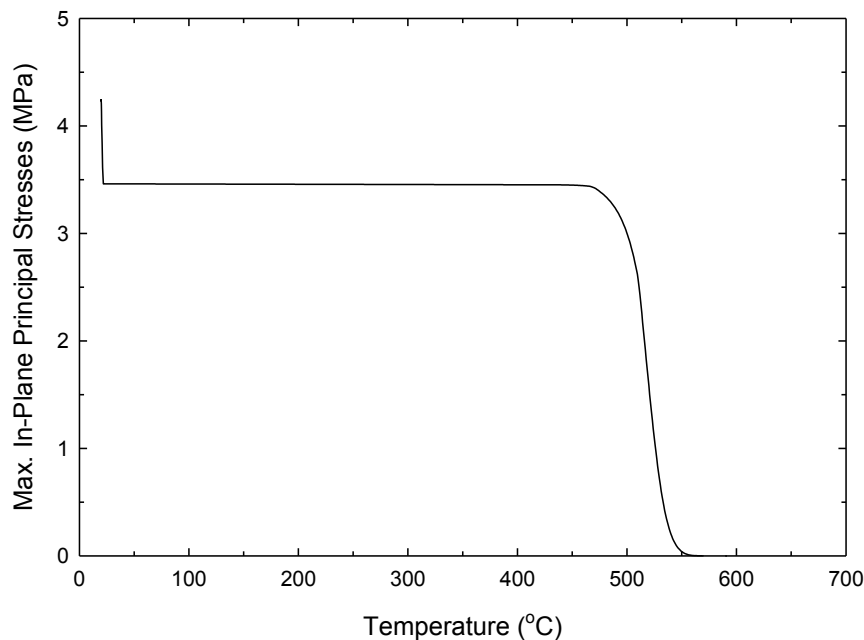


Figure 5.4 Stress distribution inside a cylindrical sample subjected to cooling from 590°C to 20°C at the rate of 0.25°C/s.

In interpreting the stress results for this validation case, the results have been limited to the stress at the center of the cylinder. Clearly the cooling rates vary from point to point. To illustrate the effect of this variation on the residual stresses, in Figure 5.5 the maximum in plane principal stress in the r - θ plane is plotted over the entire cylinder taking into account structural relaxation for both elastic and viscoelastic behaviors.

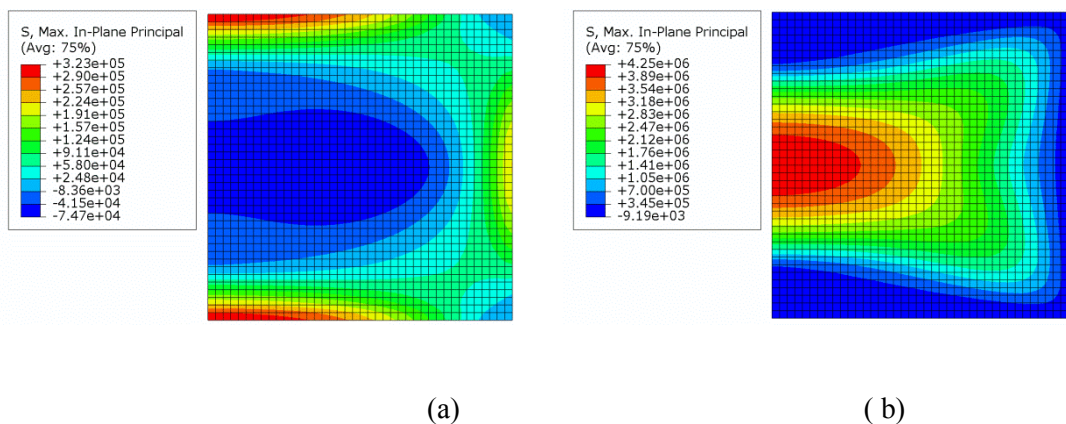


Figure 5.5. Comparison of the maximum principal stress in the r - θ plane for cooling from 590°C to 20°C using structural relaxation and the two different stress relaxation behaviors: a) elastic, b) viscoelastic.

The results in Figure 5.5 show that for structural relaxation only, the center of the cylinder has a low value of residual stress than can be misleading when comparing the relative contributions from stress and structural relaxation. Clearly Figure 5.5 shows that the effects of structural relaxation alone give rise to stresses on the same order of magnitude as when stress relaxation is also considered. Furthermore, the contour results show opposite trends: Figure 5.5a has the minimum stresses in the center, which Figure 5.5b has the maximum stresses in the center.

Finally, in order to assess the sensitivity of T_{SL} on the residual stresses at the center of the cylinder, the same numerical experiment was performed for cooling from 600°C to room temperature (20°C). The T_{SL} value was artificially modified such that for each of its selected values, the constant, $C_2 = T_R - T_{SL}$ in Eqn. (5.6) and the resulting viscosity-temperature curve was constrained to pass through the following two experimentally determined points: $T_R = 575^\circ\text{C}$, $\eta = 10^{8.9543}$ Pa·s and $T_R = 588.8^\circ\text{C}$, $\eta = 10^{8.355}$ Pa·s. The results of the analysis are presented in Figure 5.6.

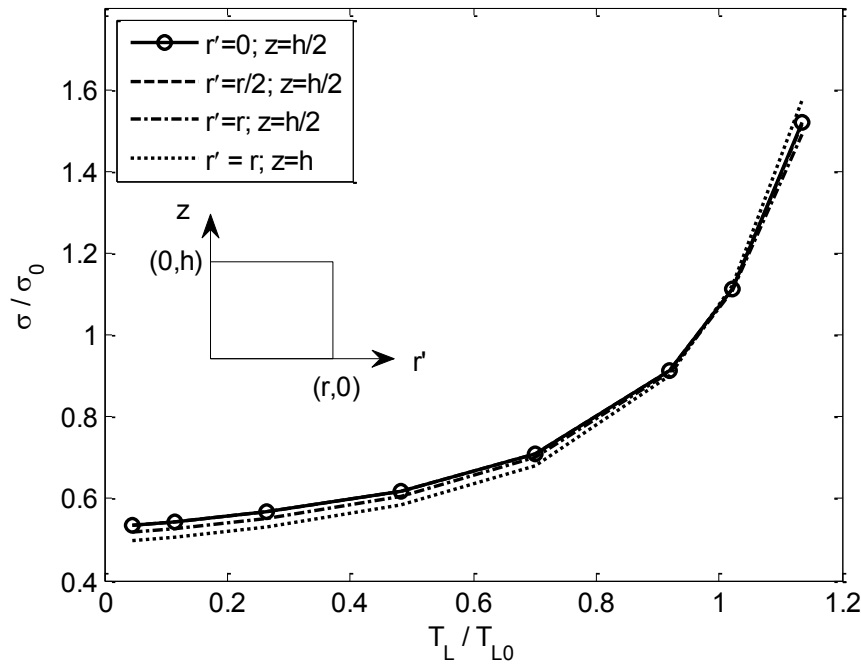


Figure 5.6 Effect of choice of T_{SL} on the maximum (residual) principal stress in the r - θ plane at the four given locations within the lens. The vertical and horizontal scales are normalized with respect to the baseline values of $\sigma_0 = 4.24e06$ and $T_{SL0} = 440^\circ\text{C}$.

The results in the Figure 5.6 show the residual stresses drop as T_{SL} is lowered since the material has more time to rearrange to relieve stress. Compared to the baseline case for $T_{SL} = 440$

°C , the residual stresses drop by about 55% when T_{SL} approaches room temperature and rise by about 50% as T_{SL} approaches T_g . As shown in Figure 5.6, this order of change is consistent throughout the cylinder and gives an indication of the error in assuming an incorrect value of T_{SL} .

5.3.2 Validation Example 2: Quenching of infinite Plate of Soda-Lime-Silicate Glass

In this validation example the problem of residual stress generation within a Soda-Lime-Silicate (SLS) slab quenched from a temperature of 738°C to a room temperature of 20°C is studied using numerical simulations. The experimental data for this example was originally reported by Gardon [33]. This example was later revisited analytically by [34] and via simulations by Carre and Daudaville [20]. In this study the glass was modeled as a viscoelastic body exhibiting both the stress and structural relaxation phenomena following [20]. The simulations in the present study consider the material properties for SLS glass provided by in the Carre and Daudaville [20] and [18]. The simulation results were compared with the experimental results published in [34].

Four sets of numerical experiments were performed considering the different thermal expansion behavior of glass that included: 1) a constant value of the thermal expansion coefficient of liquid glass (α_L) [20] during the entire cooling period, 2) a constant thermal expansion coefficient of solid glass (α_G) [20] during the entire cooling period, 3) a thermal expansion coefficient as a function of temperature based on TNM theory with the structural relaxation constants provided in [20] and 4) thermal expansion coefficient based on TNM theory with the structural relaxation parameters extracted based on the SLS data provided in [18]. The numerical experiment considering items 3 and 4 involved implementation of a user defined subroutine to account for thermal expansion (UEXPAN) and TRS behavior of glass (UTRS) in the Abaqus software. The residual stresses were sought across the thickness of slab at the end of

cooling of glass to room temperature (20°C). The four different cases of the thermal expansion coefficient variation with the temperature are shown in the Figure 5.7.

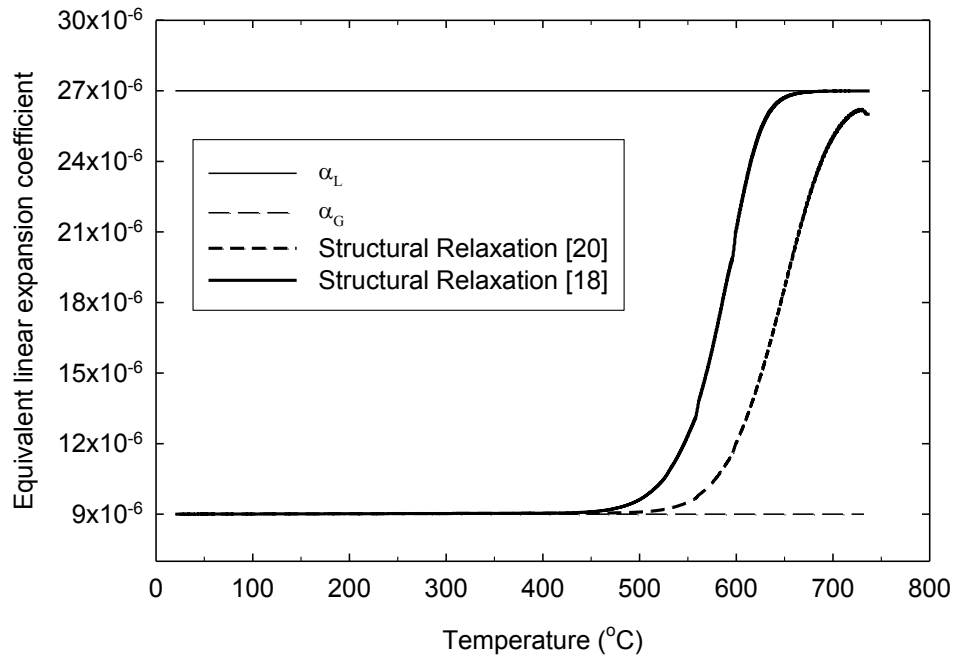


Figure 5.7 Comparison of different thermal expansion behavior of glass based simple assumptions (α_L and α_G) and structural relaxation properties from literature [18 and 20].

The two horizontal lines in Figure 5.7 indicate the coefficient of thermal expansion for the liquid (solid horizontal line) and solid state of the glass (dashed horizontal line). While, the non-linear response of the thermal expansion to the temperature variation is due to including the effect of structural relaxation. Next the residual stress results are presented.

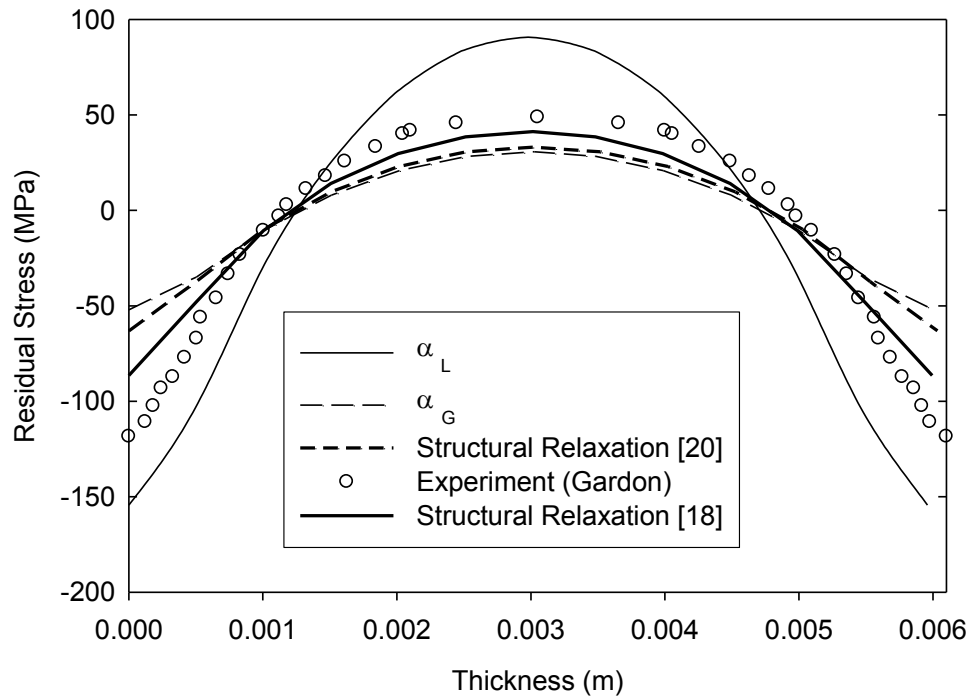


Figure 5.8. Stresses inside a quenched Soda-Lime-Silicate plate from literature [34] and using simulations with a different expansion behaviors given in Figure 5.7.

The residual stress results from each of the numerical experiments are presented in Figure 5.8 along with the experimental data obtained from [34]. The birefringence data reported in [34] having units of nm/cm was converted to psi units using the relation, $1 \text{ nm/cm} = 5.3 \text{ psi}$, that was provided in [35] and then easily converted from psi units to MPa units. The cases of constant thermal expansion coefficient $\alpha = \alpha_L$ and α_G provide upper and lower bounds for the residual stresses, with α_G corresponding to very rapid cooling and α_L to very slow cooling. The stress results of the simulation involving the use of the structural relaxation parameters provided in [20] are closer to the residual stresses obtained by simple assumption of α_G over the entire cooling

period. This indicates the given structural relaxation parameters [20] produce an effect of the relaxation process leaning more towards a glassy or solid state of the glass. This was also evident from the order of magnitude of the structural relaxation times ranging from about 10^2 to 10^4 , reported in [20] which later found to be about five orders of magnitude higher. Thus, the structural relaxation parameters were suspected to cause the disagreement between the experimental and simulation results. In order to explain the anomalous results, the structural relaxation constants, namely the relaxation time and an exponent in the KWW expression (τ , and β) for SLS glass provided in [18] were used to calculate the prony series parameters for structural relaxation that yielded the relaxation times in range of 10^{-3} to 10^{-1} . The results of this numerical experiment are shown by the solid thick line in Figure 5.8, which indicates an improvement in the residual stress estimation.

The residual stress results for the glass slab cooled during quenching were originally reported (in units of nm/cm) by [33], while Carre and Daudaville [20] revisited the problem using numerical simulations. The authors of the study [20] may have incorrectly interpreted the original stress results into the units of MPa. This interpretation yielded the stress distribution curve that was much closer to the numerical curve produced by considering the thermal expansion of liquid glass (α_L) over the entire period of cooling shown in Figure 5.7. They also had a close agreement with their numerical results with the interpretation of original stress results. This appears to be a case of using inconsistent material property data in a numerical simulation, even though the results agreed with the experimental data. In this case it seems that both the input data to the simulation and the experimental data were wrong. This example also shows that a careful understanding of the thermal expansion coefficient behavior is required to obtain realistic values of the stresses and the importance of a correct characterization of the material behavior of glass.

5.3.3 Validation Example 3: Sandwich Seal Test

The problem of thermal stresses in a sandwich seal, originally performed by Scherer and Rekhson [19] both experimentally and analytically, was revisited computationally by Soules et. al [32] using MARC and by Ananthasayanam [5] using the Abaqus software program. The experimental procedure performed by Scherer and Rekhson [19] involved cooling of alumina (Al_2O_3) sandwiched between G-11 glass ($T_g \sim 522^\circ\text{C}$) strips. The seal was made by stacking the plates of alumina and glass and heating them to 618°C under a small pressure to soften the glass. The glass then wets and bonds to the ceramic while the seal cools to room temperature ($T = 20^\circ\text{C}$) at a rate of $3^\circ\text{C}/\text{min}$. The stresses were measured using photoelastic techniques and compared with the theoretical calculations. The theoretical solution involved a phenomenological model of viscoelasticity and structural relaxation [31] and matched the experimental data well. A significant part of the solution in [19] was the assumption (constraint) that the structural relaxation reduced time was same as the stress relaxation reduced time.

The finite element implementation and validation of this problem by Ananthasayanam [5] was based on data provided in [19] for the viscosity, stress and structural relaxation functions of G-11 glass and their temperature dependence. Conversion from the “b-function” approach used in [19] to a prony series in [5] made use of six terms for structural relaxation and three terms for stress relaxation. The solutions presented in [5] included the reduced time assumption in two ways. In the first approach, which is based on the approach used throughout this dissertation, the viscosity as a function of temperature must be provided within ABAQUS via a WLF fit. In order to do this it was first necessary to reproduce the solution in [19], which is described below.

The property of glass at the reference temperature ($\tau_{pr}(T_{pr})$) and its variation with the given temperature ($\tau_{pi}(T)$) was considered to be dependent on the fictive temperature (T_f) value of that property as follows:

$$\frac{\tau_{pi}}{\tau_{pr}} = \exp \left[\frac{-H}{R} \left(\frac{1}{T_{pr}} - \frac{x}{T} - \frac{(1-x)}{T_{fp}} \right) \right] \quad (5.7)$$

The important properties such as viscosity and volume of the glass were assumed to have the same fictive temperature dependence ($T_{f\eta} = T_{f\omega}$). Based on this equation and knowing the reference viscosity, it is easy to calculate the viscosity of the glass for a range of temperatures. A WLF fit of this function can then be made and used as an input to ABAQUS. In the second approach a direct way to include Equation (5.7) was used. In this case the input of the temperature dependent viscosity into the Abaqus software based on Equation 5.7 was achieved via the UTRS subroutine without the need to first solve for the viscosity. This subroutine enables the enforcing of the time-temperature shift factor, $A[T(t)]$ for viscosity, to be equal to that from the structural relaxation (Equation 5.7). Comparison of the viscosity as a function of temperature using the two approaches is shown in Figure 5.9.

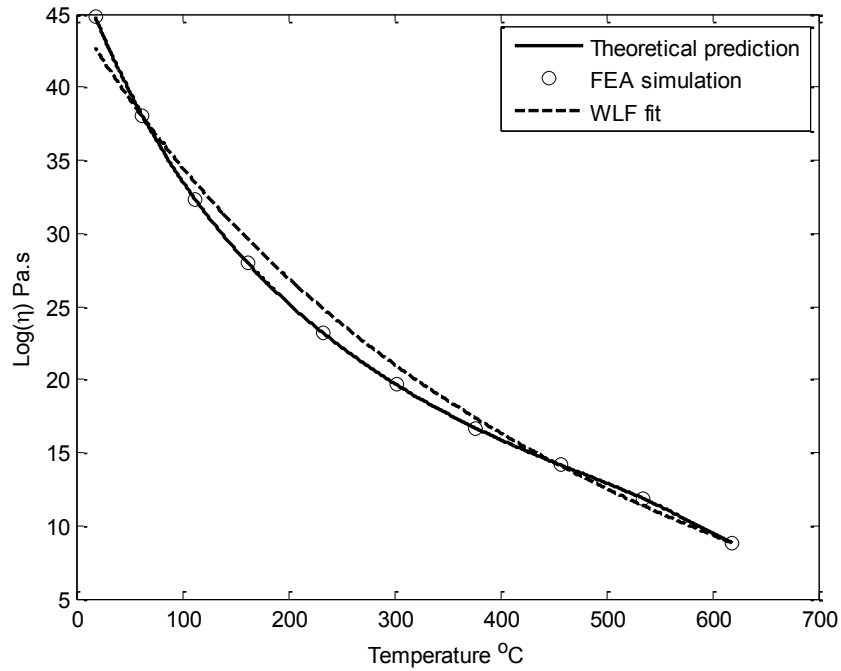


Figure 5.9 Viscosity of G-11 glass predicted based on Equation (5.7) and experimental data [19] (solid line), FEA simulation output from UTRS (circles) and WLF fit (dashed line) of the entire data.

As seen from the figure the results from Equation (5.7) and the points obtained from the UTRS subroutine match very closely. It can be observed that the WLF fit crudely approximates the viscosity due to the peculiar nature of the curve near the glass transition temperature range ($T_g \pm 50^\circ\text{C}$). This section of the curve is concave down, which is an artifact of enforcing Equation 5.7 within a temperature range where the fictive temperature, T_f , is very sensitive to the temperature. It was observed in [5] that a standard WLF approximation of this viscosity data led to a lower residual stress values in the seal. Therefore, it was necessary to accurately input the temperature dependent viscosity into the Abaqus software via UTRS subroutine. This implementation ensured the fact that viscosity of G-11 glass in the glass transition region has the “structural” dependence rather than a simple Arrhenius dependence. The above behavior was also shown to be valid for soda-lime silicate glass [29]. Therefore, a finite

element implementation of this behavior lead to a more accurate modeling of the viscosity of G-11 glass as compared to the WLF parameter representation, which was the key to the improvement as reported in [5]. For the completeness of the discussion, the stress solutions to this sandwich seal problem via finite element analysis with and without the implementation of UTRS subroutine are shown in Figure 5.10.

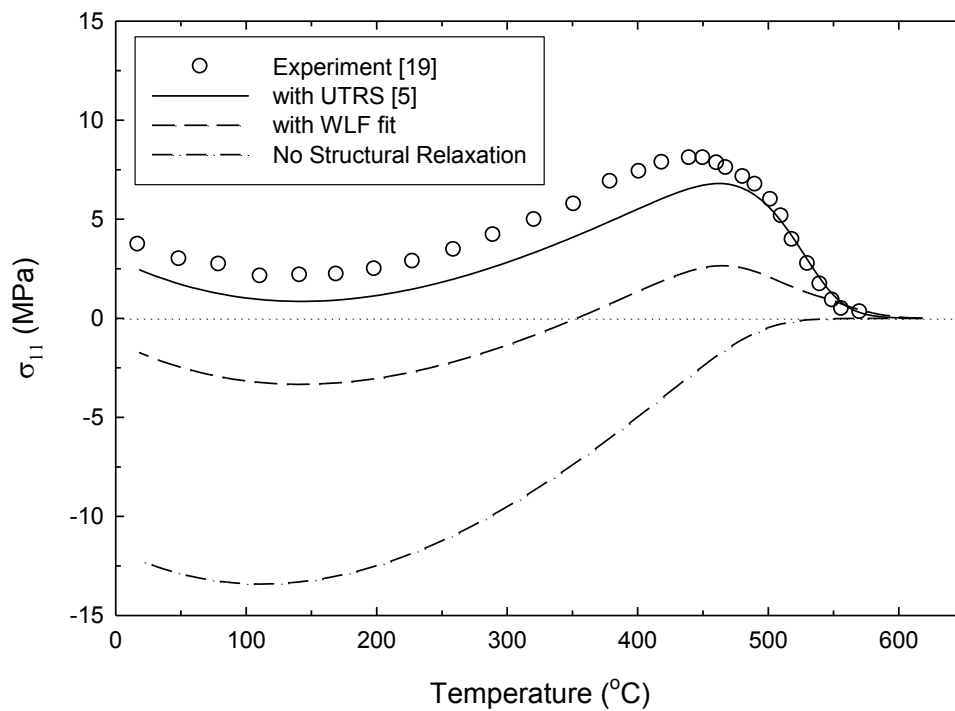


Figure 5.10. Stresses in the sandwich seal with UTRS subroutine implementation (solid line), with WLF parameter input (dashed line), and effect of no structural relaxation (letting $x=1$ in Equation 5.7) (dash and dotted line) compared with the experimental predictions (circles).

5.4. Results

5.4.1. Convergence Study

Results in this study rely on the accurate prediction of the final size and shape of a molded lens and also the accurate evaluation of the transient stresses during molding and the residual stresses that remain after the molding process is complete. A convergence study of the final size and shape of lens was previously considered by Ananthasayanam et al. [4]. In the current study a numerical convergence study of the stress state inside the lens was performed to ensure that these values converge to within a certain tolerance limit. A steep meniscus lens shape was selected as this lens shape is expected to have a higher shape deviation and an overall higher magnitude of residual stress distribution upon cooling. In this numerical study the lens was subjected to the complete thermo-mechanical cycle experienced by a typical lens during the actual molding operation with the process parameters defined by Ananthasayanam et al. [4]. Frictional contact was assumed between the glass and mold interface using the Coulomb friction law. In-plane principal stresses and out-of-plane principal stresses are evaluated at different intervals during the molding process. The study was conducted for three different meshes and a mesh with different values of the parameter CETOL, which is a creep strain rate error tolerance defined in Abaqus that controls the accuracy of implicit integration scheme. The results of this convergence study are presented in Table 5.2 and compare percent changes in the value, time and location of the maximum in-plane principal stress for the baseline and finest meshes.

Molding Stage	% change in maximum value of in-plane principal stresses	% change in time at which the maximum stresses occur	% change in geometric location where the maximum stresses occur (co-ordinates)	
			X	Y
Pressing	13.7	79.9	-6.51	-0.01
Slow Cooling	3.97	0	-0.07	-0.18
Gap creation	3.97	0	-0.07	-0.18
Cooling #2	0.26	0	0	-0.29
Release	0.24	0	0	-0.73
Cooling #3	0.43	0	0	0.61
Cooling #4	-0.69	2.97	0	-0.30

Table 5.2. Convergence study of steep meniscus lens during various stages of lens molding. Reported values indicate percentage change of values obtained for a refined mesh (20,499 elements) relative to values for a baseline mesh (13,641 elements).

As seen from the table, the reported percent change is converged to within about 4% for the Slow Cooling stage to the End of Process (Cooling #4 stage). But that is not the case for the Pressing stage as the three parameters of location, value, and time have larger error. The stresses are very high at the beginning of the pressing stage and are difficult to converge due to the complex contact conditions involving hot glass and mold. However, as shown in the results at the end of the process, this early error dissipates. This convergence is further justified by the results in Figure 5.11, which show the converged values of the in-plane principal stress distribution at a vertical section about 5 mm away from the axis of lens at different times during molding for all three of the meshes considered.

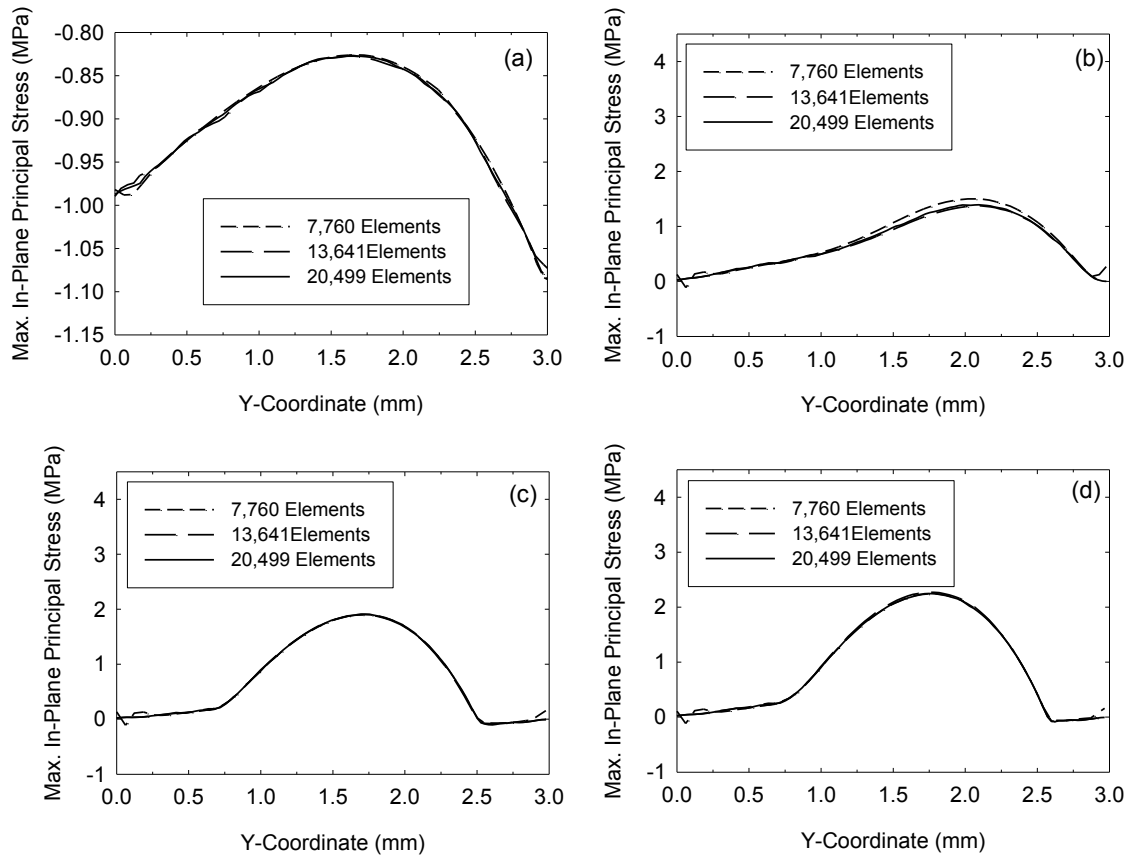
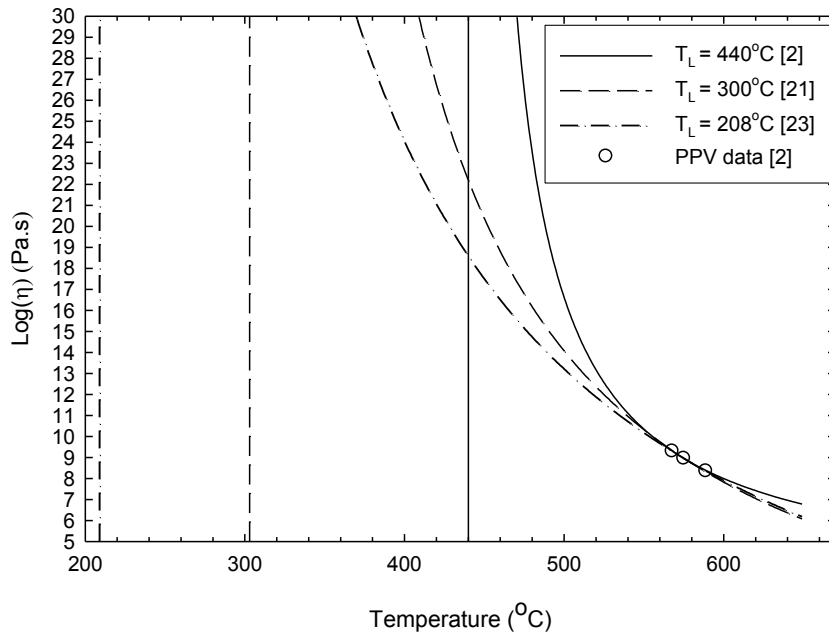


Figure 5.11. Convergence of In-Plane principal stresses at a vertical section 5 mm away from central axis of the steep meniscus lens for different meshes and different molding stages considered. (a) End of Pressing, (b) End of Slow Cooling, (c) End of Gap creation, (d) End of Process.

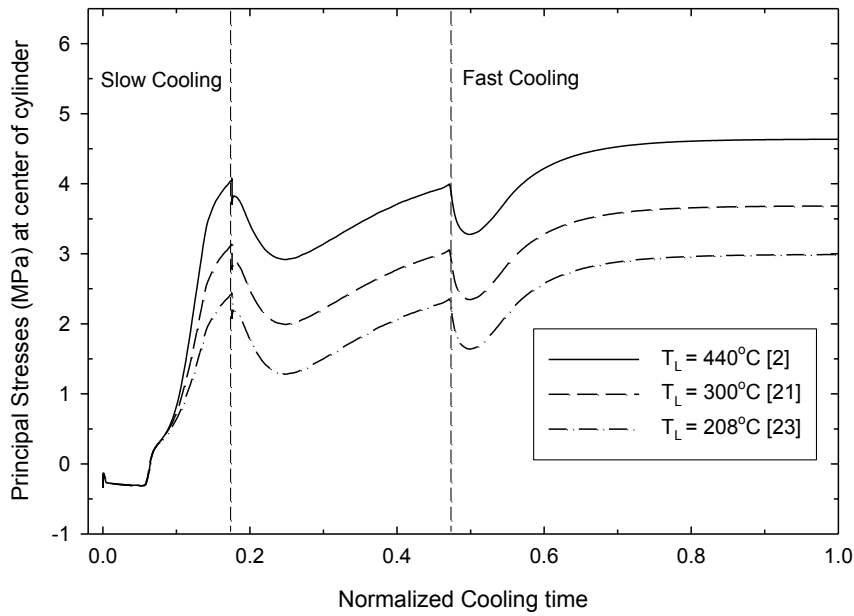
5.4.2. Molding of a Simple Cylinder

A glass sample in the shape of a cylinder with diameter, $D = 10$ mm and height, $H = 5.3$ mm was subjected to a molding cycle and residual stress results were analyzed. The cylinder was pressed to a final height of about 3.3 mm while maintaining the thermo-mechanical conditions similar to those of the molding cycle given in [3,4]. The focus of this study is how the TRS fit affects the residual stresses as quantified by the maximum in-plane ($r-\theta$) principal

stress. Three different TRS fits were considered based on: 1) PPV measurements using $T_L = 440\text{ }^\circ\text{C}$ [2] 2) PPV and BBV measurements [22] and 3) Best fit of the recent PPV and BBV data [24]. The second and third fits made use of a few data points near the glass transition and softening regions and the viscosity data obtained from the cylinder compression test using PPV [2]. The results in Figure 5.12a give the three different TRS fits, while residual stresses as a function of time during the molding cycle are provided in Figure 5.12b.



(a)



(b)

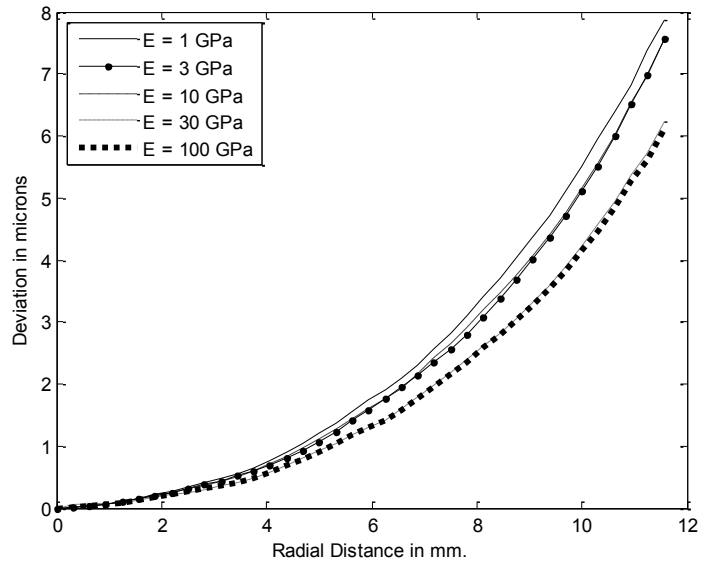
Figure 5.12 (a) Temperature-viscosity relationship calculated by best fit of WLF equation and corresponding data (b) Evolution of stress with respect to cooling time for various TRS fits. Vertical lines indicate the value of T_L for respective curve obtained by using the best fit.

The maximum in-plane principal stresses reduce significantly for the viscosity-temperature curve having a lower temperature at which an infinite viscosity is predicted. This shows the importance of characterizing correctly the viscosity of the glass within the entire temperature range of interest. While the results in Figure 5.12a show that the three curves vary significantly at lower temperatures, all curves pass closely through the three (triangle symbol) experimentally determined values of viscosity using PPV cylinder compression test. The T_L values as defined by an infinite viscosity for the three curves are: dark solid line (440°C), dashed line (303°C) and dotted curve (209°C). Recalling from the validation #1 study, a value of about $T_L = 300^\circ\text{C}$ gives an “actual” T_L of about 440°C. The final residual stresses for the TRS behavior that has the lowest T_L is about 55% of the result with the highest T_L .

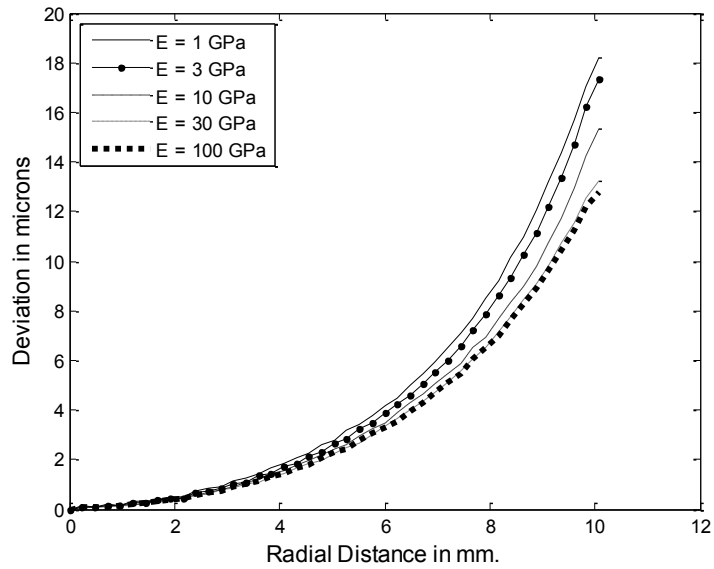
5.4.3. High temperature elastic modulus (E)

The study in this section considers the possibility of a strong dependence of the elastic modulus on temperature. The temperature dependence of the elastic modulus of the glass was changed from its room temperature value of about 100 GPa to a value of 1GPa at high temperature while keeping the equilibrium viscosity of the glass the same. This change was assumed to occur between 510°C and 560°C as a linear function of the temperature. The drop in elastic modulus of glass as temperature increases was observed in [25]. In this section a sensitivity analysis of the effect of the high temperature elastic modulus on lens profile deviation is performed for both a bi-convex and a steep meniscus lens.

The results of Figure 5.13 show lens shape deviation vs. high temperature elastic modulus for the Bi-convex and steep meniscus lenses. The deviation increases as the value of the high temperature elastic modulus drops below its room temperature value.



(a)



(b)

Figure 5.13. Sensitivity of high temperature Elastic modulus on shape deviation for (a) Bi-Convex (b) steep meniscus Lens.

The change in deviation mainly occurs before and during the gap creation stage. During the slow cooling stage, which precedes the gap creation stage, the pressing force is reduced to a maintenance force that is about 1/3 of the pressing force. The slow cooling stage is followed by a

gap creation stage in which the maintenance force drops to zero. A lower value of elastic modulus causes higher elastic mechanical strains during the stages when the magnitude of the applied force drops to zero, which results in higher (permanent) lens shape deviation. Perhaps since elastic strain occurs more freely as the elastic modulus decreases, viscous flow to relieve stress is less likely to occur, which in the end results in larger deviation. Due to competing permanent deformation mechanisms, this explanation is speculative. It is possible that for a different geometry the opposite effect would occur.

5.4.4 Reference temperature (T_R)

The reference temperature (T_R) is the temperature of the glass at which the viscoelastic properties of the glass are evaluated in an experiment. Based on T_R and other parameters, the viscoelastic behavior of the glass over the entire temperature range can be determined. Hence, it is critical to know this temperature accurately. Given the uncertainties in determining the actual temperature of the glass during high temperature creep experiments, it is often difficult to know the reference temperature accurately. In this study an uncertainty of $\pm 20^\circ\text{C}$ in the actual value of the reference temperature was considered. The uniform shift in T_R causes a subsequent uniform shift in the viscosity-temperature curve of the glass. This affects the thermal history of the molded lens causing a change in the profile deviation. This shift also results in different press time (t_{pr}) as the "shifted glass" will have a different viscosity-temperature relationship. In this numerical experiment, the press time was adjusted to have the same center thickness for the respective lens type. All other parameters were kept unchanged.

The results in Figure 5.14 show the effect of reference temperature on the deviation for both types of lenses. As expected the shape deviation changes as the value of T_R is varied. Press times for all cases are given in the legend of the Figure.

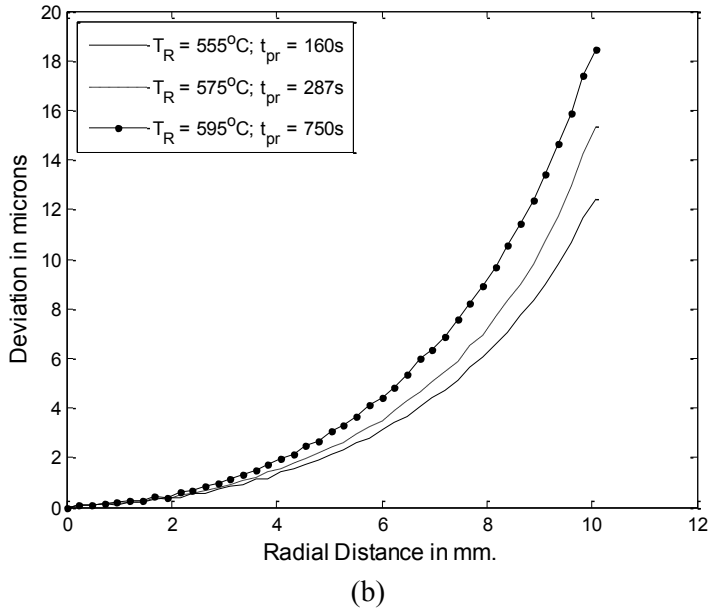
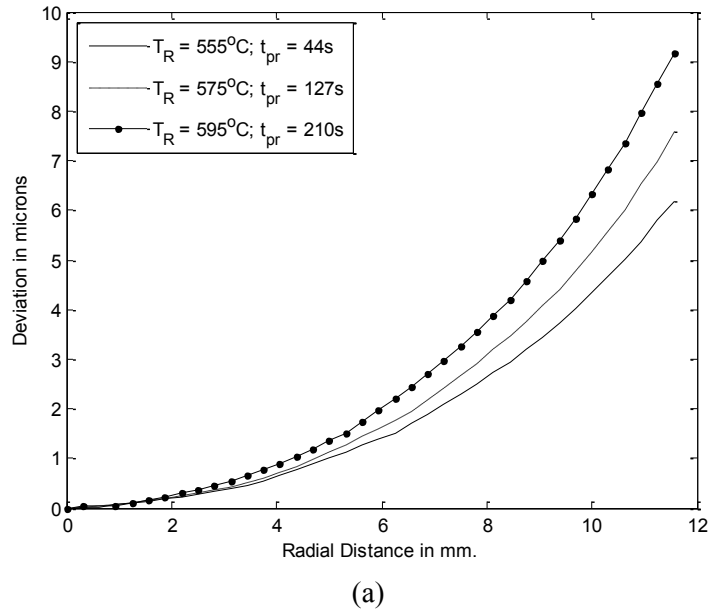


Figure 5.14. Sensitivity of Reference Temperature (T_R) on shape deviation for (a) Bi-Convex (b) Steep meniscus lens

The results in Figure 5.14 show that it takes longer to press the lens with a higher T_R , while keeping the other parameters unchanged, including the heat transfer coefficient at the lens and

mold interface. This occurs because the temperature at which the lens is molded also increases with higher T_R . Since the lens molded with different T_R has a different thermal history, the deviation of such a lens will be different. Thus, when T_R was changed by $+20^\circ\text{C}$, the molding temperature also increases which caused a change in shape deviation of about 2 microns for the bi-convex lens and about 4 microns for the steep meniscus lens. Lowering the T_R by 20°C lowers the deviation by about one micron for the bi-convex lens and by about 2 microns for the steep meniscus lens. During a typical stress relaxation experiment, the actual temperature of the glass can easily be less than the temperature recorded by the thermocouple, in which case the value of T_R will be underestimated.

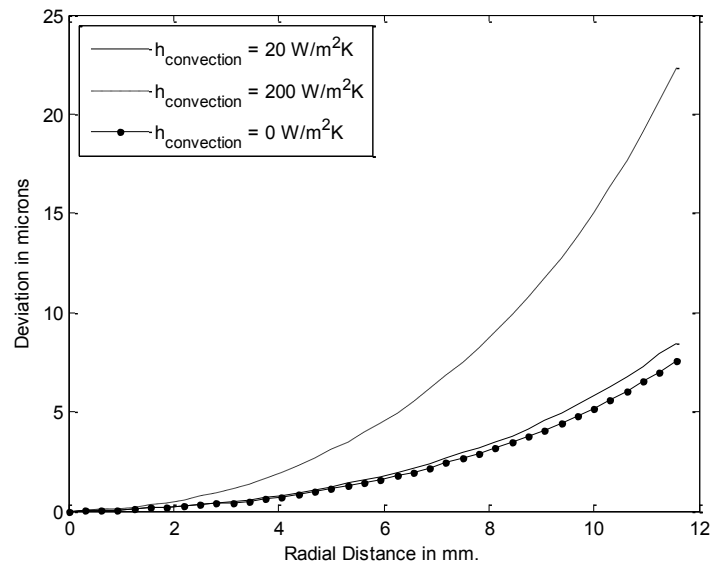
5.4.5. Convective heat transfer coefficient ($h_{\text{convection}}$)

During the molding process heat transfer occurs via conduction, convection and radiation. During the cooling stage, the primary mechanism of heat transfer is convection due to nitrogen flowing in the molding chamber. In the previous study by Ananthasayanam [5] this stage of the cooling process was taken into account indirectly by the application of temperature boundary conditions based on processing temperature data taken near the lens region. In this section a more direct approach is used that assumes some of the nitrogen flow actually has direct contact with the lens during the fast cooling cycle when a gap exists between the lens and upper mold. Convection is ignored during the pressing and slow cooling cycles since pressing is done in a vacuum and the lens is in contact with the molds during slow cooling. As stated in the introduction, Yi et. al [6] modeled the convection heat transfer coefficient between a lens and the surroundings throughout the heating and cooling stages.

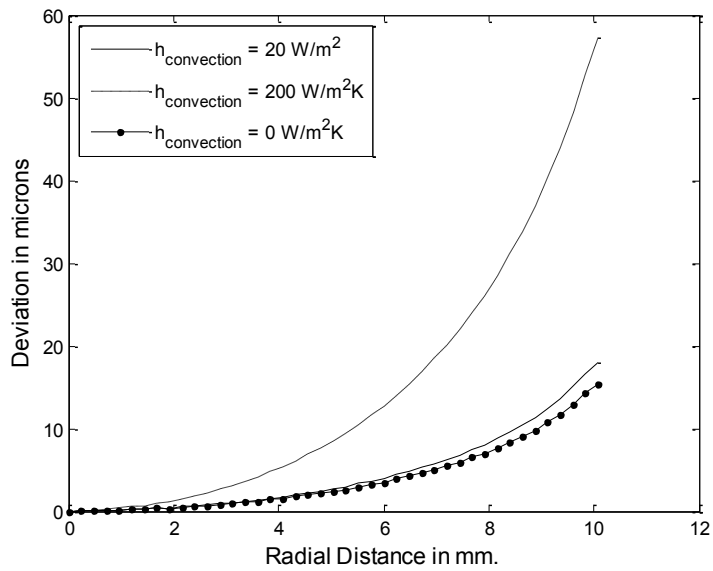
The baseline simulation case in this study has a convection coefficient between the glass lens and surroundings is set to zero and the heat transfer between the lens and molds only occurs

through contact gap conductance between the glass lens and molds. This case corresponds to molding a lens in a vacuum environment. In order to model the convection heat transfer in Abaqus, a value of the film coefficient (h_f) and surrounding temperature (T_∞) was defined along the boundary of the lens and mold in the beginning of the fast cooling stage of the lens molding process, when the temperature of glass is below the glass transition temperature (T_g) in range of about 510°C.

The results in Figure 5.15 show the lens shape deviation for the different convective heat transfer coefficients considered. The effect of modeling convective heat transfer is to increase the rate of heat transfer from the lens, consequently cooling it faster than the baseline simulation case.



(a)



(b)

Figure 5.15. Sensitivity of convective coefficient ($h_{\text{convection}}$) on shape deviation for (a) Bi-Convex (b) Steep meniscus lens

As the lens cools faster the glass has less time to accommodate for shape change due to structural rearrangements, which results in an increase in deviation. The change in deviation is calculated

based on deviation of the baseline case with $h_{\text{convection}} = 0$. For a higher heat transfer coefficient ($h_{\text{convection}} = 200 \text{W/m}^2\text{K}$), the change in deviation is about 15 microns for the bi-convex lens and about 44 microns for steep meniscus lens. When a relatively low value of coefficient is used ($h_{\text{convection}} = 20 \text{W/m}^2\text{K}$), the change in deviation for both types of lenses is less than 2 microns.

5.4.6. Choice of stress relaxation function

It was previously determined that the choice of stress relaxation function has a negligible effect on the lens shape deviation, but the effect on the residual stresses induced inside the lens at the end of the molding cycle is significant. The presence of higher residual stresses inside a molded part increases its susceptibility to fracture caused by processes such as annealing [23] and affects the birefringence [28]. Hence it is important to understand the residual stress state within a molded lens for different stress relaxation functions. For the three different stress relaxation models discussed in Section 5.2, the in-plane principal stress at a section 5 mm away from the symmetry axis within a bi-convex lens at different time intervals during the lens molding process are presented in Figure 5.16.

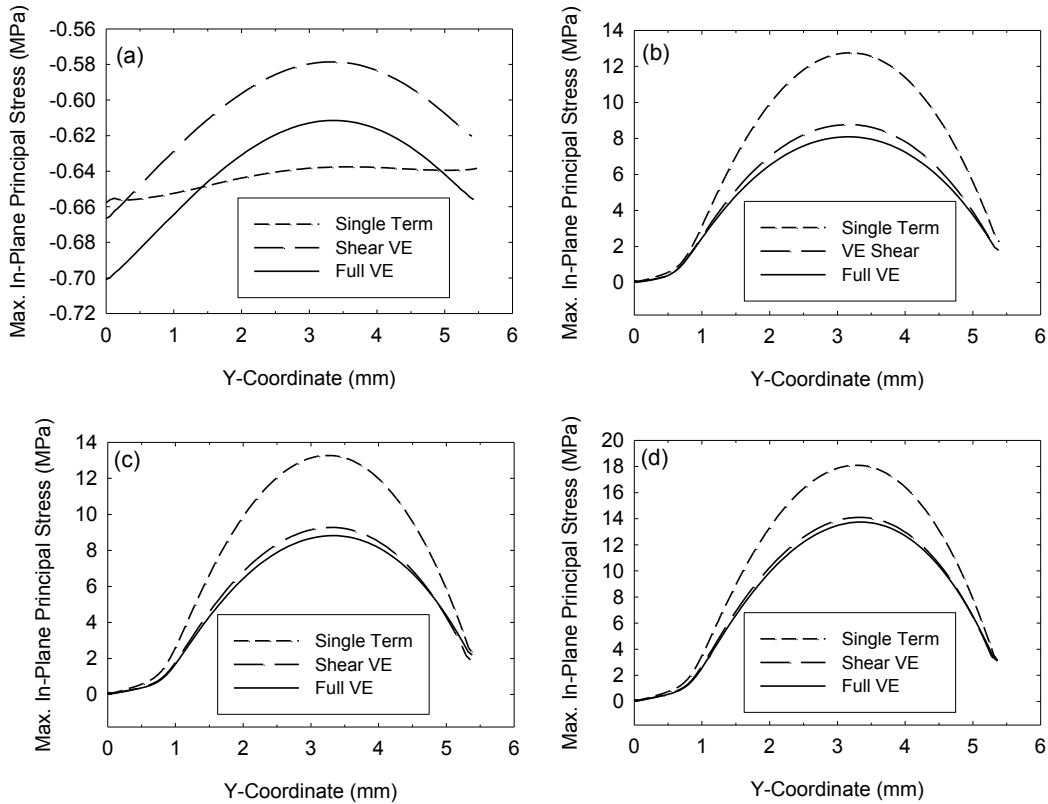


Figure 5.16. Bi-Convex: Effect of Stress relaxation modeling detail on stress state at a vertical section 5 mm away from central axis. (a) End of Pressing, (b) End of Slow Cooling, (c) End of Gap creation, (d) End of Process.

As seen from the figure, as the material behavior changes from a single term prony series to the more realistic multiple term series of a “Full Viscoelastic” characterization, the stresses inside the lens decrease in value. When the stress relaxation function is represented by a single prony term, the stress estimates become conservative. Similar observations were made for the steep meniscus lens shape at different intervals of time during molding cycle, as shown in Figure 5.17.

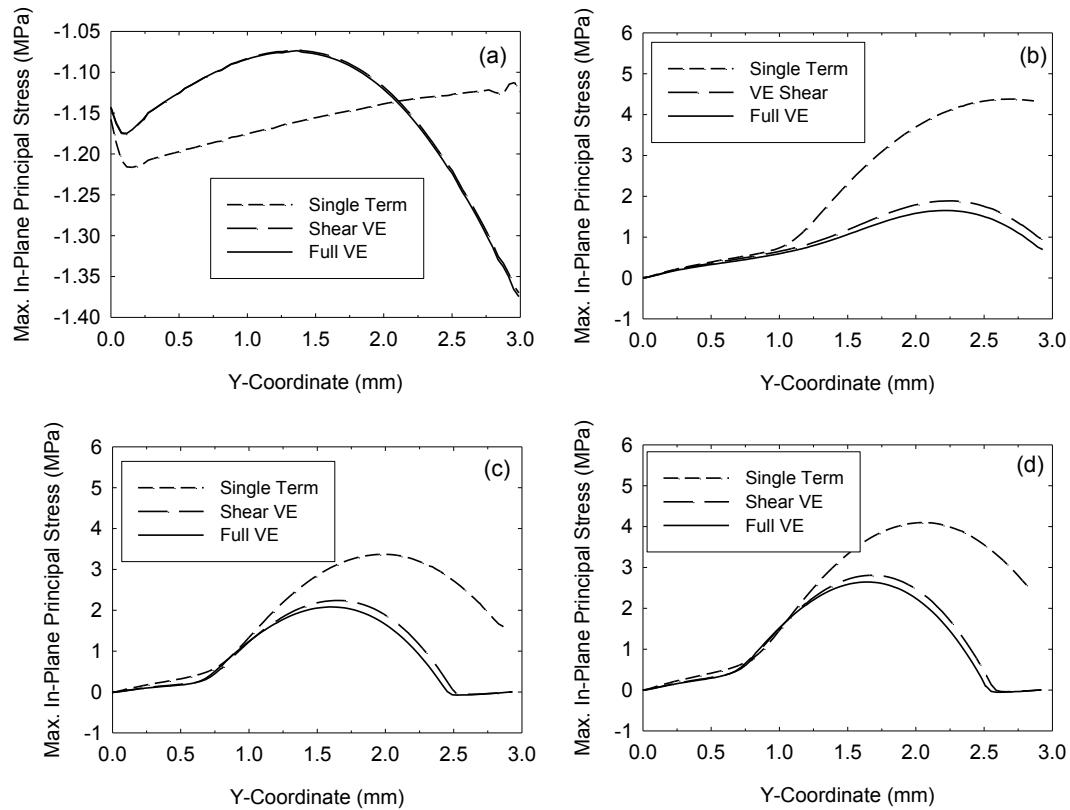


Figure 5.17. Step Meniscus: Effect of Stress relaxation modeling detail on stress state at a vertical section 5 mm away from central axis. (a) End of Pressing, (b) End of Slow Cooling, (c) End of Gap creation, (d) End of Process.

The estimates of residual stresses inside the lens at the end of the process were significantly higher if the simplified assumption regarding the material model is made in the analysis. The shear viscoelastic material model that allows viscoelastic relaxation of the shear component of the deformation gives a reasonable estimate of the stresses as compared to a single term approximation. It appears as though the added fidelity of the bulk response is not important for the case studied.

5.4.7. Stress Birefringence Calculations

Stress birefringence inside a molded lens is an inevitable outcome of the molding process. Birefringence or double refraction is a phenomenon where a light wave entering a material will be split into two plane polarized components that are perpendicular to one another. These waves will, in general travel through the material at two different speeds, as one will be retarded with respect to another as they pass through the material [25]. As a result the waves will have phase difference at the exit of the material point. The birefringence inside a molded lens is mainly caused by thermo-mechanical processes induced by the molding operation, which cause a deterioration of optical properties. Such birefringence is referred to as Stress birefringence or Structural birefringence.

Stress birefringence in the following examples was calculated based on the formula

$$B = C(\sigma_r - \sigma_\theta) \quad (5.8)$$

where, B is Birefringence in nm/cm, C is the stress optical coefficient ($C = 2.29 \times 10^{-05} \frac{\text{nm}}{\text{cm}} \cdot \text{Pa}^{-1}$) [27] and σ_r and σ_θ are the inplane maximum and minimum principal stresses in units of Pa. Using Eqn. (5.8) and making use of the capability presented earlier in this Chapter, it is a very simple matter to calculate the birefringence. The birefringence plots for the bi-convex lens shape for the three stress relaxation behaviors in Eqns. (5.2 – 5.4) are presented in Figure 5.18. The plots show the stress birefringence when viewed from above; hence, it involves only radial and circumferential stress components in the calculations as given by Eq. (5.8). The contour plots for the stress birefringence provided in this study show the overall birefringence distribution at the end of the molding cycle. The lighter shades in these plots indicate a lower stress birefringence values and dark shades show relatively high stress birefringence within the lens geometry. Figure 5.18 shows the trend that the full viscoelastic material behavior of Eq. (5.4)

gives less birefringence, which is a slightly improved birefringence response than the viscous material assumption. Just as with stresses in Figures 5.16 and 5.17, the viscous assumption gives a more conservative estimate, and similarly the most sophisticated characterization, if it is correct, gives potentially the most accurate results.

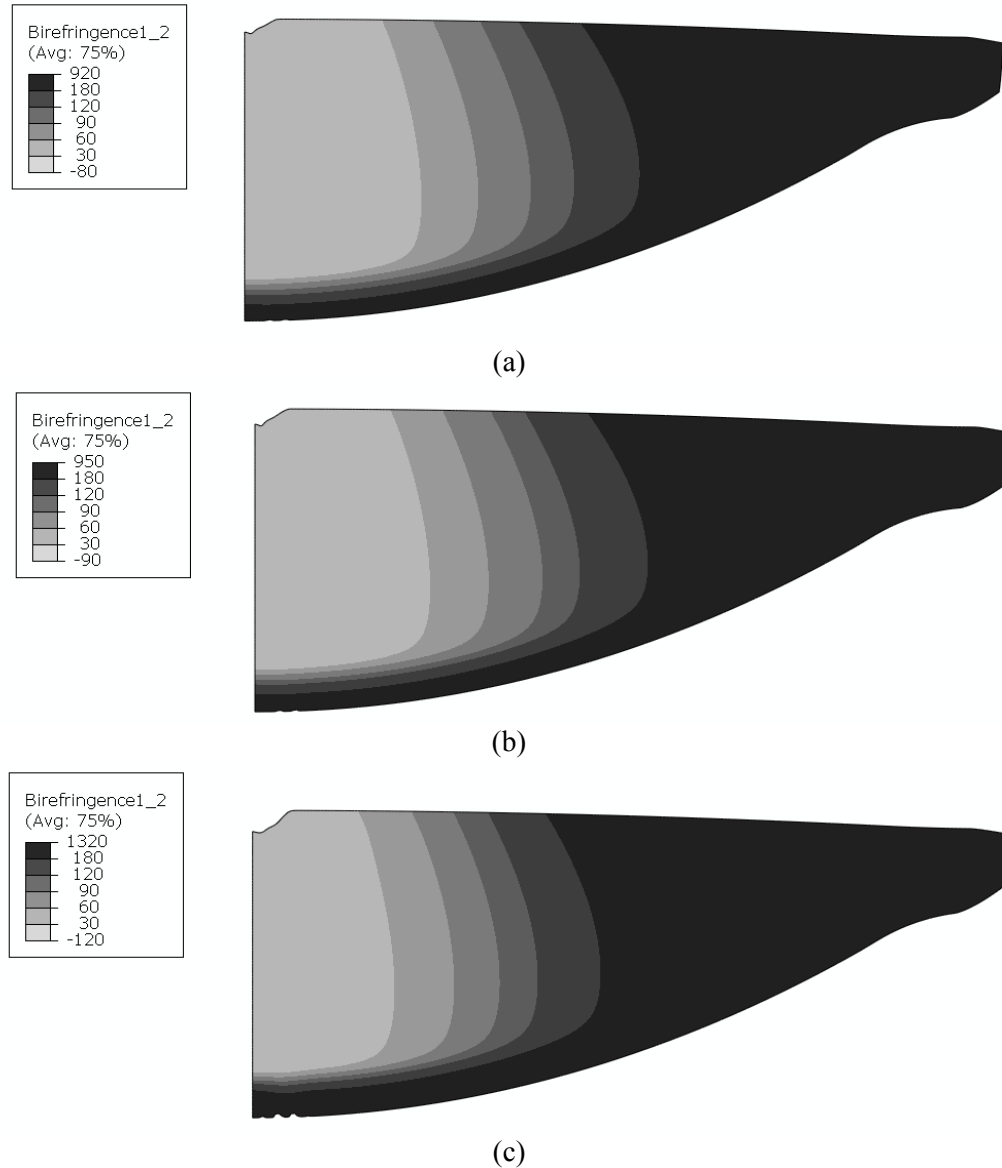
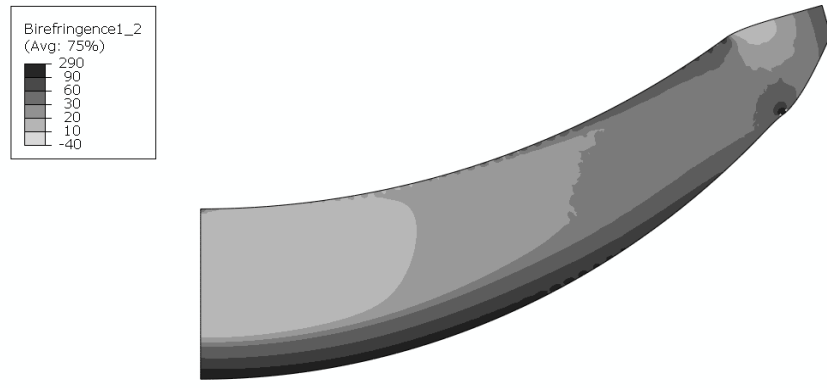
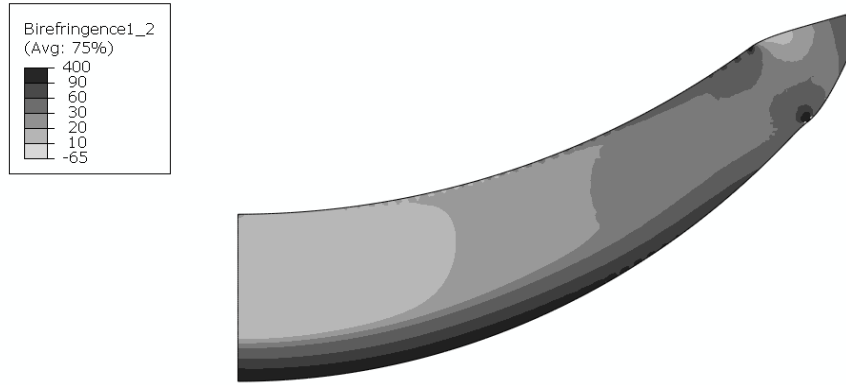


Figure 5.18. Stress birefringence (nm/cm) inside the Bi-convex lens shape after molding for different material behavior assumptions (a) Full Viscoelastic (Eq. 5.4) (b) Shear Viscoelastic (Eq. 5.3) and (c) Single term Shear model (Eq. 5.2).

The birefringence for the steep meniscus lens is shown in Figure 5.19 for the three different viscoelastic material behavior assumptions as presented in Figure 5.18. Just like the previous bi-convex results, the viscous assumption leads to a higher birefringence distribution inside the lens.



(a)



(b)



(c)

Figure 5.19. Stress birefringence (nm/cm) inside the steep meniscus lens shape after molding for different material behavior assumptions (a) Full Viscoelastic (Eq. 5.4) (b) Shear Viscoelastic (Eq. 5.3) and (c) Single term Shear model (Eq. 5.2).

In a final study in this Chapter, the birefringence distribution in both lenses was plotted along different vertical sections of the lens. In Figure 5.20 the case of the bi-convex lens is considered and the stress birefringence distribution is plotted along the thickness of the lens at the central axis ($r=0$) and at a radial distance 5 mm away from the axis. In this plot, the value zero for the lens thickness indicates the bottom of lens, while, the maximum value indicates the top surface of lens considered. The same considerations are made in Figure 5.21 for the steep meniscus lens. These results clearly show the difference in the birefringence values as a consequence of using different viscoelastic material models. It also shows that the overall stress birefringence values are higher at the bottom edge of the lens as it cools faster than the central and top portion.

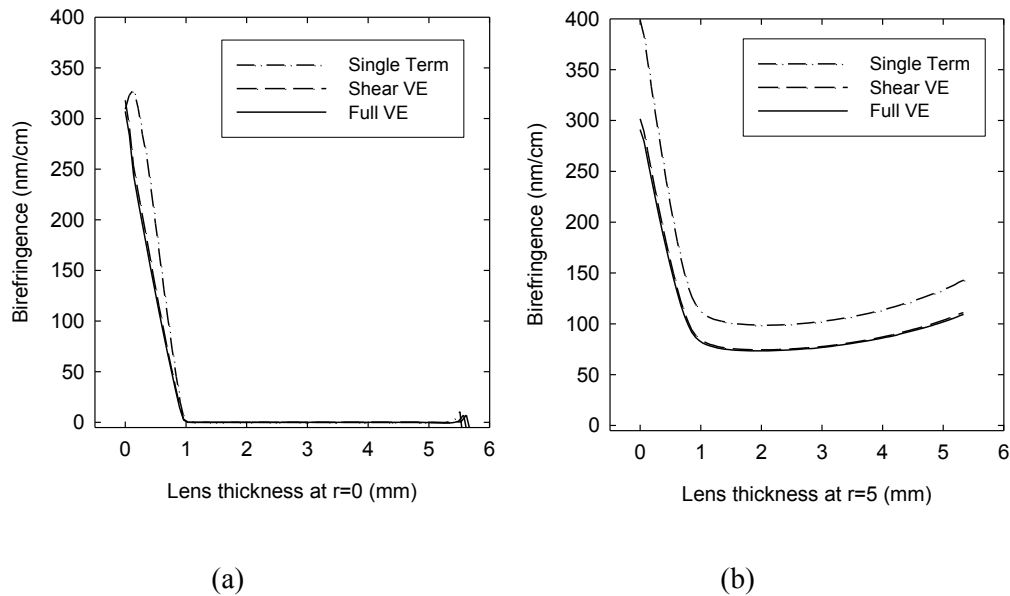


Figure 5.20. Stress birefringence distribution (nm/cm) inside the bi-convex lens shape after molding for different material behavior assumptions along the thickness of the lens at different section of lens. (a) At the central axis of the lens (b) at 5 mm away from the axis of lens.

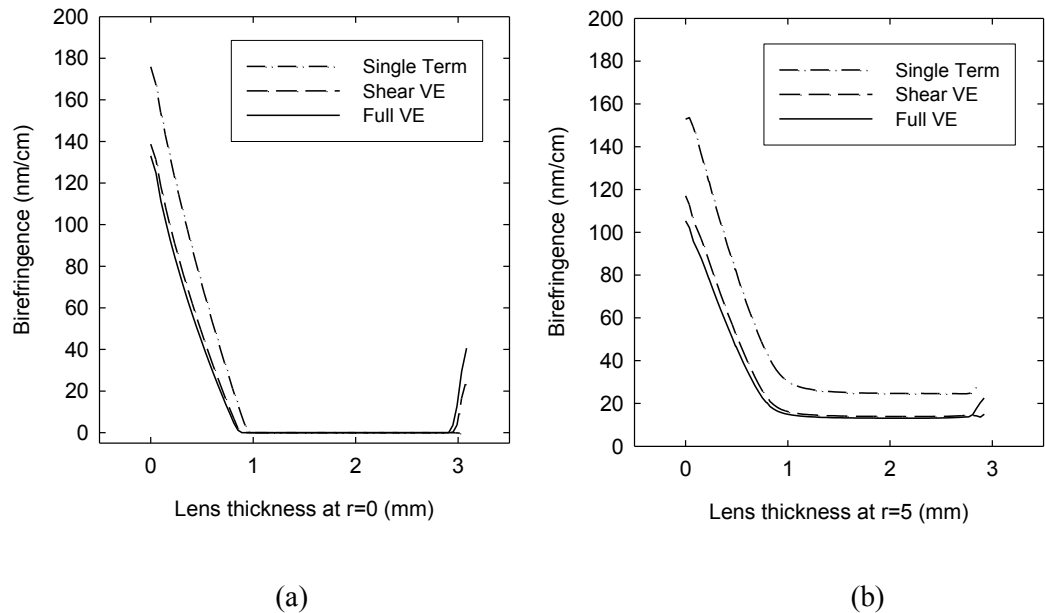
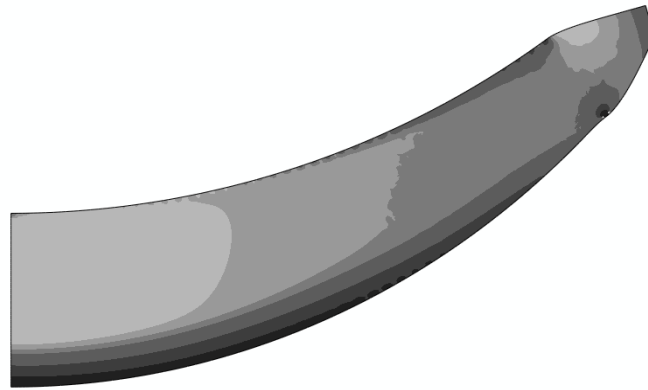
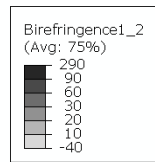
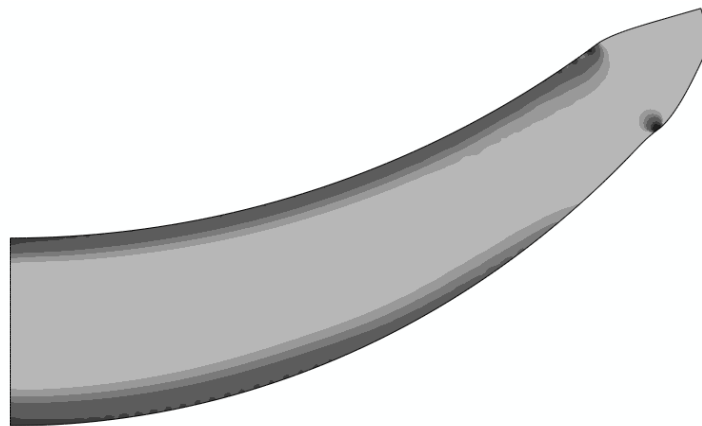
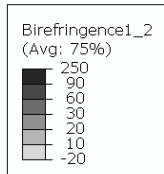


Figure 5.21. Stress birefringence distribution (nm/cm) inside the steep meniscus lens shape after molding for different material behavior assumptions along the thickness of the lens at different section of lens. (a) At the central axis of the lens (b) at 5 mm away from the axis of lens.

Given the capability to determine the stress birefringence, a sensitivity study of TRS behavior and slow cooling rate on the stress birefringence inside the steep meniscus lens will now be considered. For the case of TRS behavior, which is presented in Figure 5.22, birefringence results for two viscosity-temperature relationships were compared, which were based on 1) a WLF fit and 2) the UTRS subroutine, which involves constraining the relaxation times for viscosity and volume to be the same, (Refer to Equation 5.7 in Section 5.3.3). It was understood from the stress validation example of the sandwich seal, that the TRS behavior greatly affects the stress state inside glass during the annealing phase; hence, the effect of the same during molding simulations was explored in this sensitivity example. Viscoelastic material relaxation is used.



(a)



(b)

Figure 5.22. Stress birefringence (nm/cm) inside the steep meniscus lens shape after molding for different TRS assumptions (a) based on WLF fit of data from [2] (b) based on UTRS subroutine (the same relaxation times for viscosity and volume, Refer to Equation 5.7)

As seen from Figure 5.22, the stress birefringence distribution using the UTRS assumption has lower values over the results from Figure 5.19 and is therefore an improvement. Next, the sensitivity of cooling rates on stress birefringence will be explored.

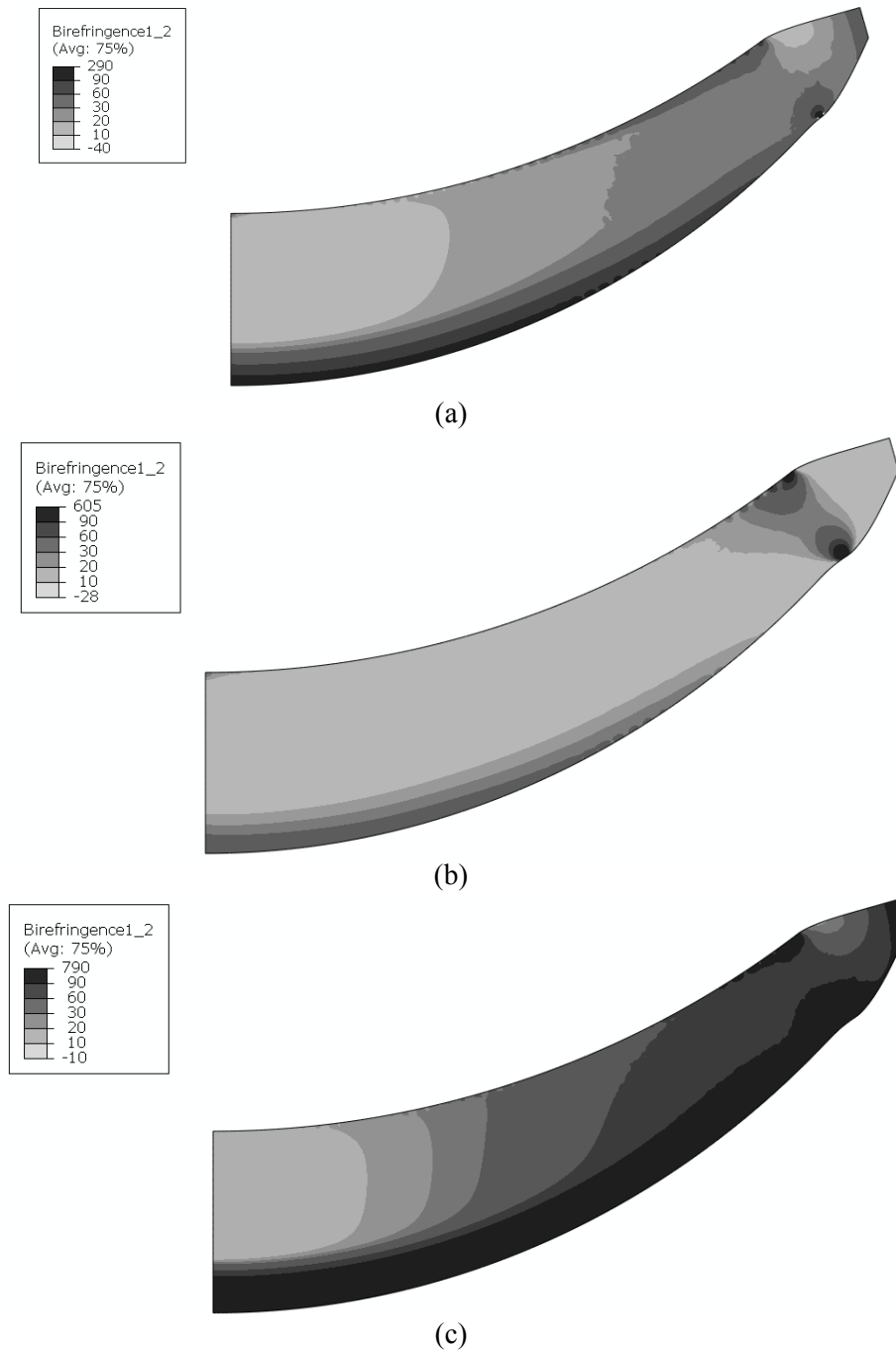


Figure 5.23. Stress birefringence (nm/cm) inside the steep meniscus lens shape after molding for different slow cooling rates during molding cycle (a) baseline case with $q_0 = 0.288^\circ\text{C/s}$ (b) with $q = 0.33 \times q_0 = 0.096^\circ\text{C/s}$ (c) with $q = 3 \times q_0 = 0.864^\circ\text{C/s}$

As seen from the Figure 5.23, the use of a slow cooling rate of 0.096°C/s makes an improvement in the stress birefringence distribution inside the lens, while, the higher cooling rate induces more residual stresses inside the lens. A similar trend in the results is expected for the Bi-convex lens. The stress birefringence distribution along the lens thickness is considered for the given sensitivity parameters in Figure 5.24. The plots presented in Figure 5.24 indicate the distribution of stresses at the central section and a section 5 mm away from axis of steep meniscus lens. The “Baseline” case in Figure 5.24 refers to the “Full VE” case in Figure 5.21. The given sensitivity cases reduce distribution of stress birefringence as compared to the “Baseline” case except for the slow cooling rate of $.864^{\circ}\text{C/s}$. The slow cooling rate of 0.096°C/s clearly reduces the stress birefringence near the top and bottom parts of the lens as expected.

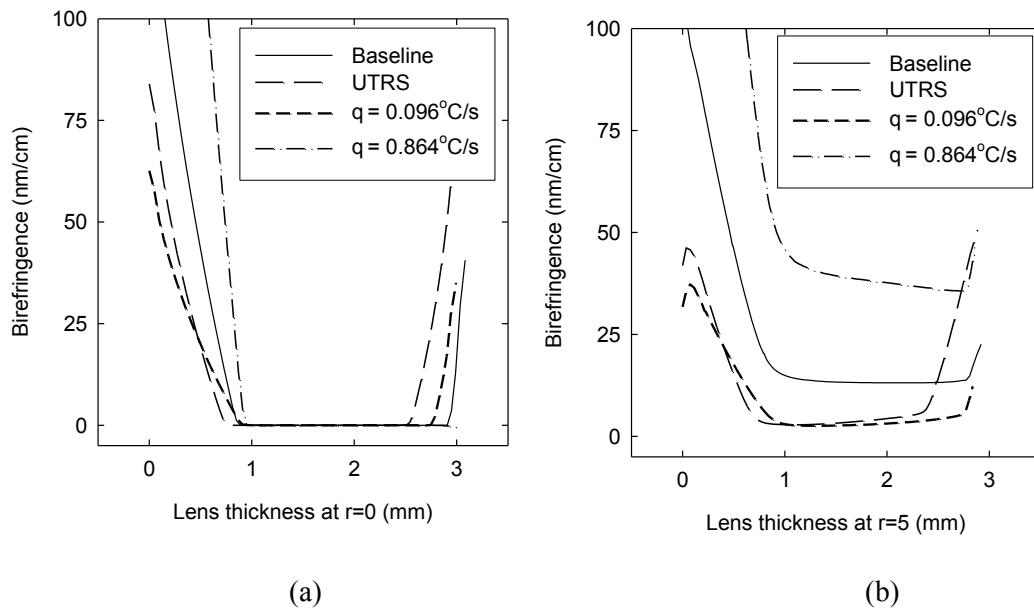


Figure 5.24. Stress birefringence (nm/cm) inside the steep meniscus lens shape after molding for TRS and slow cooling rate sensitivity study (a) At the central axis of the lens (b) at 5 mm away from the axis of lens.

The two sensitivity studies present an example of use of an improved material property definition and an optimal processing parameter (e.g. slow cooling rate) to make an improvement in the stress birefringence results of the molded lens.

5.5 Discussion

This Chapter strengthens the understanding of the role of stress relaxation characterization of optical glass in computational simulations of the lens molding process. Based on the lens molding issue of interest, the stress relaxation characterization of optical glass can be more or less important. It was pointed out in Chapter 1 that based on the literature [4] the stress relaxation parameters have an insignificant impact on the lens shape deviation. This Chapter further confirms that conclusion by testing other possible effects, but more importantly quantifies how residual stresses and stress birefringence inside the lens shape are strong functions of such a characterization.

This Chapter gives three validation examples that were used to give confidence to the current approach of calculating residual stresses. For the first well-known example in which the residual stresses vanish at the end of cooling stage, the Table 5.1 gives the order of error present in the finite element discretization method. This validation case also studies in detail the value of “ T_L ” at which glass behavior transitions from viscoelastic to elastic. The second and third examples of quenching of a glass slab and the cooling of a sandwich seal show that the level of uncertainty in parameter evaluation and/or implementation can lead to fictitiously correct results. These examples point out the need to evaluate the important parameters of both stress relaxation (for example $E(T)$ and TRS) and structural relaxation (time-temperature dependence of CTE) parameters.

The convergence study was presented in Table 5.2 validated the methodology used for stress state evaluation using the Finite Element Analysis approach. Based on the study, the coarsest mesh was found to be sufficient to provide sufficiently accurate results in lens molding of a steep meniscus lens.

For the final sets of results, residual stresses and stress birefringence were calculated for two lens types using three different levels of stress relaxation characterization presented in Section 5.2. The results showed that the choice of stress relaxation function greatly affects the stress state within lens during molding. Hopefully these results will motivate the experimentalist to more precisely characterize molding glasses. Such characterizations should enable computational mechanics to make reliable predictions and to aid in process design, as well as identify glass behaviors that could yield improved optical properties.

5.6. Conclusions

The following conclusions are made based on the current sensitivity study of two lens types.

- It is important to know the temperature dependence of the elastic modulus $E(T)$ of an optical glass as it can have a significant impact on the lens shape deviation for both types of lenses. In general, the lower the value of E , higher the residual stresses and the deviation. This conclusion is important for certain types of optical glasses including Chalcogenides, which have a low value of elastic modulus at temperatures above T_g [17].
- The change in reference temperature causes a non-negligible change in deviation of both types of lenses keeping other parameters the same except for the pressing time. The lower the T_R , the lower the press time and the deviation of a lens. Simulations

suggest that if T_R is 20°C lower than the actual value, the change in deviation is about a micron for the Bi-convex lens and about $2\ \mu\text{m}$ for the steep meniscus lens. These values are doubled if T_R is 20°C too high.

- The mechanism of convective heat transfer between the glass and mold at the end of the slow cooling stage affects the thermal history of the lens, which increases the deviation of the lens since the lens cools faster than without this mechanism.
- It is known that the lens shape deviation for both types of lenses is not sensitive to the viscoelastic stress relaxation function. Viscoelastic behavior of the optical glass during molding can be simplified by assuming the material has a viscous response in shear and an elastic response in bulk. However, this assumption will lead to an overestimation of residual stresses and birefringence inside the lens. For these cases it is important to more precisely characterize stress relaxation, which is a non-trivial task.

References

1. D. Joshi, P. Mosaddegh, J.D. Musgraves, K.C. Richardson, P.F. Joseph, "Thermo-Mechanical Characterization of Glass at High Temperature Using the Cylinder Compression Test: Part I – Viscoelasticity, Friction and PPV," *Journal of Rheology*, **57**(5), (2013), pp.1367-1389.
2. D. Joshi, P. Mosaddegh, J.D. Musgraves, K.C. Richardson, P.F. Joseph, "Thermo-Mechanical Characterization of Glass at High Temperature Using the Cylinder Compression Test: Part II – No-Slip Experiments, Viscoelastic Constants and Sensitivity," *Journal of Rheology*, **57**(5), (2013), pp.1391-1410.
3. B. Ananthasayanam, P F Joseph, D. Joshi, S. Gaylord, L. Petit, V Y Blouin, K C Richardson, D. Cler, M. Stairiker, M. Tardiff, "Final shape of Precision molded optics: Part I - Computational approach, material definitions and effect of lens shape," *Journal of Thermal stresses*, **35**, (2012) pp.550-578.
4. B. Ananthasayanam, P F Joseph, D. Joshi, S. Gaylord, L. Petit, V Y Blouin, K C Richardson, D. Cler, M. Stairiker, M. Tardiff, "Final shape of Precision molded optics: Part II - Validation and sensitivity to material properties and process parameters," *Journal of Thermal stresses*, **35**, (2012), pp.614-636.

5. Ananthasayanam, Balajee. Computational modeling of precision molding of aspheric glass optics. Diss. Clemson University, (2008).
6. A. Y. Yi, A. Jain, "Compression Molding of Aspherical Glass Lenses-A combined Experimental and Numerical Analysis," J. Am. Ceram. Soc., **88** (2005), pp. 579-586.
7. M. Sellier, C. Breitbach, H. Loch and N. Siedow, "An iterative algorithm for optimal mould design in high-precision compression moulding," Proc. IMechE Vol. **221** Part B: J. Engineering Manufacture, pp. 25-33.
8. F. Wang, Y. Chen, F. Klocke, G. Pongs and A. Yi, "Numerical Simulation Assisted Curve Compensation in Compression Molding of High Precision Aspherical glass Lenses," Journal of Manufacturing Science and Engineering, 131, Feb 2009, Issue 1, 011014 (6 pages).
9. Y-C Tsai, C Hung, J-C Hung, H-F Tseng, "Finite element prediction of the lens shape of moulded optical glass lenses," Proc. IMechE, Part B: Journal of Engineering Manufacture, **225**, (2011), pp. 224-234.
10. M. Arai, Y. Kato, and T. Kodera, "Characterization of the thermo-viscoelastic property of glass and numerical simulation of the press molding of glass lens," J of Therm. Stresses, **32**, (2009), pp. 1235-1255.
11. S. H. Chang, Y. M. Lee, T. S. Jung, J. J. Kang, S. K. Hong, G. H. Shin, Y. M. Heo, "Simulation of an aspheric glass lens forming behavior in progressive GMP process," AIP Conf. Proc. 908 (2007), pp.105-1060
12. J. Yan, T. Zhou, J. Masuda, T. Kuriyagawa, "Modeling high-temperature glass molding process by coupling heat transfer and viscous deformation analysis" Precision Engineering, **33**, (2009), pp. 150-159.
13. T. Zhou, J. Yan, J. Masuda, and T. Kuriyagawa, "Investigation on the viscoelasticity of optical glass in ultra precision lens molding process," J of Mat. Process Tech., **209**, (2009), pp. 4484-4489.
14. F. Klocke, F. Wang, Y. Wang, G. Liu, O. Dambon, A.Y. Yi, "Development of a flexible and reliable numerical simulation for precision glass molding of complex glass optics", 6th International Symposium on Advanced optical Manufacturing and Testing Technologies, Proc. Of SPIE, 8416,841603-1, (2013)
15. L. Duffrene, R. Gy, H. Burllet, and R. Piques, "Multiaxial linear viscoelastic behavior of soda-lime-silica glass based on a generalized Maxwell model," Soc. Rheol., **41**, (1997), pp. 1021-1038.
16. H. Loch, D. Krause, Mathematical simulation of glass technology, Springer, New York, 2002.
17. T. Rouxel, "Elastic properties and short-to medium-range order in glasses," Journal of American Ceramic Society, **90** [10] (2007) pp. 3019-3039.
18. Scherer, G., *Relaxation in glass and composites*, John Wiley and Sons, New York, 1986.
19. Scherer, G.W and Rekhson S. M., "Viscoelastic-Elastic Composites: II, Sandwich Seal", Journal of American Ceramic Society, **65** (8), (1982), pp. 399-406.
20. Carre, H., and L. Daudeville. "Numerical simulation of soda-lime silicate glass tempering," Le Journal de Physique IV 6.C1 (1996): C1-175.
21. H. Loch, D. Krause, *Mathematical simulation of glass technology*, Springer, 2002.

22. S. Gaylord, Thermal and structural properties of moldable glass types, Master's thesis, Clemson University, (2008).
23. M. Brown, "A review of research in numerical simulation for the glass pressing process," Proceedings of IMechE Part B, Journal of Engineering Manufacture, **221**, (2007), pp. 1377-1386.
24. Private communication with Material Science Engineering Research Team at Clemson University.
25. G. Dusserre, G. Bernhart, M. Schimidt and G. Dour, "Evaluation of viscous and elastic parameters of borosilicate glass above transition temperature using optical instrumented squeeze test," Journal of Non-Newtonian Fluid Mechanics, **166**, 21 (2011), pp. 1229-1238.
26. H. Aben, C. Guillemet. *Photoelasticity of glass*, Berlin: Springer-Verlag 1993.
27. Specification Sheet for L-BAL35 glass, OHARA, Japan. (www.ohara-inc.co.jp).
28. A. Y. Yi, B. Tao, F. Klocke, O. Dambon and F. Wang, "Residual stresses in glass after molding and its influence on optical properties," Procedia Engineering **19**, (2011), pp. 402-406.
29. S. M. Rekhson, A.V.Bulaeva and O. V. Mazurin, "Changes in the linear dimensions and viscosity of window glass during stabilization," Inorganic Materials, **7**, (1971), pp. 622-623.
30. Specification sheet, Glass Photonics Inc. (http://www.glassphotonics.com/pdfs/lam_master.pdf).
31. O.S. Narayanaswamy, "A Model of Structural relaxation in Glass," Journal of American Ceramic Society, **54**, 10, (1971), pp. 491-198.
32. T. F. Soules, R.F. Busbey, S.M. Rekhson, A. Markovsky and M. A. Burke, "Finite-Element calculation of stresses in glass parts undergoing viscous relaxation," Journal of American Ceramic Society, **70** (2), (1987), pp. 90-95.
33. R. Gardon, The "Tempering of Flat Glass by Forced Convection," Proceedings of International Congress on glass, 7th, paper no. 79, (1965), Institut National du Verre, Charleroi, Belgique.
34. O. S. Narayanaswamy and R. Gardon, "Calculation of Residual Stresses in Glass," Journal of American Ceramic Society, **52**, 10, (1969), pp. 554-558.
35. R. Gardon and O. S. Narayanaswamy, "Stress and Volume Relaxation in Annealing Flat Glass," Journal of American Ceramic Society, **53**, 7, (1970), pp. 380-385.

STUDY OF LENS CRACKING USING COMPUTATIONAL FRACTURE MECHANICS

6.1. Introduction

During the lens molding process a lens preform is subjected to a series of mechanical as well as thermal loadings and is susceptible to fracture. Issues include pre-existing flaws, the brittle nature of glass with the added complication of the fragility of certain glass types, badly designed process parameters, among others. This chapter utilizes the capability of stress prediction within the lens that was demonstrated in the Chapter 5 and identifies the critical stages during the lens molding operation during which the lens is susceptible to fracture. In the next paragraph a few basics of fracture mechanics will be reviewed and the assumptions for the analysis will be identified.

The cracking phenomena mainly includes two stages – a crack initiation stage and a crack propagation stage that needs a driving force that can be provided by the thermo-mechanical stresses present inside the lens during the pressing and cooling stages of lens molding. Under the energy criterion, the crack propagation in the material occurs when the energy available for crack growth exceeds the resistance of the material [1]. The resistance of the material to fracture (fracture toughness) is quantified by the Critical Stress Intensity Factor (SIF) commonly denoted by K_{IC} , or K_{IC} in the case of Mode I fracture. The stress intensity factor (K), which denotes the amplification of the singular stress field around the crack tip, can be used to quantify the crack driving force [1]. In general there are three modes of fracture, but the current study focuses on Mode I fracture, the details of which, including the definition of a stress intensity factor, are summarized later in this Chapter. A complication in predicting fracture in lens molding is the large temperature range experienced during cooling, which affects the value of K_{IC} . While optical

glass at room temperature is brittle in nature, at high temperature viscous flow adds ductility to the material behavior which makes the material tougher, i.e., fracture will occur at a higher value of applied K_I . Furthermore, the theory of Linear Elastic Fracture Mechanics (LEFM) which is based on the stress intensity factor may no longer be applicable at higher temperatures. The viscosity of the optical glass (L-BAL35 in our case) at the pressing temperature of $T_g + 60^\circ\text{C}$ is of order of $\text{Log}(\eta/\text{Pa}\cdot\text{s}) = 8.33$, which is most likely beyond the range of LEFM. However, as the glass cools the theory becomes more valid and the stress levels rise due to the rapid increase in the viscosity. The study of the temperature dependence of the stress intensity factor during the brittle-to-ductile transition (BDT) of standard window glass was performed by Rouxel et. al [2]. They developed a simple model to quantify BDT in glass using crack tip stress and stress intensity factor as key parameters. Their model predicted the observed increase in the apparent fracture toughness in glass near the glass transition temperature. Therefore, it will be assumed that as the glass in the current study cools below T_g , and the method of LEFM can be applied using a constant value of K_{IC} .

Fracture during lens molding, has been considered, although only by a few researchers. Cha et.al [3] reported lens breakage of Chalcogenide glass (IG4, $T_g = 225^\circ\text{C}$, $\text{CTE} = 20.4 \times 10^{-6}/\text{K}$) due to thermo-mechanical stresses caused by the low thermal conductivity and high thermal expansion coefficient of the glass. They also reported adhesion of glass to the Tungsten Carbide (WC) mold. The study reports the lens breaking and adhesion during molding operations when the glass sample was subjected to different initial heating and molding temperatures. They concluded that the IG4 glass should not be heated above T_g (225°C) in the initial heating stage and must be heated above T_s (310°C) before pressing to avoid breaking of the glass. They also reported some occurrences of adhesion of glass to mold when they implemented the above

strategy. Chien et.al [4] studied the effect of Al_2O_3 coatings on three glass types having high refractive index and T_g (530-547°C). They reported cracking at the edge of an uncoated lens at a temperature below 610°C and sticking occurred when the molding temperature was increased to 625°C on a Pt-Ir coated WC/Co mold. The problem of sticking was resolved using coating of Al_2O_3 on the glass preforms but it required a slightly higher molding temperature. Authors [5-8] have also reported fracture due to the thermal expansion behavior of different glass types in the application of lens molding.

This literature survey suggests that cracking of lenses during molding is an important issue that needs attention and that currently researchers are using ad-hoc techniques to circumvent the problem. The author of this study is unaware of a single research paper in the open literature that models the thermo-mechanical cracking of a precision molded optics.

In this chapter, a problem of cracking of lens preform during thermo-mechanical processing is addressed via computational simulations. The study assesses the magnitude of crack tip opening displacement (CTOD) when a small penny shaped crack is modeled within the lens that is subjected to lens molding cycle. The material presented below involves a brief background for the theory of fracture mechanics and its FE implementation. Following this introduction, a 2D and a 3D crack geometry are used as examples to validate the calculation of the fracture parameters for both far-field loading and thermo-mechanical loading. The examples include stress intensity factor evaluation based on the J-integral technique as well as the crack tip opening displacement and stresses near the crack tip. The analysis methodology adopted to model a crack in lens molding simulations using ABAQUS will be presented. The two scenarios of a circumferential and a radial crack that are considered for crack modeling inside a lens subjected to a molding cycle are also described. At the end, the results of crack tip opening displacement

(CTOD) calculations for the above two scenarios will be presented for two material models and cooling rates.

6.2. Stress Analysis of Cracks and Stress Intensity Factor Calculations

The stress analysis of a cracked body subjected to external forces involves seeking a closed form expression or computational solution that quantifies the stress field near the crack tip. The early analyses involved closed form solutions to the problems involving crack tip stress distribution with approaches by Williams [9] and Westergaard [10]. Williams analyzed the local crack tip stress field asymptotically and showed that for linear elastic behavior the far field boundary conditions enter into the asymptotic solution only in terms of constants, the most important of which is the stress intensity factor that multiplies the dominant one over square root of r leading term in the asymptotic series.. Williams actually considered the stresses at the corner of the plate with various included angles and boundary conditions; a crack is special case where the included angle of the plate corner is 2π and surfaces are traction free [1]. Westergaard, on the other hand showed that a limited class of problems can be solved in closed form using a complex stress function.

To illustrate the asymptotic solution obtained by Williams [1], in terms of the polar coordinate system with the origin at the crack tip as shown in Figure 6.1, the so-called Mode I asymptotic stress field in a homogeneous linear elastic body is given by,

$$\sigma_{ij}(r, \theta) = \frac{K_I}{\sqrt{2\pi r}} f_{ij}(\theta) + T f_{ij}^0(\theta) + O(\sqrt{r}), \quad (6.1)$$

where σ_{ij} is the stress tensor, r and θ are as defined in Figure 6.1, K_I is the Mode I stress intensity factor, $f_{ij}(\theta)$ is the dimensionless function of θ which is independent of the loading as long as it is symmetric [1], the quantity, T , is the T-stress which is a constant stress parallel to the crack and the remaining terms of order square root of r and higher are the higher order terms once again independent of the details of the far field loading except for constants.

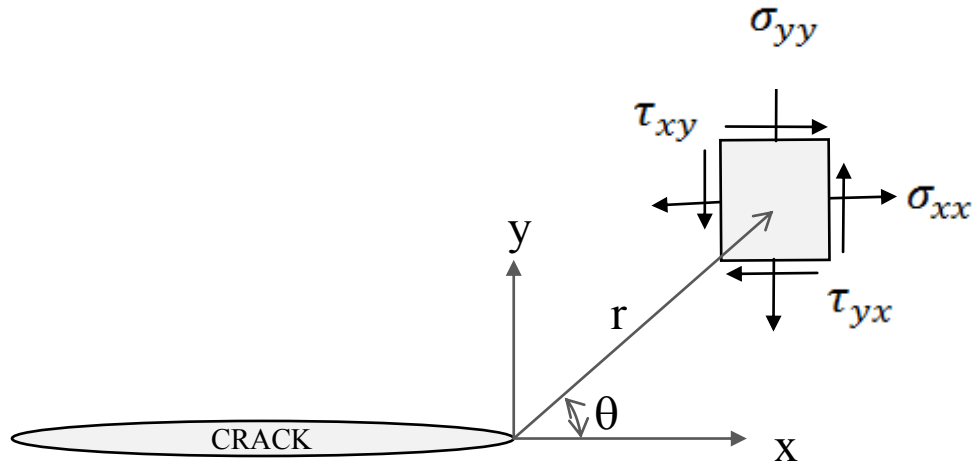


Figure 6.1. Representation of stress field around the crack tip. Crack tip also acts as an origin of cylindrical coordinate system used to define the stresses and displacements.

The stress intensity for the opening mode I when subjected to remote tensile stresses in direction normal to the crack can be written in terms of rectangular coordinates as follows:

$$\sigma_{xx} = \frac{K_I}{\sqrt{2\pi r}} \cos\left(\frac{\theta}{2}\right) \left[1 - \sin\left(\frac{\theta}{2}\right) \sin\left(\frac{3\theta}{2}\right) \right] + O(\sqrt{r}) + T \quad (6.2)$$

$$\sigma_{yy} = \frac{K_I}{\sqrt{2\pi r}} \cos\left(\frac{\theta}{2}\right) \left[1 + \sin\left(\frac{\theta}{2}\right) \sin\left(\frac{3\theta}{2}\right) \right] + O(\sqrt{r}) \quad (6.3)$$

$$\tau_{xy} = \frac{K_I}{\sqrt{2\pi r}} \cos\left(\frac{\theta}{2}\right) \sin\left(\frac{\theta}{2}\right) \cos\left(\frac{3\theta}{2}\right) + O(\sqrt{r}) \quad (6.4)$$

Clearly as the radial distance r approaches zero, the leading terms of Equations 6.1-6.4 approach infinity, while the other terms remain finite or approach zero [1]. As shown by Equations 6.1-6.4 the stresses near the crack tip vary with $1/\sqrt{r}$ regardless of the configuration of the cracked body for symmetric loading. This is also true for an arbitrary configuration which must also include Modes II and III. Similarly, the displacement near the crack tip varies proportional to \sqrt{r} for all loadings. The stress intensity factor defines the “strength” of the singularity at the crack tip and the stresses near the crack tip region increase proportional to the K .

Calculations of the stress intensity factor can be made by using different approaches, from purely analytical for relatively simple configurations to purely computational. The values of stress intensity factors for various geometric and loading configurations are summarized in classical handbooks of stress intensity factors such as Tada et al. [12]. The focus of this study is the computational evaluation of the stress intensity factor for lens molding using the Finite Element (FE) method. In the next sub-section, it will be shown by an example, how FEM can be used efficiently to capture crack tip singularity and compute the stress intensity factors.

6.3.1. Capturing the crack tip singularity using FEM

It was shown in the previous section that the singular stress field exists near the crack tip when an elastic body having a sharp crack is subjected to loading. For most of the standard geometric configurations, the solution of singular stress field in terms of the geometric parameters is available in several book and handbooks on the subject. The real world problems which involved more complex geometries, the extension of analytical approach to calculate stress intensity is very cumbersome. Fully computational solutions such as the finite element (FE) solution must be used for such problems, while the analytical methods provide accurate solutions with which to validate the computational models. In this section, it is briefly shown that how FE method can be implemented to solve for the singular field near the crack tip.

Singular elements were introduced [13] much earlier to circumvent the problem of singularity of stress field in fracture mechanics calculations. These types of elements for the case of a quadratic element solved the inherent problem of stresses being a linear function of the geometric coordinates in the typical finite element mesh. A one-dimensional quadratic elemental shape function with a mid-side node would yield a linear relationship between stress/strain and geometric coordinate (say x). It was shown that if the mid-nodes were moved to $1/4$ distance instead of half, then mathematically, the displacement, $u \propto \sqrt{x}$ and stress and strains $\propto 1/\sqrt{x}$. Thus, the “singular” or “quarter-point” elements are useful in capturing the singular field around the crack tip if these elements are correctly placed around the crack tip. In a 2-D analysis, the isoparametric 8-node quadrilateral elements are employed for crack analysis with one edge of the element collapsed and nodes on the adjacent edges moved to the $1/4$ position towards the collapsed node. Usually a ring of such elements known as a focused mesh is created around the crack tip to capture the singularity [14]. Figure 6.2 shows the typical singular quadrilateral element which has

an element edge collapsed. Depending upon the singularity requirement, the common nodes at the corner can be chosen to be either dependent or independent to move with one another.

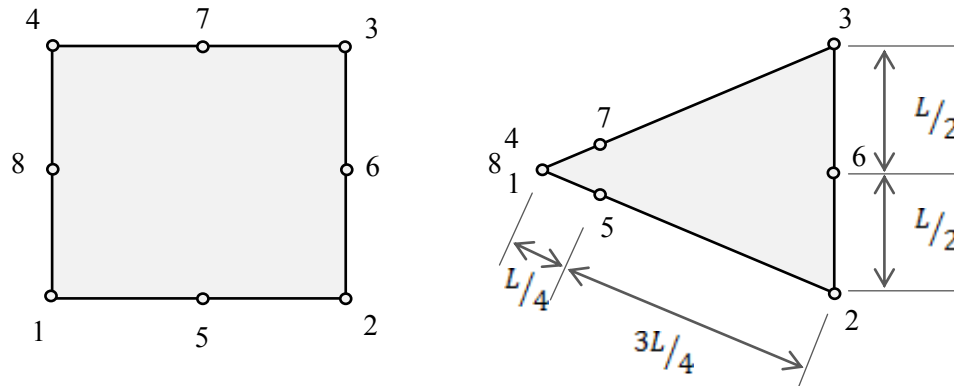


Figure 6.2. Regular Second order quadrilateral element (left), singular element with mid-side nodes 5 and 7 moved to a quarter length away from collapsed nodes 1, 4, 8 which share the same geometric coordinates (right).

The stress intensity factor can be determined by plotting the product of the σ_{yy} component of the nodal stresses along the line of the crack ($\theta = 0$) and $\sqrt{2\pi r}$ as function of ' r ' and extrapolating the data to $r = 0$ to determine the stress intensity factor. Similar techniques can be used to predict the stress intensity based on the nodal displacements which are more accurate than the stress field. This technique, known as stress-displacement matching [1], is a standard method of estimating the stress intensity factor. Other methods include computing the energy release rate (G) within the body and relating it to stress intensity (K). More recently developed techniques such as virtual crack extension method and energy domain integral method [1] are widely used today in commercial software due to their accuracy and efficiency over traditional methods.

Besides the stress intensity factor (K), J -integral is widely used in the case of the non-linear elastic fracture mechanics as the fracture parameter [1]. The J -integral, which is a path independent line integral, is usually considered as a non-linear energy release rate parameter for a body containing crack. It is also related to energy release rate parameter G in case of linearly elastic material and a unique relationship exists between J and K in this case. The J -integral can be calculated in Abaqus by using domain integral procedure [14]. Another important fracture parameter that has a unique relationship with J is Crack Tip Opening Displacement, commonly known as CTOD. Two common definitions of CTOD include the displacement at the original crack tip and the amount of opening displacement of the crack tip at the intersection of a 90 degree vertex with crack flank [1]. There also exists a unique relationship between the CTOD and J -integral for non-linear elastic materials making CTOD an important parameter for crack tip characterization. Most importantly, the use of the CTOD does not require a certain material behavior, as does J and K . Furthermore, CTOD can be estimated based on the FEA output by measuring the displacements at nodal locations near the crack tip mesh. Another important fracture parameter for materials involving creep loading is the C -integral. In this case the K and J parameters are not sufficient to characterize the creep crack growth [1]. The C_t -integral definition is related to that of J -integral by replacing strain field with strain rate and displacement with displacement rate over a contour. Due to introduction of rate dependence, the C_t -integral can characterize the crack tip conditions for viscous materials. Abaqus provides a way to calculate the C_t -integral within only the *VISCO analysis procedure, which is mainly used for quasi-static creep problems [14]. Although this procedure allows the application of an initial temperature as a prescribed initial condition over the domain, it does not allow the application of transient temperature boundary conditions and was found to be unsuitable for the lens molding simulations.

6.3. Stress Intensity Factor Validation Studies

Two validation studies for the determination of stress intensity factors for a crack in an infinite elastic medium subjected to remote tensile loading are considered in this section. The two geometries considered are a 2D infinite plane containing a central crack of length '2a' (plane stress problem) and an infinite 3D domain containing a penny shaped crack of radius 'a'. For both geometries a remote tensile stress was applied along the boundary normal to crack plane. The extrapolation method was applied to the 2-D geometry and the J-integral as evaluated by using finite element program Abaqus was calculated for both cases for a series of different contours. Benefits of the study include understanding the influence of the meshing near the crack tip region on the stress field and the identification of the influence radii near the crack tip for which the LEFM solution can be assumed to be valid, given the asymptotic nature of the stress fields given by Equations 6.1-6.4. This method relied on the idea that the full field solution at a given radial distance close to the crack tip can be approximated by an asymptotic series in terms of K and a suitable number of higher order terms. For details on using singular integral equations to determine higher order coefficients in order to study the dominance of the $1/\sqrt{r}$ term over other higher order terms in the neighborhood of the crack tip, the reader is referred to [17] and [18].

6.3.1. A through thickness crack in 2-D Infinite plane subjected to remote tension

The 2D plane stress problem of a crack of length '2a' in a very large plate subjected to remote tensile loading was considered. The finite element model in ABAQUS consisted of a crack of size $2a = 100$ microns in a rectangular plate of size 100 mm x 100 mm to represent an "infinite" plate. Only half of the plate was modeled and two vertical edges of the plate were subjected to tensile stress of 1MPa. The crack was aligned along the vertical direction (y-axis)

and the stress component σ_{xx} in front of the crack tip was evaluated for different meshes. For meshing around the crack tip, degenerated 4-node quadrilateral elements with collapsed edges (triangular shaped as shown in Figure 6.2) were used. The crack tip geometric region was divided into two regions: a circular region that has a very small radius ($a/20$) containing only an array of triangular shaped elements and an annular region that has an inner radius ($a/20$) and an outer radius (a) with the second order 8-node quadrilateral elements. The small circular region ($r = a/20$) near the crack tip was meshed with an array of “singular” quarter-point elements, while the annular region was meshed with regular 2nd order quadratic elements. The finite element mesh seeding along the radial direction in the annular region was changed from four and sixteen elements and into 36 elements along the circumferential direction. Comparison with the closed form solution and the numerical procedure to calculate the stress intensity factor from the stresses are explained below.

The full field solution for this crack problem along the line of the crack is given by

$$\sigma_{xx}(x=0, y) = \frac{\sigma_0 |y|}{\sqrt{y^2 - a^2}}, \quad (6.5)$$

or in terms of a polar coordinate system centered at the $y = +a$ crack tip,

$$\sigma_{xx}(r, \theta = 0) = \frac{\sigma_0 (r + a)}{\sqrt{r(r + 2a)}}. \quad (6.6)$$

Expanding Eqn. (6.6) about the point $r = 0$ gives

$$\sigma_{xx}(r, \theta = 0) = \sigma_0 \left\{ \frac{(r+a)}{\sqrt{r(r+2a)}} \right\} = \frac{\sigma_0 \sqrt{a}}{\sqrt{2r}} \left\{ 1 + \frac{3r}{4a} - \frac{5}{32} \left(\frac{r}{a} \right)^2 + O \left(\frac{r}{a} \right)^3 \right\}, \quad (6.7)$$

Using the definition of a stress intensity factor and (6.7) gives the well-known result,

$$K_I = \lim_{r \rightarrow 0^+} \sqrt{2\pi r} \sigma_{xx}(r, \theta = 0) = \sigma_0 \sqrt{\pi a}. \quad (6.8)$$

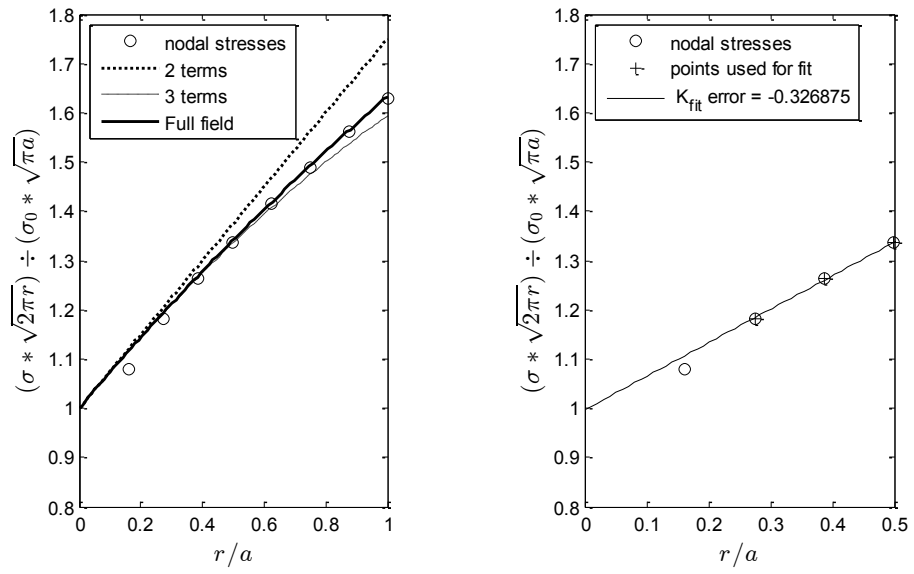
The approach used to obtain the stress intensity factor from the numerical data makes use of expressing Eqn. (6.7) as follows:

$$\frac{\sqrt{2\pi r}}{\sigma_0 \sqrt{\pi a}} \sigma_{xx}(r, \theta = 0) = 1 + \frac{3r}{4a} - \frac{5}{32} \left(\frac{r}{a} \right)^2 + O \left(\frac{r}{a} \right)^3. \quad (6.9)$$

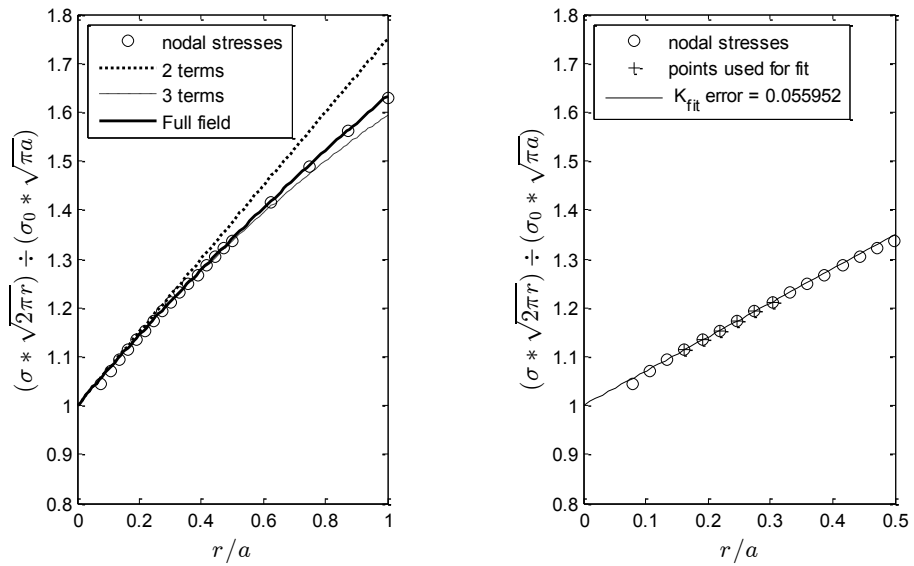
In order to compare the numerical solution with the analytical solutions, the following procedure was used to plot the numerical data:

- a) the stress field near the crack tip based on the FEA output was normalized by multiplying by $(\sqrt{2\pi r}/K_I)$
- b) the normalized stress output was then plotted as a function of normalized radial coordinate (r/a)

The normalized stresses using this procedure were plotted as a function of the normalized radial distance as shown in Figure 6.3. The analytical asymptotic solutions from (6.6) and the exact solution from Eqn. 6.9 are included in the same figure.



(a)



(b)

Figure 6.3 Comparison of the nodal stresses along the radial direction with the analytical solution for two different meshes. K estimates based on the nodal stresses for the data selected in the given range, are shown in the right. The error value in the legend indicates the percentage error in value of estimate of K with respect to the normalized value (unity). (a) 1x4x4 elements (b) 1x4x16 elements.

The comparisons in Figure 6.3 show that the numerical data matches the exact solution quite well for a fine mesh ($r/a > 0.2$), while, only for about $r/a > 0.4$ for the coarse mesh. As expected, due to problems of finite element convergence near the crack tip, there is error for small r/a . The results also show that a three-term asymptotic solution ($1 + 3/4(r/a) - 5/32(r/a)^2$) is a good approximation of the exact solution for about $r/a < 0.5$, while the two term solution ($1 + 3/4(r/a)$) is good for about $r/a < 0.25$. On the right side of Figure 6.3 the stress data was fit with a straight line. Ideally the constant term, which is representative of the stress intensity factor, would equal 1.0 and the slope would be 0.75. In making these fits it was determined that the best range of data to use was $0.15 \leq (r/a) \leq 0.5$ to make predictions of the stress intensity factor close to the actual value. Based on these fits the stress intensity factor was found to be accurate to within about 0.3%. The slope calculated was 0.68, which has a larger error. The error in value of the stress intensity factor was reduced to about 0.05% and slope to 0.7, for a dense mesh (16 elements along the contour).

Although, the above technique provided the stress intensity factor to within satisfactory limits, the methodology is not as straightforward for 3D problems with a complex stress state. Hence, the stress intensity factor output of Abaqus (K_A) using the J-integral was assessed for accuracy of the finite element software and the comparison with the analytical solution (K_0) is shown in the Figure 6.4.

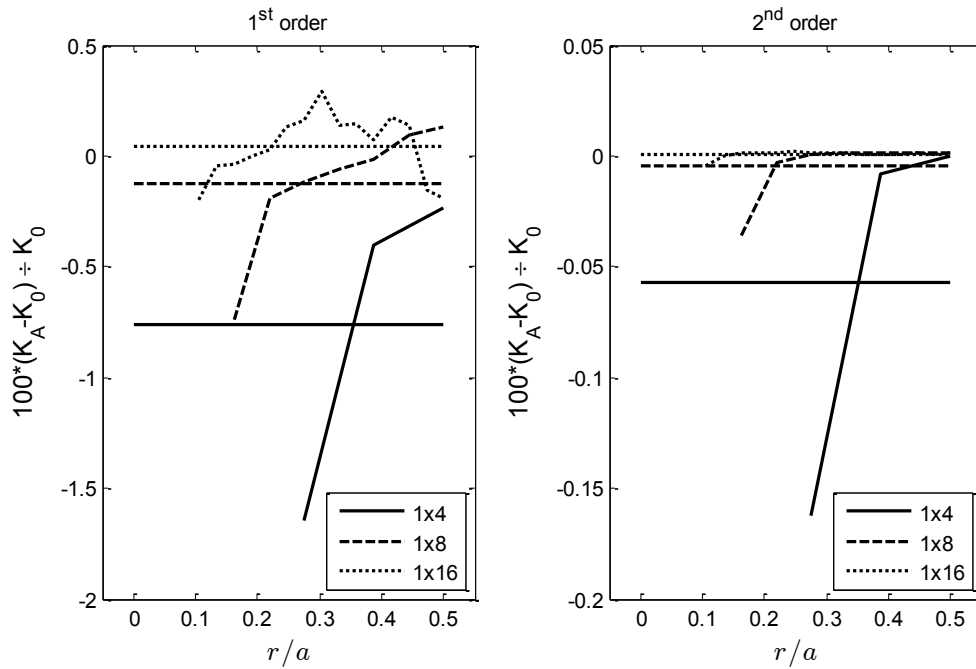


Figure 6.4. The relative error in calculation of stress intensity factor from Abaqus (K_A) and analytical solution (K_0). (Left) first order elements and (right) second order elements. Horizontal lines correspond to the mean value of the respective data points

The problem was solved with both first and second order elements and it is seen from the Figure 6.4 that second order elements were found to be within about 0.2%. While the second order elements are computationally expensive, the first order elements with the sufficient mesh density provide the stress intensity estimation within about 1%, which is determined to have sufficient accuracy.

6.3.2 Penny shaped crack in 3D infinite domain subjected to remote tension

In this subsection, the 3D version of the previous problem is presented. The crack geometry is assumed to be penny (circular) shaped and is embedded in an infinite 3D domain and subjected to a remote tension. The radius of the crack was taken to be 50 microns with the dimensions of the computational domain as 200 mm x 200 mm x 200 mm. Taking advantage of

symmetry, only half of the domain was modeled in Abaqus and two horizontal remote surfaces were subjected to a tensile stress of 1 MPa. The material property was assumed to be elastic with an input of E and ν . The crack front of the 3D crack takes a shape of a line or a curve (circle in this case). As opposed to a circular region around the crack tip in the 2D case, a half torus shaped region was created and meshed around the crack front. The details of the geometry, loading and a section of the mesh are shown in Figure 6.5.

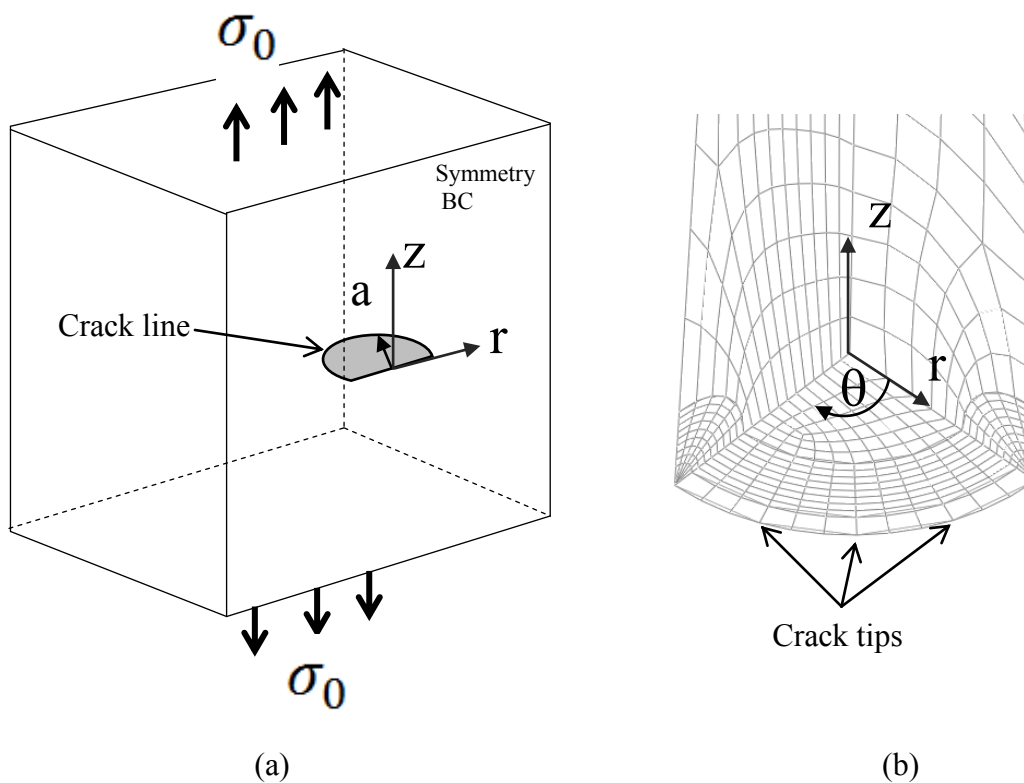


Figure 6.5 (a) Schematic of penny shaped crack subjected to remote tensile stresses. (b) Quarter-section of an actual finite element mesh near crack tip.

Abaqus allows calculation of the stress intensity factor along the crack front by computing the contour integrals around the crack tip region. Two different meshes were studied having a coarse and dense mesh around the crack-tip region. The stress intensity factor as

evaluated from Abaqus near three selected crack tip locations was compared with the analytical solution [19] as shown in the Figure 6.6.

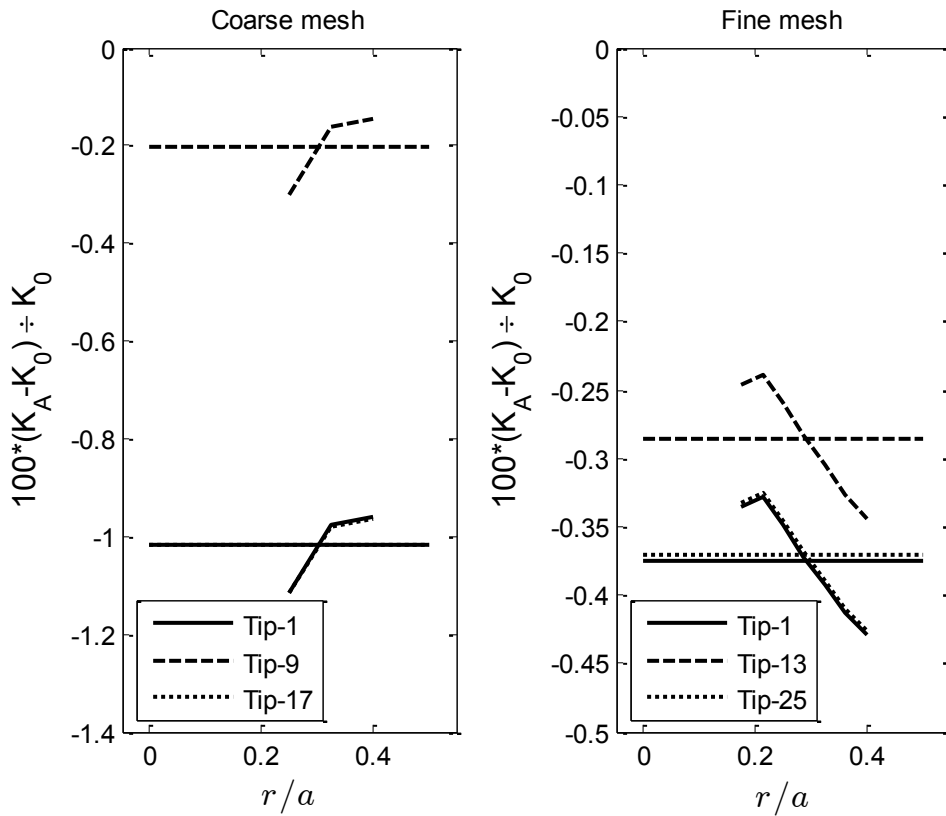


Figure 6.6. The relative error in calculation of stress intensity factor from Abaqus (K_A) and analytical solution (K_0). (Left) coarse mesh and (right) fine mesh. Horizontal lines indicate the mean value of the respective data points.

The stress intensity factor (K) was evaluated at the three crack tip locations corresponding to the directional vectors $[1,0,0]$, $[0,\pi/2,0]$ and $[-1,\pi,0]$ with respect to the r - θ - z coordinate system located at the center of the circular crack. As seen from the Figure 6.6, the stress intensity factor for the fine mesh is within the 0.5% of the value obtained by analytical results.

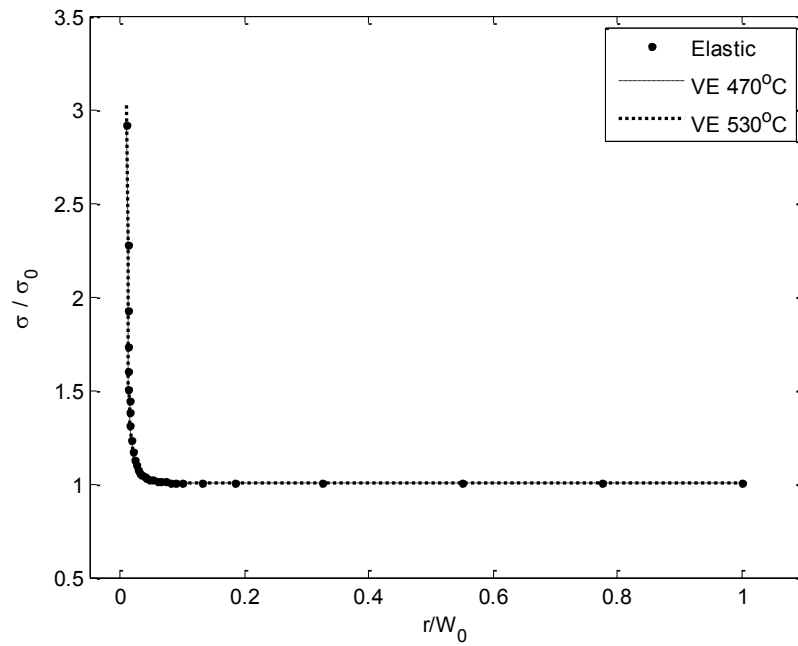
6.4. Computational Assessment of Stresses Near the Crack in a Viscoelastic Material

The material behavior in the examples given in the previous section was linear elastic and hence the verification of the FEA results with the analytical solution of stress field was possible. This section describes computational examples of the 2D and 3D geometries with a crack having a viscoelastic material behavior which is commonly observed in glass near the glass transition temperature (T_g). The first example assesses the transient stresses near the crack tip region in the viscoelastic solid transitioning from an elastic state at low temperatures to a viscous state at high enough temperatures, while the second example shows the effect of transient thermal loading on different material behavior assumptions. The key point in this study is to evaluate the effect of transitioning thermo-viscoelastic material behavior near the crack tip using the normal stress in from of the crack front and the CTOD as fracture parameters.

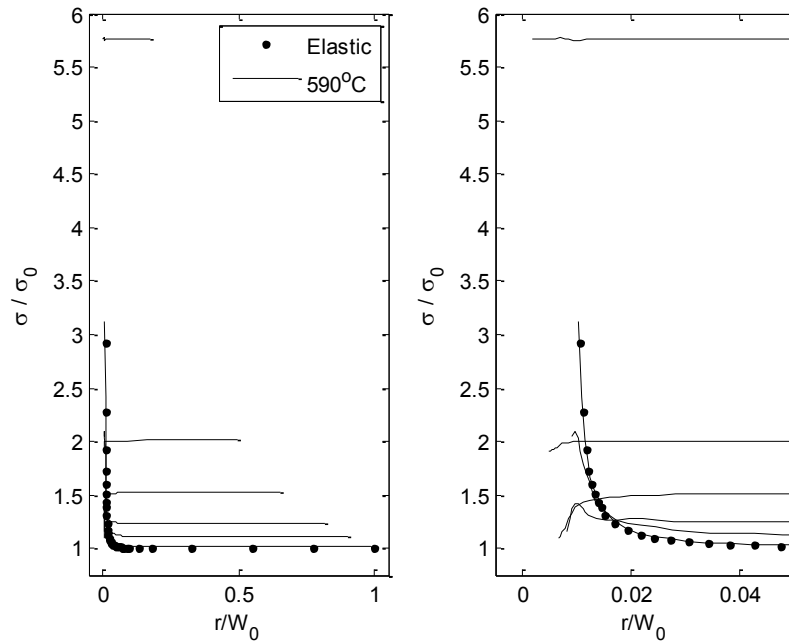
6.4.1. 2D plate subjected to steady state thermal and tensile loading

In this numerical example, a 2D plate having a viscoelastic material behavior is subjected to remote tension and is held at a constant temperature for a long enough period of time. This example enables the observation of the singular stress field near the crack tip as a function of time for different cases of temperatures. The initial temperature is varied to make the material behavior change from nearly elastic ($T_g-50^\circ\text{C}$) to viscoelastic ($T_g+50^\circ\text{C}$). The viscoelastic material constants described in Chapter 4 were used to obtain results and were compared with those obtained from the purely elastic material assumption. A small seam crack ($2a= 100$ microns) was modeled in the 10 mm x 10 mm viscoelastic domain subjected to 1MPa stress in the direction normal to the crack plane. Based on prior knowledge, a suitable mesh size was chosen along with

the linear quadrilateral elements having displacement and temperature degrees of freedom. The initial temperature was varied using values of 470, 530 and 590°C and stresses and displacements near the crack tip region were monitored. The normalized stresses are plotted near the crack tip region spanning from the crack towards the normal edge of the plate having an un-deformed width of $2W_0$.



(a)



(b)

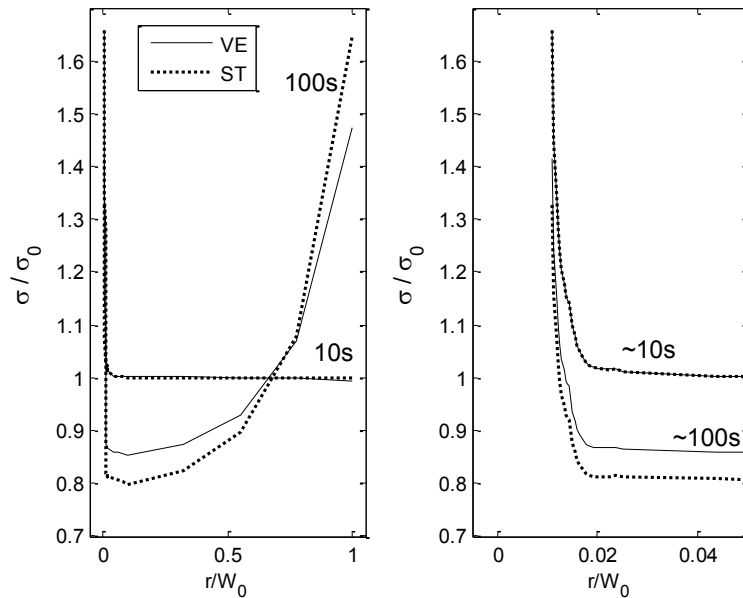
Figure 6.7. (a) Normalized stresses ahead of the crack tip at given temperature for three different cases and (b) 590°C case at different time/deformation levels (close-up view on the right). Deformation level can be inferred from the horizontal scale. For example, top curve has deformed to 25% of its original width.

The results in the Figure 6.7a show that there is a very small difference between the stress field for elastic and viscoelastic material assumption at 470°C and 530°C. The difference, however, becomes significant at 590°C, as seen from Figure 6.7b. The key point in Figure 6.7b is that the width of the plate decreases as very large viscous deformations progress. For example, for the curve coinciding with the elastic solution – time is close to 10s, the deformed width is close to the original width since the factor r/W_0 is close to 1. However, as time/deformation progresses, the width of the plate slowly decreases. For example, for a curve corresponding to a normalized stress of 2, the width of the plate has reduced to about 50% of its original value.

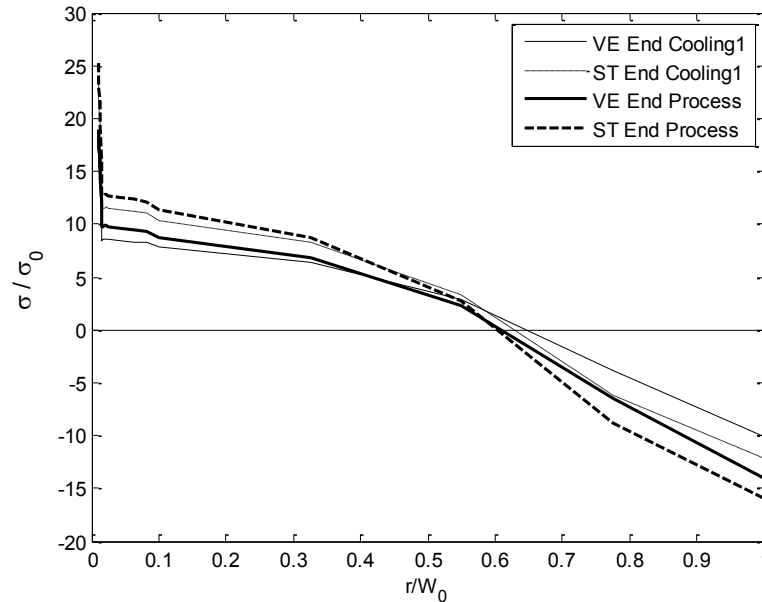
These plots reveal the relative significance of the temperature and time when a crack in a viscous material is considered.

6.4.2. 3D block subjected to tensile and transient thermal loading

In this numerical example, contrary to the previous example, a 3D geometry and transient thermal loading is considered while, the material behavior assumptions remain the same. A viscoelastic block is subjected to remote tension and transient thermal boundary conditions similar what would be experienced by an actual lens during processing. Loading consisted of tensile stress (1MPa) and initial temperature of 585°C and the block was allowed to cool to room temperature with a prescribed cooling rate. The crack tip stresses were evaluated for two viscoelastic material behavior models: full viscoelastic and viscous shear, in order to study the effect of viscous relaxation of the stress field near the crack tip.



(a)



(b)

Figure 6.8. (a) Normalized stress distribution ahead of the crack tip during slow cooling (Cooling1) stage at given times (close-up view on the right) (b) normalized stresses at end slow cooling and end of process stages for different material behaviors (VE - Viscoelastic, ST -Single Term in shear).

The Figure 6.8 shows the effect of material model on the stresses when a crack is subjected to thermo-mechanical loading. Results in Figure 6.8a indicate that material behavior has little influence during first 10s of loading and slow cooling stage, while, for the rest of the cooling time, the stresses resulting from a Single Term assumption were higher in magnitude than the full viscoelastic material assumption. The stress state inside the glass block at the end of the process in Figure 6.8b is similar to that of a tempered glass block, which has tensile stress distribution at the center and compressive stresses at the outer surface similar to Figure 5.7 of Chapter 5. Next, the crack tip opening displacement for two material models is computed and plotted as function of normalized cooling time.

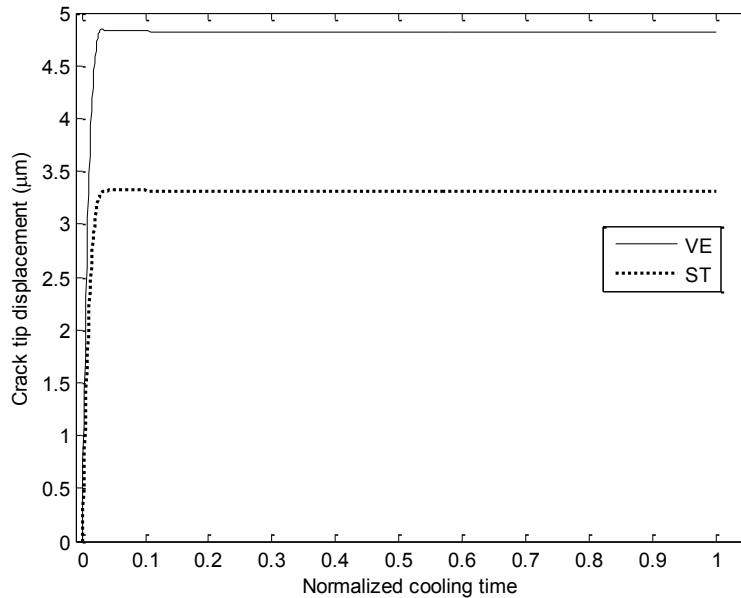


Figure 6.9. Crack tip opening displacement for different material models

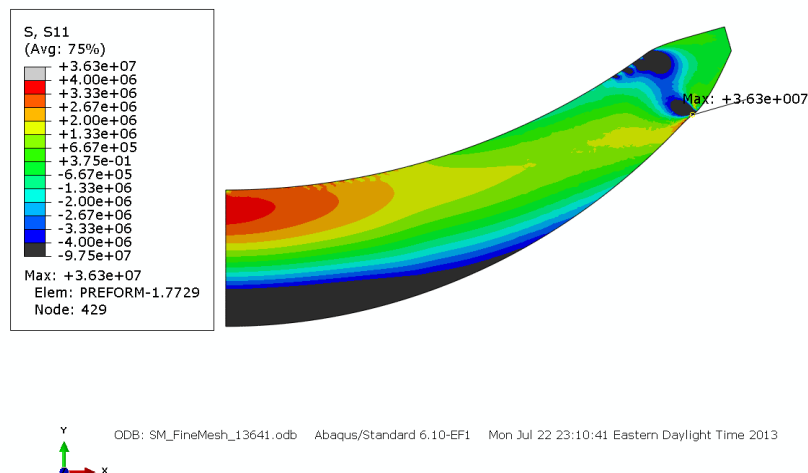
The results in Figure 6.9 indicate the viscoelastic material model has higher crack tip opening displacement than the Single Term viscous material assumption. This indicates the single term viscous assumption gives conservative results when the fracture parameter is considered which is counter intuitive as the stress results with the same assumption were found to be non-conservative.

6.5. Important Steps in Modeling Crack inside the Glass Preform Lens

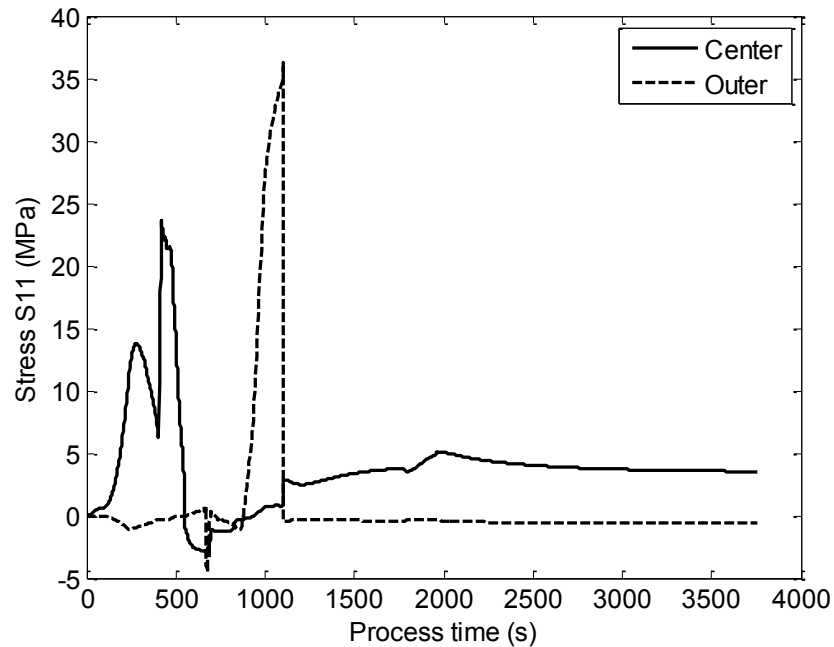
Based on the previous research experience and limited available evidence, the failure mode of the lens during molding was predominantly in the circumferential or radial direction. A circumferentially oriented crack would need stress dominant in the radial direction for advancement. Similarly, a crack whose orientation is along the radial direction would advance if there was a significant hoop stress. Hence, it was decided to model a crack in the circumferential

and radial directions inside the lens geometry and CTOD as the lens cools to room temperature from the molding temperature. The 2D axisymmetric analysis is not suitable in such a case as any crack modeled in the $r - \theta$ plane would mean the presence of a crack for the full 360° which may not be the realistic case. A full 3D model of a lens-mold assembly can be used in such a case, but for the reasons of computational efficiency, sectors consisting of 2.5 and 6.25 degrees of the 3D geometry were exploited by making use of symmetry as discussed in a later section. Separate 3D sector models for radial and circumferential crack geometry were chosen as appropriate for the analysis of the lens fracture phenomenon. In the next sub-sections, the important steps involved in building the 3D model for crack inside the lens are discussed.

6.5.1 Determination of the location of the crack geometry – based on the stress analysis performed on the 2D axisymmetric models of Bi-convex and Steep meniscus lenses, the location of the crack was determined to be the geometric location within the lens that experiences the highest magnitude of radial and circumferential stresses at the end of slow cooling stage.



(a)



(b)

Figure 6.10. (a) The location of maximum radial stresses (S_{11}) inside the lens at end of slow cooling (one half of lens shown) (b) Comparison of S_{11} at two locations: at the center of lens (solid) and near outer radius of lens (dashed)

The approximate location of highest stresses was found to be near the outer edge of the Steep meniscus lens at the end of the first cooling stage as shown in Figure 6.10a, while the stresses at center and outer periphery location of lens are compared in Figure 6.10b. The stresses reach the peak just at the end of the slow cooling stage and fall sharply after the maintenance force is removed around 1100s. This location was traced back in the un-deformed geometry of the lens preform and was chosen for modeling a 3D crack of desired size and shape. During the slow cooling stage, the molded lens experiences highest temperature gradient as it cools through the glass transition temperature range ($T_g \pm 50^\circ\text{C}$) and believed to have more impact on development and propagation of the crack.

6.5.2 Determination of the size and shape of the crack – The size of the crack was decided based on the size of allowable bubbles and inclusions present inside the preform. Usually the optical glass is free of bubbles compared to other commercial glasses due to sophisticated production process involved [15]. Still, during the manufacturing of preform, a number of bubbles and inclusions can remain inside the preform due to imperfections in the process. The preforms for the lens molding process can be in the form of: 1) precision gobs – which are semi-finished preforms that have geometry very close to final geometry of the lens. This is very economical way of producing the preforms but the target shape is restricted to Bi-convex shape preforms only [16]. 2) Polished near net shape and polished disc preforms – manufactured using classing lens production techniques. 3) Polished ball preforms – mainly spherical in shape and suitable for small size lens application such as cell phone cameras. Most of these types of preforms have some percentage of bubbles and inclusions as the bubbles are result of non-perfect refining process [15]. The bubbles can not only be produced by the melting or casting process but also during the hot forming process of the preform. The Figure 6.11, shows the bubble fogs generated during reheat-pressing of SCHOTT N-BK7[®] glass preform which was eventually damaged. As the bubbles and inclusions are part of the manufacturing process, they are usually controlled by various standards.



Figure 6.11 Bubble fogs generated during reheat-Pressing of the N-BK7[®] preform that was damaged as result of crack. The length of pattern in above picture is smaller than 2 mm. This picture is obtained from [15].

Each standard requires a manufacturing process that allows certain number of bubbles with maximum allowable size specified. Based on the Table 2 from [15], the maximum allowable bubble diameter was chosen to be 100 microns (0.1 mm). Based on this information, it was decided to model a penny shaped crack of diameter of 100 microns inside the lens preform.

6.5.3 Computation of the 3D sector angle (θ) – this value was determined for each crack type (circumferential and radial) based on the information on the stress intensity factors for collinear and parallel crack configurations given in [12]. For a circumferential crack, the circumferential spacing between the cracks was idealized as spacing between a co-linear periodic arrays of cracks in an infinite plane [12]. The solution to this problem is based on Westergaard's stress function and the functional

relationship between the stress intensity factor (K), width (w) and half crack length (a) are is given below.

$$K_I(w) = \sigma \sqrt{w \cdot \tan\left(\frac{\pi a}{w}\right)} \quad (6.10)$$

Based on the above formula, when the spacing between cracks (w) is about twice the length of the crack ($2a$) the resulting stress intensity factor with adjacent crack ($K(w)$) is about 13% higher than K_0 , which is the value of stress intensity factor for a crack without adjacent cracks. Thus, spacing between cracks in the case of a co-linear arrangement of cracks, has a great effect on the stress intensity factor. It can be seen that for $w = 15a$, the percentage difference between values of K' and K_0 is about 0.7%. This means, practically for $w \geq 15a$ the two adjacent cracks do not “see” one another. Based on this value and the above stated location of the crack, a sector angle (θ) value of 5° was decided for creating a 3D sector model in a Steep Meniscus lens. Employing the symmetry of the model, the half sector angle of 2.5° sector was modeled with a half crack length along the circumferential direction. Similarly, spacing between the radial cracks was based on an analysis of finite length parallel cracks in an infinite plane [12]. In this case, the half sector angle of 6.25° was found to be sufficient to prevent the cracks from interfering with one another’s stress intensity field. A typical radial crack would be oriented along the radial line in Figure 6.12.

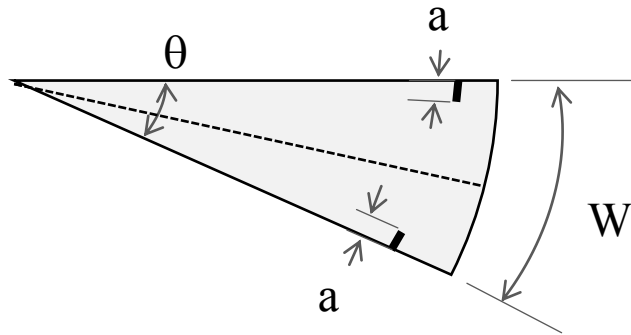


Figure 6.12 Representation of circumferential crack in a sector model.

Based on the calculated sector angles, the 3D model was built in Abaqus consisting of the Preform, Lower and Upper Mold assembly

6.5.4 3D Finite element modeling of circumferential and radial crack - It is understood that, the 3D crack modeling is complex as compared to 2D modeling due to the number of steps involved in cutting/dividing the 3D geometry to account for 3D Hexagonal meshing of the domain. A circumferential crack was modeled inside the glass preform at the pre-determined location by using a penny shaped crack of circular shape in a half sector angle of 2.5° utilizing the symmetry. This crack was oriented in a curved vertical plane normal to the radial coordinate of the lens. The crack was modeled slightly curved to simulate the actual curvature in the reality, thus allowing to expand in a circumferential direction. The circumferential crack would look like a single arc when seen from the top (along the Y-axis); while it would be seen as -a circle when seen from the center of the lens in a radially outward direction (along the X-axis). This curve acts as a “crack-line or crack front” and the surface acts as a “crack seam” for crack definition. A semi-torus shape is created around the

semi-circular curve (crack-line) that enables the creation of the wedge shaped hexahedral elements around it. The rest of the domain is divided such that it enables the mesh using the hexahedral (brick) shaped elements.

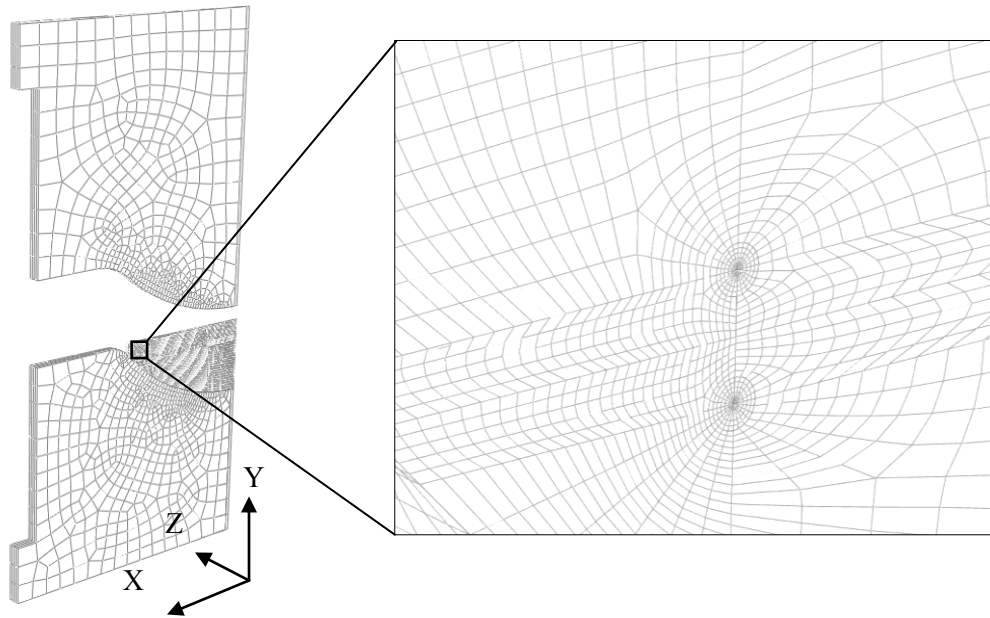


Figure 6.13 Global Mesh Model of 2.5° with detail of the mesh near the crack-line for the circumferential crack.

The Figure 6.13 shows a global mesh and details of the structure around the crack-line. As mentioned earlier, elements adjacent to the crack-line are mainly wedge shaped but have a collapsed face, sides and nodes. Figure 6.14 shows the detail of the finite element mesh around the crack line in a sectional view.

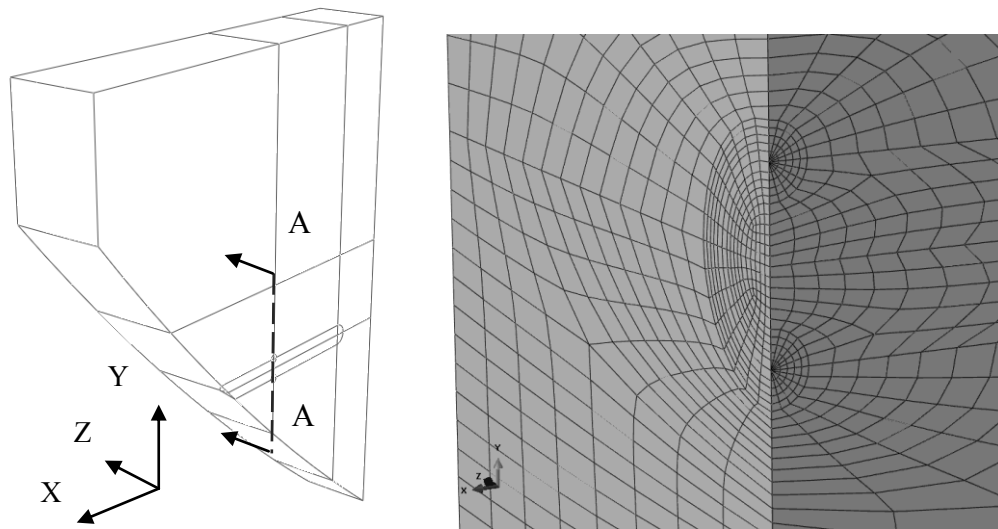


Figure 6.14. The partial geometric model (Left) for the steep meniscus lens preform having a circumferential crack and (right) meshing detail across the section A-A.

By following a similar methodology of modeling and mesh divisions, a penny shaped radial crack was oriented in the X-Y plane within the preform geometry having the half sector angle of 6.25° .

6.6 Fracture analysis methodology for lens molding in Abaqus

The fracture analysis in ABAQUS essentially involves crack modeling and finding important fracture mechanics quantities at the crack tip – such as stress intensity factor, energy release rate (J-integral), crack tip opening displacement etc. The quasi-static crack analysis as

opposed to the dynamic fracture analysis involves modeling of a crack such that it does not grow with respect to the time. Although the crack growth is not modeled in a quasi-static analysis, depending upon the stress intensity near the crack tip, the crack faces could easily open/separate and the above mentioned fracture mechanics quantities can be easily extracted as a function of time during the “transient analysis step” in Abaqus.

A mathematical crack can be inserted into the numerical domain in the form of a “seam crack” in ABAQUS/CAE and the fracture evaluation parameters such as stress intensity factor (K) and J-integral can be estimated by specifying a few input quantities by using the “*Contour Integral” command. Typically this requires a number of contours for extracting K or J values, the definition of crack tip nodes and the associated “q” vector(s) that define the crack extension direction if it were allowed to advance [14]. The crack tip singularity parameters can be specified in the “Edit Crack” dialogue box in ABAQUS/CAE [14] and a mid-side node parameter t ($0 < t < 1$) can be specified along with the choice of dependency of the duplicated nodes at the crack tip. The mid-side node parameter (t) would be equal to 0.25 for the configuration shown in Figure 6.2. The seam crack in 2D is usually in the form of a line or a curve, while in 3D it is usually in the form of a closed surface. Abaqus duplicates the nodes along the crack-line or crack face depending upon 2D or 3D nature of the problem allowing the crack to “open” during analysis. As explained earlier, to capture the singularity around a crack tip, a focused mesh approach was employed in ABAQUS; the focused mesh was made up of an array of wedge shaped elements (degenerated hexahedral elements with collapsed faces/side/nodes) in the case of 3D cracks.

The finite element analysis of lens molding involves about ten analysis stages during which the glass preform goes through series of thermo-mechanical cycles to take the desired lens shape. It was assumed that during pre-heating or pressing stage, due to the high temperature of

the preform, the presence of viscous stress relaxation mechanisms, it is less likely that stresses higher than critical value would generate during this period. Hence it was assumed that a crack in the form of inclusion or bubble present inside the lens preform during the slow cooling stage would experience a higher stress intensity as the lens is quickly cooled through the glass transition temperature ($T_g \pm 50^\circ\text{C}$). Thus, the crack geometry was “introduced” inside the preform domain at the beginning of the slow cooling stage. Due to technical limitations involved in Abaqus regarding the crack “introduction” or making “modifications” of the finite element model in between successive analysis steps, the original, single ten stage analysis run was broken down into two analysis runs: Run1 – first four stages from heating to pressing stage were analyzed and Run2 – remaining six stages from slow cooling to cooling up to room temperature were analyzed.

The important steps in fracture analysis of lens molding are explained below:

- A. During the first run (Run1) a crack geometry was modeled inside the lens preform as explained in the previous section at the beginning of the heating stage.
- B. The nodes belonging to the crack face elements of the crack geometry were constrained to have the same temperature and displacement degrees of freedom using tie constraints (*TIE option in Abaqus [14]). This ensured that the crack faces were *not* “open” until the pressing stage is finished.
- C. During the Run1 analysis, the thermo-mechanical history of the entire model during the last (pressing) stage was written in the state file (.stt) generated by Abaqus so that it can be used in the subsequent run (Run2).
- D. The input file for the next run (Run2) was modified to eliminate the tie constraint definition from the previous run (Run1). This technique enabled the crack to be “propagated” and the evaluation of the fracture related parameters during the

subsequent cooling stages. The input file modification also involved manually replacing the assembly definitions for top and bottom molds which was believed to be performed automatically by Abaqus.

- E. Apply the prescribed boundary conditions involving the initial state from the previous run (Run1) to the entire model and run the analysis. This boundary condition enables the temperature, displacement and stress states from the previous stage to be applied to the new geometry as the initial state. This is very important step and enabled the continuity of the solution variables during the next run.
- F. An independent analysis was made to be certain that both the analysis runs made use of the user subroutine definition (*UEXPAN) during the individual runs. Thus, the structural relaxation definition was implemented during each time step of the both analysis runs.
- G. The displacement and stresses along the crack front was requested as a time-history output in Abaqus. The CTOD value was extracted at the crack tips as shown in the figure 6.15 during post-processing of results.

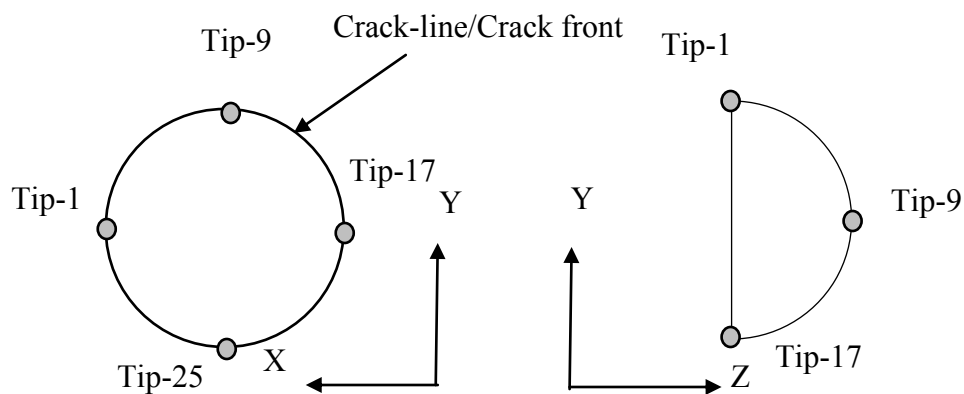


Figure 6.15. Crack tips used in reporting stress intensity factor results, radial crack (left) and circumferential crack (right).

H. For the two given crack configurations, the CTOD values calculated and compared for two different material models and two different cooling rates.

6.7 Computational Results of Crack Modeling Inside the Lens

The finite element analysis using Abaqus software was performed as outlined in the previous section on the steep meniscus lens and the results are presented in this section. The main aim of this work is to gain an understanding of the possible failure of a lens during the molding process. In order to assess the failure, the stresses near the crack tip were plotted at sections defined along the crack tips. The crack tip opening displacement was also calculated and plotted as a function of temperature for two crack configurations – circumferential and radial. The normal stress distribution near the crack tip at the end of the slow cooling stage was plotted in Figure 6.16 for two crack configurations. Three main parameters were considered for comparison, viscoelastic material behavior (VE), simplified material response with viscous assumption (ST), and increased cooling rate (by factor of three) during slow cooling stage with the VE material assumption.

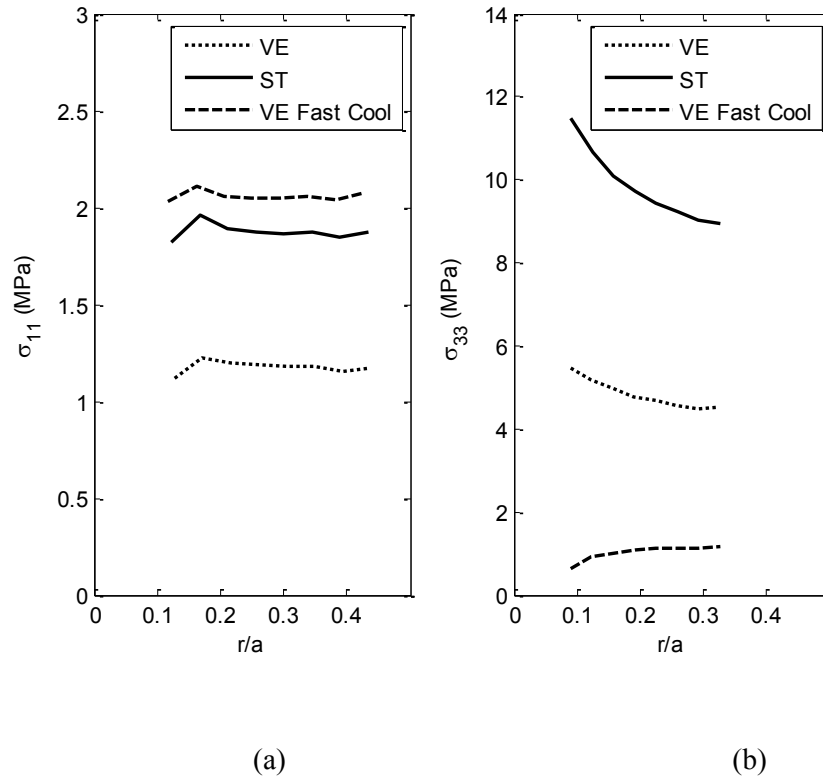
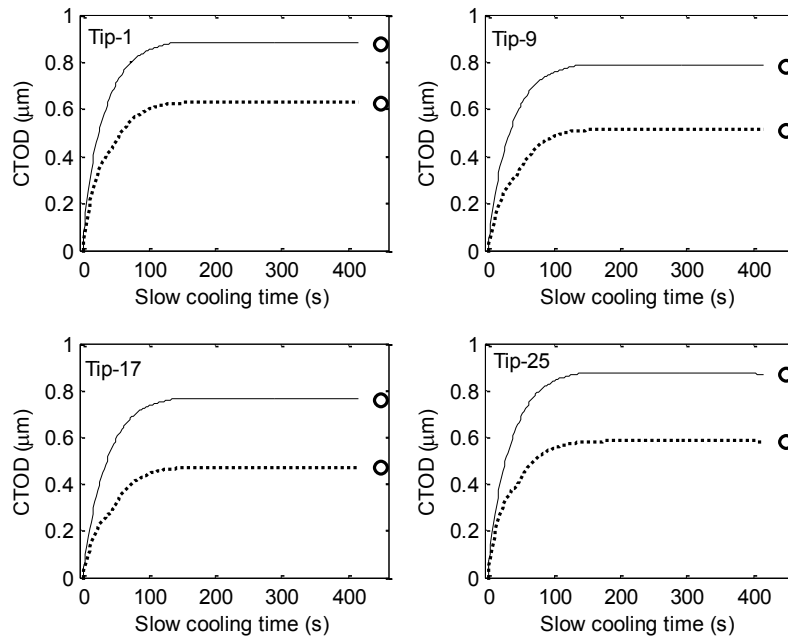
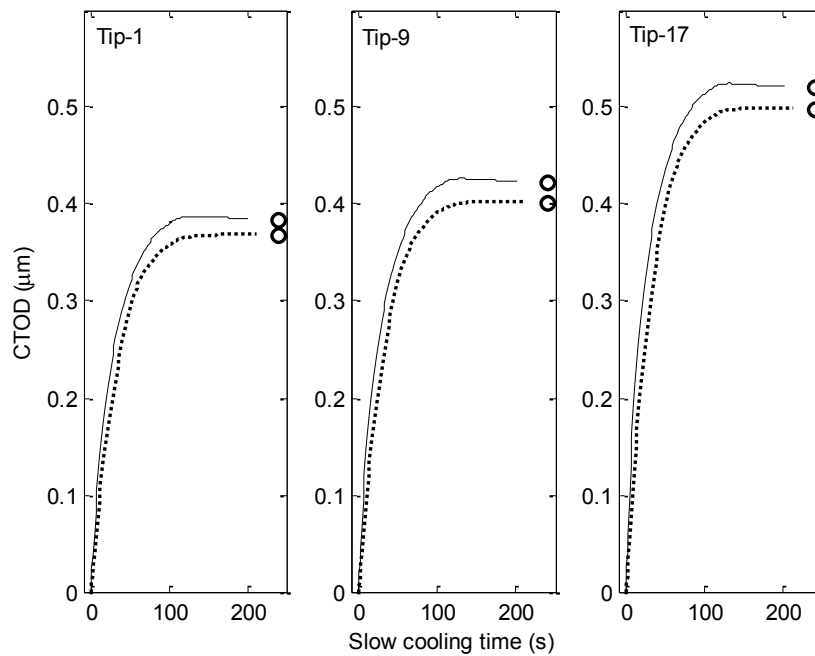


Figure 6.16. Normal stress distribution near the crack tip for (a) Circumferential crack, (b) Radial crack

The results in Figure 6.16 show the normal stresses in the vicinity of radial crack are higher in magnitude than those in the circumferential crack configuration. For the circumferential crack, the stresses do not vary significantly along the crack plane away from the crack tip ($r/a = 0$) and the stresses for the case with higher cooling rate dominate. For the radial crack configuration, the variation of stresses along the crack plane is noticeable with the viscous material behavior assumption case dominating among three cases. Crack tip opening displacement (CTOD) values for different material behavior will be considered next.



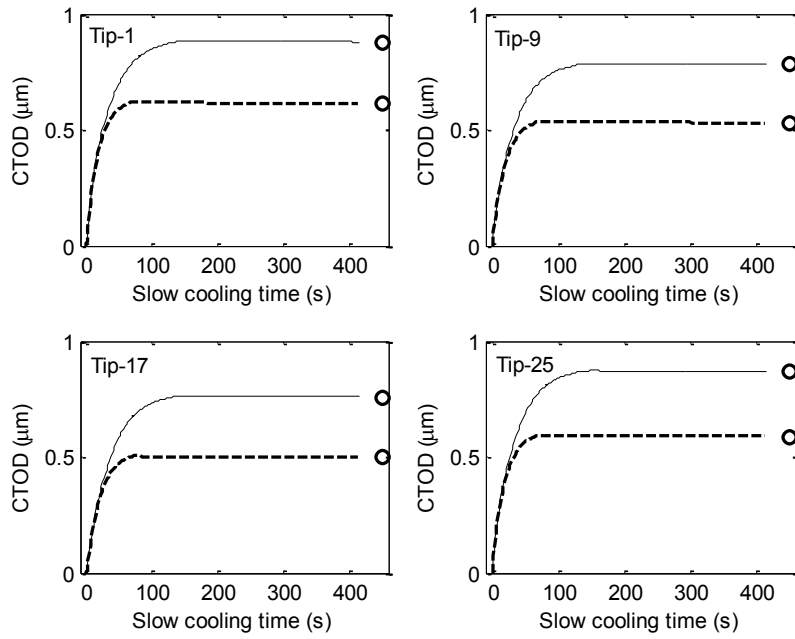
(a)



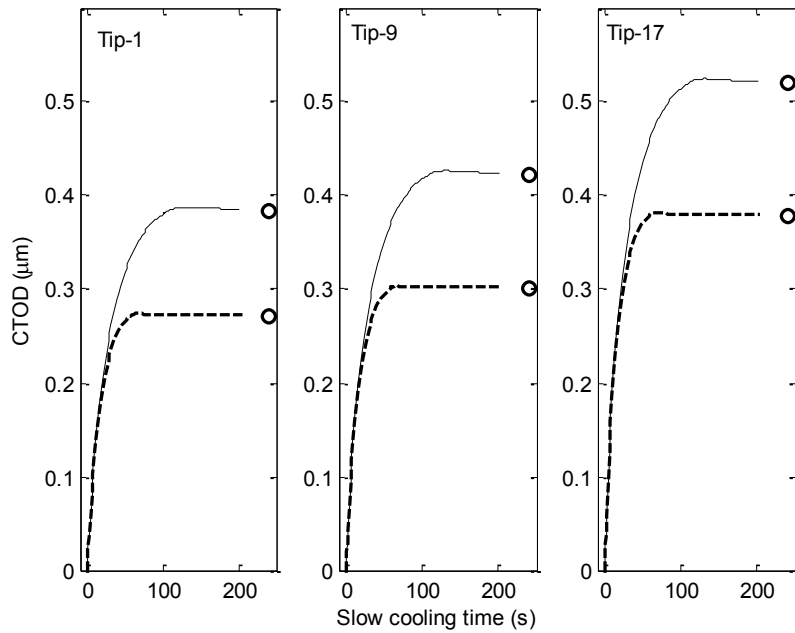
(b)

Figure 6.17 Comparison of CTOD for Full VE material (solid) and Single term shear relaxation (dashed) for (a) Radial, (b) Circumferential cracks. Circles indicate respective asymptotic values at end of final cooling stage.

The CTOD for the two material models is compared in Figure 6.17 for two crack configurations for slow cooling time period of about 400 s. The temperature near the crack tip corresponding at the beginning of slow cooling time was found to be about 585°C while, corresponding to $t = 200\text{s}$ and 400s , it was found to be about 538°C and 480°C respectively. As expected, the results in Figure 6.9 show that a full viscoelastic model (VE) has higher opening than the single term viscous (VE) model as the extra viscoelastic displacement mechanisms are *not* present in the later one. The difference in CTOD values for the different crack configurations can be also noted. The crack opens twice as much for the radial crack than the circumferential crack, suggesting radial crack is worst failure mode among the two for the loading and geometry considered. This also suggests that the circumferential stress dominate over radial stresses during cooling phase of the lens molding. Next, the effect of changing the slow cooling rate on the CTOD will be examined. The cooling rate during the slow cooling stage for most of the lens molding related processes is kept minimal as the preform lens is susceptible to failure as it passes through the glass transition temperature. Slow cooling rate was changed from $q_0=0.287^\circ\text{C/s}$ in the previous example to 0.864°C/s to assess the effect on the stresses and CTOD.



(a)



(b)

Figure 6.18. Comparison of CTOD for two cooling rates: $q_0 = 0.288^\circ\text{C/s}$ (solid) and $q = 3 \times q_0 = 0.864^\circ\text{C/s}$ (dashed) for two crack configurations (a) Radial, (b) Circumferential. The Viscoelastic material behavior (VE) was assumed. Circles indicate respective asymptotic values at end of final cooling stage.

The Figure 6.18 shows the comparison of the CTOD for two cooling rates considered for the viscoelastic material behavior for both the crack configurations. At the beginning of slow cooling, $t=0s$, the temperature near the crack tip is about $585^{\circ}C$ for both cooling cases considered. After about 200s of the slow cooling phase, the crack tip temperature for $q_0 = 0.288^{\circ}C/s$ case was found to be about $538^{\circ}C$, while for the case of $q = 0.864^{\circ}C/s$, it was found to be about $473^{\circ}C$. CTOD value drops as cooling rate increases for both crack configurations. The reason for this behavior is that the glass, initially hot, cools quickly due to increased cooling rate that arrests the viscous deformation near the crack tip region and prevents the more opening of crack flanks. Although the CTOD is smaller than the previous example, the residual stresses in this case are higher as they are frozen in glass during the rapid cooling.

6.8 Discussion

This chapter considers a problem of failure of lens due to possibility of preexisting flaw in form of inclusion or bubble inside the preform and severity of thermo-mechanical loading during the molding operation. It was assumed that such a flaw exists inside the preform at the highly localized region that experiences the highest magnitude of normal stresses. Such region was identified based on 2D axisymmetric simulations and was subsequently chosen to model a penny shaped crack inside a 3D sector model. Based on the previous knowledge of failure of lens, two crack geometry configurations – radial and circumferential crack were tested. An example problem of a penny shaped crack subjected to remote tension was solved using 3D finite model in Abaqus to understand the effect of mesh size near the crack tip on stress intensity field. The results of this analysis were found to be within 0.5% of the analytical solution. Based on this information, a detailed finite element models for each crack configuration inside the actual preform were created and analyzed in Abaqus. The glass preform is subjected to cooling through

transition temperature during slow cooling stage under presence of maintenance force. This being the severe stage when a potential crack may grow under the influence of favorable stress field, a mathematical crack was “introduced” inside lens geometry. During this stage, high temperatures prevail inside the lens preform and the viscous mechanisms are also active, hence, the stress intensity or the J-integral were not useful fracture parameters to predict the fracture. Crack tip opening displacement (CTOD), being independent of the material behavior along with the stresses ahead of the crack tip were the parameters that were chosen to be favorable for this problem.

6.9 Conclusion

- The comparison of the stress field near the crack tip obtained by using FEA with the analytical results in case of 2D and 3D crack cases show satisfactory results for sufficiently refined mesh. Results were obtained close to 1% with the theoretical answer (Figures 6.3, 6.4 and 6.6).
- For a viscoelastic (VE) plate subjected to remote tension for a long time, the stresses near the crack tip for initial temperature $T_0 = 470^\circ\text{C}$ and 530°C are found to be agreeing well with the stresses near crack tip in an elastic plate. Due to large deformations, the stresses for VE case with $T_0 = 590^\circ\text{C}$ do not agree with elastic stresses except at very early stage of loading (Refer to Figure 6.7). This makes the use of stress intensity factor (K) unusable at higher temperatures.
- The Crack Tip Opening Displacement (CTOD) is used alternatively as a fracture parameter at high temperature. The 3D penny shaped example subjected to thermo-mechanical loading shows effect of material behavior on CTOD. (Figure 6.9).

- Based on the lens molding simulation containing crack, the stress distribution near the crack tip indicate the radial crack configuration is more severe than the circumferential crack. (Figure 6.16). Comparison of the CTOD values obtained from the simulation, also support this conclusion. The CTOD values for radial crack are about twice as higher than those of circumferential crack. (Figure 6.17)
- The full viscoelastic material is likely to open the crack faces more than the material with the single term shear assumption (Figure 6.17). Thus the full VE assumption in simulations give a conservative fracture results than the single term shear relaxation assumption.
- The CTOD values are lowered as the cooling rate during slow cooling stage was increased by a factor of three.

Reference:

1. T. L. Anderson, Fracture mechanics: fundamentals and applications. CRC press, 2005.
2. T. Rouxel, J-C Sangleboeuf, "The brittle to ductile transition in a soda-lime-silica glass", Journal of non-crystalline solids, 271, (2000), pp. 224-235.
3. Cha. et.al, "Effect of temperature on molding of chalcogenide glass lenses for infrared imaging applications." Applied Optics, 49, 9, (2010), pp. 1607-1613.
4. H. H. Chien, K. J. Ma, C.H. Kuo and S.W Huang, " Effect of Al₂O₃ coated glass preform on glass mold sticking behavior", Surface and Coatings Technology, In Press.
5. M. Onozawa, Optical glass for mold pressing having softening capability at low temperature, US patent no. 5607886. (1997).
6. K. J. Ma et.al, "Molding Plano-convex lenses using through-Hole WC/Co plate as a mold", Applied Mechanics Materials, Vol. 217-219, (2012), pp. 2138-2141.
7. A.Q. Tool, "Relation between elastic deformability and thermal expansion of glass in its annealing range", Journal of American Ceramic Society, 29, 9, (1946), pp. 240-253.
8. A. Symmons and B.Auz, "Design considerations and manufacturing limitations of Insert Precision Glass Molding (IPGM)", Proceedings of SPIE, 8489, Polymer Optics and Molded Glass Optics: Design, Fabrication, and Materials II, 84890H,

- (2012), pp. Cha. et.al, "Fabrication of molded Chalcogenide-glass lens for thermal imaging application", *Applied Optics*, 51, 23, (2012), pp. 5649-5656.
9. M. L. Williams, "On the stress distribution at the base of a stationary crack", *Journal of Applied Mechanics*, 24 (1957), pp. 109-114.
 10. H.M. Westergaard, "Bearing pressures and Cracks", *Journal of Applied Mechanics*, 6, 1939, pp. 49-53.
 11. www.solidmechanics.org
 12. H. Tada, P. C. Paris, and G. R. Irwin. *The Analysis of Cracks Handbook*. New York: ASME Press, 2000.
 13. Chan, S. K., I. S. Tuba, and W. K. Wilson. "On the finite element method in linear fracture mechanics", *Engineering Fracture Mechanics*, 2, 1, (1970), pp. 1-17.
 14. *Abaqus Analysis User's manual*, version 6.10 (2010), Simulia, Providence RI.
 15. Schott Technical Information on Advanced Optics: TIE-28: Bubbles and Inclusions in Optical Glass.
 16. Schott Technical Information on Advanced Optics: TIE-40: Optical Glass for Precision Molding.
 17. B. Ananthasayanam, M. Capitaneanu and P.F. Joseph, "Determination of higher order coefficients and zones of dominance using a singular integral equation approach," *Engineering Fracture Mechanics* 74, no.13, (2007), pp. 2099-2131.
 18. C.Y. Hui and A. Ruina, "Why K? Higher order singularities and small scale yielding," *International Journal of Fracture*, 72, (1995), pp. 97-120.
 19. I. Sneddon, "The distribution of stress in neighbourhood of a crack in an elastic solid," *Proceedings of Royal Society of London Series A, Mathematical and Physical Sciences*, 187.1009 (1946), pp. 229-260.

CONCLUSIONS AND FUTURE WORK

7.1 Discussion

The work presented in this dissertation addresses the importance of a precise determination of the thermo-mechanical material property inputs of optical glass for an accurate prediction of the state of stress during the complex thermo-mechanical loading of a glass preform during the Precision Glass Molding (PGM) process. In addition to an accurate prediction of the residual stress state in a lens, birefringence and fracture were also considered as these are direct consequences of stress. As with many other simulations involving so-called advanced materials, the potential for the success of computational modeling to guide glass forming processing such as precision glass molding is hindered by a lack of material property inputs. Through experience with performing validation studies on the final size and shape of a molded lens [1, 2], it was apparent that accurate experimental characterization of the temperature dependent stress relaxation behavior of optical glass is well behind what is required. Therefore, the focus of this dissertation was twofold: first to identify and quantify the stress relaxation behaviors that are required to make accurate predictions of the stress state in a molded lens and second, to show how a simplified experimental approach, if applied correctly, can be used to provide the stress relaxation behaviors with sufficient accuracy.

As discussed in Chapter 2, ideally constant temperature stress relaxation experiments should be performed to isolate the responses of a targeted glass to each of the following: shear, dilatation, initial elastic response, and viscous flow. Four separate experiments will then provide these four characterizations. In addition, these experiments must be performed at the full range of temperatures expected in the processing, understanding that the interesting temperature range is

between T_g and T_g+50 . Unfortunately such data is very difficult to obtain and is unavailable in the open literature for a molding glass. However, fortunately the literature does provides one accurate characterization [3] of an oxide glass. This characterization was used to show that a full modeling of the dilation response, which is the most difficulty behavior to obtain experimentally, is unnecessary for accurate predictions of the stress state. Furthermore, it was demonstrated how to use the cylinder compression test with a standard PPV machine to obtain viscosity very accurately and to make a reasonable approximation for the viscoelastic response in shear. The direct measurement of the viscosity on the order of 10^8 Pa·s and higher is significant since standard tests for this purpose are inaccurate at this important level.

7.2 Conclusions

The following conclusions can be made:

- Viscoelastic behavior of optical glass during molding is often simplified by assuming the material has a single term prony series in shear and an elastic response in bulk. However, while this simplifying assumption is useful for predictions of, for example, the size and shape of a lens, it will lead to an overestimation of residual stresses and birefringence inside the lens, which is a conservative result. For a more accurate, non-conservative estimate of the level of stress it is important to more precisely characterize stress relaxation, which is a non-trivial task.
- Fracture simulations of a penny shaped crack inside a lens during the cooling stage with crack configurations in the radial and circumferential directions reveal the same trend for stresses as described above. However, the crack tip opening displacement (CTOD) was higher for the full viscoelastic material behavior than that for the material with a single

term response in shear. For cases considered, the radial orientation had higher stress levels than the circumferential orientation.

- A viscoelastic creep experiment involving a cylinder compressed between two flat surfaces, i.e., the cylinder compression test which can be performed in a PPV machine, was utilized to compute viscosity and viscoelastic constants assuming the friction condition at the interface between the sample and mold is known (no-slip was used in Chapter 4), the sample has minimal non-uniform temperature gradient, the cylindrical surfaces of the sample do not come in contact with the molds, the horizontal surfaces of the sample are flat and parallel to the mold surfaces and the rate of loading is small.
- Parallel Plate Viscometry was extended to viscosity above 10^8 Pa·s as long as the friction coefficient is known for the glass/mold combination at the temperature of interest. An approximate viscosity expression provided a reasonable estimate of the viscosity for the full range of friction behavior, cylinder geometry ($0.25 \leq H/D \leq 1.0$) and viscosity (10^7 Pa·s $\leq \mu \leq 10^{11}$ Pa·s). This approach can be extended to other glass types.
- A thin cylinder with a no-slip boundary condition can be used to evaluate the “bulk” relaxation response of glass. Numerical experiments with an SLS glass specimen with a height to diameter ratio of 0.1, about 98% of the total viscoelastic displacement during the creep test was attributed to the bulk relaxation mechanism. However, based on experimental data obtained herein, this percentage was only about 8% for L-BAL35, which is a moldable glass.

7.3 Future Work

Based on this research, the following topics of future work have been identified:

1. The process of finding the viscoelastic constants based on the creep displacement of the cylinder, can be optimized. Ideally, the optimizer would determine the number of Prony series terms to use and also the values of the parameters. Determination of the viscosity can also be optimized.
2. An alternative to an approach of using series of exponential terms to represent the stress relaxation function, a fractional derivative viscoelastic representation can be used to fit the relaxation data with a fewer number of parameters, which is an advantage. This will require a UMAT implementation of the calculation scheme in Abaqus.
3. Further experimental work is necessary to understand and achieve the no-slip boundary condition. Results in Chapter 4 indicate that partial slip may have occurred which would increase the measured displacement. This means that the no-slip assumption would underestimate the actual displacement. Another area of future work for the experimentalist would be to use molds with special coatings that provide very low friction. Creep data for this case might be more reliable than the no-slip data. In this case a no friction assumption would overestimate the actual displacement. Ideally, both experiments would be performed to provide upper and lower bounds.
4. By utilizing the fracture modeling technique, a process parameter optimization can be performed to reduce the production cycle time of lens molding process. However, this task requires experimental data for the fracture of glass as a function of temperature.

5. Experiments for high temperature rate dependent fracture characterization of optical glass can be useful in understanding the crack growth in viscoelastic materials subjected to thermo-mechanical stress field. A popular mode-I testing technique (Single edge notch bend or disc-shaped compact tension) can be used to determine the load (F) vs. opening displacement (Δ) for a suitable test. Then, a finite element model of the specimen based on cohesive elements can be used to estimate the fracture parameters by correlating the F- Δ obtained from simulations with the experimental results.

References

1. B. Ananthasayanam, P F Joseph, D. Joshi, S. Gaylord, L. Petit, V Y Blouin, K C Richardson, D. Cler, M. Stairiker, M. Tardiff, "Final shape of Precision molded optics: Part I - Computational approach, material definitions and effect of lens shape," *Journal of Thermal stresses*, 35, (2012) pp.550-578.
2. B. Ananthasayanam, P F Joseph, D. Joshi, S. Gaylord, L. Petit, V Y Blouin, K C Richardson, D. Cler, M. Stairiker, M. Tardiff, "Final shape of Precision molded optics: Part II - Validation and sensitivity to material properties and process parameters," *Journal of Thermal stresses*, 35, (2012), pp.614-636.
3. L. Duffrene, R. Gy, H. Burlet, and R. Piques, "Multiaxial linear viscoelastic behavior of soda-lime-silica glass based on a generalized Maxwell model," *Soc. Rheol.*, **41**, 1997, pp. 1021-1038.